IMPERIAL COLLEGE LONDON

LONG-TERM STRUCTURAL HEALTH MONITORING OF PLATE-LIKE STRUCTURES USING DISTRIBUTED GUIDED WAVE SENSORS

by

Vatche Armen Attarian

A thesis submitted to Imperial College London for the degree of
Doctor of Philosophy

Department of Mechanical Engineering
Imperial College London
London SW7 2AZ

August 2013

Declaration of originality

The contents of this thesis are the results of my own independent research conducted under the supervision of Dr. Frédéric Cegla and Prof. Peter Cawley. Where I have made use of the work of others, I have given full acknowledgment.

Vatche Attarian

27/08/2013

Copyright declaration

Abstract

Aircraft, containers, and storage tanks contain plate-like structures that are safety critical. The structures often undergo non-destructive inspections. The inspection frequency tends to be over-conservatively high, and it may be possible to reduce the intervals between inspections to realize cost savings. This goal can possibly be realized by automated structural health monitoring (SHM) of structures using sparse active guided wave sensor arrays. Guided waves are sensitive to small defects and can propagate long distances across feature dense plates. Thus, a guided wave SHM system that enables reliable detection of critical defects or monitoring of their growth can potentially be used to reduce the frequency of inspections for real structures.

Industrial guided wave SHM systems must be reliable throughout prolonged exposure to temperature, humidity, and loading changes encountered in operation. Research at Imperial College shows that temperature compensation and subtraction between monitored guided wave signals and baselines acquired from healthy plates enables detection of 1.5% reflection change over areas ~1 m^2 in the presence of thermal swings and uniform liquid layers. These results and findings from scattering studies indicate it may be possible to detect reflections from hole type defects and notches affecting structures during their operation. An issue is that demonstrations of SHM system capabilities have only been shown in controlled laboratory tests within short periods following baseline acquisition. There is concern whether sustained exposure to service conditions will subject transducer elements to irreversible changes and introduce variability in baseline subtraction results that would mask signals due to slowly growing damage.

This thesis studies the reliability of guided wave SHM for monitoring plate-like structures over longer time periods. The theoretical characteristics of the fundamental Lamb waves and their use to monitor and detect damage are reviewed. Strategies for sensing and signal processing are described alongside experimental validation of their performance. The effectiveness of the SHM system is tested in experiments where damage-free plates are exposed to British weather as well as thermal variations in an environmental chamber. The monitoring capabilities of bonded piezoelectric sensors are quantified and compared to the performance achieved using electromagnetic acoustic transducers. Experimental results and findings from simulations of bonded piezoelectric transduction establish that performances achieved with bonded sensors degrade due to variations in the properties of adhesives used to attach sensors to plates. EMATs are relatively stable and capable of enabling detection of 1.5% reflection change at points away from the edges of plates after sustained exposure to thermal cycling loads.

Acknowledgments

I would like to thank various people for their assistance and encouragement.

I am grateful to my supervisor Dr. Frédéric Cegla for his guidance, support, as well as commitment to the adventure. I have benefited much from his mentorship as well as that from my advisor Prof. Peter Cawley from whom I have learned a great deal and whose commitment to R&D has been inspirational. I thank you for your efforts alongside those of Prof. Mike Lowe to cultivate such a well resourced research group, and for providing me the opportunity of joining it.

Thanks go to all colleagues of the NDE Group who have contributed their help and advice. I would like to especially thank Dr. Thomas Clarke and Prof. Peter Nagy for the useful technical discussions. I would also like to acknowledge Joe Corcoran and Attila Gajdacsi for coding the data acquisition programme I employed in Chapter 6, Dr. Xiaoyu Xi for developing the template on which I have typeset this thesis, and Dr. Peter Huthwaite for enduring my questions about English. Furthermore, I am indebted to Mr. Dave Tomlin who consistently delivered precisely machined prototypes when he was at Imperial. God bless your kind soul Dave.

A heartfelt thanks go to my mother Marie and father Armen whose love has meant the world to me during this undertaking. And, Raffi, you showed me to the door that passing through which I have come to realize that there is little need as yet for me to search for where my time has gone. Your sacrifices amount to at least as many as the number I made in working on this.

Contents

1 Introduction 30

1.1 Motivation 30

1.2 Thesis outline 33

2 Guided waves in plates and SHM principles 35

2.1 Guided wave propagation in plates 35

2.1.1 Modes of propagation 36

2.1.2 Dispersion 37

2.1.3 Interactions with defects and structural features 39

2.1.4 Environmental effects 42

2.2 Monitoring techniques 44

2.2.1 Arrangement and operational modes of sensors 44

2.2.2 Damage detection 45

2.2.3 Compensation for environmental effects 49

2.3 Guided wave SHM system for long term stability evaluations 51

2.4 Summary 53

3 Strategies for sensing and signal processing 55

3.1 Introduction 55

3.2 Transducer type selection 56

3.3 Bonded piezoelectric sensor design 57

3.3.1 Wave propagation model and its theoretical validation 57

3.3.2 Bonded PZT transducer and excitation of the S0 mode 59

3.3.3 Encapsulation 64

3.3.4 Experimental validations 71

3.4 Signal processing methods 74

3.4.1 Automated temperature compensation and baseline subtraction 75

3.4.2 Imaging 80

3.5 Summary 83

4 Initial long term weather exposure experiments 85

4.1 Introduction 85

4.2 Background 86

4.3 Outdoor monitoring experiment 87

4.3.1 Specimen and monitoring location 87

4.3.2 Baselines and noise floor 89

4.3.3 Monitoring results 91

4.4 Variability analysis 96

4.4.1 Studies of the first S0 arrival 96

4.4.2 Unexplained noise influences 99

4.5 Tests to determine causes of SNR declines 103

4.5.1 Electrical impedance measurements 104

4.5.2 Normal incidence ultrasonic scans 105

4.5.3 Visual inspection of adhesive layers 110

4.6 Summary 111

5 Long term stability with temperature cycling 113

5.1 Introduction 113

5.2 SHM experiments 114

5.2.1 Experimental setup and monitoring timeline 114

5.2.2 Baseline subtraction stability 117

5.2.3 Investigation into sources of variability 120

5.3 Simulations 123

5.3.1 FE model and validation of simulation techniques 123

5.3.2 Sensitivity to adhesive properties 127

5.4 Measurements on bulk adhesive samples 129

5.4.1 Specimens and test methods 129

5.4.2 Signal processing and data 130

5.4.3 Discussion of results 130

5.5 Summary 131

6 Stability of an alternative transduction mechanism 132

6.1 Introduction 132

6.2 Electromagnetic acoustic transducers 133

6.2.1 EMAT for excitation of the S0 mode on steel plates 133

6.2.2 Pitch catch data acquisition at low voltages 136

6.3 Monitoring experiments 141

6.3.1 Stability study design 141

6.3.2 Monitoring results 144

6.3.3 Variability analysis 150

6.4 Summary 152

7 Conclusions 154

7.1 Thesis review 154

7.2 Findings 156

7.2.1 Bonded piezoelectric sensors 156

7.2.2 Low voltage EMATs 158

7.3 Implications for SHM R&D 158

7.4 Suggestions of future work 159

Appendices

A Material properties 163

A.1 FE modeling 163

A.2 SPECTRUM simulations 164

B First radial resonance frequency of bonded PZT discs 165

C Correcting data for signal changes in the pulse at the S0 arrival 167

D Sensitivity of pitch catch data to the properties of the bond between PZTs and a plate 169

References 172

List of Figures

1.1 (a) The fuselage of an airplane, (b) shipping containers, and (c) an oil storage tank are examples of plate-like structures in ageing infrastructural systems. 30

2.1 (a) Phase velocities with overlaid sketches of material deformations in aluminum plates which illustrate mode shapes of the S0 mode and A0 mode and indications of their respective wavelengths λ_{S0} and λ_{A0} at 100 kHz on a 2 mm thick plate, and (b) the group velocities of the various plate waves. Figures produced using DISPERSE [39]. 37

2.2 (a) Five cycled, 100 kHz toneburst as excitation signal and as simulated wavepackets of the (b) S0 mode and (c) the A0 mode which have propagated distances of 500 mm (black) and 1000 mm (grey) on a 2 mm thick aluminum plate. Figures produced using DISPERSE [39]. 38

2.3 The analytical amplitude of (a) 1000 kHz-mm A0 scatter and (b) 200 kHz-mm S0 scatter from through holes of diameters D on 2 mm thick steel plates which result from the interaction of waves propagating 500 mm to the holes and 500 mm onwards to monitoring points. Results are shown as dB values normalized by the input amplitude and were calculated using the analytical implementations in [24]. 41

2.4 The amplitude of 950 kHz-mm S0 scatter from 15 mm long, 2 mm wide through thickness notches oriented along 90°-270°on a 3.18 mm thick aluminum plate which result with the interaction of waves that propagate 500 mm in the directions indicated by the arrows to the notch and 500 mm onwards to monitoring points. Results are adapted from [47], and are shown as dB values normalized by the amplitude of the input being at incident angles of (a) 0°, (b) -45°, and (b) -90°. . 42

2.5 The predicted effects of δT=1^{o}C on time shifts associated with crests of S0 and A0 waves of aluminum plates (values scale linearly with p and δT.) The results were calculated using v_{ph} from DISPERSE [39] and $\frac{\partial v_{\mathrm{ph}}}{\partial T}$ from [56]. 44

2.6 (a) Pitch catch signals collected on a 2 mm thick, 1.25 m square aluminum plate using a sensor pair with the transmitting PZT at (x = 0.8 m, y = 0.3 m) excited by 5 cycled, 100 kHz tonebursts and a receiving PZT at (x = 0.8 m, y = 0.6 m) recording the data with 100 averages from the damage-free plate, $b(t)$, and after a D = 5 mm hole is drilled at (x = 0.29 m, y = 0.72 m), $c(t)$, and (b) a schematic of the ideal result from the perfect subtraction of the signals in (a). 47

2.7 The results obtained from the subtraction between the experimental baseline signal acquired from the healthy structure and current signal acquired after the structure has been damaged (of Figure 2.6(a)) for there being 1°C discrepancy in temperatures at which the signals are recorded along with the results obtained after processing data using the compensation algorithms described in detail in Chapter 3. 51

3.1 (a) Axisymmetric FE model of the plate having thickness th_{plate} and large arrows that indicate the direction and location of displacement inputs. Discrepancy in (b) the ratio of surface in-plane to out-of-plane displacements and (c) the phase velocities of simulated S0 mode propagation; errors are relative to values from DISPERSE. 58

3.2 Axisymmetric FE model of ∅ 20 mm PZT disc having thickness th_{PZT} and 250 µm bonding layer on an aluminum plate of thickness th_{plate}; the illustration is not to scale, has top and bottom electrodes of the PZT designated using a +V and ground symbol respectively, and hollow circles indicating points at which velocities were monitored. . . 61

3.3 The magnitudes of the velocity responses for the S0 mode and the A0 mode obtained from the simulated motions of the mid-plate thickness node at r = 300 mm with 1 V applied to bonded PZTs having (a) th_{PZT} =1 mm on a 5 mm thick plate and (b) th_{PZT} =0.5 mm on a 2 mm thick plate. 63

3.4 The energy in 5 cycled tonebursts of the S0 mode relative to that in the weaker A0 pulse at r =300 mm as a function of f_c of tonebursts applied to PZT discs having (a) th_{PZT} =1 mm on 5 mm thick plates and (b) th_{PZT} =0.5 mm on 2 mm thick plates. The gray lines indicate the resonance frequencies f_r of the bonded PZT discs. 64

3.5 Isometric views of the cap which show (a) the winding of wires and (b) the housing for PZT discs as well as (c) an axisymmetric cross section of the encapsulated transducer with parameters identified which were finalized using FE analysis. 65

3.6 The magnitudes of the velocity responses for the S0 mode and the A0 mode obtained from simulated mid-plate thickness motions at r = 300 mm with 1 V excitation of a bonded 20 mm diameter, 0.5 mm thick PZT disc that is encapsulated using an Al cap of h =10 mm, th_{ring} =2 mm on a 2 mm thick Al plate. 65

3.7 Operational deflection shapes (ODSs) of the bonded 20 mm diameter, 0.5 mm thick PZT disc at (a) 50 kHz, (b) the ODS of the PZT encapsulated with an aluminum cap of h =10 mm, th_{ring} =2 mm at 50 kHz, and (c)-(d) the ODSs at 110 kHz; displacement magnitudes are indicated via grayscale bands. Note the scales in (a)-(b) are different from those in (c)-(d). 66

3.8 The magnitudes of the velocity responses for the S0 mode obtained from simulated mid-plate thickness motions at r = 300 mm with 1 V excitation of 0.5 mm thick bonded PZTs which are encapsulated with aluminum caps having th_{ring} =2 mm and (a) h =10-14 mm as well as (b) h =6-8 mm along with the result for the unencapsulated PZT on a 2 mm thick plate. 67

3.9 The magnitudes of the velocity responses for (a) the S0 mode and (b) the A0 mode obtained from simulated mid-plate thickness motions at r =300 mm with voltage excitation of the 20 mm diameter, 0.5 mm thick PZT disc, and the results obtained with similar excitation of the PZT encapsulated using caps made of anodized aluminum or HDPE and which have h =6 mm, th_{ring} =1 mm. 69

3.10 The S0 wavepacket and that of the weaker A0 pulse at a distance of 300 mm from encapsulated (HDPE caps of h =6 mm, th_{ring} =1 mm) and unencapsulated (a) 20 mm diameter, 0.5 mm thick PZTs excited using 5 cycled, 100 kHz tonebursts on 2 mm thick plates and (b) the results from FE analyses with 1 mm thick versions of the PZT excited using 8 cycled, 170 kHz tonebursts on 5 mm thick plates; signals calculated using the particle velocities monitored at the mid-plate thickness node of FE models. 70

3.11 (a) The laser doppler vibrometer (LDV) measurement configuration and plots comparing the measured (dotted lines) and simulated (solid lines) spectra of the in-plane S0 and out-of-plane A0 velocities on the surface of (a) 2 mm and (b) 5 mm thick aluminum plates at r =300 mm and r =420 mm, respectively, from 20 mm diameter bonded PZT discs of th_{PZT} that are excited with the inputs used in Figure 3.9; maxima in S0 spectra have been used to normalize (b)-(c) to allow comparisons. 72

3.12 Pitch catch data obtained using (a) unencapsulated and (b) encapsulated 20 mm diameter, 0.5 mm thick PZTs bonded on a 2 mm thick, 1.25 m square aluminum plate with separations of 300 mm in the configuration of Figure 3.11(a) and (c)-(d) the data obtained using the 1 mm thick PZTs bonded with separations of 420 mm in the configuration of Figure 3.11(a) on the 5 mm thick plate; the tonebursts used in Figure 3.9 were applied to the transmitting PZTs. 74

3.13 Block diagram of the temperature compensation and baseline subtraction algorithm which combines subtraction, optimal baseline selection (OBS), and optimal stretch in order to calculate the temperature compensated residual signal. 77

3.14 Amplitudes of residuals relative to the S0 arrival amplitude obtained by subtracting a current signal acquired at 40°C from optimally stretched versions of baselines collected at (a) 40.5°C and (b) 42°C using a sensor pair on a 5 mm thick aluminum plate. 79

3.15 Amplitudes of residuals relative to the S0 arrival amplitude that result from (a) subtracting the signals in Figure 2.5 as well as results from subtracting $c(t)$ from (b) the optimal baseline and (c) an optimally stretched version of this baseline. 80

3.16 (a) Array of bonded PZTs (circles) on a 2 mm thick container panel and (b) the residuals from compensated baseline subtraction of pitch catch data monitored using transmitting and receiving sensors 4 and 1, respectively, from the undamaged structure and after a ∅ 10 mm hole is drilled at the X in (a). Photo and data adapted from [36]. . . . 82

3.17 Images of the 2.1 m x 1.25 m area of the container panel marked using dashed lines in Figure 3.17 in its (a) damage-free state and (b) in the presence of a hole drilled at the marked X. Sensor locations are shown using circles and results were obtained by processing array data with the ellipse algorithm. Reproduced using data from [36]. . . 83

4.1 (a) Schematic of the array of sensors (numbered circles) and the thermocouples (squares) on the 5 mm thick, 1.25 m square plate, (b) diagram of the data acquisition system, and (c) photograph of the instrumented anodized aluminum plate and steel weights (circled) which corroded outdoors; arrows in (a) originate at the plate center. . 89

4.2 (a) Example baseline signal (grey) recorded at 40.5°C and the beam spread corrected difference signal (black) calculated by subtracting signal recorded at 40°C from optimally stretched version of the baseline, and (b) the amplitudes of the residual relative to that of the S0 arrival. 90

4.3 Images of the defect-free plate at various temperatures with 0.5°C gap to the nearest baseline with the sensor locations superimposed using circles. Results were obtained by processing array data acquired in the environmental chamber with the ellipse algorithm and are shown on a [-45,-30] dB scale to allow comparisons. 91

4.4 The mean values of beam spread corrected residual signals (relative to 1st arrival amplitudes) calculated after temperature compensation and subtraction between monitored signals and baselines collected in the environmental chamber. Results shown for various combinations of transmitting and receiving sensors. 93

4.5 Images of the plate generated using the processed residuals for SHM data collected outdoors (a) 1, (b) 3, (c) 6, and (d) 11 weeks after baseline collection; results shown on a [-45,-30] dB scale to allow comparisons. 94

4.6 The mean values $\bar{I}$ of I within the area surrounded by sensors and the values within a standard deviation σ_I of the mean as a function of monitoring time t. The line is the linear fit $\hat{I}$ applied to the mean values. 95

4.7 (a) The standard statistics of pixel intensities within the area bounded by the sensors versus temperature and linear fit to mean values along with (b) errors in regressions using monitoring time (black) and temperature (gray) as fit variables. 95

4.8 The radial distribution function, $M(r)$, for increasing monitoring times. 96

4.9 (a) The amplitude of the first S0 arrival and (b) raw waveform SNR in the progression of the outdoor test. 98

4.10 Wavepackets at the arrival time of the directly transmitted S0 mode in data monitored using sensor pairs (a) Transmitter 1 - Receiver 3 and (b) Transmitter 4 - Receiver 1 when plate temperatures were 15°±0.5°C; results normalized by the S0 arrival amplitude. 98

4.11 (a) Generated signal of S0 arrivals between transmitting PZT 1 and receiving PZT 2 with inset of zoomed in region showing time delays for ±0.25°C gaps in 0.1 µs window near zero crossing of 102 µs and (b) the band-limited random noise signal (gray) which is added to the signal of (a) to produce the corrupted signal having SNR=7 (black). . 100

4.12 Boxplot summarizing the relationship between means of residual signals and varied SNR of simulated SHM array data; Q_1 and Q_3 are quartiles 1 and 3 respectively, and IQR stands for the inter-quartile range. Twenty realisations at each SNR value. 100

4.13 (a) Residual signals relative to the first S0 arrival amplitude for varying simulated change to SNR values (legend indicates SNR values) in signals from outdoor test and (b) comparisons in synthetically generated and experimentally observed relationships between mean residual values and SNR. 102

4.14 Photograph of (a) newly bonded and sealed transducer as well as (b)-(d) various sensors from the sparse array of the 5 mm thick anodized aluminum plate that had been outdoors for 6 months since commencing monitoring (>9 months from initial environmental exposure); annotations pertain to adhesive used as sealant. 103

4.15 Magnitude of the electrical impedance versus frequency for (a) newly bonded transducer, (b) free PZT disc, (c)-(d) bonded transducers from the outdoors test for which debond indicators were apparent, and (e) bonded transducer from outdoor test for which there was capacitive decay. 105

4.16 (a) Multilayer structure of the transducer bond and (b) simulated pulse/echo response of an ultrasonic probe at normal incidence produced using outputs from SPECTRUM [125]. Plot in (b) has time 0 set to the beginning of the plate surface echo, which has been clipped in order to facilitate visualization of the direct reflection from the plate-adhesive interface I_1 and the reverberations of interest (described in text.) 107

4.17 (a) The setup of the ultrasonic probe (cylinder) in the mount with alignment knobs (light gray), leveling legs (triangles), and programmed probe movement (dotted lines) used to acquire c-scans at normal incidence and the (b) side and (c) top down views showing samples and scanned areas; the circle in (c) signifies the bonded transducer location. 109

4.18 Typical ultrasonic A-scan waveform acquired at normal incidence. . . 109

4.19 Images of the energy ratio $E(x,y)$ generated for (a) a new transducer bond and for (b)-(c) two sensors which had been environmentally exposed in the long term monitoring experiment; the first reflection from the PZT and plate backwall reflections used to produce these images. 110

4.20 Photograph of the adhesive layers for two transducer bonds that had been exposed to outdoor environments with circle in (b) indicating separation from plate. 111

5.1 (a) A 2 mm thick, 1.25 m square aluminum plate in the environmental chamber having PZT disc sensors bonded with separation of p =0.42 m, (b) DAQ for acquisition of pitch catch signals from multiple pairs of PZT sensors, and (c) timeline for thermal profiling and SHM of plates in chamber experiments. 116

5.2 Examples of trends in residuals plotted on a dB scale for pairs of sensors bonded with DP105 and Araldite 2011 adhesive using (a) first and (b) second baseline sets; monitored data was acquired with transmitting and receiving PZTs respectively bonded using DP105 at (x =0.835 m,y =0.625 m) and (x =0.415 m,y =0.625 m) on a 2 mm thick, 1.25 m square aluminum plate and using Araldite 2011 at (x =0.835 m,y =0.938 m) and (x =0.415 m,y =0.938 m) on a second 2 mm thick, 1.25 m square aluminum plate. 118

5.3 Residual values at the first S0 arrival time (.), mean values of residuals in the range $t_{\text{1st arr}} < t < t_{\text{coverage limit}}$ (○), maxima of residuals (□), and linear fits to mean values of residuals (solid black line) evaluated using full data from the DP105 adhesive pair of Figure 5.2 versus thermal cycles since acquisition of (a) first and (b) second baseline sets, and (c) drift rates from linear fits to mean values of residuals from data with all adhesives. Data from 2 mm thick, 1.25 m square aluminum plates except for Araldite 2014 which is from a 2 mm thick,1 m square plate. 119

5.4 Difference signals for varying monitoring times from baseline acquisition with different wave packet arrivals designated (S0 for first S0 arrival, A0 for first A0 mode, and “near edge” for the S0 mode reflection from the closest edge); data are from monitoring using the pair of sensors bonded with DP105 adhesive of Figure 5.2. 120

5.5 Signal-to-random-variability-ratios (SRVR) in SHM data from sensor pairs bonded with various adhesives and (b)-(e) signal-to-coherent-variability-ratios (SCVR) in the vicinity of arrivals from various features with “near edge” used to designate the S0 reflection due to the edge which involves minimum propagation distance for relevant sensor pairs. Median and quartile values based on 6 realizations of difference signals acquired within ±3 thermal cycles around each monitoring time. Data from 2 mm thick, 1.25 m square plates except for Araldite 2014 which is from a 2 mm thick,1 m square plate. 122

5.6 (a) Strain signal, $\varepsilon(t)$, contributing to the voltage of a receiver PZT at $r = p$ =0.42 m which was estimated using the simulated strains on the surface of the plate in the FE model of Figure 3.2, (b) results of simple subtraction between signal of (a) and the simulated signals at temperature gaps, δT, and (c) comparison of amplitudes of subtracted signals to dB values of theoretical residual, $s_{\max}$, at S0 and A0 arrivals.126

5.7 (a) Simulated current signals with indicated changes input to epoxy moduli; boxes used to show zoomed areas of signals. (b) Residuals computed from temperature compensation and subtraction between simulated current signals and simulated baselines. 128

5.8 Average percent change in longitudinal velocities, $\bar{v}_{\mathrm{L}}$, relative to initial values, $\bar{v}_{\mathrm{L0}}$, with the progression of thermal cycling of the various adhesives used to bond sensors to plates. 130

6.1 (a) Axisymmetric diagram of the EMAT geometry from [40] with the pancake coil made of 46 turns of wire, each of width w = 340 µm, spaced d = 100 µm apart in a ring of radii R_1 = 4.5 mm, R_2 = 14 mm and the magnet standoff, h=4 mm, along with (b) a photograph of the components used in sensor assemblies; magnets sit on the rim in (b). 134

6.2 (a) Setup for measuring the surface displacement field due to a transmitting EMAT at (x =0.415 m, y =0.625 m) on a 2 mm thick, 1.25 m square steel plate, (b) the surface displacements measured at (x =0.835 m, y =0.625 m) with the EMAT excited using 5 cycled, 200 kHz tonebursts of 56 Vpp, and (c) the extracted ratio of the envelope detected amplitude of the in-plane surface displacement of the S0 mode divided by the out-of-plane surface displacement of the A0 mode (statistics from tests with 5 EMATs.) 136

6.3 (a) The DAQ system used to excite transmitting EMATs (Tx) and record signals at receiving EMATs (Rx), and (b) the result of applying 20 Vpp 5 cycled, 200 kHz tonebursts to Tx and using 150 sweeps to record the signal received by Rx at a distance of 420 mm on a 2 mm thick, 1.25 m square steel plate. 138

6.4 (a) The signal flow and functions of the DAQ system used to generate the Golay codes g_a and g_b, sequentially apply encoded inputs to Tx, and acquire $x_a(t)$ and $x_b(t)$ at Rx to compute pitch catch signals $x(t)$, (b) the input signal containing 2^8 5 cycled, 200 kHz tonebursts encoded using the 1st sequence g_a of a Golay code pair, and (c) $x(t)$ computed with data acquired using the sequence of Figure 6.4(b) and its complement, averaged 150 times; results in (c) obtained with the sensor pair used in Figure 6.3(b). 140

6.5 The maxima of residuals (black) from the subtraction of pitch catch data acquired in rapid succession using Golay coded excitation and post-processing methods vs log of the number of averages and acquisition times (grey.) Statistics are from data collected with 9 sensor pairs configured similarly as the pair used to obtain Figure 6.3(b). . . 140

6.6 (a) The array configuration on the 2 mm thick steel plate, (b) schematic of the wiring between the coil electrodes (grayscale), the multiplexer, and the acquisition system (Figure 6.3(a)) with connections shown to use EMAT 2 as Tx and EMAT 5 as Rx. 142

6.7 Pitch catch signals obtained by excitation of Tx 2 with 2^8 long Golay coded sequences of 5 cycle Hanning windowed tonebursts with centre frequency of 200kHz and processing data saved at the receiving EMATs. 143

6.8 The pitch catch signals computed with data acquired using sensor pair Tx 3 - Rx 6 and when there are (a) 3, (b) 5, and (c) 8 cycles in the toneburst of inputs. 143

6.9 The residuals resulting from subtraction between pitch catch signals acquired at (a) 20.25°C and (b) 25°C and optimally stretched versions of a baseline acquired at 20°C using sensor pair Tx 3 - Rx 6 and the maxima of the maximum amplitudes of residuals within the indicated time gates of (c) the S0 mode and (d) the A0 mode as a function of δT from processed array data; 2^8 long Golay coded sequences of 5 cycled, 200 kHz tonebursts of 20 Vpp were applied to Tx and 150 averages were used to save received signals. 144

6.10 The window that was applied to SHM data collected using the EMATs in order to gate out the breakthrough and superimposed dashed lines showing start (gray) and end times (black) of cosine taper. 146

6.11 Compiled residuals obtained using data from sensor pairs (a) Tx 3 - Rx 6 (0.42 m separation between Tx and Rx), (b) Tx 3 - Rx 5 (0.46 m separation between Tx and Rx), and (c) Tx 3 - Rx 4 (0.52 m separation between Tx and Rx.) 147

6.12 The maxima of residuals (□), mean values of residuals in the range between $t_{\text{1st arr}}$ and the time for the reflection from the point involving the longest transmitter-edge-receiver path (○), and linear fits to mean values of residuals (solid black line) evaluated using processed data obtained with sensor pair Tx 3 - Rx 6. 148

6.13 Images of the plate generated using the ellipse algorithm and all of the residuals from processed array data after exposure of specimens to (a) 3, (b) 150, and (c) 250 thermal cycles. Temperatures at which data were acquired are indicated on the left for each row of images and sensor locations are shown using white circles. 149

6.14 (a) The plate with the sensor array and dashed region for which statistics of pixel intensities I were computed, (b) the mean values $\bar{I}$, and (c) the maximum values of I computed for images generated using data collected at 25°C plotted as a function of monitoring time. 150

6.15 Percent change in (a) the SRVR indicator, the amplitudes of (b) the breakthrough signal and (c) the wavepacket at the first S0 arrival, and (c) the SCVR indicator in the vicinity of the S0 reflection from the edge that involves minimum propagation distance; all results are relative to initial values and are plotted as a function of monitoring time. Legend in (a) applies to all plots. 152

B.1 (a) The magnitudes of the in-plane velocity responses of ⌀ 20 mm PZT discs of thicknesses th_{PZT} bonded on 2 mm thick aluminum plates which were obtained from the simulated motions of the node on the circumference of the PZTs with 1 V excitation of them and (b) the extracted resonance frequencies f_r as a function of th_{PZT}. . . . 166

C.1 The mean values $\bar{I}$ of I within the area surrounded by sensors and the corresponding values $\bar{I}_{TFcorrected}$ in gray from images generated using the residuals computed with the data corrected using Equation C.1. Lines are the linear fits applied to the mean values with each data. . . 168

D.1 (a) Plane strain model of a 0.5 mm thick, 20 mm wide transmitting PZT and 250 µm bonding layer on a 2 mm thick aluminum plate and (b) the model with a receiving PZT of the same dimensions included at the distance that matches the sensor pitch used in tests of Chapter 5. Monitoring points are indicated using hollow circles. All other designations signify the same parameters as do corresponding ones in Figure 3.2. 170

D.2 (a) Strain signal $\varepsilon(t)$ of the S0 arrival at p =0.42 m which was estimated using outputs from simulations with the model of Figure D.1(a) and (b) the wavepacket at the S0 arrival in the received signal computed using monitored voltage responses from simulations with the model of Figure D.1(b); results are normalized to have unity amplitude. 171

D.3 (a) Results of subtracting the baseline signal computed using simulated outputs from the model of Figure D.1(b) and signals at δT =0.25°C and the signals calculated using outputs with indicated changes input to the epoxy moduli around the S0 arrival, (b) corresponding results computed using outputs from the model of Figure D.1(b). 172

D.4 The residuals computed by subtracting the same signals used in Figure D.2 from optimally stretched versions of baseline signals with simulated outputs from the model of (a) Figure D.1(a) and (b) Figure D.1(b). 172

List of Tables

3.1 Parameters and range of values studied for encapsulation development. 67

5.1 Manufacturer supplied information for adhesives used to bond sensors. 116

5.2 Temperature dependence coefficients used to adjust material properties in FE model to obtain baseline signals with different temperature changes. 125

5.3 Phase velocities and coefficients which relate change in v_{ph} with temperature for the fundamental Lamb modes at frequency thickness of 0.2 MHz-mm from [39, 56]. 125

A.1 Mechanical properties of non-piezoelectric materials from [142]; *Young's modulus of a material is real valued if loss factors is indicated as N/A. 163

A.2 Properties of the PZT from [152]. 163

A.3 Material properties from [39, 152]. 164

List of Symbols

$b(t)$	Baseline signal, as a function of time
c^E	Stiffness coefficient, under constant electric field
$c(t)$	Current signal, as a function of time
$c_a(t)$	Analytic values of current signal, as a function of time
$c_{TFcorrected}(t)$	Current signal corrected for changes in S0 arrival
d	Distance
e	Piezoelectric stress constant
$E(x, y)$	Energy ratio at grid point (x, y)
E_{Al}	Young's modulus of aluminum
E^*	Dynamic Young's modulus
f	Frequency
f_c	Centre frequency
f_{null}	Frequency associated with point of local minimum
f_r	Resonance frequency
f_s	Sampling frequency
$\mathcal{F}$	Fourier transform
g_a, g_b	Complementary sequences of Golay code pair
G^*	Dynamic shear modulus
h	Height
$I(x, y)$	Pixel intensity at grid point (x, y)
k	Integer
$M(r)$	Radial distribution function
N	Total quantity
$OB(t)$	Optimal baseline, as a function of time
p	Propagation distance
Q_{n}	Quartile n
r, θ, z	Cylindrical coordinates
R	Radius
$s(t)$	Subtracted signal, as a function of time

Continued on next page...

-Continued from previous page

$s_a(t)$	Analytic values of subtracted signal, as a function of time
$S(t)$	Beam spread corrected values of $s(t)$, as a function of time
t	Time
T	Temperature
th_{plate}	Thickness of plate
th_{PZT}	Thickness of PZT
th_{ring}	Thickness of ring in encapsulation for PZT disc sensor
v	Velocity
v_{gr}	Group velocity
v_{L}	Longitudinal wave speed
v_{ph}	Phase velocity
w	Width
$W(t)$	Tukey window, as a function of time
x, y, z	Cartesian coordinates
$x_a(t), x_b(t)$	Received signal after encoded input is applied to transmitter
$x(t)$	Pitch catch signal computed with cross-correlation, as a function of time
Z	Electrical impedance
α	Linear coefficient of thermal expansion
δ	Change
ε	Strain
ϵ^S	Permittivity, under constant strain
λ	Planar wave mode wavelength
$\lambda^{(3D)}$	Circular-crested wave mode wavelength
ν	Poisson's ratio
θ	Angle
$\varnothing$	Diameter

List of Abbreviations

AE	Acoustic emission
DAQ	Data acquisition system
EMAT	Electromagnetic acoustic transducer
EMI	Electromagnetic interference
FE	Finite element
IQR	Inter-quartile range
LDV	Laser Doppler vibrometer
MUX	Multiplexer
NDE	Non-destructive evaluation
OBS	Optimal baseline selection
ODS	Operational deflection shape
PZT	Lead zirconate titanate
RMS	Root mean square value
SCVR	Signal-to-coherent variability ratio
SHM	Structural health monitoring
SNR	Signal-to-noise ratio
SRVR	Signal-to-random variability ratio

Chapter 1

Introduction

1.1 Motivation

The aerospace, shipping, and energy storage infrastructural systems around the world contain many safety critical plate-like structures. Examples of these are the aircraft fuselage, containers, and the oil storage tank shown in Figure 1.1. Such structures must be maintained regularly so that they can be used up to and sometimes beyond their design service lives without integrity issues. The inspection procedures adopted for the upkeep of ageing aircraft is outlined in the next paragraph, and precedes a description of how SHM systems could increase the efficiency of logistics in maintenance programmes.

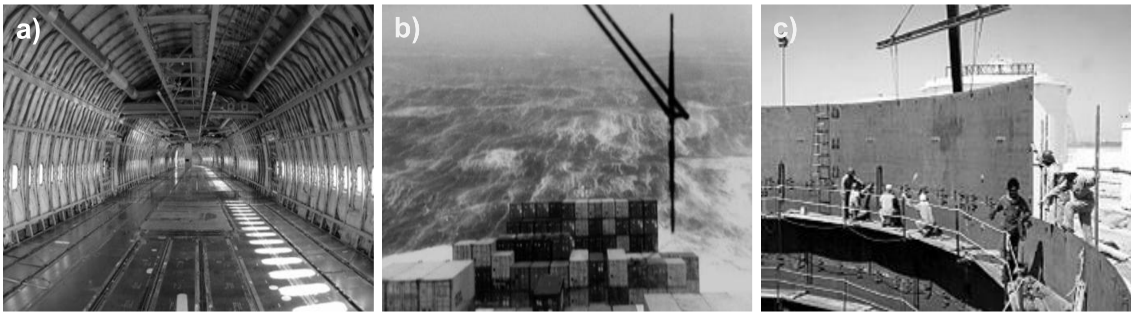

Figure 1.1: (a) The fuselage of an airplane, (b) shipping containers, and (c) an oil storage tank are examples of plate-like structures in ageing infrastructural systems.

Damage tolerant design criteria are used to maintain fleets of airplanes [1–3]. Aircraft assemblies are periodically inspected and repaired so that they remain airworthy. Subsequent inspections are scheduled when crack growth models predict that cracks could have grown to sub-critical sizes that are detectable [3, 4]. The aircraft structures must be prepared and various components disassembled prior to undergoing manual eddy current tests and ultrasonic evaluations [2, 5, 6]. These tests get repeated frequently in order to compensate for uncertainties in NDE results and predictions of the crack growth phenomena. The efforts required to prepare, access, reinspect, and reassemble structures as well as the associated flight disruptions result in significant costs to the owners of the aircraft [5].

Automated SHM systems which use small numbers of permanently installed sensors to provide information about physical changes in plate-like structures and the growth of small defects would be very useful for these industrial applications. Monitoring systems could provide early warnings about damage growth which could be used to relax inspection intervals. There would be less need to manually access and prepare structures and less disruption in their normal operation, which implies cost savings for the owners of the assets [5]. Furthermore, SHM systems could supply frequent alerts about cracking and corrosion processes which can be used to increase the reliability of assessments and service life predictions respectively [6, 7]. SHM would be practical if systems provide indications of the onset and growth of cracks (several mm long), small holes (<1 cm in diameter), and corrosion over larger areas (>1 m^2) of plate-like structures such as spars, wing sections, and frame components in aircraft [2] or container panel doors [8, 9].

SHM is a large research field and studies have focused on exploiting techniques tracking changes in vibration, strain, acoustic emission (AE), and guided wave propagation [10]. The vibration based techniques rely on tracking natural frequency or mode shape changes and can be used to detect stiffness reductions. However, these approaches are generally insensitive to critical defect sizes in the applications of concern [11, 12]. Measurements of strain could be used to detect smaller defects [13] but they are too localized to enable detection of isolated defects with small numbers of sensors [14]. The measurements of low frequency ultrasonic waves can be used to achieve coverage of 1 m^2 areas while remaining sensitive to holes having diameters

<1 cm and millimeter long cracks with relatively low sensor density [15]. Wave propagation signals can be monitored passively when it results from acoustic emission (AE) produced within structures experiencing damage. The use of transducers to actively transmit the waves that are sensed will be referred to as guided wave SHM in this thesis.

The passive AE systems use distributed sensors to record wave propagation signals which exhibit amplitudes that exceed set thresholds expected for events such as crack growth and corrosion [7, 16, 17]. Research has confirmed that the methods enable detection of AE signals which have propagated long distances in complex structures [18, 19]. Though this finding suggests AE systems may enable good coverage in some industrial applications, several drawbacks associated with them prevent their use in others. Firstly, certain damage types (e.g. ductile fracture) which commonly affect structural metals do not produce readily detectable levels of AE [7, 18]. Also, the sensors of AE systems must be constantly supplied with power in order for them to detect damage and must therefore be plugged into a power source. Moreover, AE signals are sensitive to noise sources including fretting (common in riveted and bolted structures) [7] and electromagnetic interference (EMI) [18] which have been reported to cause unacceptable increases in the likelihood of false calls in practice [20].

Guided wave SHM systems that use transducers to actively excite and monitor wave propagation signals can enable detection of the defects of concern. This is because guided wave techniques achieve good sensitivity to hole type defects [21–24] that are targeted in the shipping industry in addition to notches [25–27], cracks [28–30] and corrosion induced damage that affects structures in aircraft and tanks. Accurate assessments of defects can be made using guided wave techniques and, in a monitoring scenario, random noise is not an issue because one can average many signal acquisitions to form a clean signal. Long range inspections using lead zirconate titanate (PZT) sensors for active guided wave transduction have been very successful and commercial systems for the screening of pipelines [31] and rails [32] exist. The structures screened using these systems are very feature sparse, while the plate-like structures in the applications considered in this thesis typically contain closely spaced features. The overlapping echoes associated with guided wave reflections off features readily complicate propagation signals recorded using sensors on plate-like structures. Transducer designs, arrangements, as well as processing algorithms to discriminate damage and interpret data collected from sensors on these relatively complex structures have been developed to cope with these problems [31, 33–35]. However, the signal processing methods that enable defect detection in feature dense plates are complicated and they have only been verified over periods of <3 weeks within laboratory environments [36]. Before widespread adoption of active guided wave SHM systems based on these techniques, concerns about their reliability need to be investigated. It is to address these concerns that this thesis aims to determine the long term stability of guided wave SHM systems designed for in situ detection of defects and their growth in plate-like structure.

1.2 Thesis outline

This thesis will follow the sequence of topics described below.

Chapter 2 reviews theoretical aspects of guided wave propagation in plates along with common defect detection approaches and the challenges to the practical implementation of these for monitoring real plate-like structures. The chapter concludes with an overview of the particular SHM system studied.

Chapter 3 describes the strategies for bonded PZT based transduction and signal processing used in guided wave SHM studies in this thesis. Encapsulated bonded piezoelectric transducer designs which preferentially generate the fundamental symmetric Lamb wave mode on 2 and 5 mm thick aluminum plates are presented. Finite element (FE) modelling and validation tests were used in the design process and are described. The remainder of the chapter outlines the automated defect detection and localization algorithms which were used to process the data obtained with such sensors throughout the thesis.

The performance of a prototype SHM system used to monitor a 5 mm thick anodized aluminum plate exposed to extended periods of outdoor weather is evaluated in Chapter 4. The quantified measures of random noise and their influence on the guided wave SHM signal processing approaches are independently demonstrated.

The efficacy and outcomes of applying various sensor diagnosis techniques are compared.

The conclusions of Chapter 4 established that interfacial adhesion issues cause amplitude declines in guided wave data which makes it difficult to detect small damage. In order to achieve long term stability better adhesives were sought. Data was collected with sensors bonded using various adhesive systems that were subject to cyclical thermal exposures in Chapter 5. The trends from post-processing the collected data confirmed that detection of small defects progressively deteriorated. Simulations of transduction as well as measurements on bulk samples of adhesives quantitatively demonstrate the significant influence of changes in the properties of the adhesives used to bond sensors. It was shown that the continuous change in adhesive bulk properties, due to curing processes or other mechanisms, could explain the performance drifts that were measured in the SHM system.

The findings in Chapter 5 indicate that the construction of a bonded transducer for SHM purposes requires very stable adhesives. While it may not be impossible to find adhesive systems more suitable than the ones tested, investigations in Chapter 6 examine the potential to develop an alternative transduction mechanism. The results of evaluations with electromagnetic acoustic transducers (EMATs) and a low voltage data acquisition system are presented.

Finally, the conclusions and major contributions of the thesis are outlined in Chapter 7.

Chapter 2

Guided waves in plates and SHM principles

This chapter introduces the guided plate wave types in Section 2.1 and the characteristics of the Lamb waves that are most commonly considered for SHM purposes. The techniques used to monitor the propagation of guided waves for the detection of defects in plate-like structures are reviewed in Section 2.2. Section 2.3 describes how the findings of Section 2.1 and Section 2.2 were used to develop a robust SHM system whose long term stability could be explored in this thesis.

The chapter makes use of existing models to arrive at estimates of the velocities, scattering behavior, and temperature dependent characteristics of Lamb waves. The results provide the basis of the contributed justification for monitoring the S0 mode in the SHM system. An up to data review of strategies considered for SHM in the monitoring system is also provided, and it is shown that applying the adopted methods of baseline subtraction to original pitch catch data results in robust detection of a $\varnothing$ 5 mm hole drilled in a 2 mm thick aluminum plate undergoing 0.5°C change.

2.1 Guided wave propagation in plates

Guided wave propagation in plates is a topic well described in textbooks [37, 38]. This section reviews those characteristics most relevant to developing guided wave

SHM systems for the metallic plate-like structures of concern.

2.1.1 Modes of propagation

The bulk material of homogeneous solids supports the propagation of longitudinal and shear waves. The interaction of these waves with the boundaries of plates gives rise to the propagation of two particular types of guided waves: Lamb wave modes and shear horizontal (SH) wave modes. The Lamb modes have particle motions lying within the plane defined by the propagation direction and plate thickness, and are classified according to whether motions are symmetric (S) or antisymmetric (A) about the mid-thickness. The motions of SH waves lie in the plane orthogonal to the propagation direction and plate normal. The frequency dependent velocities and displacement shapes of all of these guided wave modes are usually obtained by numerical solution of the transcendental wave equations using, for example, DISPERSE [39]. The phase velocities and the group velocities of guided waves are the two relevant types of velocities that can be calculated. The phase velocity v_{ph} corresponds to the rate at which crests of a wave move at one frequency. The group velocity v_{gr} indicates the speed associated with propagating wavepackets containing a superposition of waves of similar frequency. The phase velocities and group velocities of the low frequency guided wave modes for an aluminum plate which were calculated with DISPERSE are shown in Figure 2.1(a) and Figure 2.1(b) respectively. Sketches of the material deformations are overlaid in Figure 2.1(a), and show the uniform in-plane and out-of-plane motions that are characteristic of the S0 mode and the A0 mode respectively.

Multiple guided wave modes exhibit non-zero velocities at any frequency as shown in Figure 2.1. The figure shows that various modes can propagate, and the superposition of their reflections from structural features generally produces complicated guided wave signals. Minimizing the number of propagating modes facilitates the interpretation of guided wave data [31, 33]. In order to limit the number of modes that propagate it is advisable to stay below the cut-off frequency for the A1 mode shown in Figure 2.1(b). There are only three wave modes that propagate in this frequency range, with the fastest being the S0 mode followed by the SH0 mode and A0 mode. Selectively inducing displacements that match the mode shape of any of these fundamental modes in the region below the A1 cutoff frequency can be exploited to preferentially excite that mode [40–42]. It is desirable to achieve omnidirectional excitation of the chosen guided wave mode in the SHM applications. Omnidirectional excitation of the SH0 mode is relatively difficult to achieve and simple to accomplish for either fundamental Lamb mode [41]. This study focused on exploitation of the fundamental Lamb waves as a result and the rest of the section reviews their characteristics.

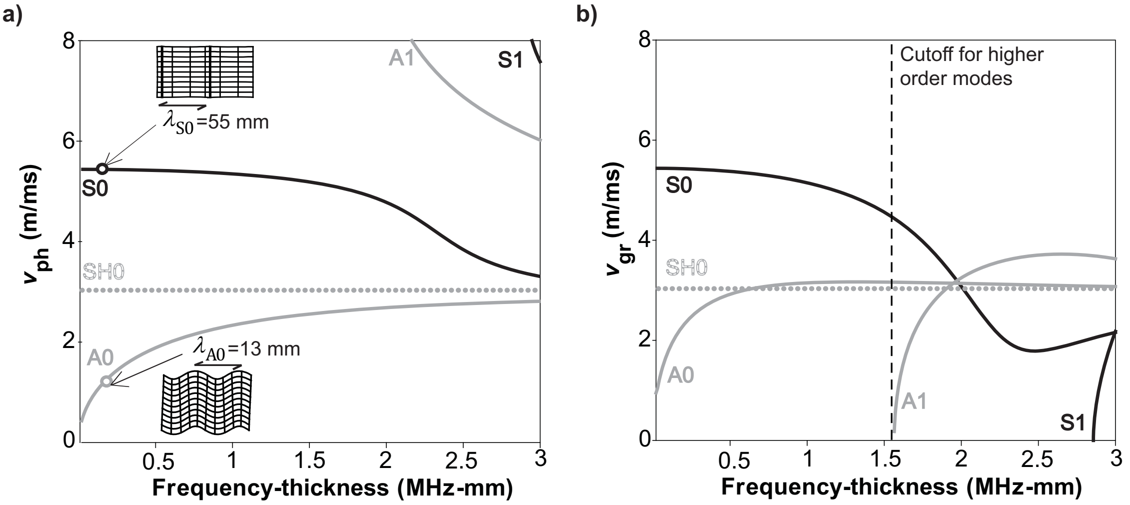

Figure 2.1: (a) Phase velocities with overlaid sketches of material deformations in aluminum plates which illustrate mode shapes of the S0 mode and A0 mode and indications of their respective wavelengths λ_{S0} and λ_{A0} at 100 kHz on a 2 mm thick plate, and (b) the group velocities of the various plate waves. Figures produced using DISPERSE [39].

2.1.2 Dispersion

The frequency dependence of guided wave phase velocities gives rise to dispersion, a phenomenon which causes distortions and loss of amplitude in propagating wavepackets and needs to be accounted for during mode selection [38]. The A0 mode is highly dispersive in the low frequency range whereas the S0 mode exhibits these features near the A1 mode cut-off as indicated in Figure 2.1(b) [43].

Figure 2.2 shows a 5 cycled, 100 kHz Hanning windowed excitation signal and the simulated wavepackets of tonebursts of the S0 and the A0 mode that have propagated 500 and 1000 mm on a 2 mm thick aluminum plate. The S0 tonebursts of Figure 2.2(b) do not appear distorted from the signal in Figure 2.2(a) while the A0 wavepackets in Figure 2.2(c) exhibit amplitude reduction and elongation as a result of dispersion. These amplitude decreases limit the propagation range of the mode. Furthermore, any gains in resolution due to the A0 wavelength being smaller than the S0 wavelength would be mitigated by the temporal elongations of pulses of the sort observed in Figure 2.2(c) [44].

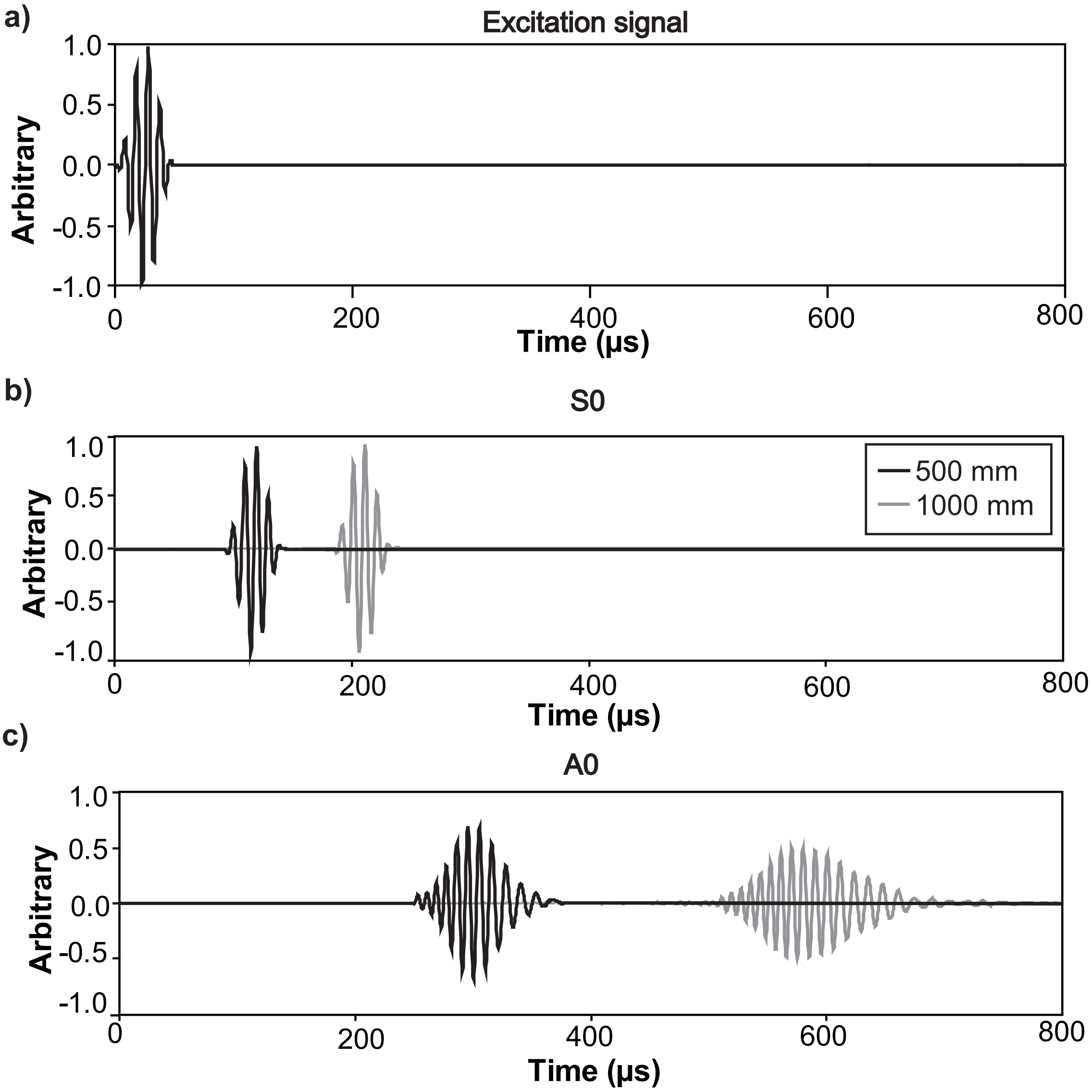

Figure 2.2: (a) Five cycled, 100 kHz toneburst as excitation signal and as simulated wavepackets of the (b) S0 mode and (c) the A0 mode which have propagated distances of 500 mm (black) and 1000 mm (grey) on a 2 mm thick aluminum plate. Figures produced using DISPERSE [39].

2.1.3 Interactions with defects and structural features

The behavior of the fundamental Lamb mode interactions with defects and structural features have to be considered to achieve suitable sensitivity to defects over large areas and transmissibility across typical features of real structures. The detection of holes and cracks are crucial in the applications of concern [2, 7, 9] and therefore the characteristics of the S0 mode and A0 mode interactions with these defects are described first.

The detection of hole type defects having diameters D on the order of 10 mm or less on metallic plates that are at least 2 mm thick is a major concern in this thesis. Therefore, the scattering behavior of non-dispersive waves of the S0 mode and A0 mode from holes having $D < 10$ mm are presented [22–24]. A program in which Dr. Frédéric Cegla had implemented the experimentally validated analytical models of [24] was used to estimate the scatter resulting from the interaction of S0 and A0 waves propagating 500 mm from point sources to through holes of varying diameters on a 2 mm thick steel plate. The amplitudes of scatter were evaluated at monitoring points 500 mm away from the holes in order to illustrate amplitudes of reflection change which must be detected at typical distances. The cylindrical decay of waves which is expected for their circular crested propagation [23, 30, 45] has been accounted for in the normalized amplitudes of scatter which are shown using polar plots for the A0 mode at 1000 kHz-mm and the S0 mode at 200 kHz-mm in Figure 2.3. These frequency-thicknesses are chosen to consider the behavior of non-dispersive waves of the modes below the A1 mode cut-off. As the amplitudes and patterns in scatter do not vary much with changes in frequencies over the ranges in which each mode is non-dispersive, the results illustrate representative scattered fields of non-dispersive waves of each mode.

The amplitudes of A0 scatter shown in Figure 2.3(a) are greater than the amplitudes of S0 scatter from the ⌀ 3 mm hole which are plotted in Figure 2.3(b). This finding indicates it is advantageous to monitor higher frequency A0 waves which facilitate easier detection of very small holes. It should be noted, however, that this advantage is primarily a result of the wavelength of the higher frequency A0 waves being much smaller than those of the lower frequency S0 waves. It is significant that the amplitudes of S0 scatter from the holes of slightly larger diameters (i.e. $D \geq 6$ mm) are on the order of the amplitudes of A0 scatter from these defects. There is also generally less directivity in scattered fields of the S0 waves than there is in the fields of the A0 mode; this is because the holes behave like point scatterers in the cases involving incidence of the S0 waves at the lower frequency-thickness product. These directivity results confirm that monitoring amplitudes of low frequency S0 scatter are more suitable for detecting physical changes in the hole type defects of concern over a large range of angles. This capability is important for the SHM applications of interest which typically require detection of the slow growth of such defects having arbitrary orientations with respect to wave actuation and sensing points.

Cracks are another important defect which affect structures in the applications of interest [2, 7]. Studies indicate that the scattering patterns which result from the interaction of S0 and A0 waves from crack-like defects exhibit directivity that depends on the dimensions and the relative orientations of wave actuation and reception points [25–30, 46–49]. As higher frequency A0 waves are less suitable for detecting hole type defects at arbitrary angles, the scattering behavior of the S0 waves from crack-like defects will be exclusively considered. In particular, the scattering behavior estimates of [47] were used to calculate the amplitudes of scatter which result with 500 mm propagation and interaction of 300 kHz S0 waves (λ_{S0} =17 mm) with a 15 mm long, 2 mm wide through thickness notch oriented at various relative angles on a 3.18 mm aluminum plate at monitoring points 500 mm away from the defect. The cylindrical decay of circular-crested wave propagation has been accounted for in the normalized amplitudes of scatter which are shown in Figure 2.4. The results show that the interaction between S0 waves and the notch results in complicated scattering patterns with local maxima and minima that occur at angles that strongly depend on the angle of the incident wave with respect to the notch orientation. For instance, the amplitudes of reflected S0 waves decrease for incident waves that align more closely with the orientation of the defect (i.e. note the smaller amplitudes of reflections in Figure 2.4(c) compared with those in Figure 2.4(a) or (b).) This result is expected as the reflection of the incident wave parallel to the crack only contains scattering contributions from wave diffraction off the crack tip [28, 30, 48]. It should be noted that though the notch length of 15 mm is on the order of λ_{S0} in the case analyzed, studies have shown that the strong angular dependency of scatter can be expected for notches of varying length [30, 46, 49]. Therefore, despite the demonstrations that crack lengths and depths can be correlated with the amplitudes of reflected S0 waves [26, 28, 29], the findings in Figure 2.4 illustrate that it is necessary to monitor S0 wave propagation with waves transmitted and received at various angles if cracks at unknown locations or any changes in their size are to be feasible to detect.

It is also important to consider the interactions of the fundamental Lamb modes with plate edges as well as their relative capabilities to transmit across features such as stiffeners which are commonly found in the plate-like structures of concern. Studies indicate that the waves of the S0 mode convert to the SH0 mode when obliquely incident on a plate edge [50], and that waves of the A0 mode that reflect off this common feature undergo phase changes and other behavior which complicate the positioning of sensors used to record its propagation [51]. With respect to transmission of waves across features typically found in real plate-like structures, research has confirmed the capability of S0 waves to transmit fairly evenly across stiffeners [52] and corrugations [36]. On the other hand, waves of the A0 mode only transmit across stiffeners and corrugations for relatively limited ranges of incidence angles [36, 53].

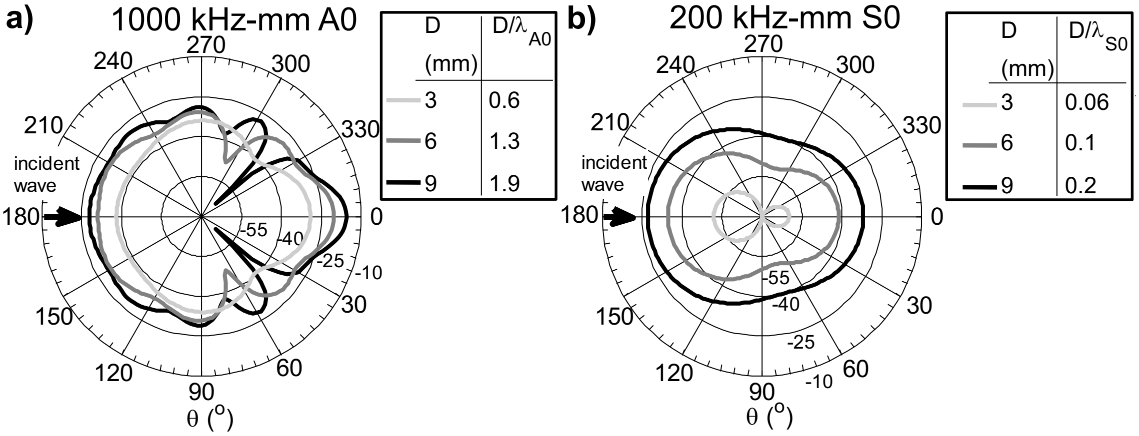

Figure 2.3: The analytical amplitude of (a) 1000 kHz-mm A0 scatter and (b) 200 kHz-mm S0 scatter from through holes of diameters D on 2 mm thick steel plates which result from the interaction of waves propagating 500 mm to the holes and 500 mm onwards to monitoring points. Results are shown as dB values normalized by the input amplitude and were calculated using the analytical implementations in [24].

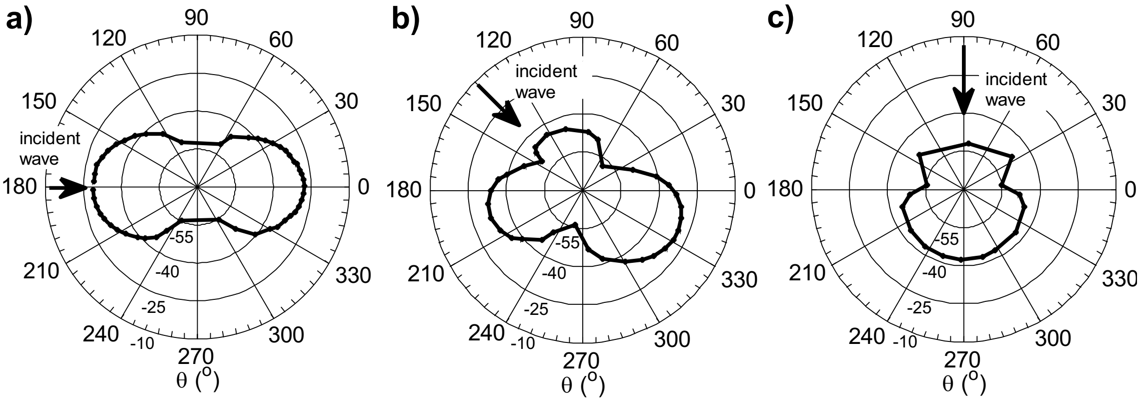

Figure 2.4: The amplitude of 950 kHz-mm S0 scatter from 15 mm long, 2 mm wide through thickness notches oriented along 90°-270°on a 3.18 mm thick aluminum plate which result with the interaction of waves that propagate 500 mm in the directions indicated by the arrows to the notch and 500 mm onwards to monitoring points. Results are adapted from [47], and are shown as dB values normalized by the amplitude of the input being at incident angles of (a) 0°, (b) -45°, and (b) -90°.

This section briefly summarized aspects of the scattering behavior of the fundamental Lamb wave modes which are important to consider in developing SHM systems for plate-like structures. The scattering behavior is complex though studies suggest that holes, notches, and cracks can all be potentially detected. Non-dispersive S0 waves are better suited than A0 waves for the purposes of detecting the hole type defects of concern in instances when their locations are unknown. It is evident that S0 wave propagation should be monitored at multiple angles if the measurements are to be useful for the purposes of detecting cracks. S0 waves also transmit more uniformly across feature dense sections of plate-like structure.

2.1.4 Environmental effects

Real plate-like structures experience variable environmental conditions [54]. Temperature changes as well as applied stresses are expected to affect structures in most industrial applications. This section describes how these sources of variability influence the geometry and elastic constants which change the plate dimensions and the wave velocities v respectively.

Thermal swings of δT cause Lamb waves propagating over distance p to undergo time shifts δt that can be calculated by differentiating the relation for arrival time, i.e.

$$t = \frac{p}{v}, \tag{2.1}$$

with respect to both p and v [35, 55]:

$$\delta t = \frac{p}{v}(\alpha - \frac{1}{v}\frac{\partial v}{\partial T})\delta T \tag{2.2}$$

where α is the relevant coefficient of thermal expansion (e.g. 23E-6 °C^{-1} for aluminum.) It is important to consider the effects that temperature changes have on the time shifts for waves of each fundamental Lamb mode as these determine the phase changes that must be differentiated by methods used to detect defects over large areas [35]. Therefore, Equation 2.2 was evaluated with v_{ph} from Figure 2.1 and values of $\frac{\partial v_{\mathrm{ph}}}{\partial T}$ extracted from the results which were calculated for an aluminum plate with thermal stress and thermally varying elastic properties in [56]. The calculated time shifts for the S0 mode and the A0 mode in the example aluminum plate structure are plotted in Figure 2.5. The plot shows that A0 waves exhibit substantially larger time shifts across the ultrasonic frequency range. These results can be explained by noting that the term involving α in Equation 2.2 is at least an order of magnitude smaller than the term involving the reciprocal of the velocity squared, which is larger for the slower A0 mode.

Apart from thermal variation, the loading of structures introduces changes in Lamb wave propagation velocities. However, the strains that loads introduce are anisotropic and therefore a directional dependence of Lamb wave speeds will be introduced and needs to be accounted for in order to determine associated effects on wave dispersion. Researchers have analyzed how applied tensile [55, 57, 58] and biaxial stresses [59] affect Lamb wave velocity dispersion. The experimental results from the studies have shown that both S0 [55] and A0 [58] phase velocities exhibit a linear dependence on load magnitude and sinusoidal dependence with angle between propagation direction and the loading axis. Theoretical estimates of acoustoelastic effects using modified third-order elastic constants in [59] have been able to accurately account for the trends in tests.

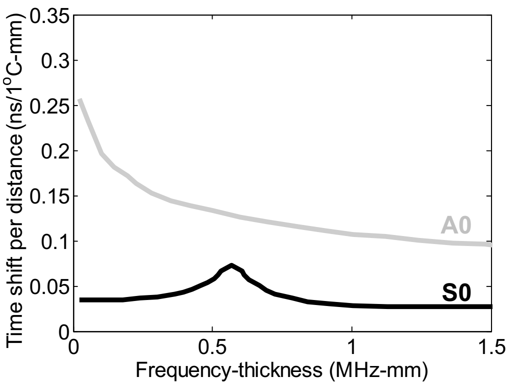

Figure 2.5: The predicted effects of δT=1^{o}C on time shifts associated with crests of S0 and A0 waves of aluminum plates (values scale linearly with p and δT.) The results were calculated using v_{ph} from DISPERSE [39] and $\frac{\partial v_{\text{ph}}}{\partial T}$ from [56].

2.2 Monitoring techniques

A practical SHM system should enable sensitive detection of the scattered fields from small defects over areas of feature dense structures experiencing variable environmental conditions with few sensors. This section reviews the techniques for sensor use and the signal processing methods that have been researched to allow practical detection of defects.

2.2.1 Arrangement and operational modes of sensors

Sensors should be arranged and operated to achieve maximal coverage of large areas. Sparsely distributed networks have sensors separated by several multiples of the interrogating wavelengths while single unit arrays, such as the one used in [60], have sensors in regular arrangements and within close proximity of one another. Sparse arrays of sensors can be used to cover larger areas, and increase the probability of detecting damage whose orientation causes there to be minimal scatter toward the sensors of single unit arrays [34, 41, 61, 62]. The practical difficulties with attaching the obtrusive and complicated electronics required to support concentrated arrays are other reasons which have prompted researchers to develop Lamb wave SHM systems that rely on sparse sensor arrays [45, 63].

The sensors of the arrays can be operated in pulse/echo or pitch catch mode in order to record guided wave data. In pulse/echo mode, the transmitting transducer is used for reception of propagation signals. With the pitch catch operation of sensors, however, a pair of sensors is used in which one transmits the signal and the second sensor is used to receive the signal. Of foremost concern is the usefulness of a particular operational mode for detecting small holes and cracks. Pulse/echo measurements are best for detecting backscatter. However, as can be seen from the figures in Section 2.1.3, defects do not necessarily scatter evenly in all directions and amplitudes of backscatter may be minimal. Pitch catch sensors can be more useful for picking up scattered signals at a range of different angles, which maximizes the chance of receiving high amplitude signals that are scattered by a variety of defects.

Furthermore, the backscatter that is monitored with pulse/echo use of sensors is severely affected by thickness transitions that are common in many real plate-like structures [64]. On the other hand, pitch catch measurements have been found to be suitable for recording signals transmitted across sections of gradually varying thickness such as those found in aerospace components [19, 65]. Pitch catch operation also requires less complicated electronics and prevents issues with individual sensor malfunctions (e.g. electrical wiring problems) from necessarily compromising area coverage. Finally, the pitch catch use of sensors increases the number of measurements and, consequently, reliability of extracted information.

2.2.2 Damage detection

In many plate-like structures, the overlapping arrivals of reflections from features (e.g. edges, rivets, and stiffeners) complicate wave propagation and generally mask the scattering due to small defects. Signal processing must be applied to data in order to allow damage detection. Algorithms are being developed for these purposes, and they include statistical pattern recognition, baseline subtraction, and techniques which evaluate extents to which data exhibits signal changes estimated to be produced by damage. The progress with these damage detection strategies are reviewed in this section.

Statistical pattern recognition

Statistical pattern recognition approaches track variations in quantitative indicators extracted from recorded guided wave data in order to infer whether they are indicative of the structure being damaged [10, 15]. Principal component analysis, machine learning, and cointegration have recently been considered for these purposes as described in [10, 66]. The computational complexity of the algorithms and the lack of straightforward approaches to correlate observed changes in output quantities to the sizes/locations of defects are drawbacks associated with the methods.

Baseline subtraction

A simple damage detection approach subtracts a currently acquired signal from a baseline signal that was acquired from the structure in a healthy state [35, 41, 61, 67]. The resulting subtracted signal should reveal the changes due to defects and enable straightforward detection of their presence. An example using data acquired within this work, where a defect is introduced on a monitored 2 mm thick, 1.25 m x 1.25 m aluminum plate is used to illustrate the principle behind this method. A 20 mm diamter, 0.5 mm thick PZT disc having screen printed electrodes is bonded on the plate and used to preferentially excite 5 cycled, 100 kHz tonebursts of the S0 mode having group velocity v_{gr} =5430 m/s. Figure 2.6(a) shows the baseline signal, $b(t)$, normalized by the Hilbert envelope based amplitude of the S0 arrival that is recorded using a bonded PZT sensor at a distance $p = 300$ mm from the transducer. Damage is introduced after acquisition of this baseline by drilling a ∅ 5 mm through hole at a known location. The current signal, $c(t)$, recorded following the drilling has been offset, normalized by the S0 arrival amplitude, and superimposed on Figure 2.6(a) to allow comparisons with $b(t)$. The reflections from the plate edges complicate both signals and make it impossible to discern any change in $c(t)$ at around the expected arrival time of the reflection from the hole (annotated in the plot.) However, the signal resulting from baseline subtraction [35]

$$s(t) = b(t) - c(t) \tag{2.3}$$

should register the scattered signal due to the defect. A schematic of the ideal result from the perfect subtraction of the signals in Figure 2.6(a) has been corrected for beam spread using [21, 41]

$$S(t) = s(t)\sqrt{\frac{tv_{\mathrm{gr}}}{p}} \tag{2.4}$$

and is plotted in Figure 2.6(b). Equation 2.4 is applied as is customary [41, 68] in order to ensure that amplitudes in results get weighted properly so that signals due to waves propagating via points at varying distances from transducers produce similar responses. Simply subtracting recorded guided wave signals using Equation 2.3- 2.4 will not enable small defect detection if there are changes in operating conditions without compensating for environmental effects (as will be discussed in Section 2.2.3.)

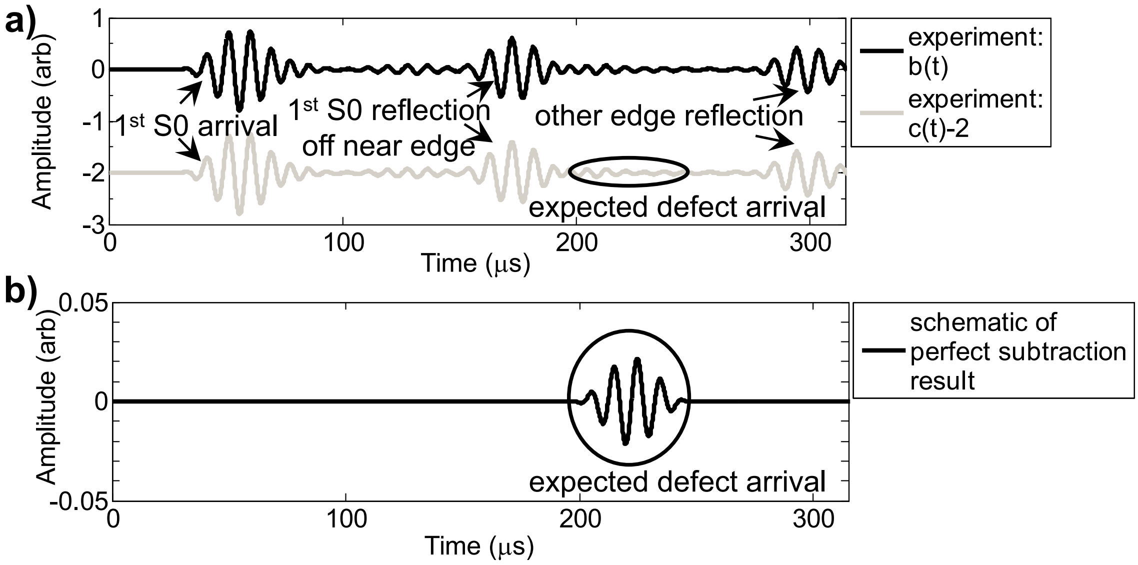

Figure 2.6: (a) Pitch catch signals collected on a 2 mm thick, 1.25 m square aluminum plate using a sensor pair with the transmitting PZT at ($x = 0.8$ m, $y = 0.3$ m) excited by 5 cycled, 100 kHz tonebursts and a receiving PZT at ($x = 0.8$ m, $y = 0.6$ m) recording the data with 100 averages from the damage-free plate, $b(t)$, and after a $D = 5$ mm hole is drilled at ($x = 0.29$ m, $y = 0.72$ m), $c(t)$, and (b) a schematic of the ideal result from the perfect subtraction of the signals in (a).

Tests on structures ranging from simple and welded plates to container panels [36] have shown that baseline subtraction does enable detection of a variety of defects including artificially introduced holes, roughness defects, and notches [34, 47, 61, 69, 70]. Such defects may be detectable with as few as 2 sensors for a 12 m x 1 m area as shown in [67]. Imaging of subtracted signals using the methods of [71–73] has allowed localization of simulated defects in structures. The additional incorporation of scattering information has enabled the sizes of ∅ 2 mm through holes [74] and the orientations of through thickness notches [47] to be better captured in imaging studies. These results indicate baseline subtraction based methods may potentially allow sizing and characterization of defects in addition to their detection and localization.

Other damage detection methods

Researchers have also integrated modeling the effects that damage types produce on guided wave signals into defect detection schemes. Researchers have modeled how damage changes the relative time delays in arrivals of Lamb wave modes and investigated the feasibility of tracking this parameter from recorded guided wave data for detecting defects [75, 76]. While delamination was successfully detected using these approaches [75], problems have been reported in detecting cracks and simulated corrosion in metallic plates [76]. Others have empirically modeled energy dissipation due to damage and tracked the time-frequency energy content extracted using wavelet representations of signals for detecting notches as well as delaminations [77, 78]. Localization of defects using the wavelet based detection approaches has required probabilistic weighting of indicators which further complicates the algorithms and makes them difficult to use for defect sizing/characterization.

An approach in [79] exploits pairs of sensors attached on the opposite surfaces of structures to record propagation data from which the mode converted signals are extracted and their amplitudes tracked in order to detect notches. While interesting, the sensor installation required for this notch detection strategy is challenging to achieve in practice. A method which also employs analysis of only certain signals in recorded data is described in [80]. This technique relies on adaptively filtering the propagation patterns associated with sources in order to isolate the scattering from defects, and has been effective for detecting and localizing a rod glued on a plate within the area surrounded by sensors.

The damage detection approaches described in this section have allowed discrimination of certain types of defects over limited regions of simple structures and are not useful for detecting various forms of damage over larger areas of densely featured plates. Therefore their use for a general SHM system is limited.

2.2.3 Compensation for environmental effects

A practical guided wave SHM system must enable the reliable detection of damage in structures that experience environmental variability [31, 54]. Even small variations in temperature or loading can significantly affect guided wave velocities. The associated time shifts in wave arrivals can contribute variability to signals which can easily mask the scattering from small defects [81–83]. Thus, there is a need to compensate for the effects environmental changes have on wave propagation so that robust damage detection is achieved in real operating conditions. While various techniques have been developed for these purposes [66, 75], the baseline subtraction based methods are the most established [31, 63, 84–86] and the progress with these approaches is discussed.

A major source of concern with the use of subtraction are that thermal swings of ≥0.3°C can sufficiently alter wave velocities so that the associated arrival time changes contribute coherent post-subtraction variability which easily masks the presence of small defects in practice [35, 84]. In order to illustrate these effects, the experimentally obtained signal $c(t)$ has been subtracted from $b(t)$ when there are discrepancies of 1°C in temperatures at which these signals are recorded. The subtraction is computed using the raw signals as defined in Section 2.2.2 rather than using signal envelopes. The envelope based methods are not adopted despite being less sensitive to temperature dependent time shifts in wave arrivals because the technique causes unacceptable reduction in detection sensitivity as demonstrated in [35]. The subtracted signal which is computed has been plotted in Figure 2.7. The result shows temperature related variability at the arrivals of the S0 mode and the reflections off plate edges exhibit higher amplitudes than the scattered signal due to the hole.

In order to overcome these effects, monitored signals are typically compared to a collection of baselines recorded when the structure is exposed to the range of expected environmental conditions, and the time bases of signals are commonly stretched/compressed in order to compensate for unaccounted discrepancies in the arrival times [84–88]. The results obtained after subtracting signals that have been compensated for temperature effects (using versions of these algorithms that will be described in Chapter 3) are overlaid in Figure 2.7. Compensation has lowered the amplitude of post-subtraction variability at points where there are no expected signals due to the hole. The signal scattered from the defect can be distinguished around the expected arrival time. This result clearly shows that defect detection is possible in the presence of temperature changes if the right compensation techniques are used. These compensation strategies and their use with baseline subtraction enable detection of 1.5% reflection changes over 1 m^2 areas of plate-like structures undergoing other environmental changes [31] including uniform liquid loads if a suitable mode is being monitored [63].

Applied stresses have been shown to cause the detectability of defects with baseline subtraction to be compromised when signals are acquired with the structure experiencing greater than 20% load difference [58, 83]. Recent research indicates load mismatches can be deduced using approaches such as those developed in [89] so that only data obtained when there is less than 20% difference in the state of stress in the structure is compared to baselines. It would be preferable to exploit theoretical understanding of the effects of applied loads in order to develop compensation strategies such as those used to correct wavenumber deviations and improve crack detectability in [58].

The long service lives of the structures in all applications require stability in defect detection capabilities of monitoring systems, an issue which has not been as well addressed in studies of guided wave SHM. The aspects of studies which address reliability issues of detection approaches have either neglected or been inconclusive about the influences of environmental exposures [82, 90]. Most of the studies exclude characterizing source influence on monitoring system performance in practical situations. Recent studies which have involved environmental exposures [91, 92] have primarily studied individual aspects of SHM systems rather than the suitability of the components as well as algorithms which could be used to detect damage in practice. Some researchers at the University of Bristol and Ohio State who use baseline subtraction based methods for damage detection have relied on updating baselines [68, 93]. Research at Bristol which was focused on monitoring a larger steel tank structure in an outdoor environment showed that there are unexplained changes in test data, and indicated that 10% of signals acquired during a 40 day period needed to be constantly added to their baseline set. While diagnostic evaluations [91, 94] can be used to improve methods to continuously update baselines in the future, the strategies would imply missing the detection of slow defect growth which is the predominant nature of the fatigue crack growth or corrosion induced damage which affect metallic plate-like structures. Such concerns lead to the need to further investigate the long term stability of guided wave SHM. Therefore, the background knowledge reviewed in this chapter was used to develop an SHM system for studies of its long term stability as described in detail in the next section.

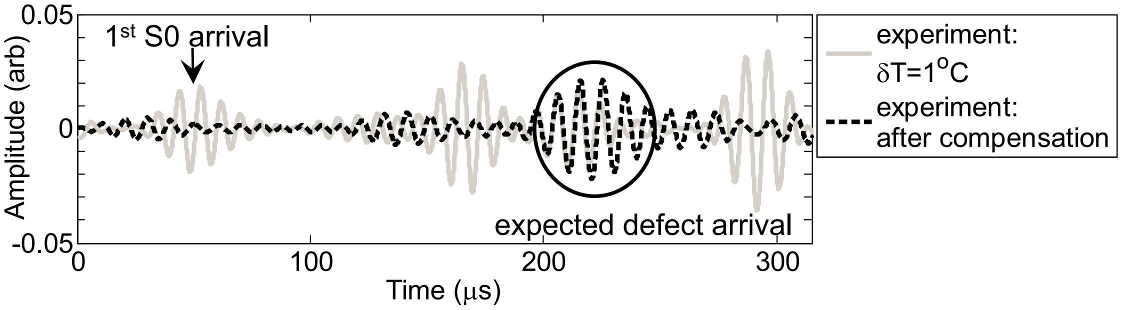

Figure 2.7: The results obtained from the subtraction between the experimental baseline signal acquired from the healthy structure and current signal acquired after the structure has been damaged (of Figure 2.6(a)) for there being 1°C discrepancy in temperatures at which the signals are recorded along with the results obtained after processing data using the compensation algorithms described in detail in Chapter 3.

2.3 Guided wave SHM system for long term stability evaluations

The outstanding issue of the long term reliability of guided wave SHM was investigated in depth throughout the remainder of this thesis using the monitoring system and strategies described in this section.

A guided wave SHM system was used which was based on monitoring low frequency (<1 MHz-mm) S0 wave propagation. The S0 mode was chosen for the following reasons:

- the S0 mode is the fastest guided wave mode in this frequency range, which means a directly transmitted S0 wavepacket can be easily identified as the first arrival in recorded data (whereas an A0 wavepacket can be hard to distinguish among signals associated with wave reflections off edges and other features)
- S0 waves are non-dispersive in this frequency range and have wavelengths larger than those of non-dispersive A0 waves, which means their amplitudes get less affected by linearly attenuative materials over fixed propagation distances.
- the energy leakage from out-of-plane displacements of the A0 waves in the presence of fluid loads make this mode unusable for SHM of certain structures (e.g. structures in oil storage tanks [95])
- the amplitudes of S0 scatter from hole type defects of concern do exhibit less directivity than A0 scatter as discussed in Section 2.1.3
- the S0 mode transmits more uniformly across features such as corrugations and stiffeners
- the arrival times of S0 waves vary less appreciably with thermal swings as described in Section 2.1.4.

It was decided to monitor pitch catch propagation patterns using sparse sensor arrays and post-process recorded signals using baseline subtraction methods. The use of sparse arrays of sensors operated in pitch catch mode enables broadening the coverage areas achieved and increases the probability of detecting damage exhibiting directional scattering characteristics with relatively simpler electronics as discussed in Section 2.2.1. Compensation of guided wave data and baseline subtraction were adopted as these damage detection techniques are the only approaches which enable robust detection and localization of damage signifying as small as 1.5% reflection change on complex structures experiencing various environmental changes (as discussed in Section 2.2.3.)

The monitoring studies started with analysis of the detection capabilities that can be achieved using the PZT transducers and the signal processing implementations described in Chapter 3. All investigations employed comparisons between monitored signals and baselines collected upon the instrumentation of structures with sensors. The exposures of weathering and cyclical thermal variation are expected in all applications, and the results of investigations of their effects on monitoring capabilities and sensors are analyzed in Chapter 4 and Chapter 5 respectively. An alternative option of using electromagnetic acoustic transducers (EMATs) to preferentially excite and monitor S0 wave propagation is evaluated for its capability in Chapter 6.

2.4 Summary

This chapter presented the basics of guided wave propagation in plates, and reviewed monitoring techniques which show potential for enabling practical guided wave based SHM of real plate-like structures.

The waves which can propagate in plates are introduced prior to describing the characteristics of the fundamental Lamb waves which were considered to be monitored as part of an SHM system. The characteristic effects of dispersion on S0 and A0 wave propagation are reviewed alongside aspects of the scattering characteristics of each mode which should be analyzed so that SHM systems can be designed to achieve sensitivity to defects over larger areas of feature dense structures. In order for an SHM system to reliably enable monitoring of the structures in applications, one should account for how expected changes in temperatures and applied stresses influence the monitored mode. Therefore a brief summary is provided about how these sources of environmental variability affect propagations of S0 waves and A0 waves.

Subsequent sections discuss the progress with monitoring techniques that have demonstrated potential to enable practical guided wave based SHM of large plate-like structures. The advantages of arranging sensors in distributed networks and operating them in pitch catch mode have been outlined. The processing methods employed to detect defects in guided wave data recorded using arrays of sensors and the extents to which compensation for environmental effects have been realized are reviewed.

The final section summarizes justifications for choosing to monitor propagation patterns of the S0 mode using sparse arrays of transducers along with the reasons for adopting baseline subtraction based damage detection strategies. This section also provides an overview of subjects including detailed descriptions of the SHM system and the different studies used to investigate its long term reliability for small defect detection, which are covered in the rest of the thesis.

Chapter 3

Strategies for sensing and signal processing

3.1 Introduction

This chapter discusses the practical implementation of an SHM system. Different transduction mechanisms are considered in Section 3.2. Section 3.3 describes developments with PZT based sensors which were selected and optimized for monitoring the propagation of low frequency S0 waves. Data collected with these sensors need to be processed for practical defect detection, and the algorithms implemented for these purposes are discussed in Section 3.4.

A novel outcome of the work in this chapter is the design of a cap for bonded PZT transducers with the experimental confirmation of the capability to generate stronger waves of the S0 mode compared to the A0 mode in 2 and 5 mm thick aluminum plates. These developments are realized by building upon work with existing FE models [41] with which it is also found that PZTs must be dimensioned for the plate thickness of relevance in order to be able to excite the S0 mode away from the resonance of transducers. Procedures for acquiring baselines in an environmental chamber which are used throughout the thesis are also presented and their use to collect data which is processed with automated processing methods is shown to result in adequate temperature compensation for SHM purposes.

3.2 Transducer type selection

Various transducers including PZTs, EMATs, and fiber optic sensors can be used to generate and record wave propagation signals in a guided wave SHM system. Researchers have demonstrated that PZT based sensors can generate high amplitude guided waves and exhibit good sensitivity to their propagation over distances exceeding 1 m even in complex structures [36, 96, 97]. PZTs can be used to manufacture small and unobtrusive transducers relatively cheaply. Geometric selection and bonding of appropriately polarized PZTs can be exploited in order to strongly excite the fundamental Lamb wave mode of interest [91, 96].

EMATs are lower sensitivity devices which may be used to generate Lamb and SH waves, and can be installed on ferritic metals relatively easily without any couplants [40, 42, 48, 98]. It is for this advantage and its potential for use at high temperatures that EMATs have been developed and example applications are those by MKCNDT [99] and ClampOn [100]. EMATs often require high voltage inputs as well as sophisticated electronics and bulky high power auxiliary equipment, which are not generally desirable in monitoring applications [67, 101].

Fibre optic sensors are relatively lightweight and have been considered for their flexibility and ease with which they can be integrated into networks for multiplexing [4]. The sensors are not particularly mode selective, and many Lamb wave sensing systems based on the transducers have required different actuators as a result [15]. Breaks along any of the fibres of these sensors can also compromise all sensing capabilities, and thus they were not chosen in this work.

The sensors consisting of bonded PZT discs are the cheapest among the various options for transduction, and they may be used with the simplest actuation and sensing electronics. It is for these advantages and the experience with developing mode selective sensors based on PZTs that they were chosen and the transducers described in Section 3.3 were initially used in evaluations.

3.3 Bonded piezoelectric sensor design

A guided wave SHM transducer needs to have certain characteristics:

- selective excitation and reception of a Lamb wave mode [31, 91, 102], which was chosen to be the S0 mode in this work for the reasons provided in Section 2.3
- stable output over the operating frequency range which implies the transducer should not exhibit resonances near the frequency at which it is operated [84, 96]
- robustness to environmental influences which include wetting and moderate amplitudes of stress being applied to electrical connections of sensors.

FE analysis was employed in order to optimize the geometry of PZT transducers and develop an encapsulation with a strain relief system that would meet these objectives. The outcomes and the experimental validations of the adopted sensor and encapsulation designs are described in the following sections.

3.3.1 Wave propagation model and its theoretical validation

The Abaqus FEA software was used for FE analysis as it allows to fully model the bonded PZT assembly [41]. Since the PZT could only be defined in the Standard module of Abaqus FEA, this frequency domain solver was used to analyze all models. In order to ensure accurate and usable results, the modeling was split into small steps of increasing complexity with each step being validated in sequence. The initial steps involved modeling Lamb wave propagation in 2-5 mm thick aluminum plates, followed by incorporation of the bonded PZT and encapsulation.

The omnidirectional excitation of S0 waves is sought and this has been shown to be possible using PZT discs whose dynamics can be modeled axisymmetrically [41]. In order to eventually build up models to study the dynamics of round transducers an axisymmetric model of plates was initially developed and analyzed (rather than a 2D plane strain model which is conventionally used to simulate Lamb wave propagation.) The geometry of cross sections of the plates having 1 m radius, such as the example of thickness th_{plate} =2 mm shown in Figure 3.1(a), were modeled. Elastic square CAX4 elements that had linear shape functions and 0.25 mm side length were used to create structured meshes of the cross sections which were assigned the material properties of aluminum (see Table A.1 of Appendix A.) This mesh size is smaller than 4% of the smallest wavelengths of concern (i.e. wavelengths of 300 kHz A0 waves being 6.7 mm on a 2 mm thick aluminum plate), which is sufficient discretization for good results [103]. The rows of elements located between r =500 mm and r =1000 mm were assigned cubically increasing viscoelasticity in the radial direction for the purposes of preventing interferences from edge reflections. These elements are colored gray and labeled the "absorbing layers" in Figure 3.1(a). Displacement inputs were applied to the mid-plate thickness node on the symmetry axis. Inputs were directed in the in-plane ($+r$) and out-of-plane ($+z$) directions as shown in Figure 3.1(a) in order to excite S0 and A0 waves respectively. The frequency of the inputs was varied in increments of 1 kHz from 50-300 kHz which is near the cut-off frequency for the first higher-order Lamb mode of 5 mm thick plates. The steady state magnitude and phase of displacements in the resulting wave field were monitored on the surface and at the mid-thickness of the plate at r = 300 mm from the symmetry axis (circled points in Figure 3.1(a).)

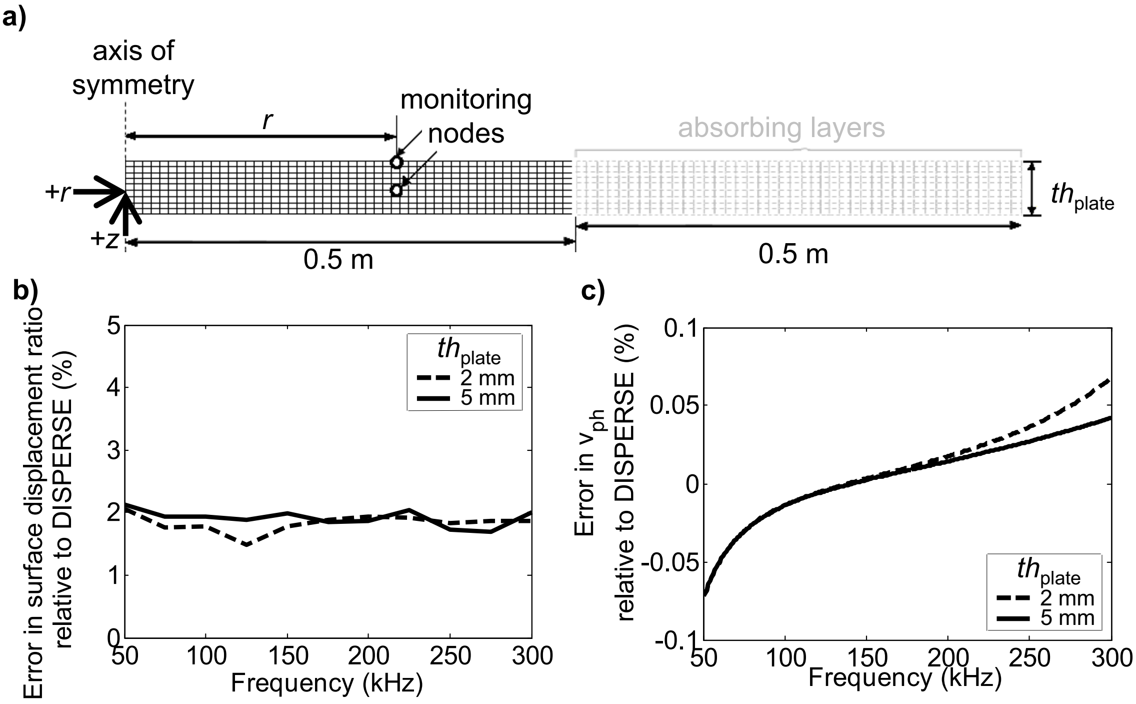

Figure 3.1: (a) Axisymmetric FE model of the plate having thickness th_{plate} and large arrows that indicate the direction and location of displacement inputs. Discrepancy in (b) the ratio of surface in-plane to out-of-plane displacements and (c) the phase velocities of simulated S0 mode propagation; errors are relative to values from DISPERSE.

In order to validate the model results, the ratios of monitored in-plane to out-of-plane surface displacements were compared to the values from the theoretically predicted mode shapes calculated using DISPERSE [39]. The resulting errors are plotted in Figure 3.1(b) for simulations of 2 mm and 5 mm thick plates. These results are representative of the low level of discrepancy (<2.5% error) that was found for both combinations of modes and the various thicknesses of plates modeled. Additionally, the phase of the in-plane and out-of-plane displacement responses were monitored at nodes along the mid-thickness of the plate at points separated by 3 mm between r =300 mm and r =515 mm; the responses were sampled every 3 mm in order to ensure sufficient spatial sampling to accurately unwrap the phase values obtained from simulated propagation of waves having wavelengths of 6.7 mm. The unwrapped phase values for the frequency and the relevant displacement component associated with predominant motion in each Lamb modes were used to calculate the angular wavenumber and the desired phase velocity in turn. The percent error in the calculated phase velocities relative to values that were obtained from the DISPERSE software are plotted for the S0 mode on 2 mm and 5 mm thick plates in Figure 3.1(c). The very small errors are most likely due to differences between the axisymmetric geometry of the plate modeled in the FE simulations and the 2D plane strain assumption of the analytical solution. The discrepancies were deemed acceptable for the purposes of this work and no further refinements were undertaken.

3.3.2 Bonded PZT transducer and excitation of the S0 mode

The simulations of the fundamental Lamb wave propagations were accurate to within 2.5% error. This was thought to be sufficient validation so that the next step could be taken and the PZT discs and adhesive layers were incorporated into models. The model of the transducer assembly was used to study how it may be possible to achieve preferential excitation of the S0 mode (over the A0 mode) at frequencies away from the resonances of bonded PZT discs.

Small temperature change and associated material property variations can produce large amplitude changes and phase shifts in the waves excited with transducers operated around their resonance [84]. This is undesirable for stable transduction and therefore off resonance operation that results in strong signals is sought. In order to determine the frequency ranges which would best enable off resonance selective transduction of S0 waves, the model shown in Figure 3.2 was used to study the dynamics of the bonded PZT and its effects on the excited guided waves; the simulations are similar to those documented in [41]. A structured mesh consisting of square CAX4 elements for the plate and epoxy as well as CAX4E elements for the PZT were used to discretize the parts in the model which were assigned the material properties in Appendix A.1. It was decided to use the same mesh size as used in Section 3.3.1 and in [41]; simulations with models discretized using meshes which were 2 to 4 times as dense did not alter analysis findings. Initially ⌀ 20 mm PZT discs of thickness th_{PZT} =1 mm were considered for plates of all thicknesses as these sensors were successfully used in previous studies [35, 36, 84]. Analyses were run with the bottom electrode of the PZT grounded and its top electrode subject to 1 V at each frequency over the range 50 to 300 kHz. The peak in the magnitude and change in the phase of the in-plane velocity at the node on the circumference of the PZT was used to determine the frequency of the first radial resonance f_r of the transducer. This resonance is the primary source of instability with thermal changes [84]. Thus, f_r and the frequencies of the -6 dB bandwidth points of the resonance were tracked to select excitations outside the transducer resonance.

Simulations were used to optimize the excitation of the S0 mode relative to the A0 mode on 2 and 5 mm thick aluminum plates; these thicknesses were chosen as plates of these dimensions are common in aircraft. The study was undertaken to limit the interference of the unwanted A0 mode in recorded guided wave data. Voltage excitation was applied to the PZTs in the FE models, and the particle velocities were monitored at the node in the middle of the plate that is located at r =300 mm; the in-plane and out-of-plane velocities at this node are characteristic of the S0 mode and the A0 mode respectively and were used to obtain the response of each mode.

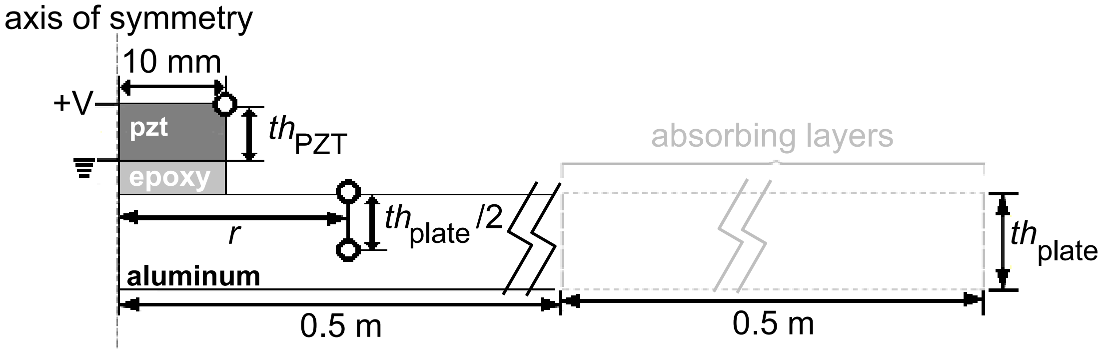

Figure 3.2: Axisymmetric FE model of ⌀ 20 mm PZT disc having thickness th_{PZT} and 250 µm bonding layer on an aluminum plate of thickness th_{plate}; the illustration is not to scale, has top and bottom electrodes of the PZT designated using a +V and ground symbol respectively, and hollow circles indicating points at which velocities were monitored.

The magnitudes of the velocity responses obtained from the simulation with the PZT on the 5 mm thick plate are plotted in Figure 3.3(a). The peak in the S0 response is primarily reflective of the radial resonance of the PZT. The A0 response contains several minima as well as peaks; the first minimum occurs at the indicated frequency,f^{A0}_{null}, of 154 kHz. The first minimum in A0 transmission occurs when out-of-plane motion in the PZT suppresses propagation of the A0 mode as a result of matching between the PZT disc diameter and the circular crested wavelength of the A0 mode $\lambda^{(3D)}_{A0}$ [91]. In order to confirm this phenomenon was being predicted well, $\lambda^{(3D)}_{A0}(f^{A0}_{null})$ was calculated using λ_{A0} from DISPERSE [39] and knowledge of the circular and planar Lamb wave excitabilities from [40]. In this case, $\lambda^{(3D)}_{A0}(f^{A0}_{null}$=154 kHz)=21.4 mm which is different from the transducer diameter of 20 mm by 7%; the discrepancy is likely due to effects of the bond layer being non-negligible and affecting the frequency at which suppression of the A0 mode is achieved as described in, for instance, [91]. f^{A0}_{null} was tracked as a desirable frequency to operate transducers in order to strongly excite S0 waves and suppress the propagation of A0 waves.

FE analysis with the same PZT bonded on a 2 mm thick plate indicated that f^{A0}_{null} is close to 100 kHz in this case; this frequency is also near the resonance of the coupled transducer plate assembly. Simulations that were used to investigate the effects of varying th_{PZT} confirmed the frequency of this resonance increases with thinner PZT discs of the same diameter (see Appendix B for details.) The 20 mm diameter PZT of the smallest thickness, i.e. th_{PZT} =0.5 mm, that was available from suppliers was adopted in order to shift the transducer resonance furthest from f_{null}^{A0}. This thinner PZT was incorporated into FE models, and simulations were used to obtain the velocity responses for the S0 and A0 modes using the same approach used for the case of the thicker PZT on the 5 mm thick plate. The magnitudes of the velocity responses for both modes are plotted in Figure 3.3(b). The first minimum in the A0 response occurs at the frequency when $\lambda_{A0}^{(3D)}$ equals the PZT diameter (i.e. $\lambda_{A0}^{(3D)}(f_{null}^{A0}$=97kHz)=20.5 mm which is very close to 20 mm.) The frequency f_{null}^{A0} of the first minimum in the A0 response occurs far below the PZT resonance, which confirms the PZT may be feasibly operated around f_{null}^{A0} in order to suppress the presence of the A0 mode.

Hanning windowed tonebursts are used to excite Lamb waves over a selected range of frequencies near the point at which suppression of the unwanted Lamb wave occurs, and were considered as voltage inputs to apply to the transducers [27]. Previous research has shown the inputs applied to transmitting PZTs must result in > 8 dB relative purity of the Lamb mode being monitored in order to ensure effectiveness of the adopted unimodal temperature compensation strategies (described in Section 3.4.1 [41].) Five cycled tonebursts of various centre frequencies f_c up to 200 kHz were used as inputs and the energy in the S0 mode (relative to that in the A0 mode) was evaluated using simulation outputs to determine the input with which to achieve optimal excitation of this mode. Five cycled tonebursts of f_c <200 kHz were evaluated, which allowed inferences for inputs having centre frequencies up to the 2nd PZT resonance (around 250 kHz.) The in-plane velocity response of the S0 mode and the out-of-plane velocity response of the A0 mode monitored at the node in the middle of the plate were multiplied by the FFTs of the 5 cycled tonebursts at different f_c to calculate S0 and A0 spectra. The area under the resulting S0 spectra over that under the A0 spectra allowed calculation of the $S0/A0$ mode amplitude ratio at each f_c (this quantity equals the ratio of area underneath the Hilbert envelope of the wavepacket at the S0 arrival to that underneath the envelope of the pulse at the A0 arrival according to Parsevals Theorem [104].)

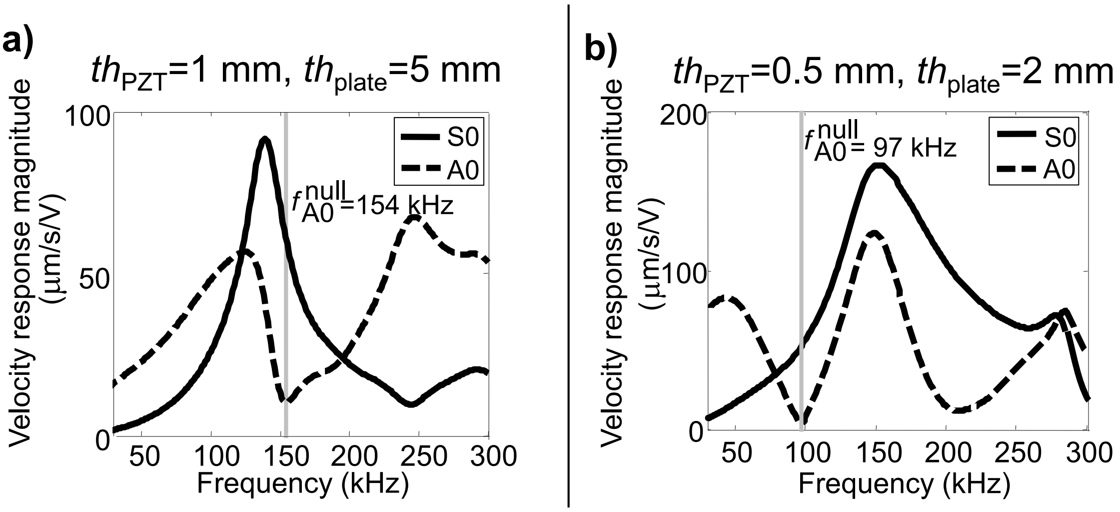

Figure 3.3: The magnitudes of the velocity responses for the S0 mode and the A0 mode obtained from the simulated motions of the mid-plate thickness node at r = 300 mm with 1 V applied to bonded PZTs having (a) th_{PZT} =1 mm on a 5 mm thick plate and (b) th_{PZT} =0.5 mm on a 2 mm thick plate.

The resulting mode amplitude ratios are plotted as functions of f_c for transducers on 5 and 2 mm thick aluminum plates in Figure 3.4(a)-(b) respectively. The resonance frequency, f_r, of the transducers are indicated using the superimposed vertical gray lines. The local maxima and minima that are respectively labeled A and B in the curves occur close to the frequencies at which relevant multiples of $\lambda_{A0}^{(3D)}$ match the transducer diameter and cause suppression or stronger excitation of the A0 mode. The frequencies associated with the local maxima in the plotted ratios of Figure 3.4 are 165 kHz and 98 kHz for the transducers on 5 and 2 mm thick plates respectively, and they are well separated from f_r; it should be noted that these frequencies lie outside the -6 dB bandwidth points associated with the resonance too. The area underneath the envelope of the waveform at the S0 arrival is larger than the area underneath the envelope of the weaker pulse at the A0 arrival by >15 dB with inputs at these centre frequencies.

Analysis of the ratios of Hilbert envelope based amplitudes of S0 and A0 wavepackets were computed too, and indicated that S0 tonebursts have amplitudes that are >8 dB higher than those of A0 wavepackets through the use of 5 cycled tonebursts at these f_c on 2 mm and 5 mm thick plates. It is therefore recommended to apply tonebursts consisting of ≥5 cycles and f_c of 165 kHz and 98 kHz to the PZTs bonded on 5 mm and 2 mm thick aluminum plates respectively in order to achieve off resonance transduction of sufficiently selective S0 waves for the purposes of SHM.

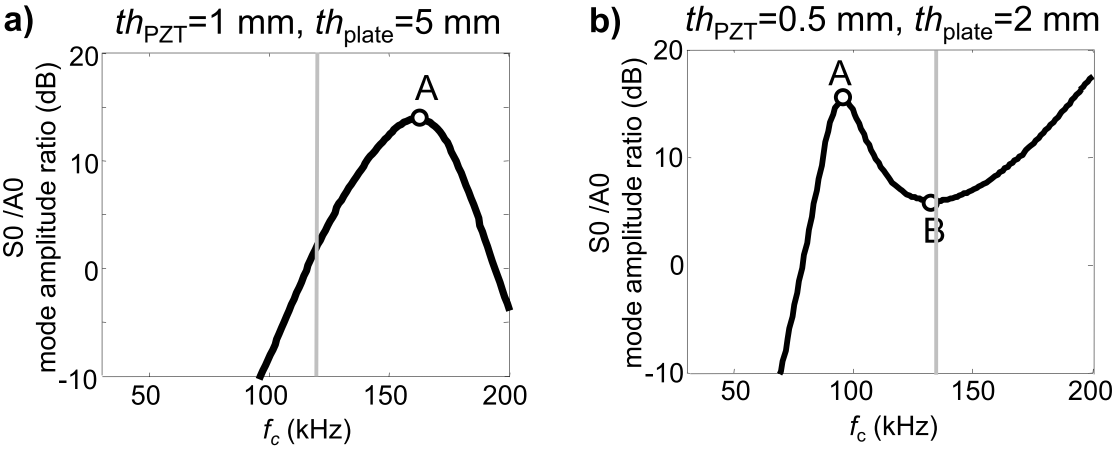

Figure 3.4: The energy in 5 cycled tonebursts of the S0 mode relative to that in the weaker A0 pulse at r =300 mm as a function of f_c of tonebursts applied to PZT discs having (a) th_{PZT} =1 mm on 5 mm thick plates and (b) th_{PZT} =0.5 mm on 2 mm thick plates. The gray lines indicate the resonance frequencies f_r of the bonded PZT discs.

3.3.3 Encapsulation

The use of the sensors in outdoor environments requires that the electrical connections to the transducers are weatherproofed and strain relieved. Encapsulation of the PZT discs with the cap shown using isometric views in Figure 3.5(a)-(b) was used to achieve these tasks. The thicker black lines in the diagrams show the coaxial cable and the arrows indicate the pattern used to wind it through the sequence of ∅ 3 mm holes in the embodiment for strain relief. The stripped wires from the ends of the cable within the cap are connected to transducers using procedures that depend on the electrode configuration of PZTs used. In instances involving the use of a PZT having standard screen printed disc shaped electrodes, the live wire is soldered to the exposed surface of the PZT disc and a separate ground wire is connected to a different point on the plate as in [41]. The live and ground wires are soldered to the respective surface electrodes on a PZT disc whenever one having a wrap around electrode is used. The PZT disc is pressed against the ridge in order to fit it into the cap. All holes on the cap are sealed using the adhesive (Loctite 9483, Loctite, UK) which is then used to bond the assembly to structures. An axisymmetric diagram of the encapsulated PZT bonded on a 2 mm thick plate is shown in Figure 3.5(c) with various dimensional parameters identified.

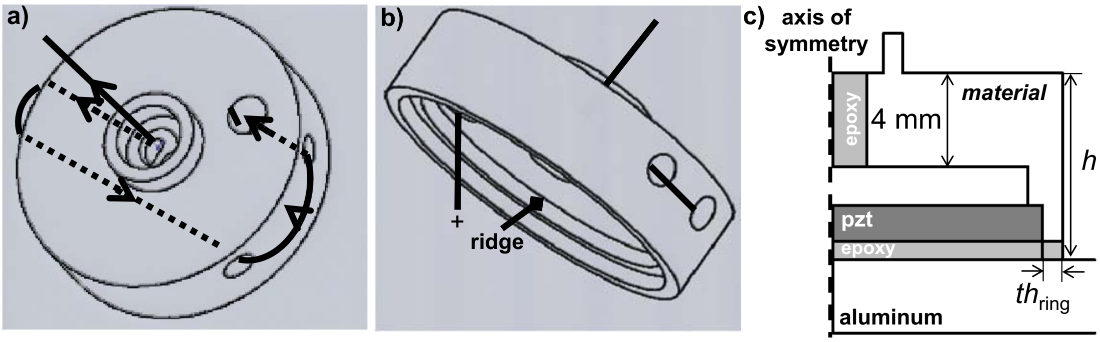

Figure 3.5: Isometric views of the cap which show (a) the winding of wires and (b) the housing for PZT discs as well as (c) an axisymmetric cross section of the encapsulated transducer with parameters identified which were finalized using FE analysis.

An anodized aluminum cap of height h =10 mm and ring thickness th_{ring} =2 mm was initially considered for encapsulation because a prototype could be built within college machine shops. The cap was incorporated into FE models and simulations similar to those described in Section 3.3.2 were used to obtain the velocity responses for the the S0 mode and the A0 mode. The magnitudes of velocity responses from analyses with the transducer on a 2 mm thick plate are plotted in Figure 3.6. There are undesired peaks in the S0 response at 110, 135, and 180 kHz. There are changes around the peak in A0 transmission at 50 kHz which are apparent when comparing the dashed curve to the result of Figure 3.3(b).

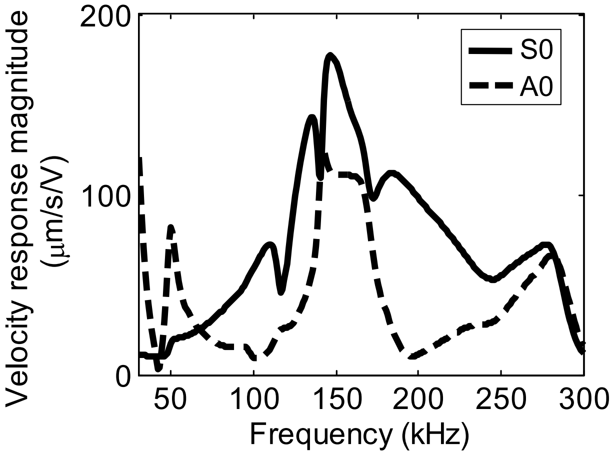

Figure 3.6: The magnitudes of the velocity responses for the S0 mode and the A0 mode obtained from simulated mid-plate thickness motions at r = 300 mm with 1 V excitation of a bonded 20 mm diameter, 0.5 mm thick PZT disc that is encapsulated using an Al cap of h =10 mm, th_{ring} =2 mm on a 2 mm thick Al plate.

Operational deflection shapes (ODSs) showing relative amplitudes of motion at different points in the encapsulated transducer under the influence of its operating forces were computed and compared to ODSs of the unencapsulated transducer to determine the mechanisms causing changes in their responses [105]. The scaled ODSs obtained at 50 and 110 kHz are shown in Figure 3.7. The ODSs of Figure 3.7(b),(d) show portal frame type vibrations in the cap [105]. The out-of-plane motions at 50 kHz and expansion/contraction of the shell at 110 kHz are apparent in the ODS of Figure 3.7(b) and Figure 3.7(d) respectively; the 110 kHz vibrations influence transducer motions close to the region around f_{null}^{A0} of this transducer. The dimensions h, th_{ring}, and the material were properties identified as influential to these dynamics. These parameters were varied over the range of values shown in Table 3.1 in order to minimize the undesired influences of the vibrations in the cap.

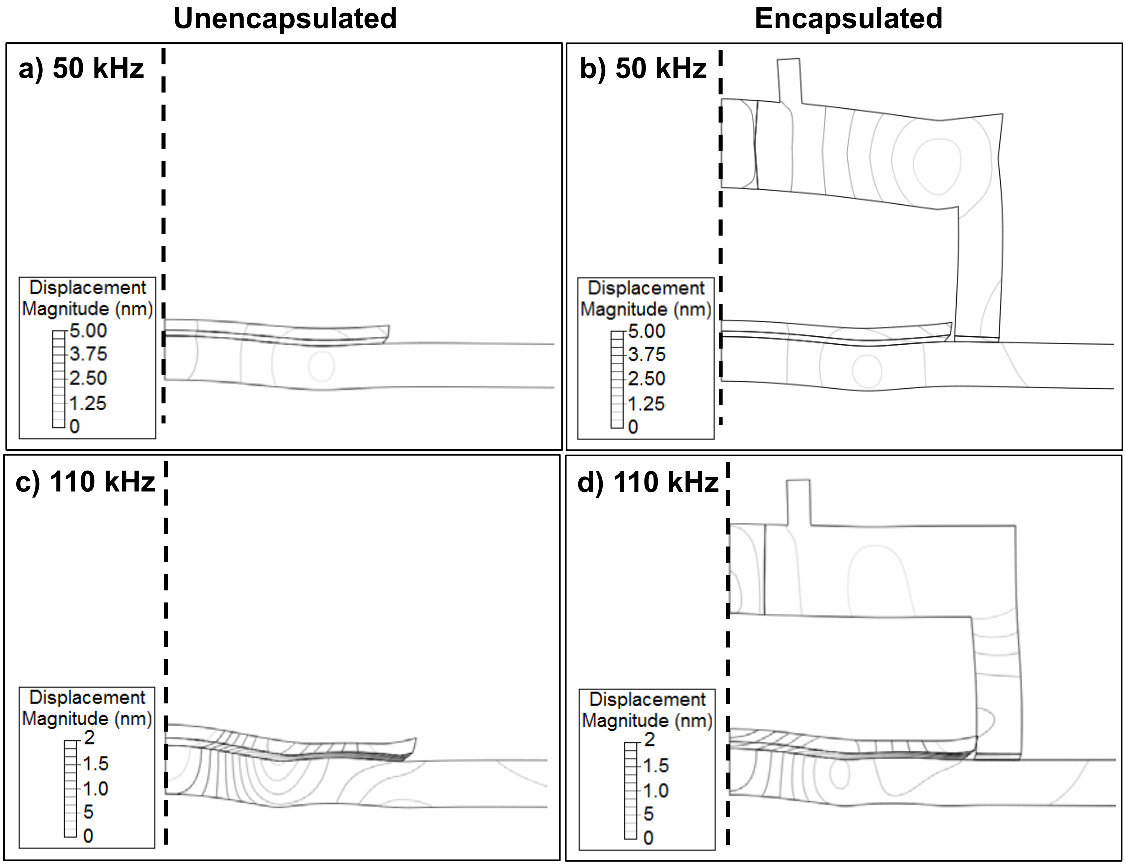

Figure 3.7: Operational deflection shapes (ODSs) of the bonded 20 mm diameter, 0.5 mm thick PZT disc at (a) 50 kHz, (b) the ODS of the PZT encapsulated with an aluminum cap of h =10 mm, th_{ring} =2 mm at 50 kHz, and (c)-(d) the ODSs at 110 kHz; displacement magnitudes are indicated via grayscale bands. Note the scales in (a)-(b) are different from those in (c)-(d).

Table 3.1: Parameters and range of values studied for encapsulation development.

Parameter	Values studied
h	6-14 mm
th_{ring}	0.5-5 mm
material	anodized Al,HDPE

As the natural frequency associated with bending of a cylinder varies inversely with its length [105], initial studies focused on how to adjust h to shift associated in-plane vibrations in the cap out of the region around f_{null}^{A0}. Simulations were used to monitor mid-plate thickness motions with incremental (2 mm) change in h. The magnitudes of the velocity responses for the S0 mode that were obtained from the simulations are plotted in Figure 3.8 in a 50 kHz range around f_{null}^{A0}; results are split into two ranges of h for clarity. Figure 3.8(a) shows that increases in the frequency associated with the motion within the cap of Figure 3.7(d) correlates with decreases in h. Figure 3.8(b) indicates decreases in h shift this resonance out of this bandwidth. This analysis led to the choice of a cap of 6 mm height, which equals the smallest value of h allowing accommodation of the soldered electrical connections and strain relief system.

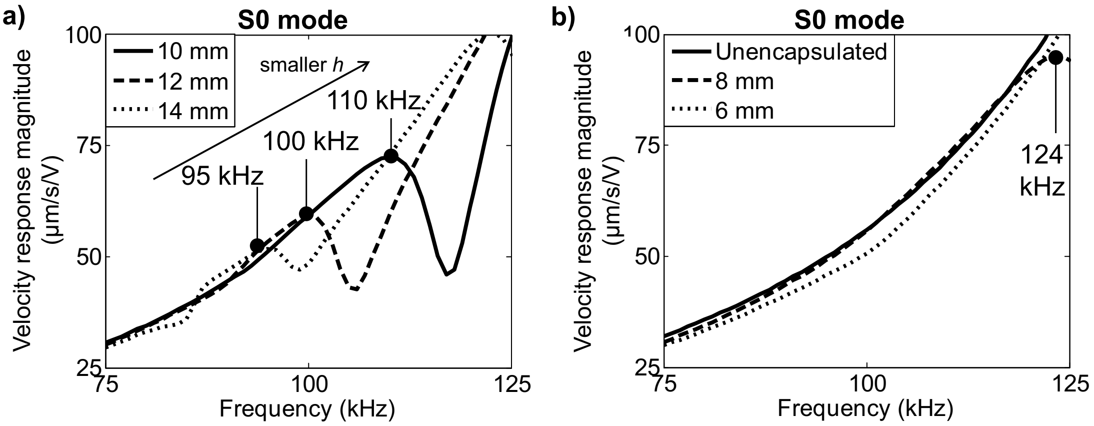

Figure 3.8: The magnitudes of the velocity responses for the S0 mode obtained from simulated mid-plate thickness motions at r = 300 mm with 1 V excitation of 0.5 mm thick bonded PZTs which are encapsulated with aluminum caps having th_{ring} =2 mm and (a) h =10-14 mm as well as (b) h =6-8 mm along with the result for the unencapsulated PZT on a 2 mm thick plate.

Reducing h effectively eliminated undesired in-plane vibrations in the region around f^{A0}_{null} though this did not eliminate the effects on out-of-plane velocities. Decreasing th_{ring} to 1 mm (with h =6 mm) to further reduce coupling of cap and plate vibrations only resulted in slight improvements in S0 purity (relative to A0.) Material changes were sought thereafter to examine whether mismatches in acoustic impedances (between cap and plate material) could be exploited to eliminate remaining vibrations. Simulations were run with caps made of HDPE material (see Appendix A for material properties) which was identified as a candidate for its processability and durability. The in-plane and out-of-plane particle velocities were monitored at the mid-thickness node of the plate, and used to extract S0 and A0 velocity responses respectively for the case of transduction with PZTs encapsulated using caps made of this material. The magnitudes of the velocity responses are plotted in Figure 3.9 along with the results when caps made of aluminum are used and the PZT discs are not encapsulated at all. The similarity between the responses obtained through simulations with HDPE caps and unencapsulated PZTs led to the choice of HDPE as the cap material.

Simulations with encapsulated transducers on 2 and 5 mm thick aluminum plates were used to confirm that the final cap design (h =6 mm, th_{ring} = 1 mm, material=HDPE) effectively minimized reverberations. The PZTs of FE models were excited with 1 V at frequencies up to 300 kHz, and the velocity responses for the S0 mode and the A0 mode were obtained from the monitored wave field at the mid-plate thickness node located 300 mm from the transducers. The velocities from simulations involving 2 mm and 5 mm thick aluminum plates were weighted by the FFTs of 5 cycled, 100 kHz tonebursts and 8 cycled, 170 kHz toneburst respectively. IFFTs were applied to the resulting velocity spectra in order to calculate the propagations of S0 and A0 wavepackets that may result with inputs that were being considered. Figure 3.10(a) and (b) show the time traces for cases of S0 and A0 motion in 2 and 5 mm thick plates, respectively, along with superimposed results from simulations involving the unencapsulated transducers. The wavepackets of both modes transmitted from the encapsulated transducers cannot be distinguished from those transmitted from the unencapsulated PZTs. These results suggested that the changes to the cap design ensured it would be suitable for encapsulation.

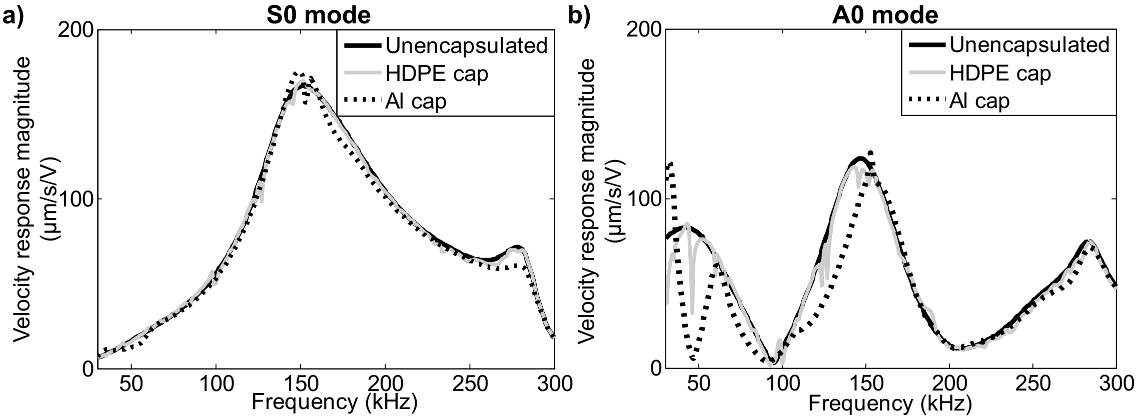

Figure 3.9: The magnitudes of the velocity responses for (a) the S0 mode and (b) the A0 mode obtained from simulated mid-plate thickness motions at r =300 mm with voltage excitation of the 20 mm diameter, 0.5 mm thick PZT disc, and the results obtained with similar excitation of the PZT encapsulated using caps made of anodized aluminum or HDPE and which have h =6 mm, th_{ring} =1 mm.

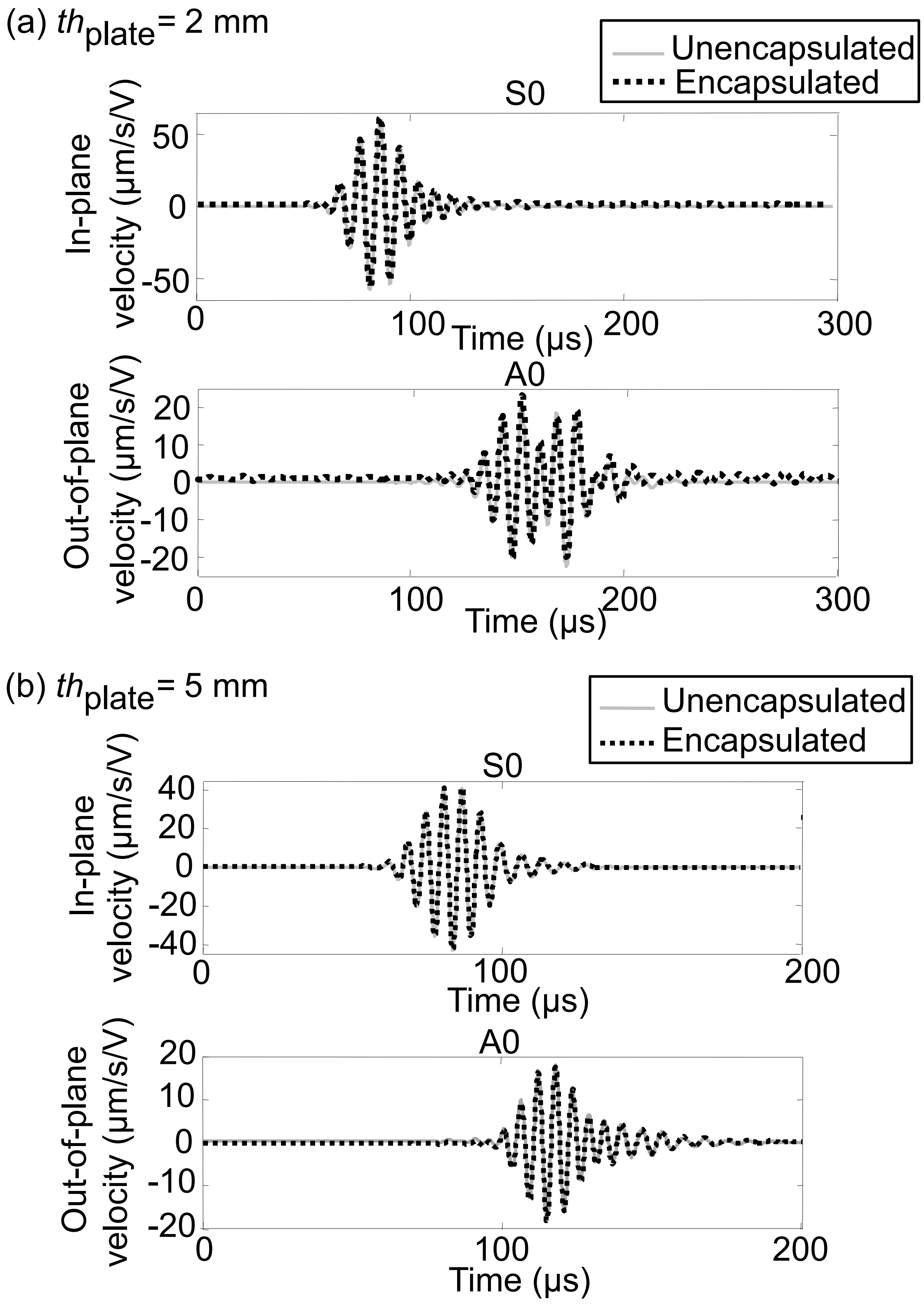

Figure 3.10: The S0 wavepacket and that of the weaker A0 pulse at a distance of 300 mm from encapsulated (HDPE caps of h =6 mm, th_{ring} =1 mm) and unencapsulated (a) 20 mm diameter, 0.5 mm thick PZTs excited using 5 cycled, 100 kHz tonebursts on 2 mm thick plates and (b) the results from FE analyses with 1 mm thick versions of the PZT excited using 8 cycled, 170 kHz tonebursts on 5 mm thick plates; signals calculated using the particle velocities monitored at the mid-plate thickness node of FE models.

3.3.4 Experimental validations

Experiments were undertaken to ensure the excitations applied to the transducers of Section 3.3.2 could practically generate strong S0 waves (relative to A0) and the encapsulations of Section 3.3.3 were effective as designed.

Laser Doppler vibrometers (LDV) having standard sensor heads (OFV-505, Polytec, DE) were used to measure the wave field from the transducers in order to verify that they excite relatively strong S0 waves on the aluminum plates for which they were developed. The setup consisting of the LDVs in the configuration of Figure 3.11(a) was used for these purposes. PZT discs of the dimensions in Section 3.3.2 which were poled through the thickness and that had wrap around ground electrodes were bonded at (x =0.475 m,y =0.625 m) and (x =0.415 m,y =0.625 m) on the 2 mm and 5 mm thick square aluminum plates respectively. An arbitrary waveform generator (33220A, Agilent, UK) in line with an amplifier (7602, Krohn-Hite, US) was used to apply inputs of 5 Vpp to the PZTs. The amplifier was needed as the interface used to upload tonebursts to the function generator was configured to output signals having amplitudes of 2 Vpp. Tonebursts of f_c =100 kHz and 170 kHz were used to excite the PZTs bonded to the 2 mm and 5 mm thick plates respectively; 8 cycles were used for the higher frequency excitations as this enabled concentration of energy near f_{null}^{A0} while only 5 cycles were used at 100 kHz to avoid temporal elongations of wavepackets (or decreases in resolution.) The beams of the LDVs were focused at the observation point on top of reflective tape which was adhered to the plate surface at distances of 300 mm and 420 mm from the PZTs bonded to the 2 mm and 5 mm thick specimens respectively; this positioning allowed temporal separation of the S0 wavepacket, the weaker A0 pulse, and the reflections from the plate edges. An oscilloscope (44Xi, Lecroy, UK) was used to record signals of the surface velocities output from the LDV decoder (OFV-5000, Polytec, DE) using 100 time averages and a sampling frequency f_s =10 MHz. The in-plane and out-of-plane components of the velocity field were calculated from these measurements [106]. The wavepackets at the S0 and A0 arrivals in the respective time traces of in-plane and out-of-plane velocities were windowed and FFTs were applied to obtain the spectra associated with the characteristic motions of the modes.

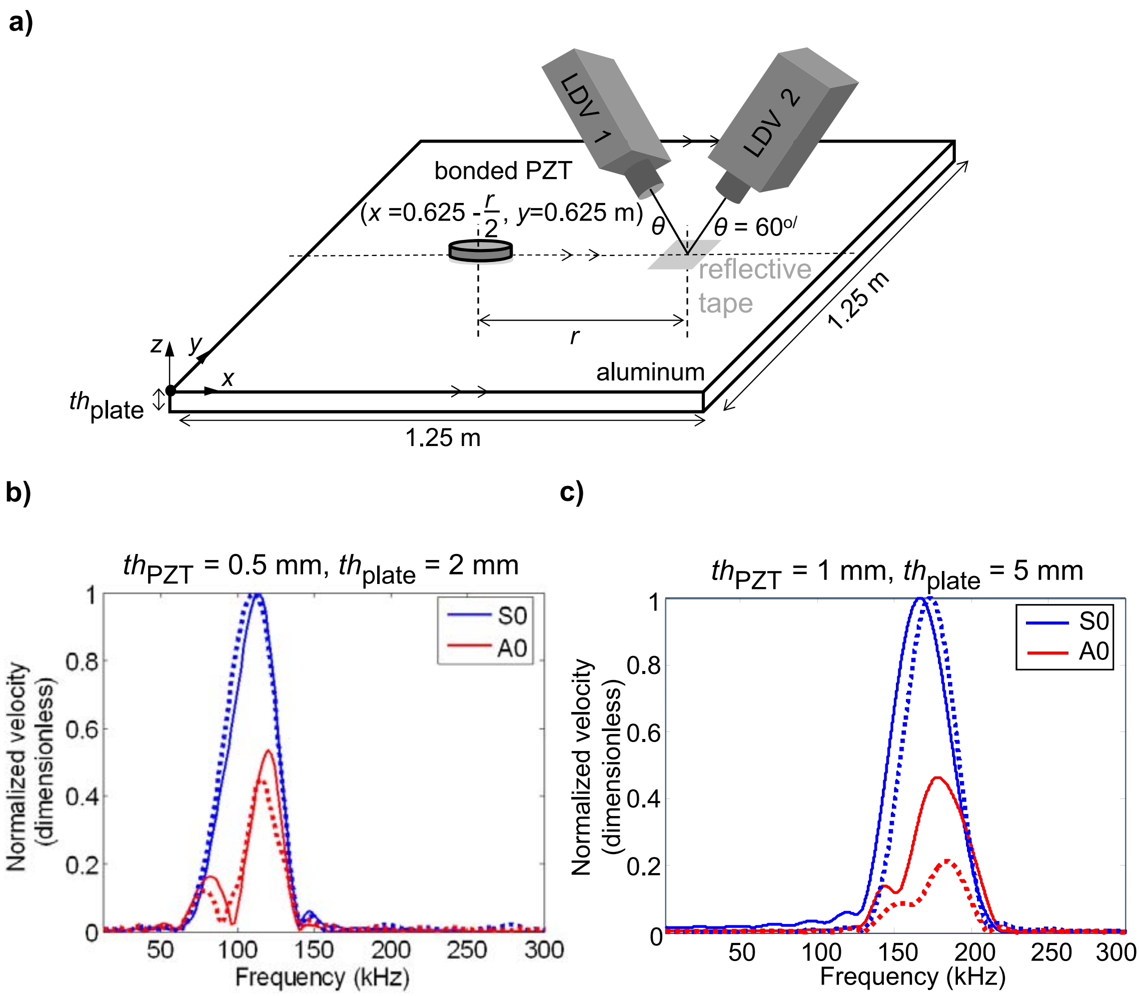

Figure 3.11: (a) The laser doppler vibrometer (LDV) measurement configuration and plots comparing the measured (dotted lines) and simulated (solid lines) spectra of the in-plane S0 and out-of-plane A0 velocities on the surface of (a) 2 mm and (b) 5 mm thick aluminum plates at r =300 mm and r =420 mm, respectively, from 20 mm diameter bonded PZT discs of th_{PZT} that are excited with the inputs used in Figure 3.9; maxima in S0 spectra have been used to normalize (b)-(c) to allow comparisons.

The magnitudes of velocity spectra were normalized by the maximum amplitudes of the spectra for the S0 mode. The results are plotted in Figure 3.11(b)-(c) along with the corresponding results from FE simulations to allow comparisons; absolute amplitudes of the velocities disagree with those obtained experimentally though normalized results are of concern for assessing relative amplitudes of motion in the two wave modes and are only considered here as a result. The plots indicate that maxima and minima in the velocity spectra occur at frequencies that are close to those obtained in simulations and show qualitative agreements in the relative proportions of the excited S0 mode and A0 mode. Minor frequency shifts are apparent in the curves obtained from tests relative to those obtained using simulations for the cases of the PZTs bonded on 5 mm thick plates. These may be due to discrepancies between the thickness or properties of the adhesive and those of the epoxy in the FE model. The characteristics in the experimentally obtained spectra are sufficiently similar to those obtained from FE modeling. Thus, the results validate the recommendation to apply the inputs of Section 3.3.2 to the PZTs in order to achieve preferential excitation of the S0 mode (relative to the A0 mode.)

Following the experiments with the laser, receiving PZT discs having wrap around electrodes were bonded at the locations where the laser was focused and used to acquire pitch catch data. This was done in order to analyze waveforms recorded between the PZTs, and to compare results to those obtained afterwards with the same sensors encapsulated using the caps of Section 3.3.3. A Wavemaker (Duet X, Macro Design Ltd, UK) function generator/receiver was used to apply 5 cycled, 100 kHz tonebursts of 60 Vpp to the transmitting PZT on the 2 mm thick aluminum plate and the signal at the receiving PZT was recorded on the oscilloscope using f_s =10 MHz. The recorded pitch catch signal is shown in Figure 3.12(a) and the waveform obtained from the test repeated with both sensors of the pair encapsulated is shown in Figure 3.12(b); time traces are plotted on the same scale up to the region at the end of the weaker A0 pulse in order to facilitate comparisons.

There are slight variations in the amplitudes of the two signals in the plots of Figure 3.12(a)-(b). These discrepancies are likely due to effects of the state of the adhesive cure being different at the times when the data was acquired. The ratios of the envelope detected amplitude of the S0 arrival to that of the maximum in the signal envelope at the A0 arrival extracted from waveforms of Figure 3.12(a)-(b) equal 21 dB and 20 dB respectively. The pitch catch signals recorded from similar tests between PZT sensors bonded on the 5 mm thick aluminum plate are shown in Figure 3.12(c)-(d). The signal amplitudes are smaller in the pitch catch data acquired using the pair of encapsulated PZTs in this case. The shape and temporal length of the wavepackets at the S0 and A0 arrivals are similar. The ratios of the amplitude of the S0 arrival to that of the weaker A0 pulse equal 25 dB and 26 dB within the signals of Figure 3.12(c)-(d) respectively. These results indicate that the developed encapsulation was fit for purpose.

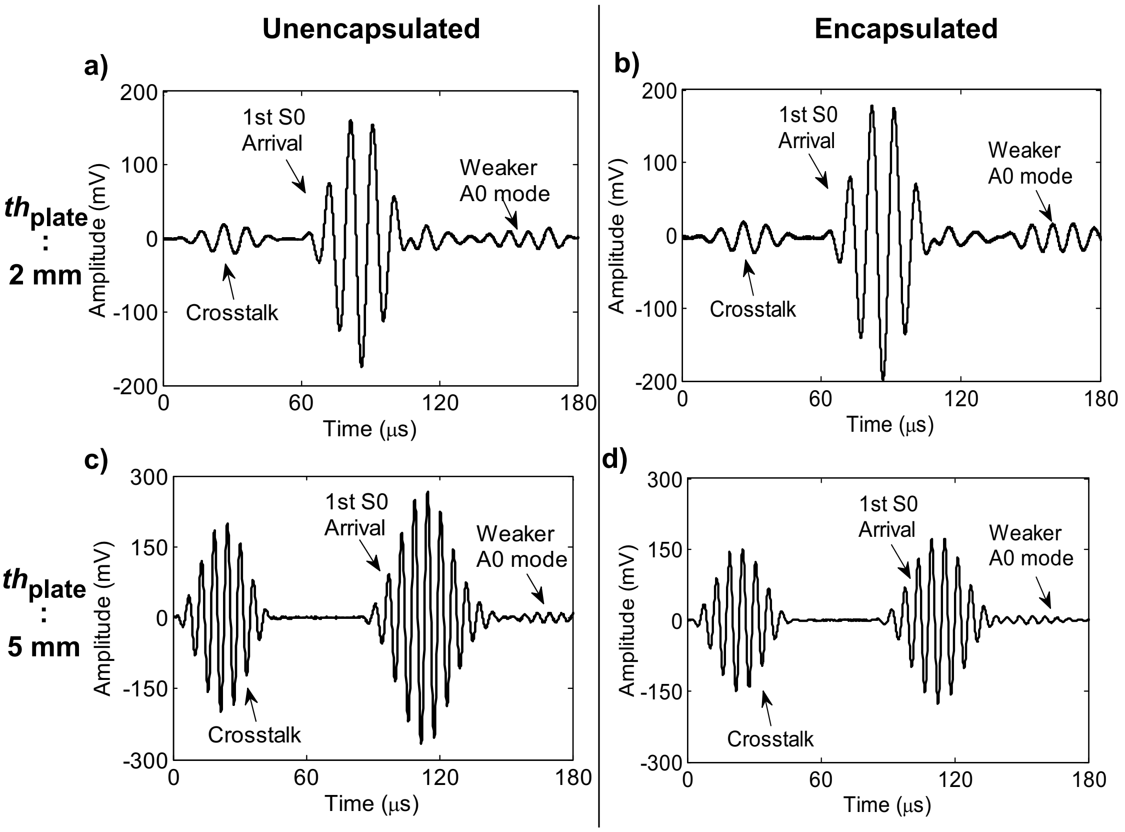

Figure 3.12: Pitch catch data obtained using (a) unencapsulated and (b) encapsulated 20 mm diameter, 0.5 mm thick PZTs bonded on a 2 mm thick, 1.25 m square aluminum plate with separations of 300 mm in the configuration of Figure 3.11(a) and (c)-(d) the data obtained using the 1 mm thick PZTs bonded with separations of 420 mm in the configuration of Figure 3.11(a) on the 5 mm thick plate; the tonebursts used in Figure 3.9 were applied to the transmitting PZTs.

3.4 Signal processing methods

Guided wave SHM systems require signal processing to convert data recorded using sensors into readily understandable maps for the discrimination and localization of defects. Baseline subtraction is a defect detection method that is adopted for the reasons discussed in Section 2.3, and it is applied after compensating guided wave signals for temperature effects using the algorithms of Section 3.4.1. The resulting subtracted signals can be used to form an image through various methods [41, 73, 107]. The delay-and-sum algorithm of Section 3.4.2 is employed as it is relatively simple and sufficient for the stability studies in this work.

3.4.1 Automated temperature compensation and baseline subtraction

Description of algorithm

Baseline subtraction is a defect detection method which evaluates the difference between baseline signals from the structure in its healthy (baseline) state and current signals monitored afterwards. This method was adopted in this thesis because it is able to handle data that contains overlapping arrivals of features (e.g. edges, welds, etc.) that are common in many plate-like assemblies and is the only approach for which compensation for environmental effects such as temperature changes have been demonstrated. Various methods have been exploited to compensate for the effects of thermal changes. A method called optimal baseline selection (OBS) was proposed in [108]. This technique requires a database of baselines be collected from the undamaged structure experiencing the range of environmental conditions expected in service, and prescribes that monitored data is subtracted from the baseline acquired when conditions most closely matched those encountered while monitored. Further research confirmed that stretching of the time bases of guided wave data accounts well for temperature related time delays that vary linearly with propagation distance [87, 88]. The combination of baseline subtraction with OBS and optimal stretch preserves detectability of 1-2% reflectors for instances of there being discrepancies of up to 0.5°C in temperatures at which signals are recorded [84–86]. Therefore, these algorithms were implemented for processing data in this work.

The algorithm is an automated version of the one that has been extensively described in [41] and is illustrated using a block diagram in Figure 3.13. Comparisons are made between each current signal and a database of baseline signals recorded over a temperature range the structures experience while they are operated in service. The current signals recorded during the monitoring periods are high pass filtered, power normalized, and subtracted from each signal in a database of baselines recorded every 0.5°C over the range of the operating temperatures (-5 to 40°C here.) Intervals of 0.5°C are used as these have been shown to be sufficient and practical for temperature compensation in [61, 84, 85]. The baseline for which the subtracted signal exhibits the minimal root mean square (RMS) value is retained as the optimal baseline; the RMS value is used instead of other metrics such as the maximum of the subtracted signal because it exhibits less sensitivity to changes such as local thermal variations [85].

A frequency domain implementation of the optimal stretch algorithm is applied to stretch/compress the time base of this optimal baseline and account for the limitation of a finite database [84]; this algorithm is adopted because it performs as accurately as recently optimized approaches to compensation [88]. The optimal baseline for each current signal is zero padded prior to computation of its FFT, as in [36]. Stretched baseline spectra are computed by interpolation of the optimal baseline spectrum onto frequency vectors with incrementally varied step sizes, as in [84]; spectral distortions are corrected using the procedures of [87]. Candidate stretched baseline signals are obtained by applying inverse FFTs to interpolated spectra. Out of all the candidate stretched baselines, the signal that results in the smallest RMS value when it is subtracted from the current signal corresponds to the optimally stretched baseline. Equation 2.3 is used to compute the difference signal between the current signal and this optimally stretched baseline. The difference signal is band-pass filtered using a cosine tapered frequency domain filter having the bandwidth of 7 cycled tonebursts as in [41], and corrected for beam spreading effects using Equation 2.4. The decibel (dB) values of resulting residual signals are evaluated by considering envelope detected amplitudes relative to those of the S0 arrival in baselines to allow comparisons between data from different sensor pairs.

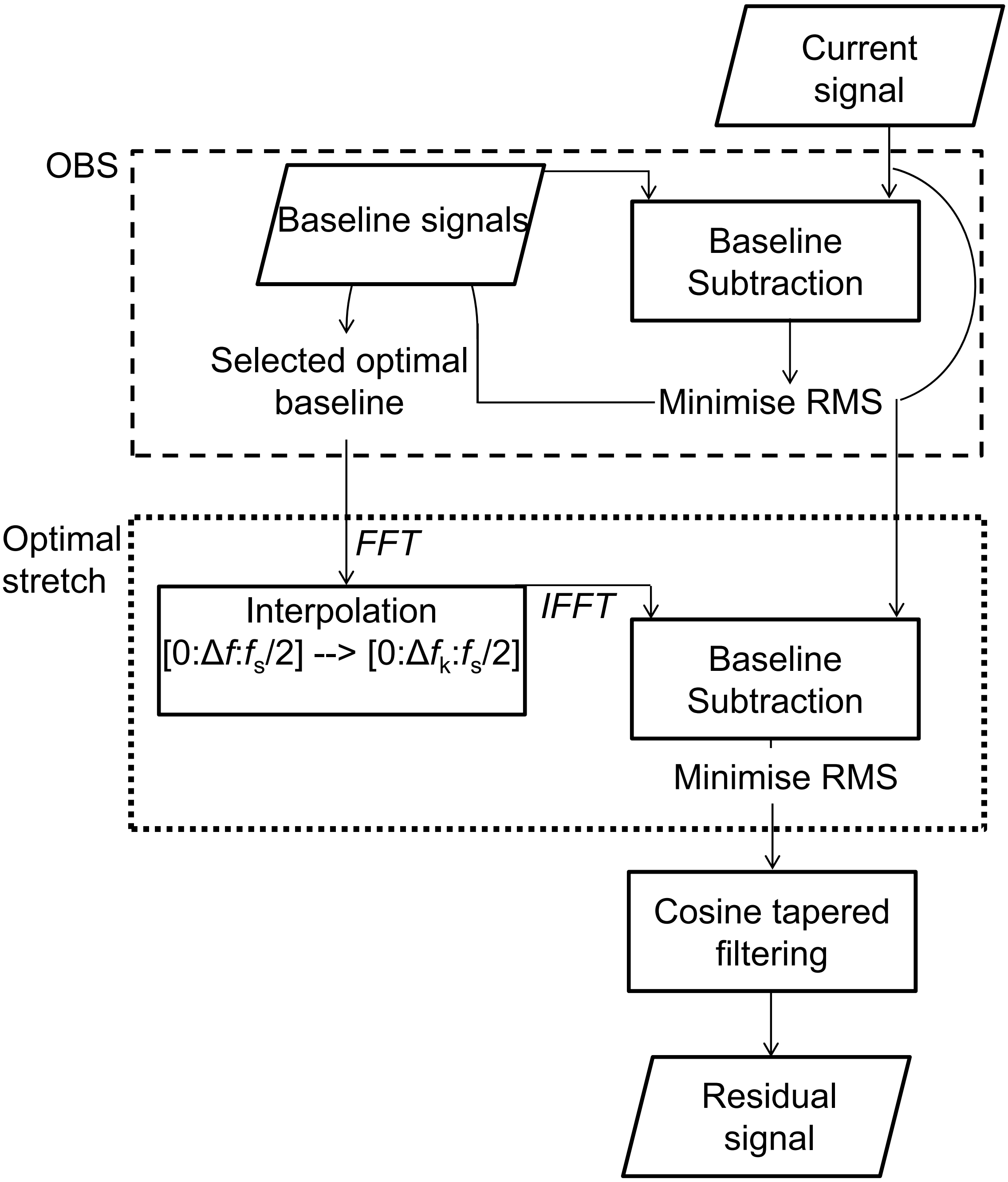

Figure 3.13: Block diagram of the temperature compensation and baseline subtraction algorithm which combines subtraction, optimal baseline selection (OBS), and optimal stretch in order to calculate the temperature compensated residual signal.

Experimental evaluations

Experiments were used to validate the effectiveness of the implemented temperature compensation algorithms. Transmitting and receiving PZT discs having screen printed disc shaped electrodes and the dimensions of Section 3.3.2 were bonded at (0.34 m, 0.42 m) and (0.73 m, 0.96 m) respectively on a 1.25 m square, 5 mm thick aluminum plate using the two component epoxy adhesive (Loctite E-05CL, Henkel, US) recommended in [41]. The plate was moved to an environmental chamber (Alpha 1550-40H, Design Environmental, UK) and cycled 6 times in the range 20-40°C. Every 2 cycles consisted of periods of baseline signal acquisition in the temperature ranges 19-21, 29-31, and 39-41°C followed by current signal collection at set points of 20, 30, and 40°C. Tonebursts of 8 cycles and 170 kHz centre frequency were sent to the transmitting PZT via an arbitrary waveform generator (33220A, Agilent, UK) and amplifier (7602, Krohn-Hite, US), and the resulting received signals were recorded using a preprogrammed oscilloscope (100 averages, f_s = 10 MHz.)

The performance of the signal processing algorithms were analyzed using the collected data. Temperatures associated with the current signals were compared with those associated with optimal baselines chosen by OBS. As the two temperatures consistently matched, this represented sufficient validation of OBS. The optimal stretch algorithm was applied to process subsets of the baseline signals acquired at temperatures that were 0.5°C and 2°C higher than those at which current signals were collected. The temperatures of the baselines were 20.5 and 22°C, 30.5 and 32°C, 40.5 and 42°C for the current signals recorded at 20, 30, and 40°C respectively. Residual signals were computed by subtracting the current signals from optimally stretched versions of the baselines. The residual signals for the current signals at 40°C are plotted in Figure 3.14; $t_{\mathrm{1st\ arr}}$ and $t_{\mathrm{coverage\ limit}}$ are the v_{gr} based arrival times of the direct S0 arrival and its reflection from the point involving the longest transmitter-edge-receiver path. The maximum amplitudes of the residuals in Figure 3.14 are close to -36 dB and -30 dB for the cases of there being 0.5°C and 2°C difference in temperatures at which current signals and baselines are recorded respectively. These values correspond to the averages of maximum residual amplitudes computed from repeating tests for 20 sensor pairs. The results are indicative of the different amount of change in signals due to varying levels of thermal change and agree with what's been found using previous implementations of optimal stretch and the PZTs on 5 mm thick plates [41].

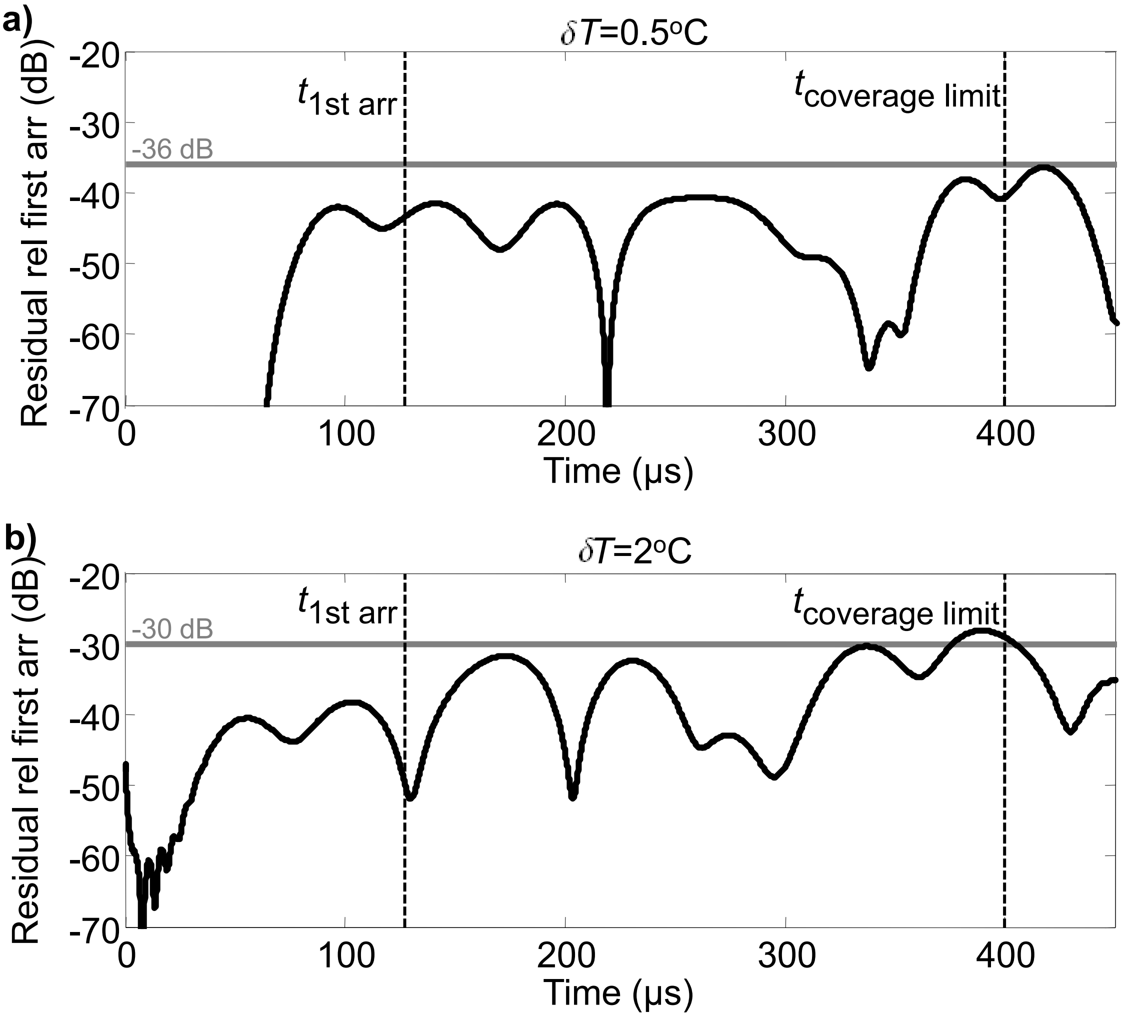

Figure 3.14: Amplitudes of residuals relative to the S0 arrival amplitude obtained by subtracting a current signal acquired at 40°C from optimally stretched versions of baselines collected at (a) 40.5°C and (b) 42°C using a sensor pair on a 5 mm thick aluminum plate.

Data was acquired using bonded PZTs on a 2 mm thick, 1.25 m square aluminum plate prior to and after drilling a ∅ 5 mm through hole on the structure as described in Section 2.2.3. This data is used to show the capability of the algorithms to suppress temperature related variability and enable robust detection of the hole. In particular, the signals from Figure 2.7 are plotted on a dB scale in Figure 3.15. The results obtained from simply subtracting the pitch catch signals when there are discrepancies of 1°C in temperatures at which the signals are recorded introduces temperature related variability at 60, 180, and 300 μs. The added variability masks the scattering due to the hole (circled in the plot.) Compensation using OBS lowers the amplitudes of residuals at these times where no reflections from defects are expected. Additional compensation using the optimal stretch algorithm results in the dashed curve, which clearly enables discrimination of the signal due to the defect with 9 dB margin above the signal from regions of undamaged structure.

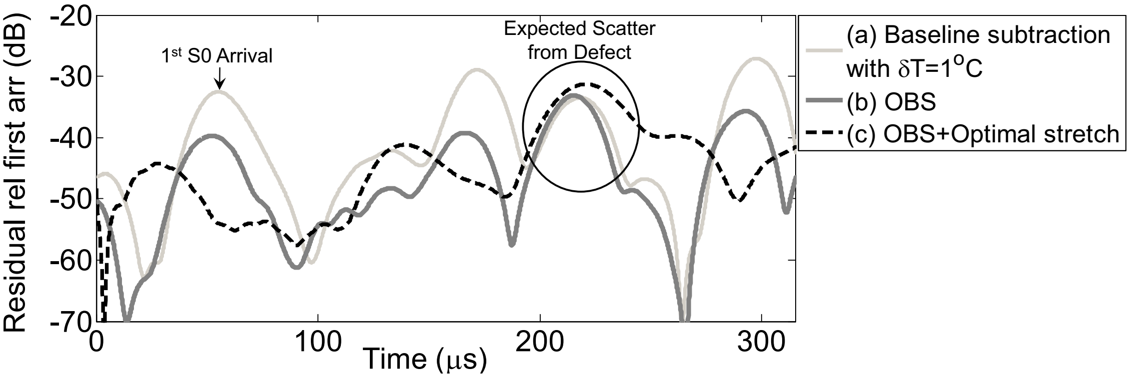

Figure 3.15: Amplitudes of residuals relative to the S0 arrival amplitude that result from (a) subtracting the signals in Figure 2.5 as well as results from subtracting $c(t)$ from (b) the optimal baseline and (c) an optimally stretched version of this baseline.

3.4.2 Imaging

Imaging is used to convert the information in the residuals from the sparse sensor arrays into visual maps which aid in making practical judgments regarding the location and severity of defects. Many of the algorithms which may be used for these purposes are described in [107]. Methods have also been developed which allow localization enhancement through probabilistic assessment of the residual signals [73] and adaptive weighting of image intensities [74]. The delay-and-sum (ellipse) beamforming technique is among the simplest of the methods to implement, relatively robust to group velocity errors [107], and allows refinements such as those discussed in [44, 74, 109]. It is for these reasons that the ellipse algorithm was adopted in this work rather than alternatives. The main aim of this work is concerned with analyzing the reliability of detection approaches rather than expanding imaging capabilities after all.

The ellipse algorithm uses a mapping function to assign pixel intensity values $I(x, y)$ to points (x, y) within coverage areas. In the implementation within this work, the current signal recorded between transmitting sensor i and receiving sensor j is subtracted from the optimally stretched baseline using Equation 2.3. The Hilbert envelope based amplitude of the result $s_{ij}(t)$ is normalized by the amplitude of the S0 arrival. The pixel values are evaluated as $s_{ij}(t_{ij}(x,y))$ where t_{ij} is the group velocity based arrival time of the wave propagating from the transmitting transducer at (x_i, y_i) to the receiving sensor at (x_j, y_j) by way of (x, y), i.e. [41]

$$t_{ij}(x,y) = \frac{\sqrt{(x_i - x)^2 + (y_i - x)^2} + \sqrt{(x_j - x)^2 + (y_j - x)^2}}{v_{\mathrm{gr}}}. \tag{3.1}$$

In order to accurately image reflection coefficients measured with the sensor pairs, $s_{ij}(t_{ij}(x,y))$ are scaled for geometric spreading of the source and scatterer as in [45, 74](rather than beam spread correction using Equation 2.4.) The dB values of resultant quantities are retained in a matrix $I_{ij}(t_{ij}(x,y))$ which corresponds to the contribution of sensor pair ij to the pixel intensity matrix. After calculating I_{ij} for all unique combinations of N sensors, results are summed and divided by the binomial coefficient $\binom{N}{2}$ to obtain the image intensity map normalized by the number of sensor pairs

$$I(x,y) = \binom{N}{2}^{-1} \sum_{i=1}^{N-1} \sum_{j=i+1}^{N} I_{ij}(t_{ij}(x,y)). \tag{3.2}$$

The implemented algorithm was evaluated using data taken from studies in which a shipping container door was monitored [36, 109]. In these studies, the area of the 2 mm thick, corrugated steel panel that is dashed in the photograph of Figure 3.16(a) was monitored with an array of 20 mm diameter, 1 mm thick PZT discs bonded at the numbered locations. Five cycled, 100 kHz tonebursts were input to sensors and the propagation patterns of the strongly excited S0 wave were recorded at the other PZT discs until pitch catch data was acquired for all unique combinations of transmitting and receiving sensors; the detailed experimental procedures can be consulted in [36]. Signals were acquired during a 3 week period to compile a baseline database which had maximum temperature gaps of 0.3°C, and current signals were recorded a week later and after a couple of weeks with a 10 mm hole drilled at the point marked by an X in Figure 3.16(a).

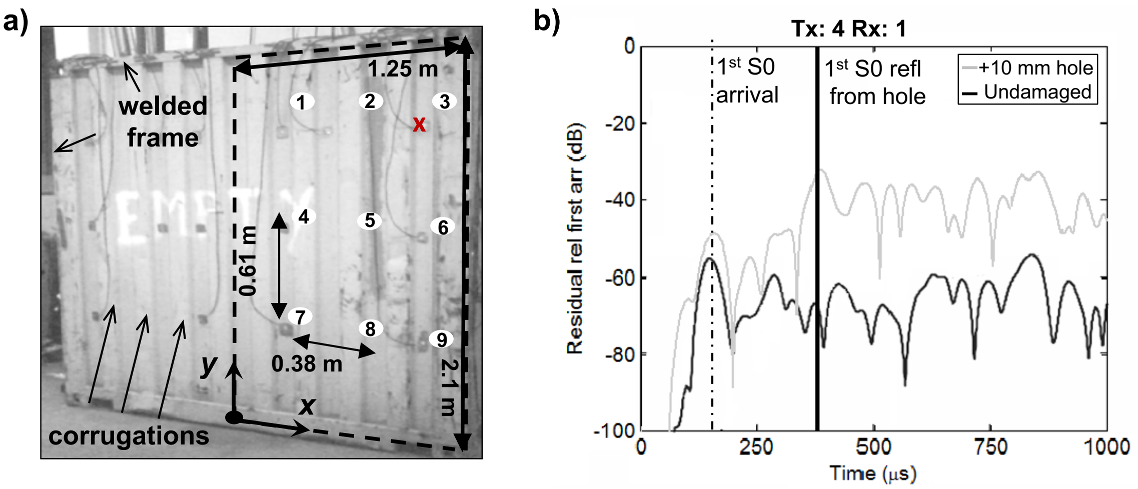

Figure 3.16: (a) Array of bonded PZTs (circles) on a 2 mm thick container panel and (b) the residuals from compensated baseline subtraction of pitch catch data monitored using transmitting and receiving sensors 4 and 1, respectively, from the undamaged structure and after a ∅ 10 mm hole is drilled at the X in (a). Photo and data adapted from [36].

Figure 3.16(b) shows sample residuals calculated by subtracting current signals from optimally stretched versions of the baselines selected using OBS in [36]. The amplitudes of residuals calculated for the undamaged structure are consistently less than -55 dB. The residual signal for the case of there being a ∅ 10 mm hole exhibits a maximum around 380 µs which is near the expected arrival time of the directly reflected S0 mode from this defect [36]. The amplitudes of the residual prior to and after 380 µs are higher in this case than for the undamaged case as well. It is not clear what could be attributed for the amplitudes of the residual being higher at times prior to the expected arrival time of the reflected pulse from the hole. The effects after the arrival of the reflection from the defect are of clearly higher amplitude and likely due to the hole presence modifying the later portions of the pitch catch signal (e.g. through reverberations of edge reflections off the defect and mode converted signals in the reflected wave field.)

The residuals for the array were combined using the ellipse algorithm and Equation 3.2 in order to calculate image maps for the right side of the panel. The map of the damage free structure is plotted in Figure 3.17(a) while that of the structure containing a ∅ 10 mm hole is shown in Figure 3.17(b). These results are plotted on the same dB scale and show that the damage free structure can clearly be discriminated from the structure containing a localized defect. The area of the image in Figure 3.17(b) that has the highest amplitudes corresponds to the location of the drilled hole. The results match closely to those obtained using the same data in [36, 109] and were assumed sufficient validation of the imaging algorithms.

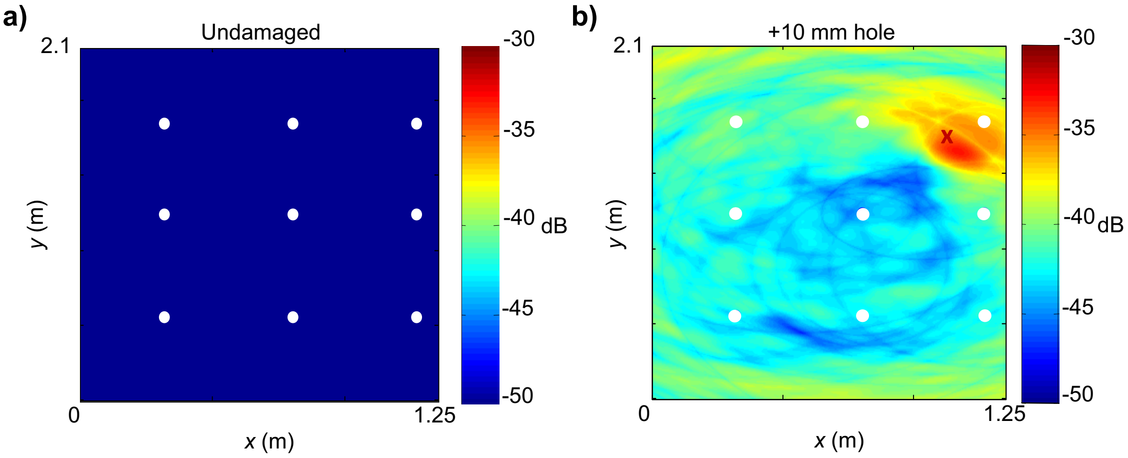

Figure 3.17: Images of the 2.1 m x 1.25 m area of the container panel marked using dashed lines in Figure 3.17 in its (a) damage-free state and (b) in the presence of a hole drilled at the marked X. Sensor locations are shown using circles and results were obtained by processing array data with the ellipse algorithm. Reproduced using data from [36].

3.5 Summary

Transducers consisting of bonded PZT discs were analyzed using FE models so that they could be used to achieve preferential excitation of low frequency S0 waves. It was found that the transducer should generally be developed for the plate thickness of relevance to enable off resonance preferential excitation of the S0 mode. In particular, 20 mm diameter discs of 0.5 mm and 1 mm thickness were found suitable for cases of the structures being 2 mm and 5 mm thick aluminum plates respectively. Further development of an encapsulation was achieved using parametric FE studies.

Experiments were used to validate the performance of operating transducers around frequencies at which the circular crested A0 wavelengths match the PZT diameter and enable suppression of this unwanted mode. Results from pitch catch tests with encapsulated versions of these transducers confirmed that the developed cap does not compromise the relative purity of the excited S0 wavepackets (over A0). It was found that S0 wavepackets could be detected in pitch catch data with amplitudes that exceeded those of the weaker A0 pulses by ≥20 dB on 2 mm and 5 mm thick aluminum plates.

The automated algorithms used to compensate data for the effects of temperature changes and compute the subtraction between monitored pitch catch signals and baselines that are used throughout this work were described. These algorithms were applied to process experimental data acquired with the developed sensors bonded on aluminum plates. Their effectiveness to compensate for temperature changes was validated using data monitored from a 5 mm thick aluminum plate that experienced thermal swings of 0.5-2°C. Further experiments were used to demonstrate the algorithms enable robust detection of a ∅ 5 mm through hole on a 2 mm thick aluminum plate.

The delay-and-sum imaging algorithm that is used to localize potential scatterers was presented. The implementation was shown to allow successful differentiation of a healthy complex container panel door and localization of a hole drilled into the structure.

Chapter 4

Initial long term weather exposure experiments

4.1 Introduction

This chapter describes a practical feasibility study in which data is analyzed from a guided wave SHM system exposed to British weather for a period of 9 months. The system consisted of the encapsulated PZT transducers described in Section 3.3. The transducers were bonded to a 5 mm thick anodized aluminum plate and used to generate and receive 8 cycled, 170 kHz tonebursts of S0 waves using the methods of Section 4.3.1. Data collected with the sensors were compensated for thermal effects using baselines collected with the specimen in an environmental chamber as discussed in Section 4.3.2. Residual signal amplitude drifts and variations in the images of the healthy plate are presented in Section 4.3.3. In Section 4.4, potential reasons for the observed increases in noise levels are studied through analyses of coherent and incoherent change in the data. Finally, Section 4.5 describes impedance readings and ultrasonic scans which were taken at the end of the monitoring period in order to assess the adhesive bonds and determine the most relevant robustness issues to the findings.

The chapter shows that the adopted adhesive and the bonding practices used to attach PZTs to a plate exposed outdoors contribute to degradation in SHM capabilities. Declines in the amplitudes of monitored guided wave signals and associated increases in noise within the portions of time traces preceding the first S0 arrival are presented as is the simulated and experimentally verified relationship between these trends and the performance of the baseline subtraction methods. Inspections show weakening of the bonds between PZTs and the plate affect the deployed sensors, and that ultrasonic scans are more sensitive than impedance readings for diagnosing bondline changes.

4.2 Background

Research has shown that the sensing and signal processing processing strategies described in Chapter 3 enable monitoring plate-like structures for small defect detection over periods <3 weeks if a careful choice of adhesive is used to bond PZTs [84]. As PZT sensors have formed the basis of various SHM systems [36, 74, 85, 110], these demonstrations and those of the survivability of transducers to electrochemical [111] as well as fatigue loading [91, 112] have been encouraging. PZT sensor exposure to high temperatures has been shown to cause some problems [91, 113] however only in temperature ranges exceeding 90°C [114]. Most of these results have been shown in simple experiments conducted within the indoor environments of laboratories. Experiments with outdoor exposure of sensors have indicated that there can be significant changes in the electromechanical impedance spectra of bonded PZTs [91]. Accelerated degradation of bonded PZTs in [92, 115] have also confirmed discrepancies in guided wave generation and reception capabilities are to be expected. Yet the effects of realistic weather exposures for a sustained period of time have not been investigated in depth.

System stability is critical to ensure baseline subtraction techniques are useful for practical damage detection over long periods of time. The compensation methods of Section 3.4.1 enable robust defect detection in plates while they undergo homogeneous thermal change of ~0.5°C [84, 85]. Appropriate mode selection [63] or feature extraction [116] may be exploited to preserve detectability in the presence of thin layers of accumulated liquid or irregular wetting respectively. These findings are encouraging though they are still based upon short term controlled experiments, and neglect factors such as the sensitivity of certain guided wave modes to humidity induced moisture uptake [82, 117], temperature gradients [118], and the possible effects of longer term environmental attack [119–121]. A longer term test was recently performed by University of Bristol researchers who monitored S0 mode propagation in an empty steel tank underneath a stairwell landing that was located outdoors [68]. There were consistent though unexplained changes of greater than 3% difference in the data, and 10% of signals acquired during a 40 day period needed to be constantly added to a baseline database that was continuously updated. The effects that prolonged exposure to realistic conditions has on the robustness of transducers in addition to the reliability of compensation and baseline subtraction methods have not been simultaneously considered, and are therefore investigated in this chapter.

4.3 Outdoor monitoring experiment

This section describes the procedures used to instrument a 5 mm thick anodized aluminum plate with an array of PZT sensors and the outcomes from outdoor monitoring of this structure for a 9 month period.

4.3.1 Specimen and monitoring location

A 5 mm thick, 1.25 m square NS4 specification aluminum plate, with an array of 5 sensors in the configuration shown in Figure 4.1(a), was used for outdoor tests. While this grade of aluminum is typically used in marine environments, phosphoric acid anodizing had been applied to prevent potential corrosion of the unpainted and exposed plate. The anodizing allowed the structure to remain defect free for the duration of environmental exposure.

The sensor array consisted of five encapsulated ∅ 20 mm, 1 mm thick PZT discs that had screen printed disc shaped silver (Ag) electrodes. Electrode surfaces were cleaned, and the surface of the plate at the locations of Figure 4.1(a) were abraded using sandpaper prior to being cleaned according to manufacturer recommendations. Thin layers of the adhesive (Loctite E-05CL, Henkel, US) that was found to be temperature stable in [84] was then applied to an electrode surface on each PZT and the surface of the plate to which it was joined. Joints were maintained in compression during the curing process using 100 g weights placed on the sensors to achieve thinner bondlines. The PZTs were then encapsulated using the caps of Section 3.3.3. The top surface electrodes of PZTs was soldered to the wire end protruding inside the caps prior to bonding and sealing caps using a water resistant epoxy (Loctite 9483, Loctite, UK.) Sensors were heated to 70°C and left to cool to room temperature before being heated again on two separate occasions to subject bonds to temperatures above those expected in operation and prevent post-curing effects as in [41]. Thermocouples (Glass fibre insulated type K, RS, UK) were also bonded to the plate at the locations indicated by squares in Figure 4.1(a) using a compound (Electrolube TBS20S, HKW, UK) formulated to provide thermal conductivity in applications involving exposure to wet environments. Temperatures were recorded using these thermocouples and a data logger (TC-08, Pico, UK.)

Guided wave propagation was recorded between the sensors using the data acquisition system (DAQ) that is schematically shown in Figure 4.1(b). This system included a high pass filter (Kemo VBF40; cutoff at 3 kHz) which was used to remove offsets in the data (from pyroelectric effects related to temperature changes) as well as a custom built multiplexer (MUX) with relays controlled automatically using MATLAB code. During typical acquisition of data using the array of sensors, 8 cycled, 170 kHz tonebursts of 5 V amplitude were produced using an arbitrary function generator (33220A, Agilent, UK) and amplifier (KH7602, Krohn-Hite, US.) The appropriate relay channel of the MUX was turned on to upload this input signal to a transducer. The relays were also turned on in succession in order to record received signals at the sensors and save them (100 time averages, f_s =10 MHz) using the oscilloscope (44Xi, Lecroy, UK.) This process was repeated for other transmitters in order to complete data acquisition.

The outdoor site at Imperial College which is shown in Figure 4.1(c) was chosen for the monitoring test. The instrumented plate was left there initially for slightly longer than 3 months in order to conduct a preliminary evaluation of whether the setup would permit defect free monitoring outdoors. Temperature fluctuations (0-12°C), wind (speeds>13 kmph), rain, hail, and snow were common during this period. The weather variability contributed to the partial corrosion of steel weights left near the setup, which correspond to the rusted masses toward the front of the plate in Figure 4.1(c). The anodized plate remained intact without observable flaws. Transducers remained functional from the beginning to the end of the time period. These observations confirmed the plate and sensors could be exploited for the monitoring trial and the setup was moved indoors for baseline signal acquisition prior to the commencement of monitoring thereafter.

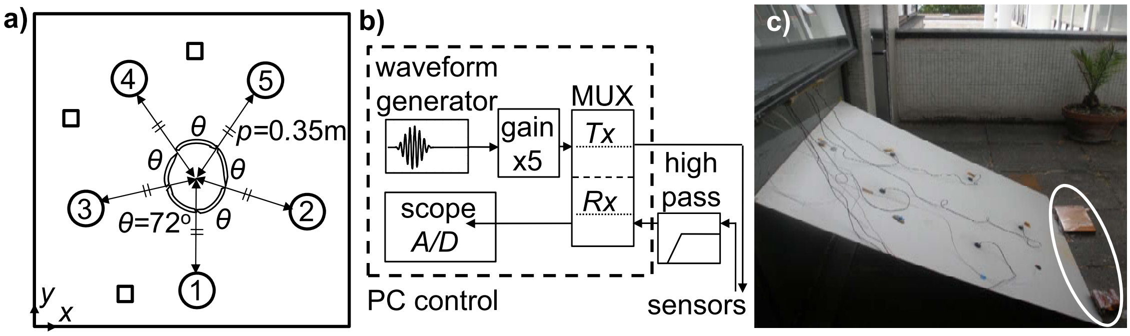

Figure 4.1: (a) Schematic of the array of sensors (numbered circles) and the thermocouples (squares) on the 5 mm thick, 1.25 m square plate, (b) diagram of the data acquisition system, and (c) photograph of the instrumented anodized aluminum plate and steel weights (circled) which corroded outdoors; arrows in (a) originate at the plate center.

4.3.2 Baselines and noise floor

A baseline database was compiled with the plate inside an environmental chamber (Alpha 1550-40H, Design Environmental, UK.) Baseline signals were acquired every 0.5°C in the range -5 to 40°C using the setup of Figure 4.1(b); temperatures were verified using the thermocouple readings and considered as encompassing the extremes of London weather. Before using the baselines, current signals were acquired at -1, 20, 30, and 40°C for the purposes of evaluating the magnitude of temperature related variability across the -5 to 40°C temperature range. All current signals were post-processed using the automated baseline subtraction algorithm described in Section 3.4.1 and a truncated version of the baseline database which consisted of all baselines except those recorded at -1, 20, 30, and 40°C (i.e. for 0.5°C gaps.) Figure 4.2(a) shows a typical baseline signal recorded at 40.5°C and the beam spread corrected difference signal which results when a time trace obtained at 40°C is subtracted from an optimally stretched version of it. Figure 4.2(b) plots the amplitudes of the residual relative to that of the first S0 arrival to more clearly show the low residual amplitude levels obtained by subtracting signals that have been compensated for thermal effects.

The ellipse algorithm of Section 3.4.2 was used to produce images of the structure using the data from the array at the various temperatures. The resultant images are all plotted on the same 15 dB scale in Figure 4.3. The maximum values of the image intensities are consistently less than -45 dB (relative to the first arrival amplitude in signals) in the result obtained at -1°C. The images produced using data acquired at temperatures >20°C have image intensities of amplitudes >-45 dB at some pixels, which are evident primarily in the form of artefacts near the edges of the plate. These differences are likely due to the glassy transition of the adhesive spanning 10-40°C, and the elastic moduli of this epoxy being more sensitive to thermal change across this temperature range [122]. Overall, the images indicated sufficiently low amplitudes in residuals (<-40 dB relative to the first arrival amplitude) so that monitoring commenced with these baselines.

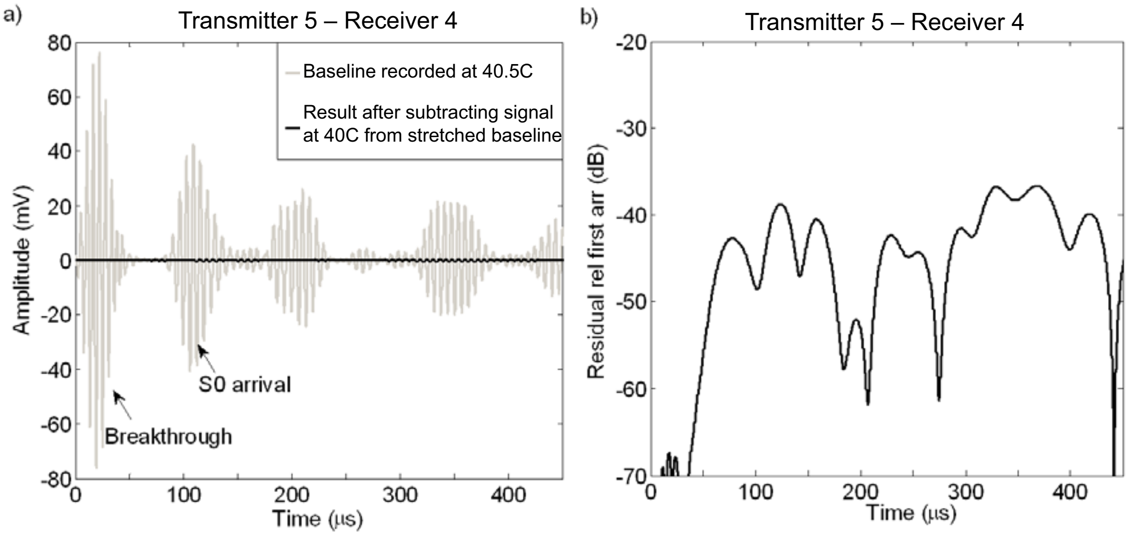

Figure 4.2: (a) Example baseline signal (grey) recorded at 40.5°C and the beam spread corrected difference signal (black) calculated by subtracting signal recorded at 40°C from optimally stretched version of the baseline, and (b) the amplitudes of the residual relative to that of the S0 arrival.

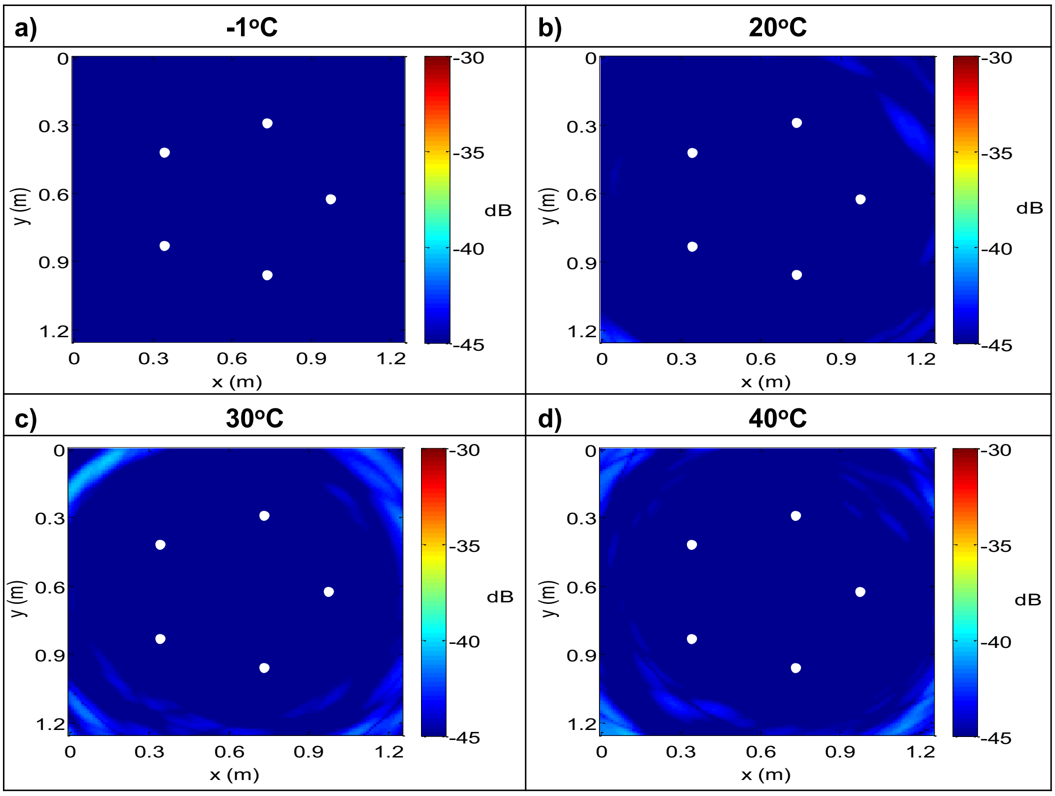

Figure 4.3: Images of the defect-free plate at various temperatures with 0.5°C gap to the nearest baseline with the sensor locations superimposed using circles. Results were obtained by processing array data acquired in the environmental chamber with the ellipse algorithm and are shown on a [-45,-30] dB scale to allow comparisons.

4.3.3 Monitoring results

Upon relocation of the plate outdoors, SHM data was acquired approximately every 6 hours for nearly 7 months after baseline collection. It was necessary to interrupt the experiment at times when issues with the filter caused it to output noise and made it necessary to reset the instrument as well as after power outages. The findings indicate it may be preferable to use a different filter or a DAQ with the waveform generator and oscilloscope in one device, and suggest it would be worthwhile incorporating an uninterrupted power supply into future setups too.

Monitored signals were compensated for temperature effects using the OBS and optimal stretch algorithms that were explained in Section 3.4.1 and used to compute residual signals. No changes were expected as no damage was introduced to the structure and it was protected from corrosion via anodizing. However, tracking maxima and mean values of residuals within the plate area suggested post-subtraction noise grew approximately linearly as a function of time for all sensor pairs. Figure 4.4 shows plots of the mean values of beam spread corrected residuals calculated using processed data from several sensor pairs as a function of monitoring time in days since the end of baseline collection (gaps in the data occur at times when the test was interrupted.) Linear regressions were applied to the data and are superimposed on the plots using gray curves. The slopes of these fits and similar fits to tracked values of residuals at the first arrival were used to determine drift rates associated with underlying trends of increasing post-subtraction noise. Slopes of these fits exhibited higher variability for lower levels of noise (values being <-30 dB relative to the first arrival amplitudes.) However, long term drift rates converged so that increases in the amplitudes of the residual noise could be expected at approximately 0.12±0.02 dB/day.

Residuals and the ellipse algorithm were used to generate images of the structure and analyze the noise trends throughout the plate. Figure 4.5 shows a typical subset of images, on [-45,-30] dB scales, that were obtained from monitored data at various times when temperatures were 15±0.5°C. As apparent in the images from the first several weeks of monitoring, low levels of noise in the central area would initially permit detection of small reflection changes (<-30 dB reflectors, for instance.) However, these capabilities are compromised by noise drifts later as the central region of the plate becomes significantly populated by artefacts (e.g. see Figure 4.5(c)-(d).)

The phenomenon illustrated by the images is summarized in Figure 4.6. The plot shows the mean $\bar{I}$ and standard deviation σ_I of pixel intensities in the area bounded by the sensors as a function of monitoring time. These results confirm that the pixel intensities also followed the linear increases of residual signal noise throughout the central region of the image, and approached ~-20 dB at 200 days. In order to evaluate whether this trend is affected by corrections being applied to the data, the monitored signals were compensated for changes in the S0 wavepacket, subtracted from optimally stretched baselines, and used to produce images. The results of this analysis are presented in Appendix C and they indicate that the corrections to the data do not change long term trends in detection sensitivity which only improves by $\sim 3-6$ dB.

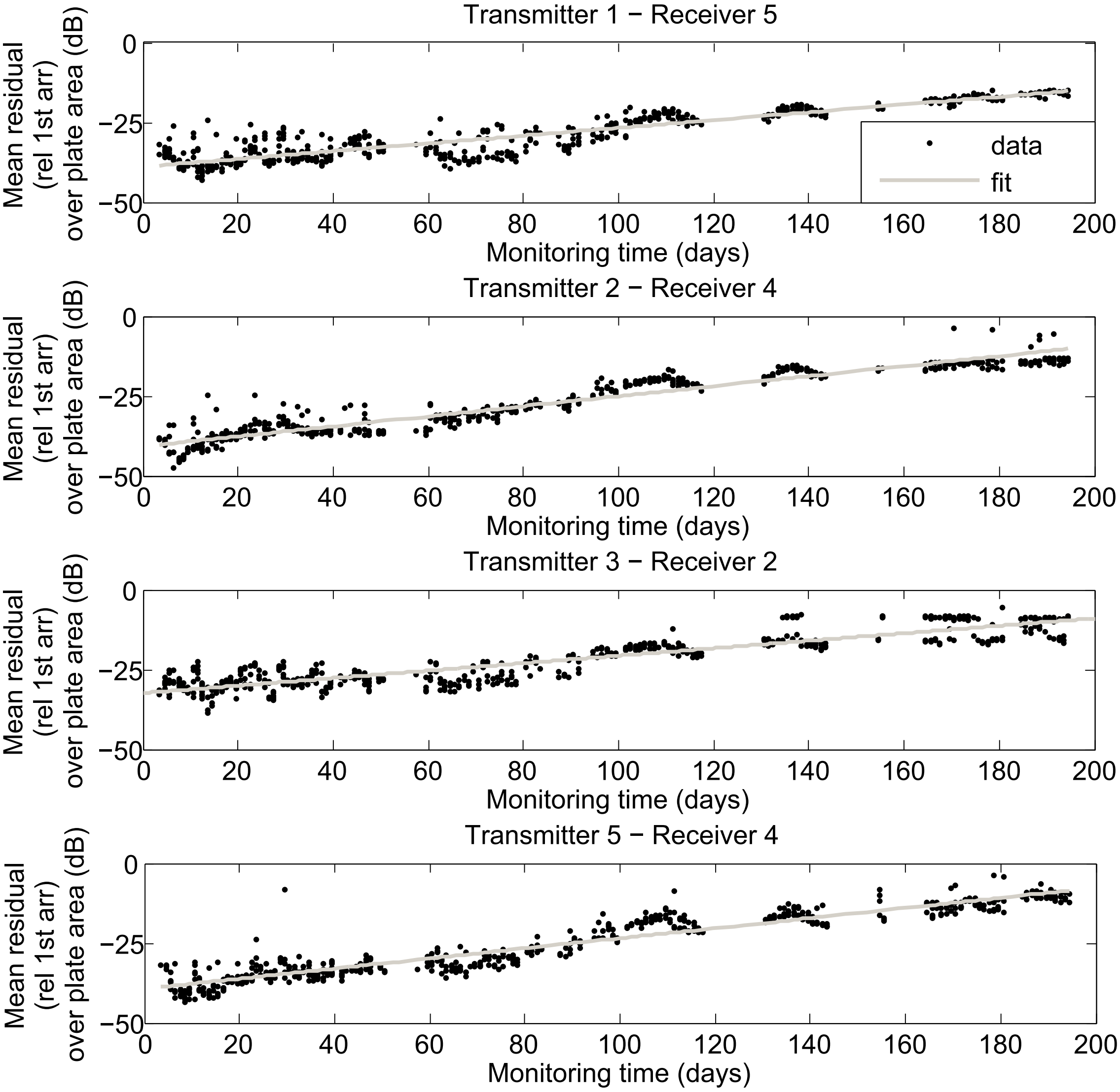

Figure 4.4: The mean values of beam spread corrected residual signals (relative to 1st arrival amplitudes) calculated after temperature compensation and subtraction between monitored signals and baselines collected in the environmental chamber. Results shown for various combinations of transmitting and receiving sensors.

A modest linear relationship between pixel intensities and temperatures was apparent when plotting them against each other. This trend, illustrated by the plot in Figure 4.7(a), was thought to arise from the correlation between higher temperatures and monitoring time (encroaching summer in the test) as opposed to underlying residual signal noise changes. To more quantitatively assess the role of either influence, errors between actual values of $\bar{I}$ and those predicted by linear fits were compared. Figure 4.7(b) shows that discrepancies with time as the fit variable (black points) are less (generally within 6 dB of actual values) than errors with temperature as the fit variable (gray squares; errors often greater than 10 dB.) This analysis suggested that ageing processes, independent of temperature variability, probably caused the observed drifts.

The spatial distribution of noise found within images was analyzed by tracking the radial distribution function, $M(r)$. This quantity was calculated by summing I at points (x,y) a distance, r, from the plate center (x =0.625 m,y =0.625 m) and normalizing by the number of contributing pixels, N, via

$$M(r) = \frac{1}{N} \sum_{\left\{(x,y) \middle| \sqrt{(x-0.625)^2+(y-0.625)^2}\right\}} I(x,y). \tag{4.1}$$

This value was computed at each data acquisition point and averaged over 3 days to yield estimates at the various weeks shown in Figure 4.8. These results indicate the spatial distribution of noise tends to exhibit similar characteristics throughout the monitoring period, with noise levels near the edges (corresponding to r =0.625 m) generally remaining slightly higher than over the remainder of the structure.

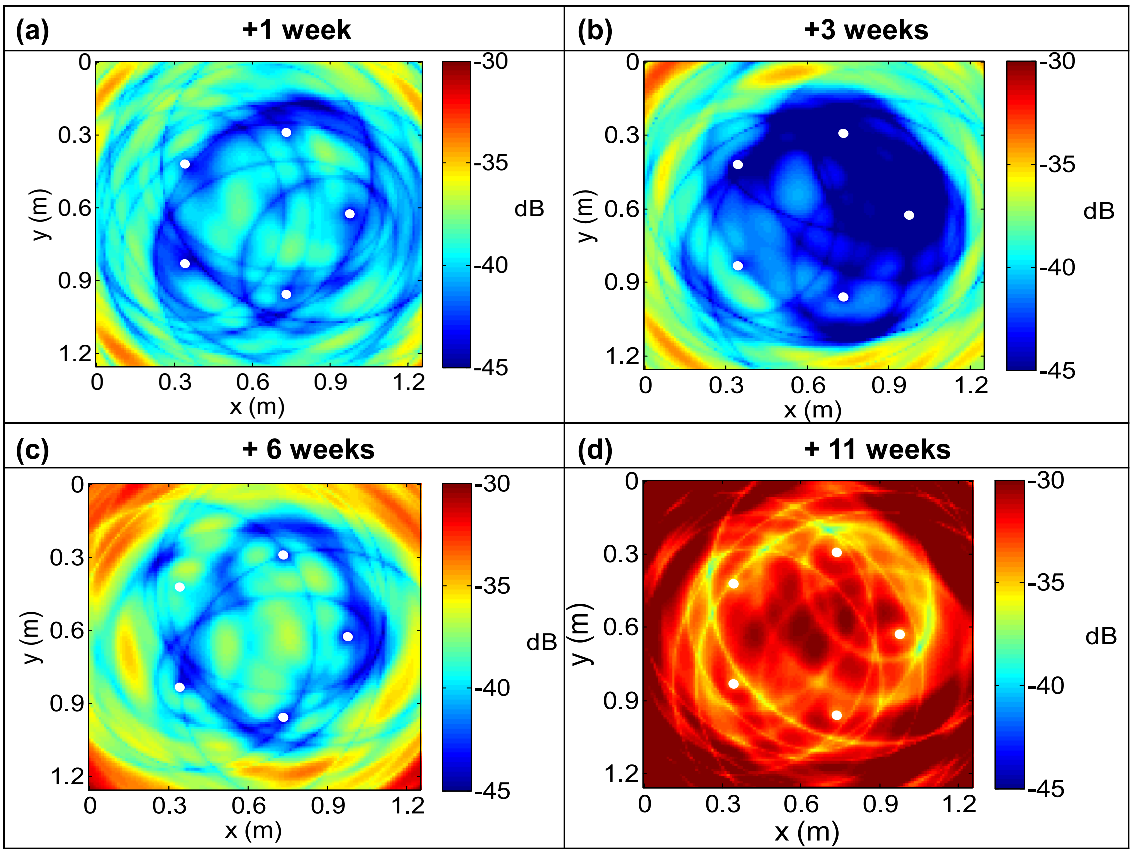

Figure 4.5: Images of the plate generated using the processed residuals for SHM data collected outdoors (a) 1, (b) 3, (c) 6, and (d) 11 weeks after baseline collection; results shown on a [-45,-30] dB scale to allow comparisons.

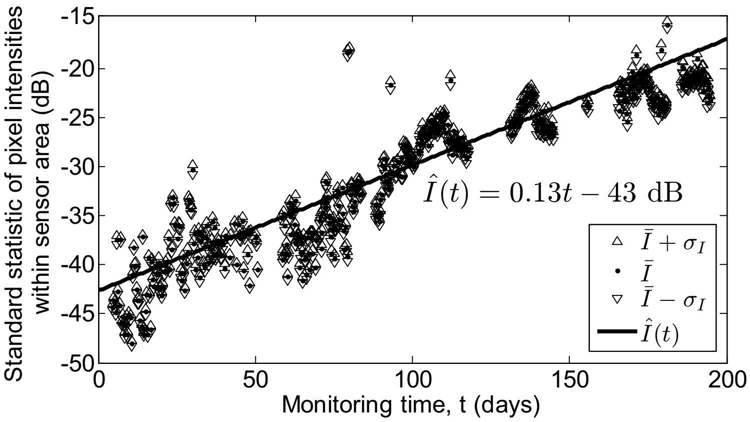

Figure 4.6: The mean values $\bar{I}$ of I within the area surrounded by sensors and the values within a standard deviation σ_I of the mean as a function of monitoring time t. The line is the linear fit $\hat{I}$ applied to the mean values.

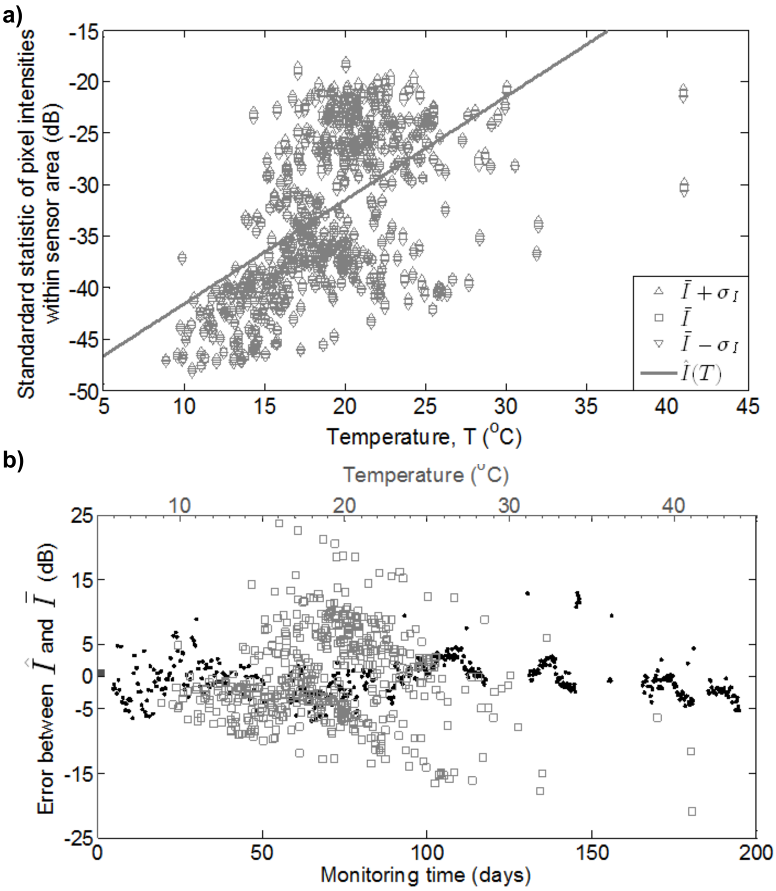

Figure 4.7: (a) The standard statistics of pixel intensities within the area bounded by the sensors versus temperature and linear fit to mean values along with (b) errors in regressions using monitoring time (black) and temperature (gray) as fit variables.

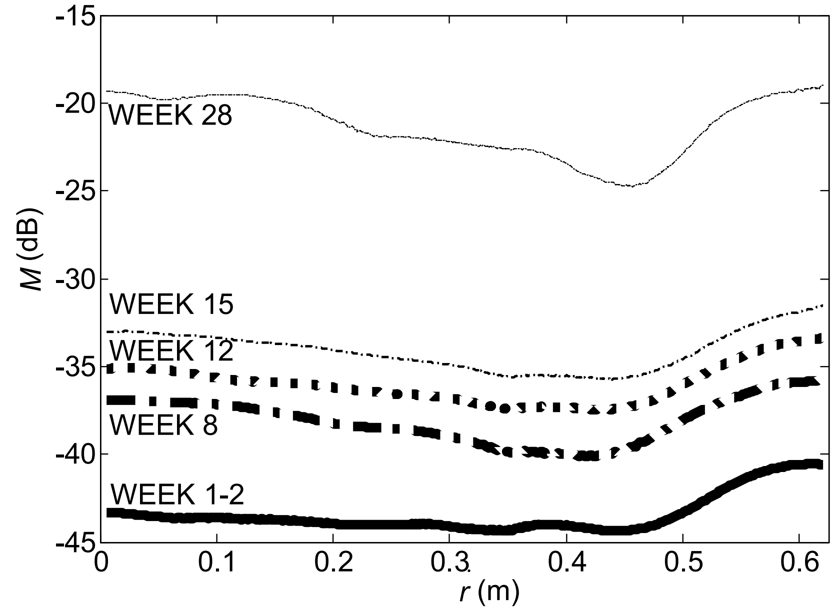

Figure 4.8: The radial distribution function, $M(r)$, for increasing monitoring times.

4.4 Variability analysis

The raw current signals were analyzed to identify changes underlying the SHM data and characterize the sources of variability which most closely related to increases in post-subtraction noise and the artefacts in the images of the defect-free structure. Various features of the directly received S0 wavefront were studied for these purposes first. This wave was considered as it corresponded to the guided wave mode for which the deployed transducers and excitation were designed. Also, the general complication of overlapping arrivals from edges made this arrival the only feature that could be analyzed in a straightforward manner for all sensor pairs. The following subsections highlight the key methods and findings of these investigations.

4.4.1 Studies of the first S0 arrival

Variability in the amplitude and arrival time of the directly transmitted S0 wavepacket was quantified. The wave of interest was identified by the local maximum in the signal envelope within the vicinity (±4 cycles) of the expected propagation time (calculated using each pair's sensor pitch and the S0 group velocity); visual inspection confirmed these searches consistently differentiated maxima in the received wave. Amplitudes exhibited significant variability from the start of monitoring and declined to 5% of initial values on average for all sensor pairs. The characteristic variability in declines are representatively illustrated through the plots on the left hand-side of Figure 4.9(a) which show first arrival amplitudes obtained from monitoring several sensor pairs (same as those in Figure 4.4); results are shown after the application of a 10 point moving average low pass filter with appropriate weighting for nonuniform acquisition times to isolate general trends from intermittent effects of outliers.

Associated changes to raw waveform signal-to-noise ratio (SNR) were quantified using the ratio of the first arrival amplitude to the mean of the values in the upper third quartile of pre-first arrival noise values; this measure was chosen as it would not be sensitive to outliers of peak noise values. While exhibiting some of the variability found for signal amplitude changes, SNR declined more gradually; representative plots on the right hand side of Figure 4.9(b) illustrate this trend.

Changes in the envelope detected arrival time of directly transmitted S0 wavepackets, which may have been introduced by the instrumentation in the progression of the outdoor test, were analyzed. Differences between arrival times in SHM data and those in corresponding optimal baselines (selected via the routines described in Chapter 3) were computed. Arrival times in signals acquired during the monitoring period deviated from values within baselines by less than 5 µs; these offsets signified maximum discrepancies of 4-7% relative to initial values. Such low discrepancies, combined with their scatter in relation to monitoring time, suggested instrumentation delays were insignificant.

The shapes of the waveforms were also assessed. Figure 4.10 shows the directly transmitted S0 wavepackets in data obtained from monitoring a couple of the sensor pairs for which results are presented above at times when temperatures were 15±0.5°C. Signals have been normalized by the maxima of the absolute values of their Hilbert envelopes to enables comparisons of shapes of signals of different amplitudes. Though the pulses don't completely overlap, likely due to discrepancies in temperatures at which signals were recorded, the wavepacket shapes appear consistently similar. The characteristics are illustrative of those revealed by inspecting data monitored using other sensor pairs too. These observations and the finding that correcting data for changes in the wavepacket did not influence the imaging results in Appendix C indicated waveform shape change was not the significant source of variability underlying degradation in SHM capabilities.

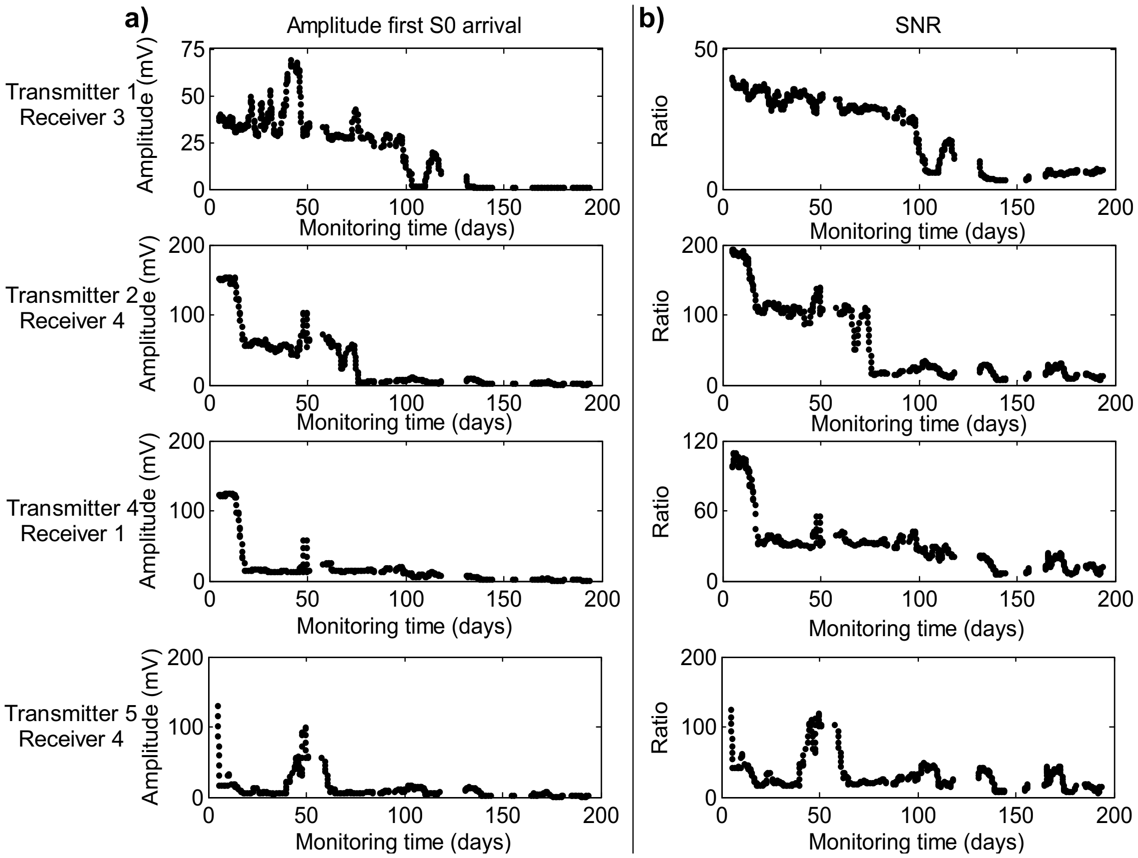

Figure 4.9: (a) The amplitude of the first S0 arrival and (b) raw waveform SNR in the progression of the outdoor test.

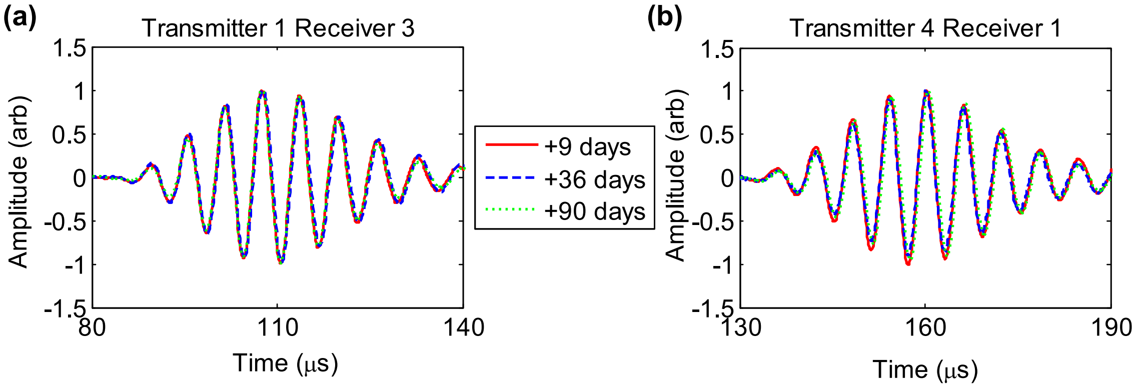

Figure 4.10: Wavepackets at the arrival time of the directly transmitted S0 mode in data monitored using sensor pairs (a) Transmitter 1 - Receiver 3 and (b) Transmitter 4 - Receiver 1 when plate temperatures were 15°±0.5°C; results normalized by the S0 arrival amplitude.

4.4.2 Unexplained noise influences

Signal amplitude declines and decreases in raw waveform SNR (see Figure 4.9) indicated increased susceptibility to unexplained noise influences over the progression of the test. The lack of association between coherent changes and the growth of post-subtraction noise suggested that these effects accounted for the majority of sensitivity losses. To more quantitatively assess the relationship between these changes and residual noise, the sensitivity of the compensation routines to raw waveform SNR was studied using simulated data at first. SNR changes observed whilst monitoring outdoors were then used to synthetically corrupt experimentally acquired SHM data to evaluate their effects on residual noise trends.

Simulated SHM data containing the first arrival and a simplified out of phase edge reflection at expected arrival times based on the S0 group velocity was generated for the array configuration of Figure 4.1(a). An example of a raw time trace for a particular sensor pair corresponds to the black curve plotted in Figure 4.11(a). Baselines were also constructed with arrival times of features offset by expected time delays δt [85] for $|\partial T|$ = 0.25°C gaps (the maximum deviation that could be expected with baselines acquired every 0.5°C.) The inset of Figure 4.11(a) shows the temperature induced delays of the first arrivals in the superimposed baselines by zooming in around the region of the first arrival. Raw waveform SNR in SHM data was varied by generating random number sequences and adding band-pass filtered versions of the scaled sequences to waveforms. Figure 4.11(b) shows the band-pass filtered random number sequence (in gray) that was added to the raw trace of Figure 4.11(a) to obtain the corrupted signal of SNR= 7 (shown in black.) Simulated signals corrupted in this manner were used to compute residuals via compensated subtraction with the baseline database synthesized as described above. Beam spread corrected residual values were computed relative to the first arrival amplitude for all sensor pairs after any relevant baseline signal stretch. The statistics associated with these signals were tracked for all pairs of the simulated array. A boxplot summarizes the range (black), quartiles (blue), as well as medians of mean residual signal values as a function of the varied SNR in Figure 4.12. The results show that the amplitudes of residual signals computed using baseline subtraction increases as the SNR value decreases. The correlation apparent in the plot of Figure 4.12 confirms the sensitivity of compensation strategies to changes in raw waveform SNR.

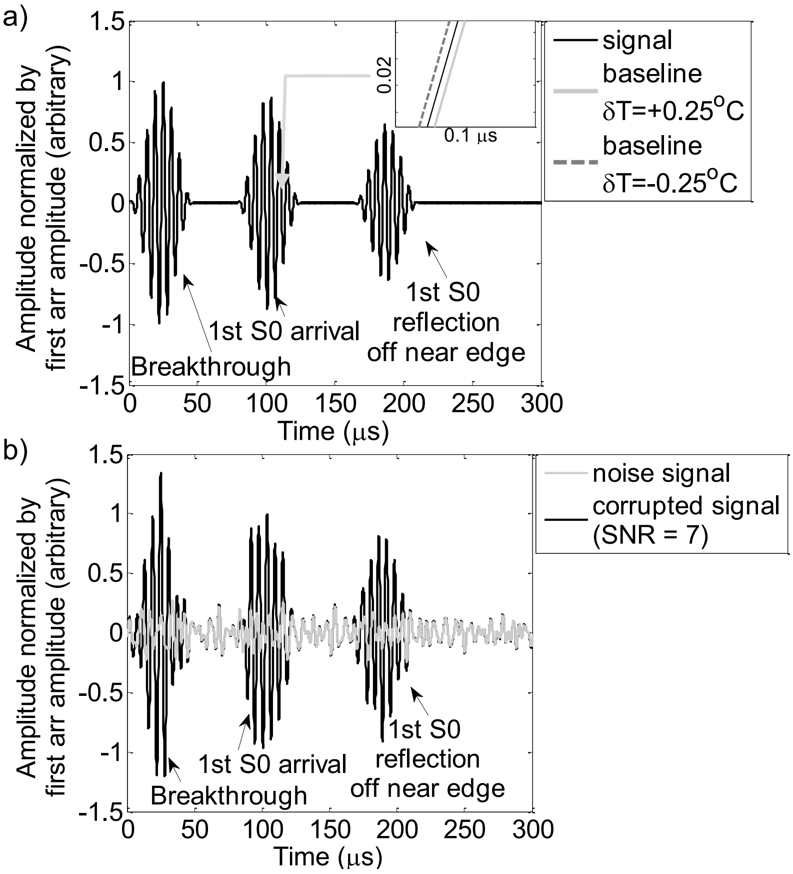

Figure 4.11: (a) Generated signal of S0 arrivals between transmitting PZT 1 and receiving PZT 2 with inset of zoomed in region showing time delays for ±0.25°C gaps in 0.1 µs window near zero crossing of 102 µs and (b) the band-limited random noise signal (gray) which is added to the signal of (a) to produce the corrupted signal having SNR=7 (black).

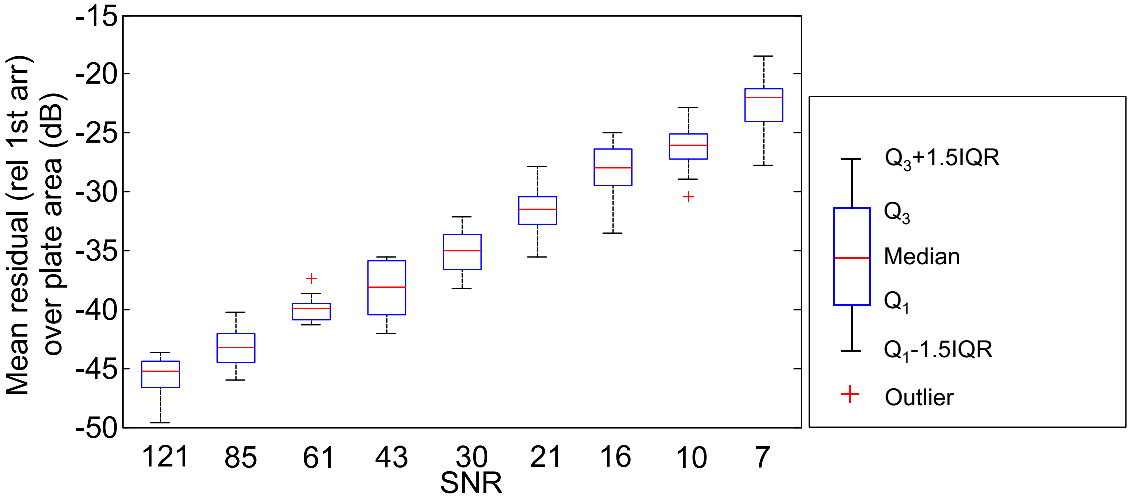

Figure 4.12: Boxplot summarizing the relationship between means of residual signals and varied SNR of simulated SHM array data; Q_1 and Q_3 are quartiles 1 and 3 respectively, and IQR stands for the inter-quartile range. Twenty realisations at each SNR value.

In order to demonstrate that changes in residual signals with weather exposure were attributable to SNR changes, band-limited random number sequences were added to SHM data collected early on (<50 days.) This was done to produce data having the SNR values measured for the relevant sensor pairs in the experiment. Corrupted signals were used to compute new residuals following temperature compensation and subtraction using the algorithms of Section 3.3.1 and the baseline database collected in the environmental chamber. Residuals corresponding to synthetically corrupted signals revealed drifts in post-subtraction noise levels similar to trends from longer term monitoring. This trend is illustrated through plots in Figure 4.13(a) which superimpose the beam-spread corrected residuals associated with original (yellow) and increasingly corrupted (darker in colorscale) data sets for the various pairs. Plots in Figure 4.13((b) show the variation in mean values of residuals with changes to the SNR; values for synthetic data are from residuals in Figure 4.13(a) and experimental values are extracted from tracked means (as in Figure 4.4) plotted against SNR. The correspondence between trends in results using synthetic and experimental data sets confirmed that the SNR declines with long term weather exposure were significant to the degradation of monitoring capabilities.

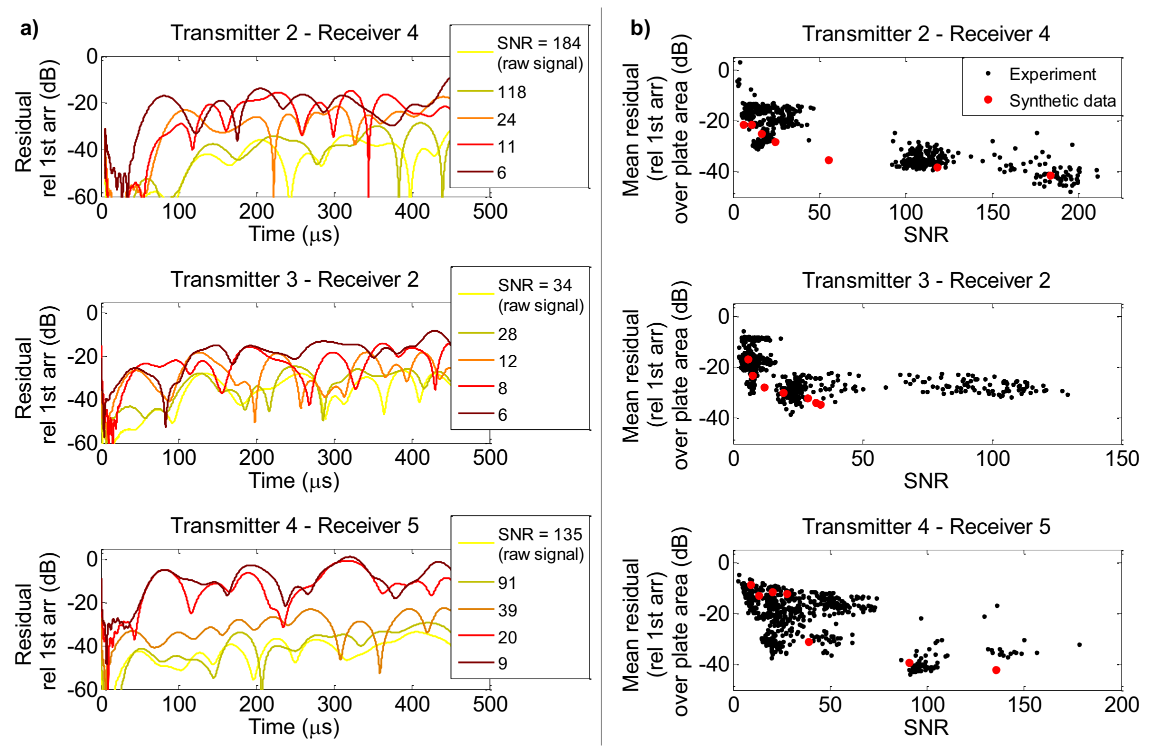

Figure 4.13: (a) Residual signals relative to the first S0 arrival amplitude for varying simulated change to SNR values (legend indicates SNR values) in signals from outdoor test and (b) comparisons in synthetically generated and experimentally observed relationships between mean residual values and SNR.

4.5 Tests to determine causes of SNR declines

The relationship between increased susceptibility to unexplained noise and post-subtraction variability growth was quantitatively demonstrated. However, the physical source underlying signal amplitude declines had to be determined through further diagnostic tests. Visual inspection revealed discoloration and plasticization among other changes in the adhesive used to seal the cap after 9 months of weather exposure. Figure 4.14 shows photographs of a newly bonded and sealed transducer alongside those of sensors from outdoor monitoring for illustration. Observations such as the ones annotated in these photographs suggested that the sealant properties changed, and likely compromised its capability to effectively waterproof and protect the more critical bond between the transducers and the plate. As structural adhesive joint durability is very sensitive to environmental attack [119–121], it was speculated that prolonged exposures may have weakened the PZT-plate interface and caused the amplitude declines (and SNR drops) reported in Section 4.4.1. It was decided to focus tests on the adhesive bond between the PZTs and the plate using techniques including impedance measurements, normal incidence ultrasonic c-scanning, as well as visual inspection of exposed layers. This section discusses the methods, findings, and implications of these tests.

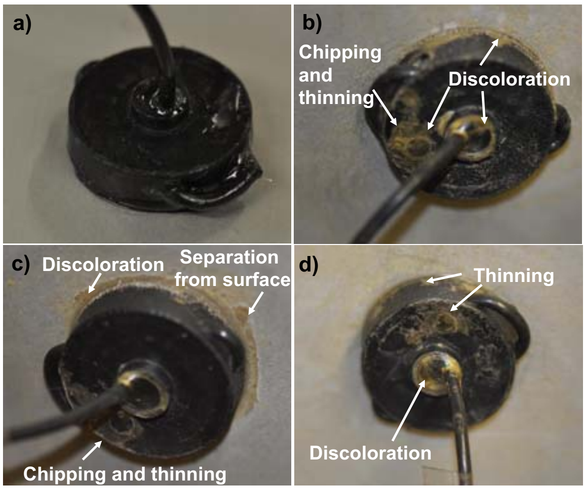

Figure 4.14: Photograph of (a) newly bonded and sealed transducer as well as (b)-(d) various sensors from the sparse array of the 5 mm thick anodized aluminum plate that had been outdoors for 6 months since commencing monitoring (>9 months from initial environmental exposure); annotations pertain to adhesive used as sealant.

4.5.1 Electrical impedance measurements

The electrical impedance responses of transducers were used to evaluate adhesive bond integrity. This technique was used as measurements have been shown [91] to readily allow differentiation of disbonds. The effectiveness of this method arises from the fact that a substantially degraded adhesive layer gives rise to the appearance of free-vibration resonance characteristics of PZT elements. The joint for well bonded sensors, on the other hand, simply shows a capacitive decay with increased frequency due to the strongly constraining boundary condition imposed by the adhesive bond. Therefore, coupling of any mechanical resonance characteristics of PZT discs into the electrical impedance can be exploited to differentiate any disbonded sensors. As transducers for the 5 mm thick plate exhibited radial resonances around 100-140 kHz, impedance spectra Z were recorded in the 50-250 kHz range using an impedance analyzer (4294A, Agilent, UK) connected to a PC through a GPIB interface.

Reference impedance readings were taken for free PZT discs and newly bonded transducers on 5 mm thick aluminum plates initially; all discs reported here were of the same nominal dimensions and material. The impedance magnitudes, $|Z|$, for these cases are plotted on a log scale as a function of frequency in Figure 4.15(a) and (b) respectively. The coupling of the fundamental radial resonance of the PZT disc and the capacitive characteristic of the transducer are evident in Figure 4.15(b) for the completely free PZT. Capacitive decay remains the sole feature in the plot of $|Z|$ for the well bonded sensor in Figure 4.15(a). Comparing measurements from the sensors exposed outdoors with these readings, suggested that two of the five sensors had at least partially debonded at the end of the monitoring period. The cases where disbond indications were apparent are highlighted through the plots of $|Z|$ in Figure 4.15(c) and (d); note the indicative peaks over the 100-140 kHz range, corresponding to the region of the expected transducer resonance. The smaller amplitude, single sided nature, and broader bandwidth of the excursions in the magnitude of the impedances plotted in Figure 4.15(c) and (d) (compared to that of the peak in the impedance of the free PZT) reflects the remaining coupling between the transducer and the underlying structure through the degraded bond. Measurements for the other sensors of the sparse array tested outdoors exhibited capacitive decay as for the case of the transducer which is shown in Figure 4.15(e).

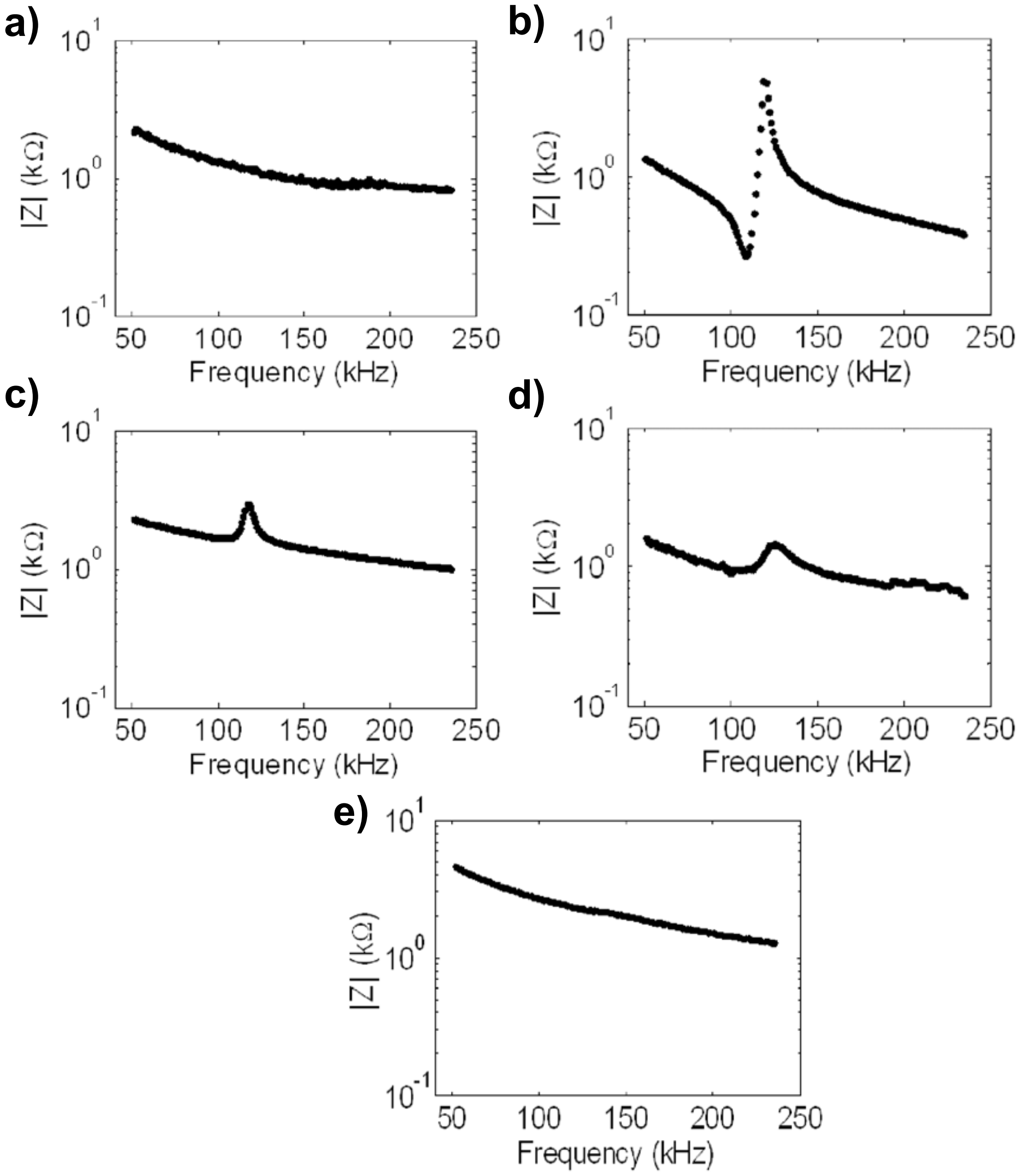

Figure 4.15: Magnitude of the electrical impedance versus frequency for (a) newly bonded transducer, (b) free PZT disc, (c)-(d) bonded transducers from the outdoors test for which debond indicators were apparent, and (e) bonded transducer from outdoor test for which there was capacitive decay.

4.5.2 Normal incidence ultrasonic scans

Ultrasonic scans of the transducers were considered for testing of the adhesive bond. This method has demonstrated effectiveness for NDE of adhesive joints [120, 121, 123, 124]. Despite the higher sensitivity that could be achieved at oblique incidence, scans with the normal incidence pulse/echo technique were used due to the relative simplicity in experimental procedures [120]. The schematic of Figure 4.16(a) illustrates a cross section of the uncapped transducer bond; the adhesive thickness indicated on this diagram equals the average value measured (ranges were 70-140 µm) using calipers upon destruction of various new bonds. Water-coupled ultrasonic energy sent to the structure from the side shown in Figure 4.16(a) would partly reflect from and transmit across the various boundaries. Intact versions of bonds would result in high transmission of energy through the adhesive layer, resulting in high levels of reflection from the interfaces and the transducer backwall. On the other hand, degraded adhesive layers would concentrate more energy in the reverberations of the plate [121] and result in lower energy signals reflected from the interfaces and the transducer backwall below the plate.

In order for this technique to work with simple time domain analysis of signals monitoring ultrasonic energy, adequate separation of reflections is necessary; limitations in capabilities to resolve echoes can hamper this as has been documented, for instance, in [123]. Therefore, the pulse/echo response of an immersed high frequency Imasonic probe (15 MHz, 56% bandwidth) situated above the multilayer transducer assembly which is shown in Figure 4.16(a) was simulated in order to determine reflections that could be readily differentiated. Bulk compression wave velocities and densities were based on the literature except for the piezoelectric layer where details were taken from the manufacturer; the detailed set of material properties can be consulted in Table A.3 of Appendix A. The freely available SPECTRUM software [125, 126] was used to obtain the frequency dependent reflection coefficients associated with the multilayer structure. Convolving the transducer response with the reflection coefficient spectrum and application of an inverse FFT allowed calculation of the time domain waveform (A-scan) that could be expected to be received by the probe. The resulting A-scan with key features identified is plotted in Figure 4.16(b). As evident from this plot, the adhesive layer interface echoes are not separated and these cannot be analyzed. On the other hand, the first echo from the aluminum plate-adhesive interface and associated layer reverberation (I_1) is well apart from the first (PZT BW1) and subsequent (PZT BW2) reflections from the bottom of the PZT layer.

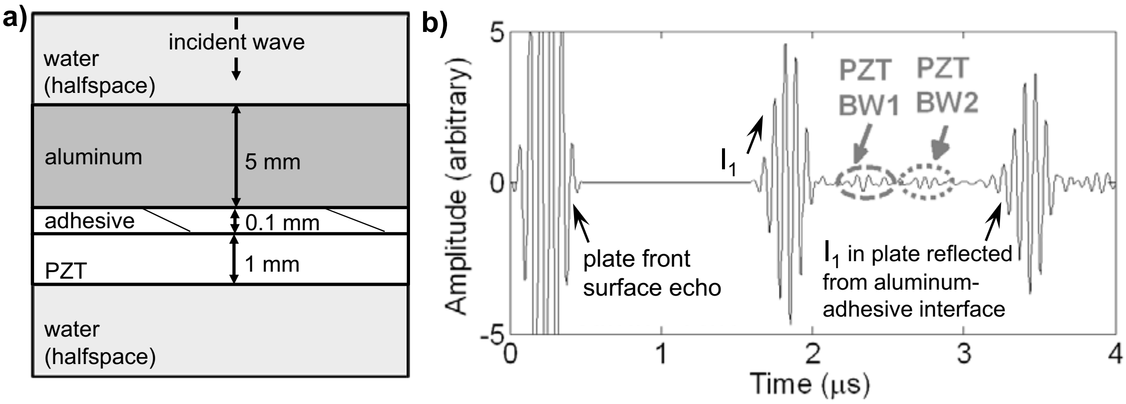

Figure 4.16: (a) Multilayer structure of the transducer bond and (b) simulated pulse/echo response of an ultrasonic probe at normal incidence produced using outputs from SPECTRUM [125]. Plot in (b) has time 0 set to the beginning of the plate surface echo, which has been clipped in order to facilitate visualization of the direct reflection from the plate-adhesive interface I_1 and the reverberations of interest (described in text.)

The reflections identified in the preceding discussion could be used to track the ratio of energy, e.g.

$$E(x,y) = \frac{\int |PZT\mathrm{BW1}(t)|^2}{\int |I_1(t)|^2}, \tag{4.2}$$

at points (x,y) where A-scans were taken to assess the bonded region. Points of better bonding correspond to higher values of E, as more energy transmits through the adhesive and reflects from the PZT backwall(s). Degradation however concentrates more energy in the reverberations of the plate leading to lower E.

The experimental setup used to acquire the c-scans for bond assessment is shown in Figure 4.17(a). To facilitate collection of data over the area of the transducer bond, the flat faced 15 MHz probe having 6 mm active diameter (IM serial number 8849 A101, Imasonic, FR) was secured in a mount on a programmable scanning frame; only the arm of the scanning frame, which was a custom built three axis stepper motor controlled apparatus, is shown for clarity. The scanning frame, probe, and test specimen surface were aligned with respect to each other in the $x-$ and $y-$axes using alignment knobs on the probe holder, the screw adjustable legs on the supports holding the water tank and specimens, and a spirit level; this was done to ensure waves were transmitted and received at normal incidence throughout scans. Figure 4.17(b)-(c) illustrate the scan configuration and the area of immersed sections of the plate containing the uncapped transducers respectively. For a typical scan, the Winspect software was used to program the motor controller (SMD03, USL, UK) and indexer (AT6400, Parker, US) in order to automatically move the arm with the probe holder in increments of 1 mm over the rectangular scan area parallel to the region of the plate encompassing the transducer bond. With each successive move in probe position, the pulser/receiver unit (UT340, UTEX, CA) was used to send amplified pulses and receive A-scans which were digitized and saved on the PC.

A-scans with the probe directly above new transducer bonds were used to confirm that the reflections from the plate backwall and transducer backwall were well separated; a typical A-scan zoomed around the vicinity of the first plate backwall, with the first several reflections from the transducer backwall, is shown in Figure 4.18. After ensuring this, scans over the area of these transducer bonds and those exposed outdoors were acquired using the procedures detailed above. The energy ratios, E, were computed over the same time gate lengths of A-scan waveforms shown in Figure 4.18 for each point in the grid of the scan using Equation 4.2 to generate images. Reference images produced for newly bonded transducers were used to calibrate the scale on which to assess E over the scanned area; images generated for the sensors exposed outdoors were considered on a grayscale for which the uniform bond of the newly bonded transducers was apparent in white. Representative images of E using the first PZT and plate backwall reflections are shown on this scale in Figure 4.19 for a new transducer bond as well as for various bonds that had been outdoors in the long term monitoring experiment; similar results were obtained when considering the ratio with the second PZT backwall as well. Regions of relatively lower energy transmission through the adhesive were discernible in images for sensors which had been subject to environmental exposure. For illustration, compare the uniform bright area in the center of the image for the case of the newly bonded transducer to the relatively darker regions in the circular areas corresponding to the transducer bond location in Figure 4.19(b) and (c). Scan results were more sensitive to subtler changes in bond state than impedance measurements, registering both large and smaller areas of poor bonding. This was true even for the cases where the latter technique had not indicated disbond; e.g for PZT 1 in Figure 4.19(c). Based on findings from this test, and readings taken with the impedance analyzer, it was determined that bond quality deteriorated nonuniformly over the progression of the outdoor test for various pairs. Environmental attack was thought to be the reason behind degradation of adhesive layers though the exact mechanism could not be determined conclusively.

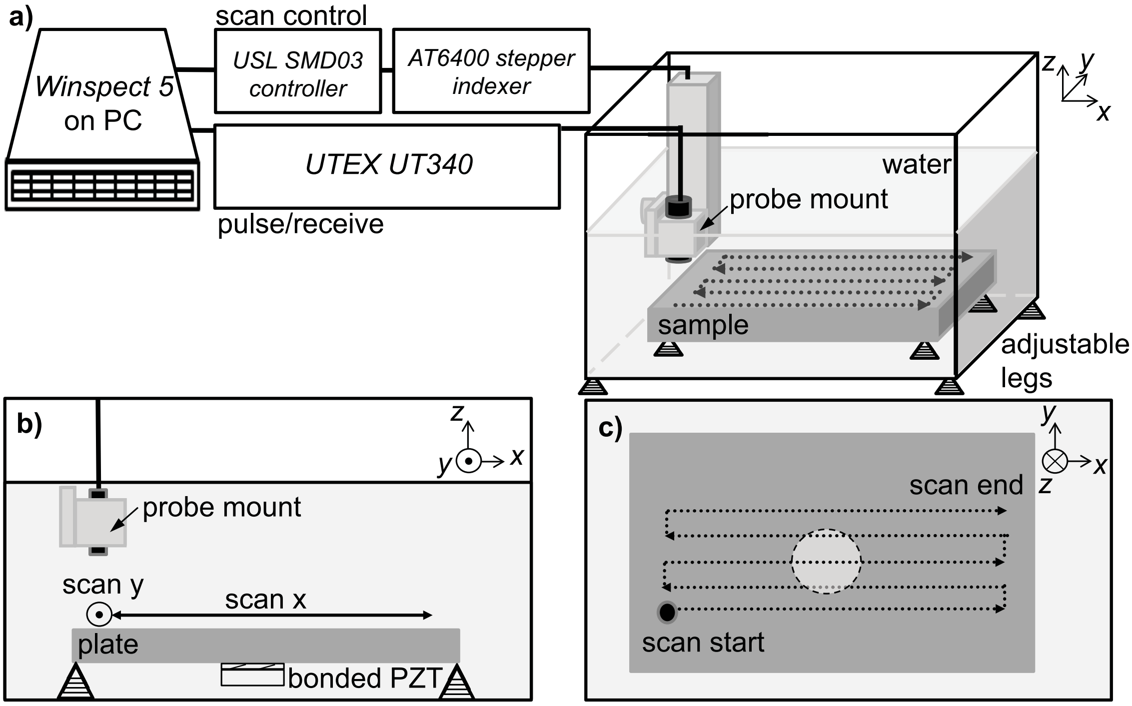

Figure 4.17: (a) The setup of the ultrasonic probe (cylinder) in the mount with alignment knobs (light gray), leveling legs (triangles), and programmed probe movement (dotted lines) used to acquire c-scans at normal incidence and the (b) side and (c) top down views showing samples and scanned areas; the circle in (c) signifies the bonded transducer location.

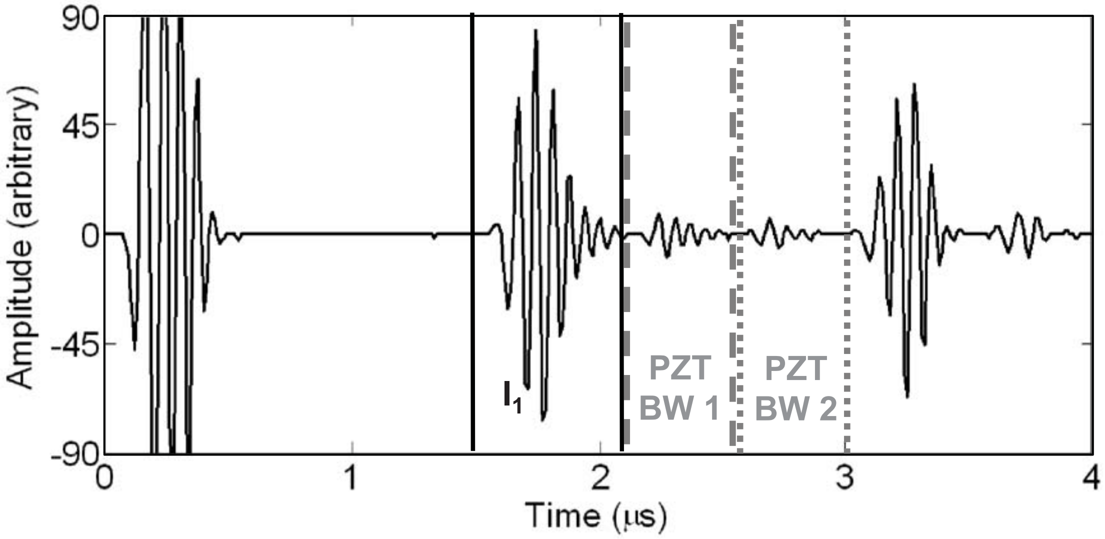

Figure 4.18: Typical ultrasonic A-scan waveform acquired at normal incidence.

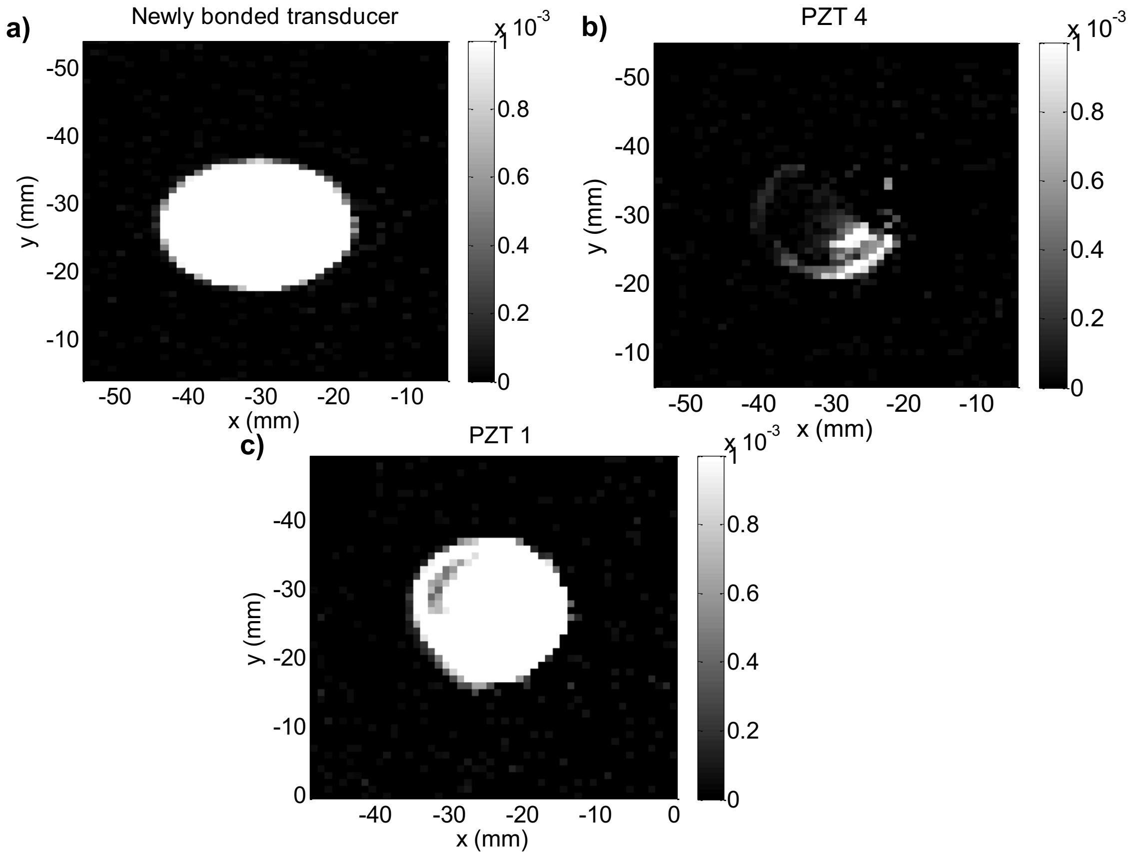

Figure 4.19: Images of the energy ratio $E(x,y)$ generated for (a) a new transducer bond and for (b)-(c) two sensors which had been environmentally exposed in the long term monitoring experiment; the first reflection from the PZT and plate backwall reflections used to produce these images.

4.5.3 Visual inspection of adhesive layers

Adhesive layers of transducer bonds were visually inspected after separating sensors from the plate. A wedge was applied at positions around the circumference of the PZT discs close to where poor bonding was suggested by images from scans. The wedge was repetitively tapped into the interface region at these points to impart minimal additional change to the adhesive layer. While subjectively determined, PZT discs were more easily detachable from the plate than when newly bonded discs had been separated to determine bond line thicknesses. These observations correlated with the findings above- that weakening of the bond was prominent at the end of the monitoring period. Some irregularities were apparent in some of the exposed layers. For instance, note the areas of discoloration, trapped water, and the globular defect in the photo of Figure 4.20(a). These indications combined with discoloration, often near the edges of the bond, suggested water ingress and chemical degradation may have influenced the adhesive bond. Inspection of the exposed adhesive layer from sample transducers of the 5 mm thick anodized structure and those that had been exposed outdoors on another (2 mm thick anodized aluminum) plate showed that the adhesive consistently remained attached to the plate. This suggested an interfacial bond failure at the transducer-adhesive interface; note, for instance, that only a small region of the film is detached from the plate in the photograph of the adhesive layer in Figure 4.20(b). This failure mode was found to be consistent with expected and observed [120, 121, 124] results in the literature. The suggestion that moisture [119, 120] weakened the bond, and ultimately caused swelling and delamination growth at the PZT-adhesive interface were judged likely [127, 128]. After all, the latter interface involved bonding to transducer electrodes (Ag composition), and the structural adhesives being used were not designed to bond to such surfaces.

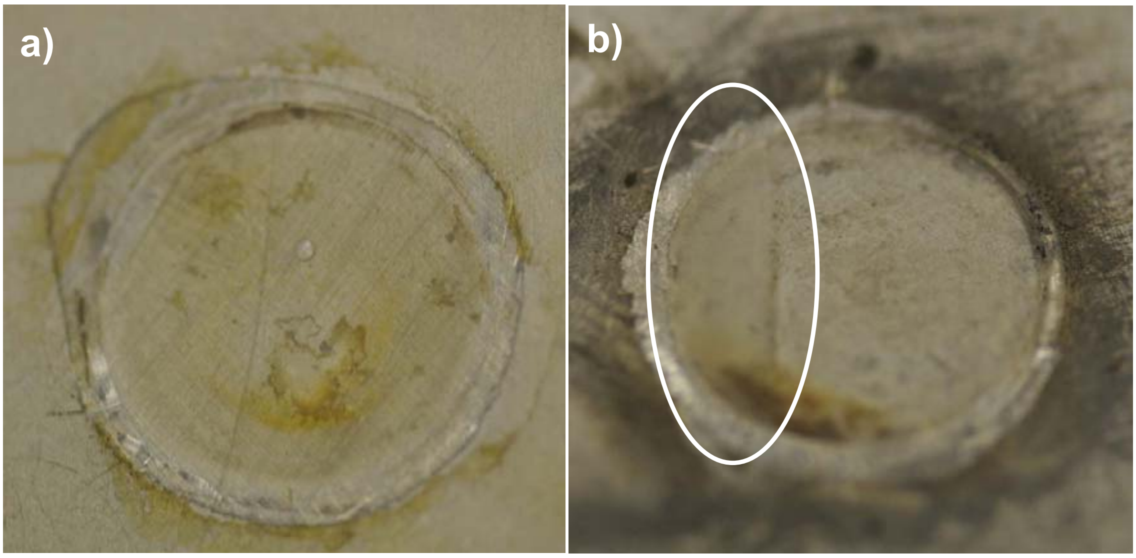

Figure 4.20: Photograph of the adhesive layers for two transducer bonds that had been exposed to outdoor environments with circle in (b) indicating separation from plate.

4.6 Summary

A long term (>9 months) outdoor test of a guided wave SHM system on an anodized aluminum plate structure was undertaken. Residuals were computed between signals from monitoring the sparse sensor array and a baseline database collected in an environmental chamber. Changes in monitoring capabilities were described. Drifts in residual noise levels were observed and quantified for all sensor pairs. Corresponding degradation in imaging capabilities was apparent. The trends were analyzed and found to be independent of recorded temperature changes, and have spatial distributions that did not vary in shape over time.

Studies of the S0 arrival confirmed that signal amplitude declines (along with corresponding SNR declines) were the primary characteristic trend apparent in SHM data. The influence of changes in SNR on post subtraction noise was quantitatively demonstrated using simulations and synthetically corrupted SHM data. The results confirmed that sensitivity of compensation strategies to random noise (with signal amplitude declines) accounted for observed trends in degradation of monitoring capabilities. This result also confirmed that consistently high SNR is required to successfully utilize guided wave SHM with the current signal processing strategies.

Diagnostic evaluations of transducer bonds were undertaken using impedance measurements, ultrasonic scanning, and visual inspection of adhesive layers. These tests confirmed that total disbonds and partial weakening of bonds at sites of the sensor electrode-adhesive interface were common for sensors that had experienced exposure outdoors. It is speculated that nonuniform bond degradation therefore contributed to signal amplitude declines. These findings suggest that a more suitable adhesive bond for electrode material should be identified.

Chapter 5

Long term stability with temperature cycling

5.1 Introduction

The tests of Chapter 4 indicated that residual signal noise levels increase and debonding of the adhesive used to attach sensors to the plates is a relevant issue. In order to continue assessments with systematic studies of the long term stability in defect detection achievable on damage-free plates, sensors were used to monitor thermally cycled aluminum plates.

This chapter presents the assessments of baseline subtraction stability as a function of thermal cycling. Section 5.2.1 describes the setup and the procedures used to collect SHM data. Analysis of residual signals and variability within guided wave data collected with this SHM system are presented in Section 5.2.2-Section 5.2.3 respectively. The results indicated that changes in the properties of the bonds between the sensors and the structures were responsible for measured drifts and increasing coherent variability within the data. This was studied in Section 5.3 by simulating the effects that adhesive property variations have on compensated subtraction results. Independent measurements of adhesive properties as a function of thermal cycling are discussed alongside the relevance of the results to monitoring trends in Section 5.4.

The major novelty of this study is it establishes that the size of defects that can be reliably detected using baseline subtraction of propagation signals sensed at bonded PZTs progressively increases due to effects that thermal cycling exposures have on transduction. The chapter contributes an investigation into the changes in capabilities of monitoring plates with PZTs that are bonded to structures using four adhesive systems. A technique allowing accurate simulation of the effects of thermal variations on SHM data is used to show the sensitivity of the performance of the adopted baseline subtraction methods to changes in the properties of the adhesive layers of bonded PZTs. This analysis and measurements on bulk samples of adhesives leads to an identification of changes in the dynamic moduli of adhesives as a source of variability affecting the SHM system.

5.2 SHM experiments

5.2.1 Experimental setup and monitoring timeline

Thickness-polarized 20 mm diameter, 0.5 mm thick PZT discs were used that had been manufactured by Noliac to each have a circular wrap around ground electrode as well as an electrically separated crescent shaped signal electrode. Connections to only one side of these PZTs were required. The PZT discs were bonded on 2 mm thick square aluminum plates having sides greater than 1 m long at separations of p =0.42 m, as shown in Figure 5.1(a). The sensors were operated in pitch catch mode with this positioning allowing temporal separation of the S0 arrival from the weaker A0 arrival and near edge reflections.

The two part epoxies of Table 5.1 were used for bonding sensors. Loctite E-05CL was chosen based on recommendations in [41], 3M DP105 and Araldite 2011 were selected among a list compiled from consultations with manufacturers about adhesives that had similar mechanical properties but better humidity and solvent resistance than Loctite E-05CL, and Araldite 2014 was chosen because of experience in the lab using it and for its greater environmental resistance. The choice of these adhesives allowed studies of the long term behavior with different bonding systems (note the different glass transition temperatures and consistencies of the various adhesives.)

The sensor electrode surfaces as well as those of the plate were cleaned according to procedures recommended by each manufacturer. Thin adhesive layers were then applied uniformly to both joint surfaces. Joints were maintained in compression during the curing process by placing 100 g weights on the sensors to achieve thinner bondlines. This was done in order to achieve thinner adhesive layers which allow better suppression of undesired waves of the A0 mode as shown in [91]. Bonds were left to cure at room temperature for at least as long as specified by each supplier. RF shielded cable ends were soldered to the sensor electrodes as shown in the zoom inset of Figure 5.1(a). Plates were then moved to the environmental chamber (Alpha 1550-40H, Design Environmental, UK.) Sensors were postcured using 3 cycles of heating from room temperature to 70°C; the temperature was kept at 70°C for one hour in between each cycle to increase crosslinking [129] and relax residual stresses as advised [41].

Sensors were connected to a custom built multiplexer (MUX) on the DAQ system that is schematically shown in Figure 5.1(b). This allowed efficient collection of SHM data from all sensors while cycling specimens according to the thermal profile of Figure 5.1(c). Baselines of pitch catch propagation patterns between sensors were obtained throughout the -5°C to +40°C range at steps of 0.5°C. Thermocouple (Type K, RS, UK) readings from points on the plates and within the chamber that were recorded with a data logger (TC-08, Pico, UK) confirmed temperatures had stabilized at each measurement point. Data acquisition was then started by sending the 5 cycled, 100 kHz toneburst inputs as recommended in Section 3.3 to the transmitting PZTs via the function generator of the Handyscope (HS3, Tie Pie Engineering Ltd., NL.) Connections to the receiving transducers were turned on sequentially using the MUX. The voltage signals resulting across the electrodes of the sensors were digitized (100 time averages, f_s =20 MHz) using the A/D converter of the HS3.

Specimens were subsequently cycled in the range from 15-35°C prior to acquisition of a second baseline set (after more than 60 cycles of exposure) and continuation of cycling; plates were kept damage free for the duration of this period. The current signals were recorded at 15, 25, and 35°C, as indicated in Figure 5.1(c), using a similar procedure as for the baselines. The experiment was continued for test periods exceeding 150 days (>220 thermal cycles of exposure.) In order to determine whether small defect growth could be reliably detected throughout the experiment, data was processed using the temperature compensation and baseline subtraction algorithms of Section 3.4.1 to compute residual signals.

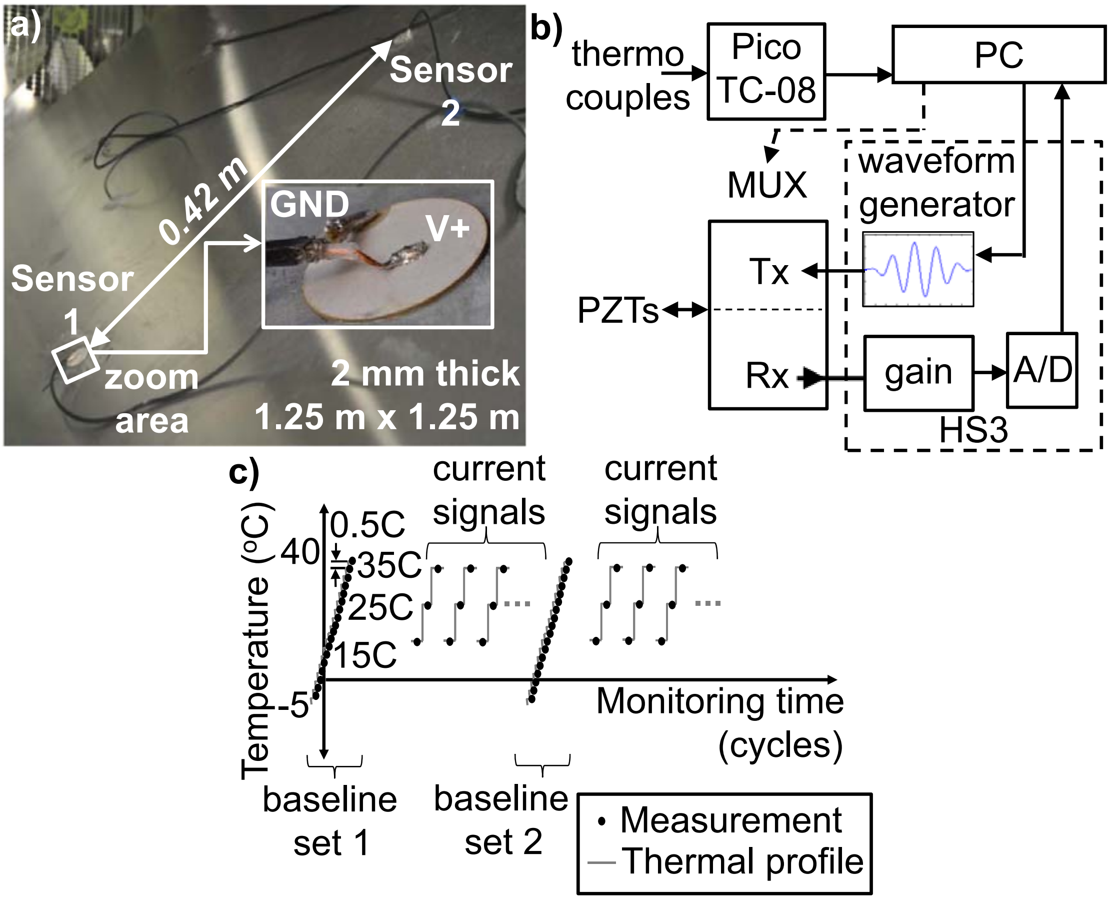

Figure 5.1: (a) A 2 mm thick, 1.25 m square aluminum plate in the environmental chamber having PZT disc sensors bonded with separation of p =0.42 m, (b) DAQ for acquisition of pitch catch signals from multiple pairs of PZT sensors, and (c) timeline for thermal profiling and SHM of plates in chamber experiments.

Table 5.1: Manufacturer supplied information for adhesives used to bond sensors.

Name	Consistency	Glass transition (°C)	α (10^6°C^{-1})	Source
E-05CL	Medium viscosity	10	38	Loctite [122]
DP105	Low viscosity	15	N/A	3M [130]
Araldite 2011	Paste	45	85	Araldite [131]
Araldite 2014	Thixotropic paste	85	21	Araldite [131]

5.2.2 Baseline subtraction stability

The purpose of the study was to analyze the long term stability of the bonded guided wave sensors and the baseline subtraction damage detection approach. Current signals collected after baseline acquisition periods of Figure 5.1(c) were processed with the temperature compensation methods of Section 3.4.1 before calculating residuals. The dB values of beam spread corrected residuals were then computed. The plots in Figure 5.2 superimpose representative residual signals at 25°C from data obtained with pairs of sensors bonded using DP105 and Araldite 2011 epoxies; $t_{\text{1st arr}}$ and $t_{\text{coverage limit}}$ are the group velocity based arrival time of the directly transmitted S0 wavepacket and the time for the reflection from the point involving the longest transmitter-edge-receiver path. The results in Figure 5.2(a) were obtained using baselines acquired at the beginning of the monitoring period. The plots of Figure 5.2(b) were produced using the second baseline database acquired after >60 cycles of exposure. Subsets of residuals are presented for the purposes of clarity though the same features were evident in all data collected with these and other adhesives.

The most significant features in the data are an increase in the amplitudes of residual signals from their initial level. For instance, note the maxima of plotted residuals are <-40 dB over the whole monitored time for low thermal cycle numbers. However, residual amplitudes drift to anywhere between -30 to nearly -20 dB after >150 cycles. These changes correspond to increases in the smallest damage size that can be reliably detected. Processing current signals with the second set of baselines resulted in lower residual amplitudes initially, as compared to the earlier monitoring times of Figure 5.2(a). The increases in the values of residuals obtained with data collected after continued cycling, however, confirms that degradation of monitoring capability is not only confined to the initial monitoring period. Indicators including the maxima of residual signals, residual signal values at the S0 arrival, and the average values of residuals in the range $t_{\text{1st arr}} < t < t_{\text{coverage limit}}$ were tracked. Figure 5.3(a)-(b) plots these quantities computed using residuals from the pair bonded with the DP105 adhesive and both baseline sets. As can be seen in these plots, all indicators exhibited similar trends in the long term.

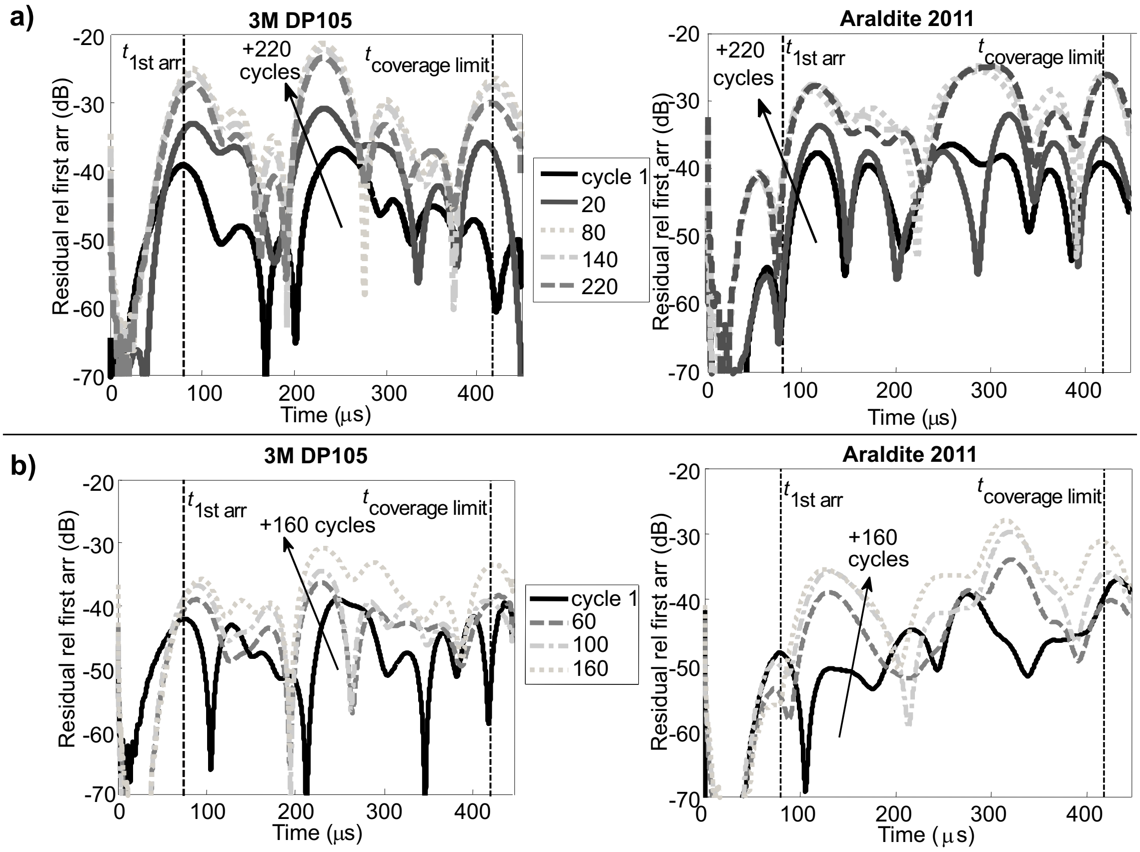

Figure 5.2: Examples of trends in residuals plotted on a dB scale for pairs of sensors bonded with DP105 and Araldite 2011 adhesive using (a) first and (b) second baseline sets; monitored data was acquired with transmitting and receiving PZTs respectively bonded using DP105 at (x =0.835 m,y =0.625 m) and (x =0.415 m,y =0.625 m) on a 2 mm thick, 1.25 m square aluminum plate and using Araldite 2011 at (x =0.835 m,y =0.938 m) and (x =0.415 m,y =0.938 m) on a second 2 mm thick, 1.25 m square aluminum plate.

Drift rates were used to analyze the effect of adhesive type on baseline subtraction stability. Linear regressions were applied to the tracked average of residuals in the range $t_{\text{1st arr}} < t < t_{\text{coverage limit}}$ versus thermal cycle number in the monitoring experiment; representative fits are shown using superimposed solid dark lines in Figure 5.3(a)-(b). Fits were applied to tracked values of indicators computed from collections of residuals for all tested transmit-receive pairs (>6 per adhesive) at each temperature (15, 25 and 35°C) in the monitoring experiment. There were no discrepancies in the range of slopes from the fits when considering drift rates from data obtained at the different test temperatures. Therefore, medians and interquartile values Q_1(25th percentile) and Q_3(75th percentile) that were computed from all data are plotted on one axis in Figure 5.3(c). The positive drift rates confirm that data from all bonded sensors exhibit drift. Drift rates associated with data collected using sensors bonded with Araldite 2011 are lower than the drift rates associated with data collected using sensors bonded with the other adhesives. In all cases, however, the minimum defect size that could be reliably detected increases markedly with thermal cycling.

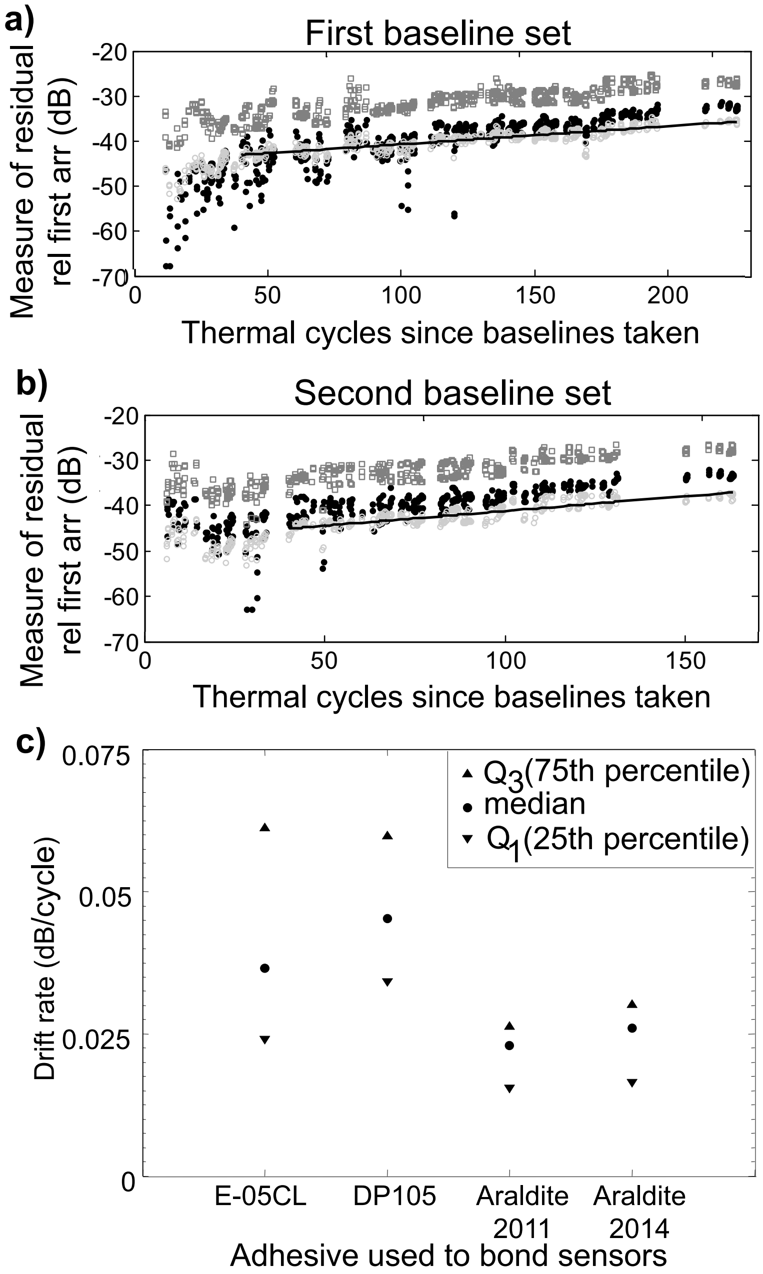

Figure 5.3: Residual values at the first S0 arrival time (.), mean values of residuals in the range $t_{\text{1st arr}} < t < t_{\text{coverage limit}}$ (○), maxima of residuals (□), and linear fits to mean values of residuals (solid black line) evaluated using full data from the DP105 adhesive pair of Figure 5.2 versus thermal cycles since acquisition of (a) first and (b) second baseline sets, and (c) drift rates from linear fits to mean values of residuals from data with all adhesives. Data from 2 mm thick, 1.25 m square aluminum plates except for Araldite 2014 which is from a 2 mm thick,1 m square plate.

5.2.3 Investigation into sources of variability

SHM data was processed further to characterize the sources of variability underlying the observed drifts in residuals. Current signals, $c(t)$, and associated optimal baselines were normalized by envelope detected amplitudes of the first S0 arrival prior to computing difference signals, $s(t)$, using Equation 2.3. $s(t)$ were band-pass filtered using a cosine tapered frequency domain filter having the bandwidth of 7 cycled tonebursts which is the same as that used in Section 3.4.1 and in [41]. The resulting signals are superimposed in Figure 5.4 for sensors bonded with DP105 at 25°C (thermal cycle numbers noted in the legend of the figure.) These waveforms are representative of results obtained from data with all tested adhesives. Visual inspection of these waveforms suggested random variability in the portion of signals prior to the first S0 arrival, $t < t_{1starr}$, remained constant; for instance, note that amplitudes are indistinguishable within the arrows of the section marked "Random" on the plot. On the other hand, there were increased coherent variability in the vicinity of reflections from features. The successive arrows next to the annotated wavepacket arrivals (S0, A0, S0 reflection from the "near edge") of Figure 5.4 highlight this characteristic.

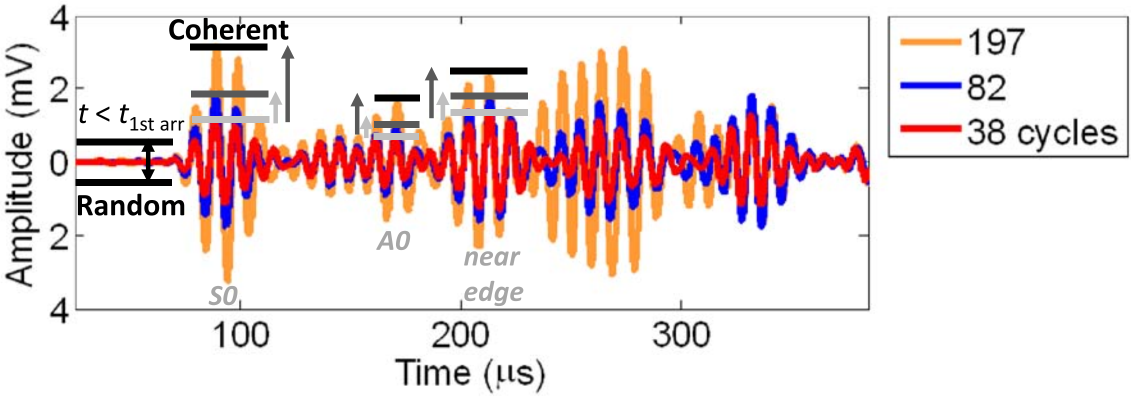

Figure 5.4: Difference signals for varying monitoring times from baseline acquisition with different wave packet arrivals designated (S0 for first S0 arrival, A0 for first A0 mode, and "near edge" for the S0 mode reflection from the closest edge); data are from monitoring using the pair of sensors bonded with DP105 adhesive of Figure 5.2.

Signal to variability ratios were used to quantitatively characterize trends in SHM data. Signal-to-random-variability ratios (SRVR) were calculated by dividing S0 arrival amplitudes by the maximum values of the Hilbert envelope based amplitudes of difference signals in times prior to $t_{\text{1st arr}}$, i.e.

$$\text{SRVR} = \frac{|c_a(t = t_{\text{1st arr}})|}{max|s_a(t < t_{\text{1st arr}})|}. \tag{5.1}$$

In Equation 5.1, $c_a(t)$ and $s_a(t)$ signify the envelopes of the relevant current signal $c(t)$ and difference signal $s(t)$ respectively that were computed using the Hilbert transform. Six current signals acquired over time spans of 6 thermal cycles around each monitoring time were used to calculate the same number of difference signals and values of SRVR. The medians and inter-quartile range of SRVR obtained with optimal baselines from the initial baseline database are plotted against monitoring times for the various adhesives in Figure 5.5(a). As can be seen in this plot, SRVR appear stable with the progression of monitoring time and are consistently >500 times smaller than signal amplitudes. Thus, random variability is negligible relative to the trends described in the previous section.

In contrast to the finding about the noise that affected the data presented in Chapter 4, the results shown in Figure 5.5(a) indicated that the influences of random noise could not be attributed for the changes in monitoring capabilities described in Section 5.2.2. Therefore, further analysis was undertaken to determine whether coherent changes affected the data presented in this chapter. Signal-to-coherent-variability-ratios (SCVR) were calculated using maxima of the envelopes of difference signals within time gates as long as input tonebursts, t_{input} , centered on arrival times, t_{feature} , of feature reflections, i.e.

$$\text{SCVR} = \frac{|c_a(t = t_{\text{1st arr}})|}{max|s_a(t_{\text{feature}} - t_{\text{input}}/2 < t < t_{\text{feature}} + t_{\text{input}}/2)|} \tag{5.2}$$

In Equation 5.2, t_{feature} were calculated by dividing the distance between the sensors by the group velocities from DISPERSE [39] and the distance associated with the transmitter-closest edge-receiver path by the S0 group velocity for the “near edge” reflection; associated wavepacket arrivals have been labelled in Figure 5.4. SCVR such as those representatively shown for pairs bonded with tested adhesives in Figure 5.5(b)-(e) consistently declined to small values at the end of tests. These results verified that coherent variability, rather than increased susceptibility to random noise, contributed to the changes in baseline subtraction results of the preceding section. Literature on epoxies and micro-electromechanical sensors (reviewed briefly in the next section) led to the hypothesis that these may be due to changes in bond-line characteristics. This was studied further by simulating signal changes caused by variations in the properties of the bond between sensors and the plate.

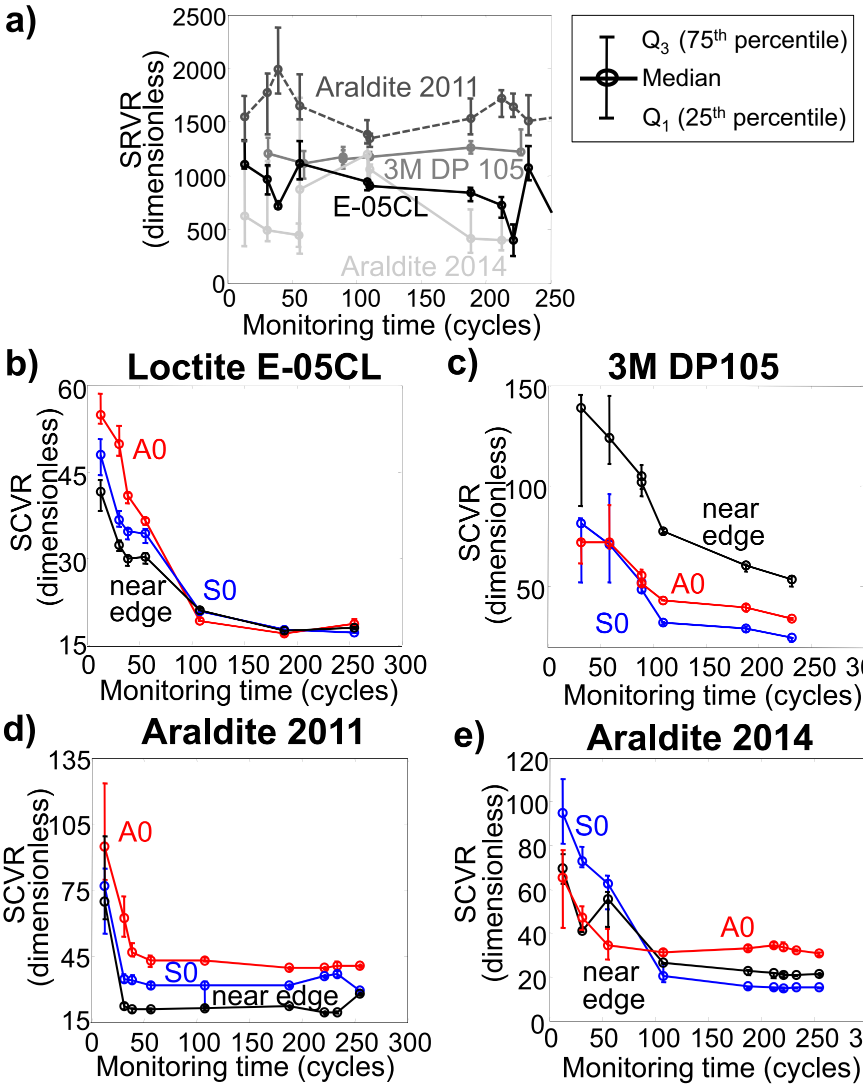

Figure 5.5: Signal-to-random-variability-ratios (SRVR) in SHM data from sensor pairs bonded with various adhesives and (b)-(e) signal-to-coherent-variability-ratios (SCVR) in the vicinity of arrivals from various features with “near edge” used to designate the S0 reflection due to the edge which involves minimum propagation distance for relevant sensor pairs. Median and quartile values based on 6 realizations of difference signals acquired within ±3 thermal cycles around each monitoring time. Data from 2 mm thick, 1.25 m square plates except for Araldite 2014 which is from a 2 mm thick,1 m square plate.

5.3 Simulations

The electromechanical characteristics of free PZT remain stable throughout prolonged environmental exposures when compared with their behavior in adhesively bonded sensors [91]. Experimental and industrial use of other micro-electromechanical sensors suggest their performance is often highly affected by adhesion issues [121, 127, 128, 132, 133]; problems have been observed even when delamination or cracks do not compromise sensor integrity. Studies have also shown the sensitivity of epoxy adhesives to environmental exposure [119–121, 124, 129, 134, 135] and ageing [134, 136–139]. Measurements of dynamic viscoelastic parameters suggest that the dynamic moduli of epoxies are particularly sensitive [133, 134, 136, 138, 139]. The density of these materials may also change [136, 137]. A study of the complex mechanisms underlying these effects lies outside the scope of this work. Based on the observation that the choice of adhesive affected performance (see Section 5.2.2) and the findings in the literature, it was hypothesized that coherent variability in residuals were due to changes in the properties of the adhesives used to bond PZTs to plates. FE studies were used to analyze how SHM data would be influenced.

5.3.1 FE model and validation of simulation techniques

The frequency domain axisymmetric transducer model shown in Figure 3.2 was used throughout the simulations. A description of the model is provided in Section 3.3. The relevant material properties are given in Appendix A.1. Square elements of 62.5 µm side length were used to mesh all parts in order to mesh the thin bond layer with a greater number of elements than was done in Section 3.3.

The PZT disc was excited with 1 V at frequencies over a range encompassing the bandwidth of the 5 cycle, 100 kHz Hanning windowed toneburst input signal. The voltage response of a receiver PZT disc was assumed to vary with the sum of radial and circumferential strains over the location where it is attached, as in [91, 102]. As strains should not vary significantly with spread over a 20 mm diameter receiver transducer at a range of 0.42 m, radial and circumferential strain responses were monitored at the node on the surface of the plate at $r = p$ =0.42 m (i.e. to match the sensor pitch of experiments.) The time traces of radial, $\varepsilon_{rr}(t)$, and circumferential, $\varepsilon_{\theta\theta}(t)$, strains were obtained by IFFT of monitored spectra at the node on the surface of the plate and summed to obtain the desired strain, $\varepsilon(t)$:

$$\varepsilon(t) = \varepsilon_{rr}(t) + \varepsilon_{\theta\theta}(t) \tag{5.3}$$

The signal which is computed with Equation 5.3 is analyzed as the voltage response of a receiver PZT varies with this quantity. A typical computed waveform is plotted in Figure 5.6(a) with the strain normalized to a maximum of unity at the S0 mode arrival. The arrivals of the S0 and A0 pulses (annotated) occur at the expected times calculated using group velocities from DISPERSE [39]. The A0 pulse has a larger amplitude (relative to the S0 pulse) than observed in Figure 3.12(a)-(b) and this is due to effects at a receiver not modelled (e.g. mode selectivity and sensitivity to strains resulting across the surface of the bond layer below it.) In order to use waveforms computed with Equation 5.3 to assess the magnitude of change which may be due to epoxy property variations, baseline data needed to be generated first.

Baseline data was simulated by adjusting relevant material properties in the FE model and re-running simulations. The ability of this technique to accurately simulate variability in baselines was analyzed for various temperature changes, δT, in the range 0°C<δT<5°C. The Young's modulus E_{Al} and Poisson's ratio ν_{Al} of Al were linearly adjusted using the temperature dependence coefficients of Table 5.2. The epoxy moduli were varied by 1% per °C as this level of change has commonly been reported [140]. The densities of aluminum, the PZT, and epoxy were divided by $(1+\alpha_{\mathrm{material}}*\delta T)^3$ using the coefficient of thermal expansion, $\alpha_{\mathrm{material}}$, for each material (see Table 5.2); α_{epoxy}=40E-6°C^{-1} is used for results though changes in this variable over the ranges of values for the different adhesives in Table 5.1 did not significantly influence the findings. The properties of the PZT were left the same as these are not significantly affected by small δT [141]. The dimensions of the FE model were not changed as variability in guided wave data is predominantly related to velocity changes rather than dimensional changes [85]. The signal in Figure 5.6(a) (i.e. at δT=0°C) was subtracted from signals predicted with different δT using Equations 2.3- 2.4. The resulting difference signals are plotted in Figure 5.6(b) on a dB scale; as expected, variability increases with greater δT.

Table 5.2: Temperature dependence coefficients used to adjust material properties in FE model to obtain baseline signals with different temperature changes.

Coefficient	$\alpha_{\text{epoxy}} * 10^6$ (°C^{-1})	$\alpha_{\text{PZT}} * 10^6$ (°C^{-1})	$\alpha_{\text{aluminum}} * 10^6$ (°C^{-1})	$\frac{\partial E_{\text{Al}}}{\partial T}$ (GPa °C^{-1})	$\frac{\partial \nu_{\text{Al}}}{\partial T} * 10^5$ (°C^{-1})
Value	40	2.1	23	-3.78	3
Source	[122, 130, 131]	[135]	[142]	[143]	[143]

The variability in these results was compared to the theoretical residual, $s_{\text{max}}(\delta T)$, expected when subtracting a signal at a temperature difference of δT from the signal obtained at a reference temperature, i.e. [85]

$$s_{\text{max}}(\delta T) = 2\pi f \left| \frac{-1}{v_{\text{ph}}^2} \frac{\partial v_{\text{ph}}}{\partial T} \delta T \right| pA \tag{5.4}$$

In Equation 5.4, f is the centre frequency (100 kHz), v_{ph} is the phase velocity, $\frac{\partial v_{\text{ph}}}{\partial T}$ is the factor relating the change in v_{ph} with temperature, p is the propagation distance (0.42 m), and A is the signal amplitude. Equation 5.4 was used with v_{ph}, $\frac{\partial v_{\text{ph}}}{\partial T}$ of Table 5.3 and A set equal to the envelope detected amplitudes of the S0 and A0 pulses in the signal of Figure 5.6(a) to compute s_{max} at these guided wave mode arrival times. The resulting values of s_{max} are plotted on a dB scale (solid lines) in Figure 5.6(b). The dB values of difference signal amplitudes from the FE simulations discussed above are overlaid on this plot using circles. The results of the FE simulations match the theoretically predicted values of residual for both the S0 and A0 arrivals across the range of δT investigated. This confirms that the simulations give realistic values for the residuals obtained when waveforms at different temperatures are subtracted.

Table 5.3: Phase velocities and coefficients which relate change in v_{ph} with temperature for the fundamental Lamb modes at frequency thickness of 0.2 MHz-mm from [39, 56].

Lamb wave mode	v_{ph} (m s^{-1})	$\frac{\partial v_{\text{ph}}}{\partial T}$ (m s^{-1} °C^{-1})
S0	5430	-1
A0	1310	-0.17

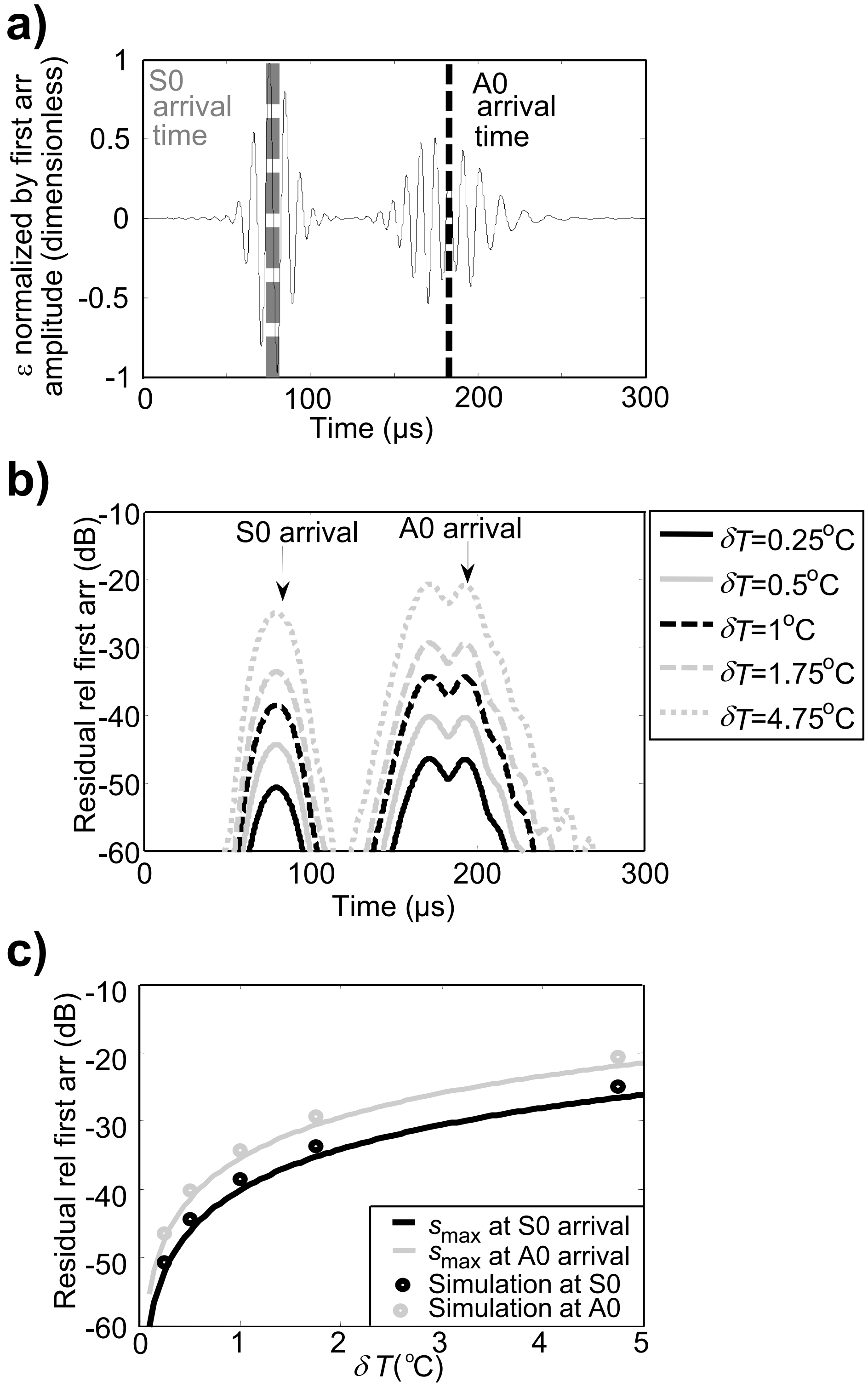

Figure 5.6: (a) Strain signal, $\varepsilon(t)$, contributing to the voltage of a receiver PZT at $r = p$ =0.42 m which was estimated using the simulated strains on the surface of the plate in the FE model of Figure 3.2, (b) results of simple subtraction between signal of (a) and the simulated signals at temperature gaps, δT, and (c) comparison of amplitudes of subtracted signals to dB values of theoretical residual, $s_{\max}$, at S0 and A0 arrivals.

5.3.2 Sensitivity to adhesive properties

As discussed above, adhesive properties are affected by ageing and cyclical thermal loading. Researchers have observed nearly 40% change in the dynamic moduli of epoxies associated with these exposures [136], though an upper bound of 20% change relative to nominal values after cure is more commonly reported [134, 137–139]. The density of epoxy adhesives typically tends to vary by <5% of initial values [136, 137]. Individual properties of the adhesive layer in the FE model of Figure 3.2 were adjusted up to the abovementioned bounds while keeping all other material properties the same. Simulations were re-run with each perturbation of the FE model, and monitored strains were used with Equation 5.3 to calculate current signals. Current signals that were obtained when the magnitudes of the epoxy dynamic moduli $|E^*|$ and $|G^*|$ were changed by different amounts relative to the nominal values are plotted in Figure 5.7(a). Discrepancies exist between the signals including variations between the black and gray curves that are highlighted within the zoom area insets of Figure 5.7(a).

The amplitudes of variability associated with the simulated property changes were then determined. Residuals were computed for the current signals by subtracting these signals from optimally stretched versions of the baseline waveform from the simulation with original material properties (i.e. of Figure 5.6(a).) In order to compare the variability in these results with those due to the maximum thermal shift (0.25°C) between current signals and optimal baselines obtained in tests, the signal at δT =0.25°C was also subtracted from an optimally stretched version of this baseline. The resulting beam spread corrected residuals have been plotted in Figure 5.7(b). The changes to the epoxy moduli result in residuals over 20 dB higher than those obtained from δT =0.25°C. These residuals correspond to transmission through the PZT-plate bond only as the simulated waveform is calculated from the plate strain rather than from a receiver transducer with another bond line. In experiments, the receiver is also bonded so by transmit-receive reciprocity, the residual levels expressed in dB will be greater; the analysis of the plane strain models described in Appendix D indicates that changes in the properties of the bond line of a receiver should contribute variability of amplitudes ~4-6 dB greater than those due to variations in the bond line of the transmitting PZT. Even though the influences on the response of a receiver PZT are not considered in the analysis results presented in this section, the predicted residual amplitudes in Figure 5.7(b) are comparable with the residuals of nearly -30 dB seen in Figure 5.2. The variations in the data are reflective of influences changes in epoxy moduli has on transduction with a PZT that induces strains in the plate mostly through shear effects at the adhesive layer. Research shows interfacial stresses are confined nearer to the edges of thinner bonds though influences of variations in adhesive layer thickness aren't analyzed as there aren't indications thickness change results in bonds exposed to the conditions studied. The effect of 5% change in epoxy density on residuals was studied as this has been observed by researchers. This change results in a residual 4 dB higher than that from a 0.25°C thermal shift, indicating that the residuals due to adhesive density changes are less significant than those due to moduli variations.

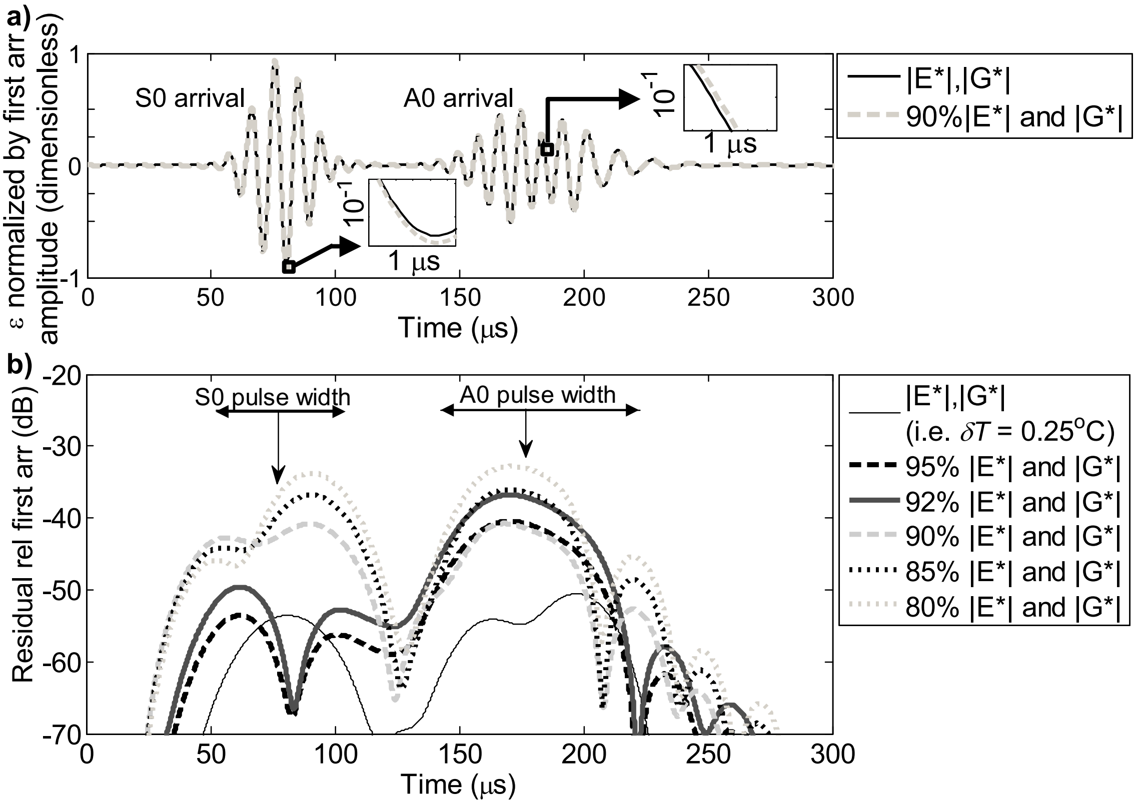

Figure 5.7: (a) Simulated current signals with indicated changes input to epoxy moduli; boxes used to show zoomed areas of signals. (b) Residuals computed from temperature compensation and subtraction between simulated current signals and simulated baselines.

The analyses in this section suggested that epoxy moduli changes were a likely source of variability in SHM data. Long term measurements on bulk adhesive samples were undertaken to determine the amount of variability which could be attributed to changes in the moduli of the adhesives used to bond the sensors to the plates in experiments.

5.4 Measurements on bulk adhesive samples

Bulk samples of the adhesives used to bond the sensors to the plates in Section 5.2.1 were thermally cycled to study how their properties are affected by cycling of the sort seen in practice. The thicknesses of the samples were periodically recorded along with bulk longitudinal wave ultrasonic data at 2.25 MHz to track changes in longitudinal velocities, and hence moduli [144]. Results of tests are presented along with a discussion of their relevance to trends in SHM data.

5.4.1 Specimens and test methods

Adhesive blocks were manufactured by injecting dual cartridge packs of epoxies (see Table 5.1) into purpose made aluminium moulds treated with mould release agent (Meguiars #8.) Five plates approximately 50 mm x 50 mm x 5 mm were cast for each of the adhesives in Table 5.1. Specimens were left to cure at room temperature for at least as long as recommended by the manufacturers. Samples were then thermally cycled in an environmental chamber using the temperature profile of Figure 5.1(c). The samples were periodically removed from the chamber to measure thicknesses and record ultrasonic data. Thicknesses were measured using a micrometer (0.02 mm, or 0.4%, precision.) Longitudinal velocities were calculated using the differences in the arrival times of the successive reflections in ultrasonic waveforms recorded using a standard 2.25 MHz, 0.5 inch (12.7 mm) diameter longitudinal wave probe (Krautkramer, AU.) Independent measurements on the bulk samples indicated that the technique enabled estimation of velocities with 1% precision. This result confirmed that good repeatability in measuring longitudinal velocities was achieved, and these measurements were tracked instead of shear velocities as a result.

5.4.2 Signal processing and data

Average sample thicknesses remained the same to within the precision of the measurement. This finding confirmed that the thicknesses of these adhesives did not change significantly with exposure to temperature cycling. The average percentage change in mean longitudinal velocities, $\bar{v}_{\mathrm{L}}$, relative to the initial mean velocities, $\bar{v}_{\mathrm{L0}}$, are plotted against thermal cycle number for the various adhesives in Figure 5.8. These results show that the velocities of E-05CL and DP105 adhesives decline by approximately 4% and that of Aralide 2014 by about 2%. In contrast, the velocity of Araldite 2011 adhesive increased by about 1%.

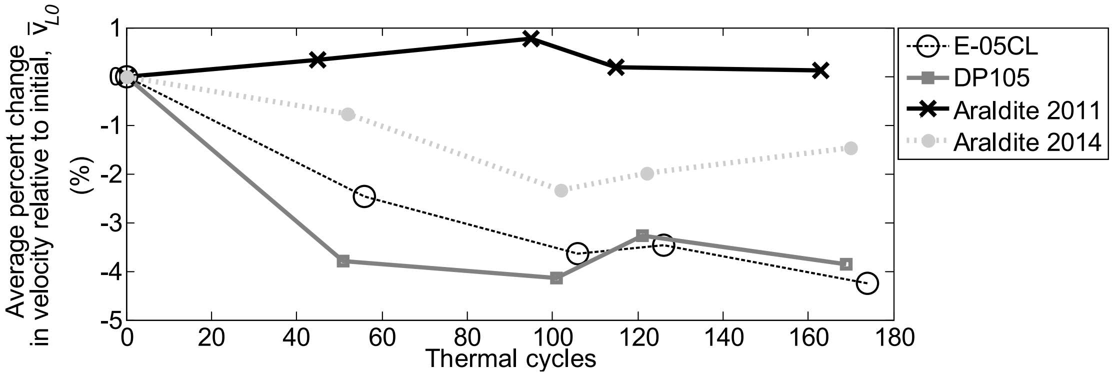

Figure 5.8: Average percent change in longitudinal velocities, $\bar{v}_{\mathrm{L}}$, relative to initial values, $\bar{v}_{\mathrm{L0}}$, with the progression of thermal cycling of the various adhesives used to bond sensors to plates.

5.4.3 Discussion of results

The elastic modulus is proportional to velocity squared [144]. Therefore, the 4% changes in the velocities of E-05CL and DP105 adhesives correspond to ~8% modulus change. The velocity changes of 2% for Araldite 2014 adhesive amounts to ~4% modulus change. The simulation results in Figure 5.7(b) and Figure D.3 suggests changes in the moduli of E-05CL and DP105 adhesives may be attributed for residual amplitudes being at least 8-16 dB higher after cycling than after baseline collection. These levels of variability account well for observed levels of variability in SHM data collected with sensors bonded using E-05CL and DP105 adhesives. The finding that Araldite adhesives exhibit relatively modest velocity change suggests factors other than moduli change may be contributing appreciable levels of the variability in SHM data acquired with sensors bonded using these adhesives. The modest changes in the velocities of Araldite adhesives and the relatively large declines in the velocities of E-05CL and DP105 adhesives do correlate well with the patterns in the drift rates of Figure 5.3(c). These results confirm that adhesive change is a credible cause of degradation in monitoring capabilities.

5.5 Summary

This chapter described investigations of the defect detection capabilities of an SHM system which uses bonded PZT sensors in order to monitor guided wave signals and baseline subtraction based methods for damage detection. The results show the variability in SHM data collected with S0 mode sensors bonded on 2 mm thick aluminum plates increases with exposure to cyclical thermal loading. The minimum defect size which can be reliably detected with 6 dB margin in residuals grows from <1.5% to >3% reflection change after 150 thermal cycles for a variety of adhesive systems used to bond the sensors to the plates. Analysis results show that the degradation in monitoring capabilities is due to coherent changes in the SHM data. It was hypothesized that these changes were due to the changes in the modulus of the adhesives used to bond the sensors to the plates. FE simulations as well as experimental tests on bulk adhesive samples indicate that adhesive modulus changes with thermal exposure are a major source of the variability in SHM data. The adhesives that showed the greatest variability in bulk properties with thermal cycling also performed poorest in the SHM experiments.

These findings confirm that a very stable adhesive is necessary to use bonded sensors for guided wave SHM of structures where echoes from different features overlap so that defects can only be detected via baseline subtraction. The results do show that Araldite adhesives are the most stable among the various adhesive systems tested. However, unless the issues with drifts in baseline subtraction results can be resolved, long term monitoring of plate-like structures to detect the growth of small defects is not feasible.

Chapter 6

Stability of an alternative transduction mechanism

6.1 Introduction

The results in Chapter 5 indicated that transducers which are adhesively bonded must be attached to plates using a very stable adhesive if they are to be used for SHM purposes. The adhesives that were tested were not suitable for enabling reliable detection of ~1.5% reflection change after specimens had been exposed to 250 thermal cycles. It may be possible that there are more stable adhesives than the ones tested. However, it was thought that a practical sensor could be more readily realized by using a transduction mechanism which does not rely on bonding. EMATs are a particular class of non-contact transducers that would be interesting to exploit. EMATs are advantageous for SHM as they can be installed easily on ferritic metal structures without requiring complicated surface preparation and assembly procedures which are necessary for bonding sensors [119–121]. The disadvantages of EMATs are their low sensitivity and the general requirement for them to be operated using complicated high power drive circuitry. Recent work at Imperial College London has made it possible to send and receive guided wave signals with EMATs using low voltage electronics. Thus it was decided to study the stability of a guided wave SHM system that uses EMATs operated at low voltages.

As in previous chapters, the SHM system exploits monitoring of omnidrectional wavefronts of the S0 mode. In this chapter, the S0 mode is generated and received using EMATs that are described in Section 6.2. This section also describes the signal excitation, acquisition, and the processing procedures which are applied in order to conduct monitoring experiments at low voltages. Section 6.3 presents experiments which were used to evaluate the SHM system and the results of the stability in its defect detection capabilities as a function of thermal cycling.

A realization of a monitoring system that uses low voltage EMATs and cross-correlation approaches of obtaining pitch catch signals is shown to be viable for SHM of plates experiencing thermal variations for the first time. The relative stability of EMATs compared to bonded PZTs is found out in studies of the long term performance of the SHM system being applied to a steel plate. Images of the central area of the steel plate generated with baseline subtraction of data monitored with an array of the EMATs highlight reliable capabilities of the system and are reviewed as are insights to further develop the technology.

6.2 Electromagnetic acoustic transducers

This section discusses the construction of the EMAT and how it allows excitation and sensing of the propagation of Lamb waves. An explanation is provided about the tests used to determine the frequency at which to operate transducers in order to generate the S0 mode strongly (relative to the unwanted A0 mode.) The following section describes the low voltage use of EMATs and the acquisition settings that were employed in order to collect the high SNR pitch catch data necessary for SHM purposes.

6.2.1 EMAT for excitation of the S0 mode on steel plates

The EMAT used in all tests is based on a design from [40] and is shown in Figure 6.1. This particular transducer was primarily chosen because it enables strong excitation of omnidirectional wave fields of the S0 mode (compared to the A0 mode) on aluminum plates [40] and it is useable on steel plates too [145]. In operation, an alternating current is transmitted to the planar annular double-sided (pancake) coil of the EMAT. The current flow induces a distribution of eddy currents in a region near the surface of a metallic plate underneath the coil which is determined by the relative positioning and the properties of the specimen, and is called the skin depth. In the region of the skin depth the induced currents interact with the static magnetic field from the NdFeB magnets, producing radially oriented Lorentz forces in the plate. The forces are strong enough to act on electrons in the metal and oscillate particles which give rise to Lamb wave propagation if the magnet is at sufficiently small standoff from the plate. The Lorentz forces determine the excitation of the Lamb waves by the EMAT on nonferromagnetic metallic plates [40]. Recent research suggests that Lorentz forces from an EMAT in this configuration also account for significant amounts of wave motion in the engineering steels of interest too [146]; in these ferromagnetic materials, there may also be additional effects of magnetostrictive forces though research confirms this EMAT configuration generates stronger Lorentz forces when used on most steels [146]. By the principle of reciprocity, an electromotive force is induced in a receiving EMAT when displacements interact with the magnetic field and cause oscillating electron flow in the receiver coil. More detailed analysis of the excitation and reception mechanisms may be consulted in [40, 146, 147]. However, the excitation mechanism and its optimization was not the primary focus of this work which was concerned with studying the long term stability in defect detection capabilities of the transduction mechanism.

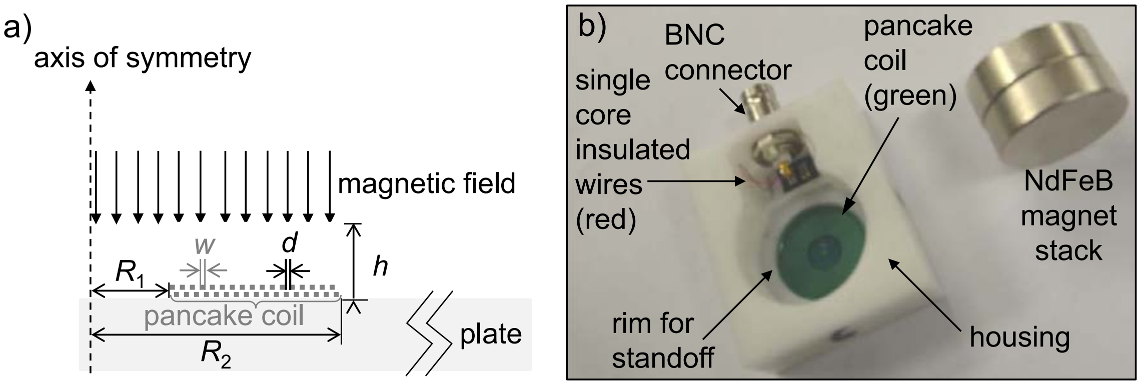

Figure 6.1: (a) Axisymmetric diagram of the EMAT geometry from [40] with the pancake coil made of 46 turns of wire, each of width w = 340 µm, spaced d = 100 µm apart in a ring of radii R_1 = 4.5 mm, R_2 = 14 mm and the magnet standoff, h=4 mm, along with (b) a photograph of the components used in sensor assemblies; magnets sit on the rim in (b).

A study of the guided wave transmission characteristics of the EMAT on a steel plate was undertaken in order to determine the frequency at which to operate it. The surface displacements the transducer generates were measured on a 2 mm thick, 1.25 m square plate using LDVs in the configuration of Figure 6.2(a). A Wavemaker (Duet X, Macro Design Ltd, UK) was used to excite the EMAT with 5 cycled Hanning windowed toneburst voltage input signals of centre frequencies in the range 130-220 kHz; in this frequency range, it is expected that the S0 mode can be preferentially excited over the A0 mode based on findings from studies with coils of the same $R_2 : R_1$ ratio [40]. An inline current transformer (CT-B1.0-B, Bergoz, FR) was used to measure the current resulting across the EMAT terminals. Measurements of the current and the impedance of the EMAT on a steel plate, which had been recorded with an impedance analyzer (4294A, Agilent, UK) prior to the LDV tests, were used to confirm that the amplitude of all inputs were ~56 Vpp. All vibrometer signals were digitized and saved on an oscilloscope (Lecroy WaveRunner 6030) using 1000 averages and f_s = 50MHz. High numbers of averages were necessary to resolve small amplitude signals such as the out-of-plane displacements at the S0 arrival.

The vibrometer signals were used to calculate the in-plane and out-of-plane components of the surface displacement field [106]. Example time traces of the surface displacements are shown in Figure 6.2(b). The ratio of the Hilbert envelope based amplitude of the in-plane surface displacement at the S0 arrival to the amplitude of the out-of-plane surface displacement at the S0 arrival is within 5% of the ratio of the corresponding displacements in the mode shapes as predicted by the DISPERSE software [39]; this was consistently the case in data collected with variations to the centre frequency of the input toneburst.

In order to determine the best centre frequency of the toneburst with which to excite the EMAT, the ratio of Hilbert envelope based amplitude of the surface in-plane displacement at the S0 arrival to the Hilbert envelope based amplitude of the surface out-of-plane displacement at the A0 arrival were computed. The maxima, mean, and minima of the ratio from independent measurements with 5 assembled EMATs are plotted in Figure 6.2(c). The results show that excited waves of both fundamental Lamb modes have fairly similar amplitudes. The A0 mode has the lowest amplitude (relative to the S0 mode) with excitations centered around 200 kHz. Based on this finding, tonebursts centered at 200 kHz were chosen to excite the EMAT.

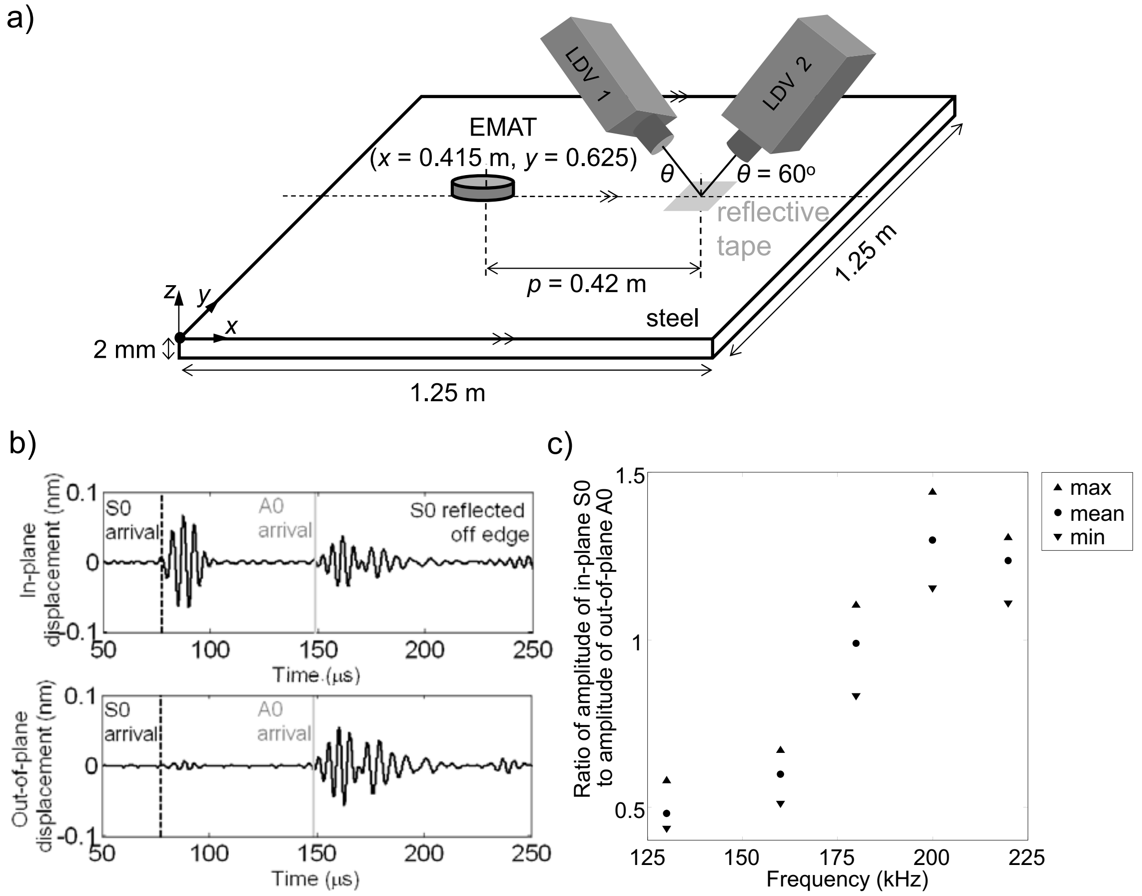

Figure 6.2: (a) Setup for measuring the surface displacement field due to a transmitting EMAT at (x =0.415 m, y =0.625 m) on a 2 mm thick, 1.25 m square steel plate, (b) the surface displacements measured at (x =0.835 m, y =0.625 m) with the EMAT excited using 5 cycled, 200 kHz tonebursts of 56 Vpp, and (c) the extracted ratio of the envelope detected amplitude of the in-plane surface displacement of the S0 mode divided by the out-of-plane surface displacement of the A0 mode (statistics from tests with 5 EMATs.)

6.2.2 Pitch catch data acquisition at low voltages

The use of the baseline subtraction based damage detection strategies that are adopted in the guided wave SHM system requires that signals of relatively high SNR be monitored. This result cannot be achieved with conventional use of EMATs without bulky high power amplifiers and averaging of many hundreds of received signals. For illustration, consider the setup in Figure 6.3(a) which is used to record pitch catch data between a pair of EMATs separated by 420 mm on a 2 mm thick, 1.25 m square steel plate in a configuration similar to the one in Figure 6.2(a). Five cycled, 200 kHz tonebursts of 20 Vpp are sent to the transmitting EMAT by the Handyscope (HS3, Tie Pie Engineering Ltd., NL.) The resulting signals at the receiving EMAT are amplified by 70 dB and band-pass filtered in the 50-250 kHz range with a custom built preamplifier prior to being saved using 150 time averages. A sampling frequency of 10 MHz is used to digitize this and all received time traces. The resulting pitch catch signal plotted in Figure 6.3(b) shows the S0 arrival and other feature arrivals though it is too noisy for monitoring purposes (i.e. the ratio of the Hilbert envelope amplitude of the S0 arrival to the maximum of the signal envelope in the portion of the time trace prior to the S0 arrival is 20 dB which is unacceptable for SHM purposes [31].) Therefore, it was decided to study the feasibility of using other data acquisition approaches in order to achieve higher SNR in guided wave data recorded using EMATs.

It is possible to obtain pitch catch data with enhanced SNR using 20 Vpp input voltage if the excitation signal is specially encoded prior to being applied to transmitters and the data acquired at receivers are post-processed in order to compute desired signals [148–150]. In this work, a method was adopted which uses complementary Golay codes to encode input tonebursts and cross-correlation and summation of received time traces for pitch catch signal recovery [150]. The technique enables measurements to be obtained quickly as one does not need to wait for the response of the test piece to damp out before triggering a subsequent measurement (which is necessary in the use of synchronous averaging.) This approach to data acquisition allows results to be obtained with enhanced SNRs which have been shown to be equivelant to those achieved using a large number of time averages [148] or higher amplitude input signals [150]. Therefore, this approach to data acquisition was adopted to collect pitch catch data with the EMATs. In order to collect the pitch catch data, a program was used which was coded by Attila Gajdacsi, Joe Corcoran, and Dr. Frédéric Cegla of the NDE Group and the procedures used for these purposes will be briefly reviewed in the following paragraphs.

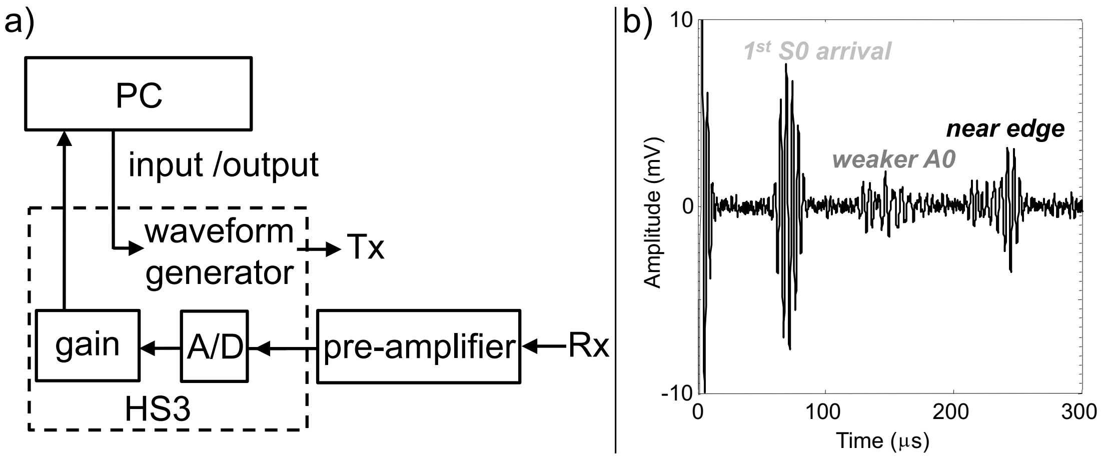

Figure 6.3: (a) The DAQ system used to excite transmitting EMATs (Tx) and record signals at receiving EMATs (Rx), and (b) the result of applying 20 Vpp 5 cycled, 200 kHz tonebursts to Tx and using 150 sweeps to record the signal received by Rx at a distance of 420 mm on a 2 mm thick, 1.25 m square steel plate.

The acquisition electronics are the same as those in Figure 6.3(a). Figure 6.4(a) illustrates the steps used to send input signals as well as the modified functions of the electronics that are used to collect the necessary data and compute pitch catch signals. At the start of data acquisition, a pair of length 2^8 Golay codes, g_a and its complementary sequence g_b, are generated as described in [151]; this sequence length is used to transmit the greatest number of 5 cycled 200 kHz tonebursts possible given the memory limitations of the Handyscope in order to achieve the highest suppression of random noise [148–150]. Each of the sequences is convolved with the toneburst in order to generate the encoded inputs. An example input signal which is computed using the first Golay code g_a corresponds to the signal in the plot of Figure 6.4(b). This signal is uploaded to the transmitting EMAT. The trace $x_a(t)$ at the receiving EMAT is amplified and filtered using the preamplifier prior to being digitized, averaged, and saved on the PC. This whole process is repeated with excitation of the transmitter using the input encoded by g_b in order to save the required signal $x_b(t)$.

In order to compute the desired pitch catch signals $x(t)$ it is necessary first to generate reference signals using convolution between the toneburst and the two sequences of the Golay code pair first. The reference signals are cross-correlated with each of $x_a(t)$ and $x_b(t)$, and the resulting outputs are summed to obtain the pitch catch signal $x(t)$ that contains accurately recovered wavepackets including those waveforms that differ from the toneburst due to influences of dispersion. For illustration of the power of the technique, Figure 6.4(c) shows a pitch catch signal obtained using the same sensor pair that was used to acquire the signal in Figure 6.3(b) and these data acquisition procedures with 150 averages of the 2^8 sequence lengths which were used in the subsequent test programme. The signal in Figure 6.4(c) has a much higher SNR than the conventionally acquired signal of Figure 6.3(b) (i.e. the amplitude of the S0 arrival to the maximum of the signal envelope in the portion of the trace prior to the S0 arrival is 42 dB.)

The Handyscope device memory does not permit sequences consisting of more than 2^8 200 kHz tonebursts to be encoded and uploaded to transmitting EMATs. This capability was not sufficient for producing a pitch catch signal of high enough SNR for SHM purposes with the methods that rely on the use of baseline subtraction. It was necessary to use an additional 150 time averages in saving received signals to further improve the SNR. There is a tradeoff between the additional increases to SNR with using greater numbers of time averages and the acquisition time which can subject measurements to the influences of ambient temperature changes. A study was therefore used to investigate the effects of varying the number of time averages used to record received signals on the ability to detect small change in SHM data.

Two pitch catch signals were obtained for each of 9 sensor pairs positioned at the points indicated in Figure 6.2 on 2 mm thick, 1.25 m square steel plates. The second pitch catch signal in each set was subtracted from an optimally stretched version of the first signal in the set. The means and the interquartile range of the resulting residual maxima are plotted alongside the time required to acquire data for each pitch catch signal in Figure 6.5. The results show that Golay coded data acquisition with >100 time averages to digitize received waveforms is necessary to realize residuals that have amplitudes smaller than -40 dB relative to the first S0 arrival (which is being targeted in the monitoring applications.) Lower amplitudes of residual are obtained with >200 time averages but the associated acquisition times do not justify the gains in detection capability (particularly as ambient thermal swings can occur in > 1min in practice.) Thus, 150 averages of received signals are used for data acquisition (this allows a pitch catch signal to be obtained in < 25 sec.)

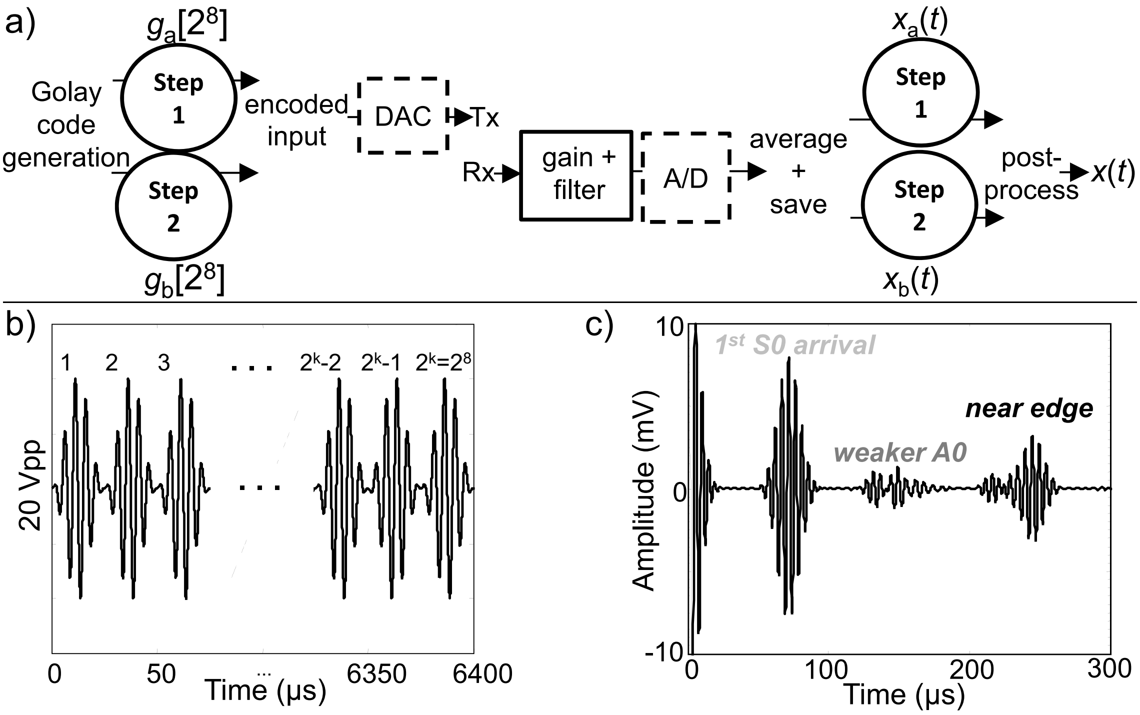

Figure 6.4: (a) The signal flow and functions of the DAQ system used to generate the Golay codes g_a and g_b, sequentially apply encoded inputs to Tx, and acquire $x_a(t)$ and $x_b(t)$ at Rx to compute pitch catch signals $x(t)$, (b) the input signal containing 2^8 5 cycled, 200 kHz tonebursts encoded using the 1st sequence g_a of a Golay code pair, and (c) $x(t)$ computed with data acquired using the sequence of Figure 6.4(b) and its complement, averaged 150 times; results in (c) obtained with the sensor pair used in Figure 6.3(b).

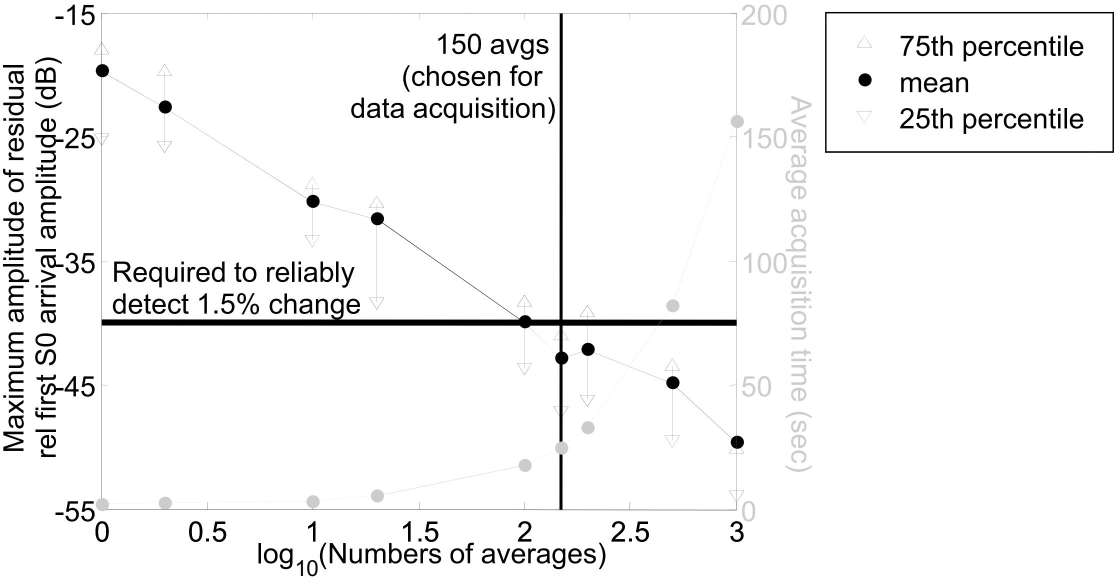

Figure 6.5: The maxima of residuals (black) from the subtraction of pitch catch data acquired in rapid succession using Golay coded excitation and post-processing methods vs log of the number of averages and acquisition times (grey.) Statistics are from data collected with 9 sensor pairs configured similarly as the pair used to obtain Figure 6.3(b).

6.3 Monitoring experiments

6.3.1 Stability study design

A 2 mm thick square steel plate having sides that were 1.25 m long was instrumented with arrays of EMAT sensors for the monitoring study. The sensors were positioned as shown in Figure 6.6(a) in order to temporally separate the breakthrough as well as the arrivals of the S0 mode and the A0 mode from all arrivals of the reflections of the S0 mode off the plate edges in the pitch catch signals. This array configuration allowed testing with propagation distances between sensors of certain pairs (i.e. Tx 1-Rx 4, Tx 2-Rx 5, Tx 3-Rx 6) that are the same as those used in the experiments of Chapter 5. The EMATs in the array were wired to a custom built multiplexer as shown in Figure 6.6(b) in order to ensure separate connections to the coils of transmitting EMATs and those of receiving EMATs which were also connected to relevant channels on the Handyscope (HS3, Tie Pie Engineering Ltd., NL.) Inputs containing 2^8 long Golay coded sequences of 5 cycle Hanning windowed tonebursts with centre frequency of 200 kHz were used to excite transmitting EMATs and signals at the receiving EMATs were recorded and post-processed in order to compute pitch catch signals. Typical pitch catch signals that were obtained after transmitting via Tx 2 and processing the data recorded using 150 time averages at the various sensors are plotted in Figure 6.7. The S0 mode and the weaker A0 arrival are consistently separated from the signals associated with reflections from the edges of the plate as desired and occur at the times expected based on group velocities from the DISPERSE software [39].

It was decided to assess whether it would be worthwhile varying the number of cycles in the toneburst of input signals. Transmitting EMATs were excited using encoded inputs consisting of 2^8 tonebursts of 3, 5, and 8 cycles. Data was captured at the receiving EMATs from which pitch catch signals were computed. Figure 6.8 plots the pitch catch signals computed with data acquired at 20°C using sensor pair Tx 3 - Rx 6. The ratio of the Hilbert envelope based amplitude of the S0 arrival to that of the weaker A0 pulse increases from 4 to 5 to 7 with changes in the number of cycles in the toneburst from 3 to 5 to 8 respectively (note the values equal the average of the ratios computed using the data acquired with the various combinations of transmitting and receiving sensors in the array.) The amplitude of the S0 arrival relative to the amplitude of the pulse at the A0 arrival is larger with increases to the number of cycles because more narrowband inputs concentrate the toneburst spectral content near 200 kHz, the frequency at which the results of Figure 6.2 show the highest S0/A0 ratio is possible with the EMAT. However, increasing the number of cycles in the input also causes temporal elongation of wavepackets, which reduces spatial resolution [44]. Therefore, it was decided to use 5 cycled tonebursts, as was done in the earlier work with PZT transduction in Chapter 5.

An experiment was used to determine the relative differences in temperatures at which to acquire baselines. The steel plate with the array of EMATs was moved to an environmental chamber (Alpha 1550-40H, Design Environmental, UK.) The chamber was used to heat the plate from 20°C to 25°C with dwells at 20, 20.15, 20.25, 20.5, 21.1, 22.5, and 25°C. At each of these temperatures, transmitting EMATs were excited using encoded inputs consisting of 2^8 tonebursts of 5 cycles and the data was captured at the receiving EMATs in the sensor array with which pitch catch signals were computed.

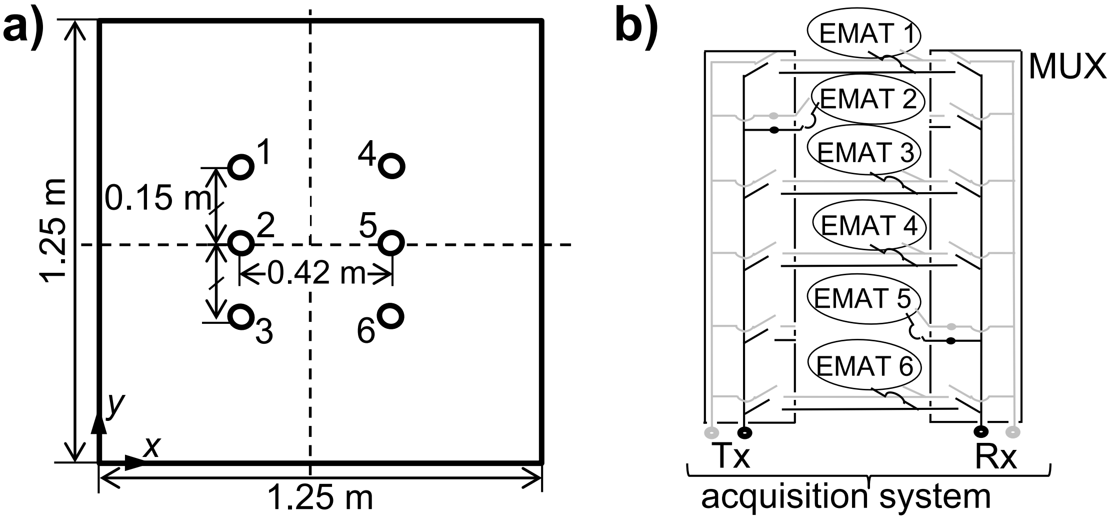

Figure 6.6: (a) The array configuration on the 2 mm thick steel plate, (b) schematic of the wiring between the coil electrodes (grayscale), the multiplexer, and the acquisition system (Figure 6.3(a)) with connections shown to use EMAT 2 as Tx and EMAT 5 as Rx.

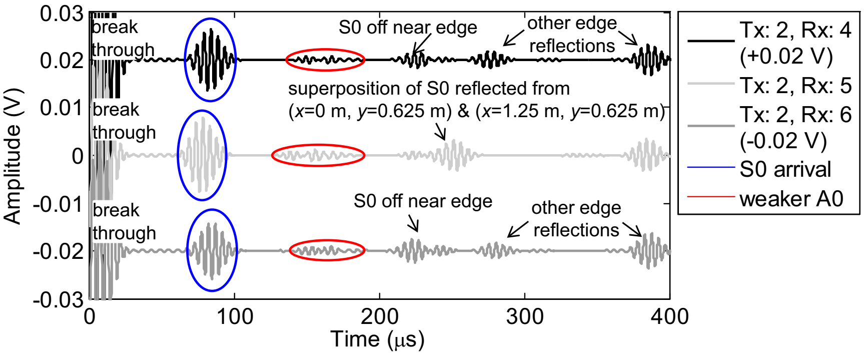

Figure 6.7: Pitch catch signals obtained by excitation of Tx 2 with 2^8 long Golay coded sequences of 5 cycle Hanning windowed tonebursts with centre frequency of 200kHz and processing data saved at the receiving EMATs.

In order to evaluate how the temperature related variability affects the ability to detect defects, residuals were computed using the pitch catch signals. In particular, the pitch catch signals at 20°C were used as baselines and the pitch catch signals collected at the other temperatures were subtracted from optimally stretched versions of the baselines. Example residuals are shown in Figure 6.9(a) and Figure 6.9(b) for cases corresponding to temperature differences δT of 0.25°C and 5°C respectively. The amplitudes of the residual is less than -40 dB when there is little temperature discrepancy (i.e. δT=0.25°C.) The amplitudes of the residual do exceed -35 dB at the S0 arrival and around 200-250 μs in Figure 6.9(b) when there is larger temperature discrepancy (i.e. δT=5°C.)

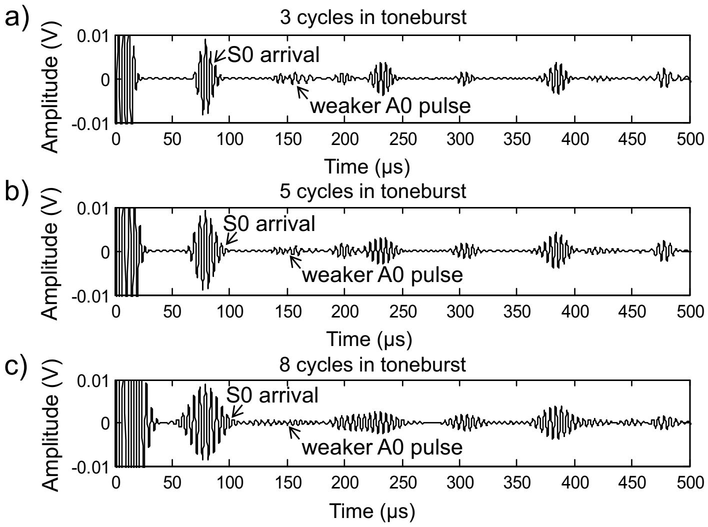

Figure 6.8: The pitch catch signals computed with data acquired using sensor pair Tx 3 - Rx 6 and when there are (a) 3, (b) 5, and (c) 8 cycles in the toneburst of inputs.

The maxima of the residuals over the indicated time gates at the S0 arrival and the A0 arrival were tracked from the processed array data in order to consider the effects that changing δT has on amplitudes of residuals; the time gate used for the A0 arrival is larger because of its dispersive characteristic. The maximum values of the tracked quantities are plotted in Figure 6.9(c)-(d) for the two modes. The results show that the residual amplitude at the S0 arrival and the A0 arrival correlate with relative temperature difference as expected [35, 85]. The amplitudes of the residuals are on the order of -40 dB when compensating and subtracting two signals acquired at a relative temperature difference of 0.25°C. Thus, a spacing of 0.25°C between baselines was used to acquire baseline sets, and the monitoring experiment commenced afterwards.

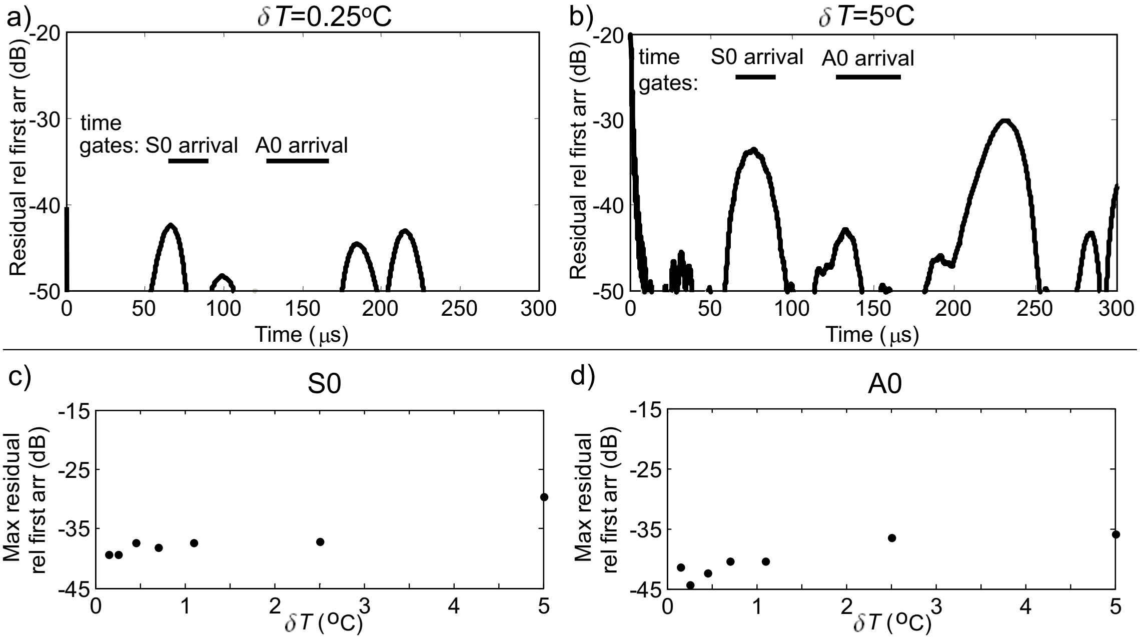

Figure 6.9: The residuals resulting from subtraction between pitch catch signals acquired at (a) 20.25°C and (b) 25°C and optimally stretched versions of a baseline acquired at 20°C using sensor pair Tx 3 - Rx 6 and the maxima of the maximum amplitudes of residuals within the indicated time gates of (c) the S0 mode and (d) the A0 mode as a function of δT from processed array data; 2^8 long Golay coded sequences of 5 cycled, 200 kHz tonebursts of 20 Vpp were applied to Tx and 150 averages were used to save received signals.

6.3.2 Monitoring results

SHM data was collected using the sensor array of Figure 6.6(a) while cycling the steel plate using the thermal profile of Figure 5.1(c) that was adopted in testing the bonded PZT sensors. All pitch catch signals were obtained using the signal excitation, data acquisition, and processing strategies described in Section 6.2.2. An initial set of pitch catch signals were obtained at steps of 0.25°C throughout the -5°C to +40°C range in order to form a baseline database. The plate was then cycled in the range from 15-35°C as shown in Figure 5.1(c) and current signals were obtained at 15, 25, and 35°C in each cycle. All the pitch catch signals were multiplied by a cosine tapered window that is shown in Figure 6.10 in order to gate out the portion of the breakthrough in each time trace. The windowed current signals were processed with the temperature compensation methods of Section 3.4.1 before computing residuals in order to analyze the long term stability of the EMATs and the baseline subtraction damage detection approach.

Figure 6.11(a)-(c) superimposes representative residual signals at 25°C which were calculated with data obtained using EMATs separated at distances of 0.42 m, 0.46 m, and 0.52 m respectively. Subsets of residuals are shown for the purposes of clarity though similar features were evident in the results from analysis of the full set of collected data. The maxima of the plotted residuals are on the order of -40 dB for processed data obtained at low thermal cycle numbers. The results show there are increases in amplitudes of residual signals from their initial level at various progressions in the monitoring period. The most consistent increases in the amplitudes of the residuals are those observed in the regions of the signals at points preceding the first S0 arrival. Note that the amplitudes of the residual in the plot of Figure 6.11(c) exceed -30 dB at the S0 arrival and near 400 µs after the plates have been exposed to greater than 140 thermal cycles. It is not clear why the residual tended to be higher around this time and there was a great deal of scatter about the trend. Typical behaviour is shown in Figure 6.12 which shows the maxima and the average values of residual signals in the range between $t_{\text{1st arr}}$ and the time for the reflection from the point involving the longest transmitter-edge-receiver path that were computed using data obtained with sensor pair Tx 3 - Rx 6.

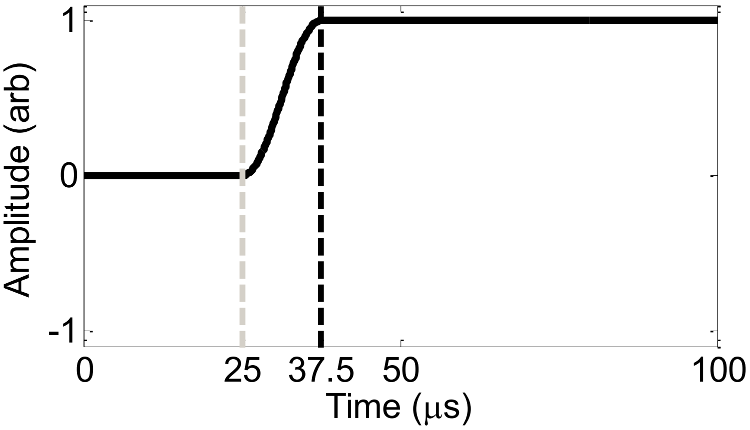

Figure 6.10: The window that was applied to SHM data collected using the EMATs in order to gate out the breakthrough and superimposed dashed lines showing start (gray) and end times (black) of cosine taper.

These statistical indicators are the same as those that were calculated for the processed data obtained with bonded sensors in Chapter 5. The trends shown in Figure 6.12 are representative of those observed in data collected with the vast majority of sensor pairs. The maximum amplitudes of residuals increase above levels associated with times immediately after baseline collection. The average values of residual amplitudes vary in a similar way as the maximum amplitudes of residuals though they exhibit less scatter. The slopes of linear fits that were applied to the average values of residuals as a function of thermal cycle number were obtained to evaluate quantitatively any long term changes. Slopes were computed from fits to the means of residual amplitudes rather than to the maxima of residual amplitudes in order to obtain values which could be compared to the drift rates of Chapter 5. The median value of the slopes for all of the processed array data was found to be 0.017 dB/cycle, which is the case that is shown in Figure 6.12. Rates of 0.006 dB/cycle and 0.026 dB/cycle were the 25th percentile and 75th percentile values respectively. Note that 0.017 dB/cycle is lower than the median drift rate of 0.023 dB/cycle which was calculated using the data obtained with PZTs bonded using the most stable adhesive (and nearly equals the 25th percentile value of the drift rate associated with this adhesive.) This confirms greater relative stability can be obtained with the low voltage EMATs.

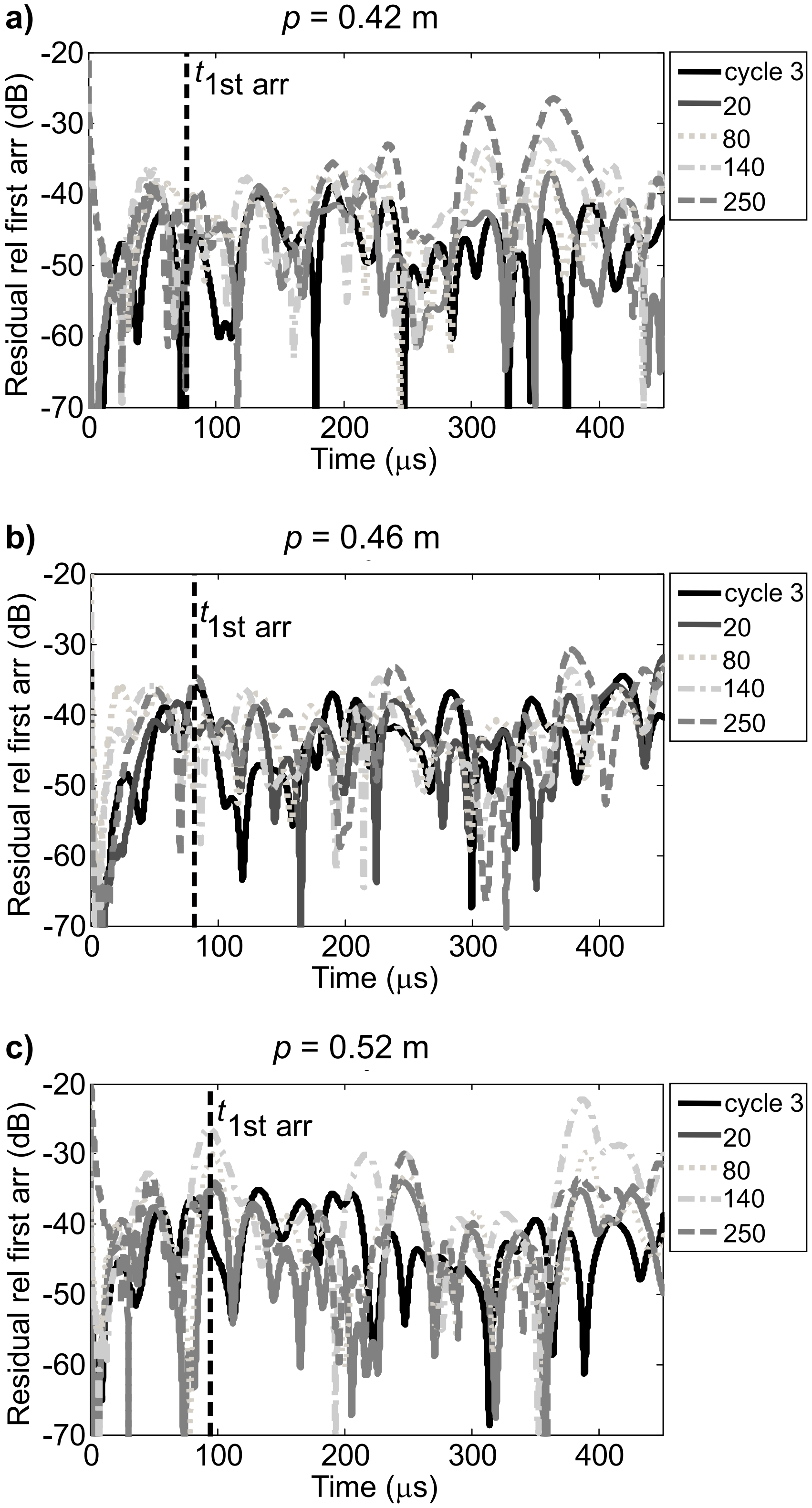

Figure 6.11: Compiled residuals obtained using data from sensor pairs (a) Tx 3 - Rx 6 (0.42 m separation between Tx and Rx), (b) Tx 3 - Rx 5 (0.46 m separation between Tx and Rx), and (c) Tx 3 - Rx 4 (0.52 m separation between Tx and Rx.)

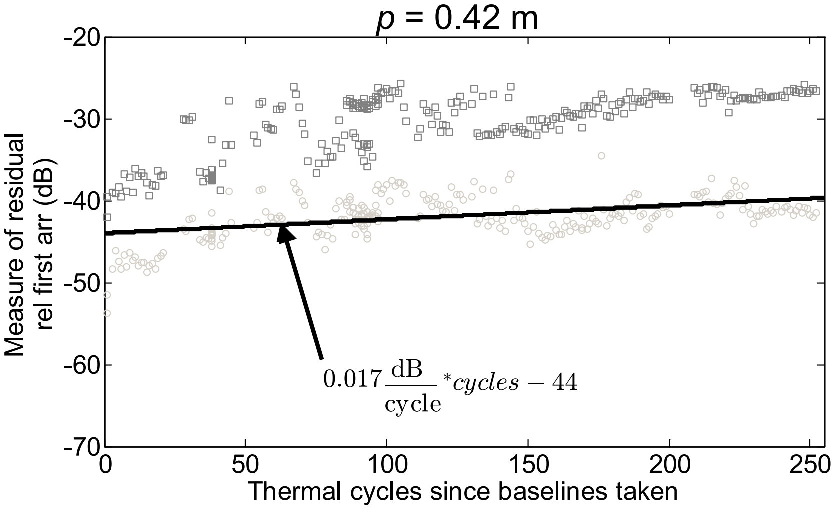

Figure 6.12: The maxima of residuals (□), mean values of residuals in the range between $t_{1\text{st arr}}$ and the time for the reflection from the point involving the longest transmitter-edge-receiver path (○), and linear fits to mean values of residuals (solid black line) evaluated using processed data obtained with sensor pair Tx 3 - Rx 6.

The residuals for the array that were computed after compensating data for thermal effects using the full set of baselines were then combined using the ellipse imaging algorithm of Section 3.4.2. The images were generated in order to determine the significance of the results for the long term monitoring capabilities of the SHM system. Figure 6.13(a)-(c) shows a typical subset of images on the same [-45,-30] dB scale that were calculated after processing the data obtained at times indicated in the column labels. The image intensities have amplitudes which are largely below -40 dB (blue) though there are artefacts at various points in the images for temperatures across the tested range (15-35°C.) Most of the artefacts appear intermittently though those in a ring near the points at the edges of the damage-free plate exhibit increasing amplitudes in the progression of the monitoring experiment. These results show that imaging effectively spatially averages the residual signals so that small defects can be detected in areas away from the edges of the plate over longer monitoring periods. The results suggest that changes due to scattering from defects which are on the order of -40 dB can potentially be detected.

The statistics which were computed for the area of the images of Chapter 4 were also calculated for the same area of the images that were generated using the processed EMAT data. The area considered corresponds to that dashed in Figure 6.14(a). The mean $\bar{I}$ of pixel intensities in the indicated area as well as the maxima of I

were tracked as a function of monitoring time. The plots in Figure 6.14(b)-(c) show statistics computed for images generated with the EMAT data which were collected at 25°C; note similar results were obtained at the other test temperatures though only the results at this temperature are shown for brevity. The results do not show any obvious trends in pixel intensities over the longer monitoring period. The mean of pixel intensities which are shown in Figure 6.14(b) do fluctuate between -52 dB and -46 dB throughout the test period. The maximum amplitudes of pixel intensities shown in Figure 6.14(c) remain below -40 dB for the duration of the experiment. These results confirm that the SHM system is sufficiently stable so that small defects (representing ~1.5% reflection change) can be reliably detected in regions where there are no strong reflectors. This capability is better than what has been demonstrated with PZTs, and suggests that guided wave SHM systems for longer term use can be potentially developed using EMATs.

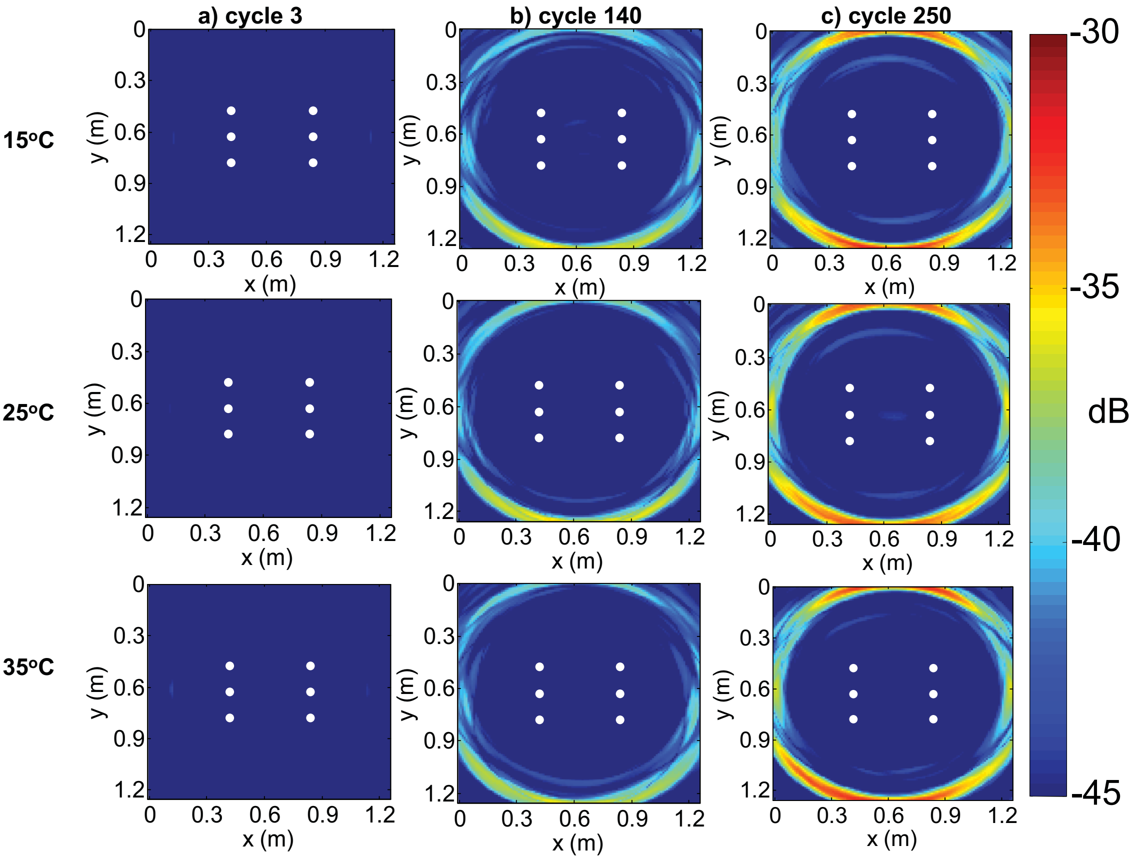

Figure 6.13: Images of the plate generated using the ellipse algorithm and all of the residuals from processed array data after exposure of specimens to (a) 3, (b) 150, and (c) 250 thermal cycles. Temperatures at which data were acquired are indicated on the left for each row of images and sensor locations are shown using white circles.

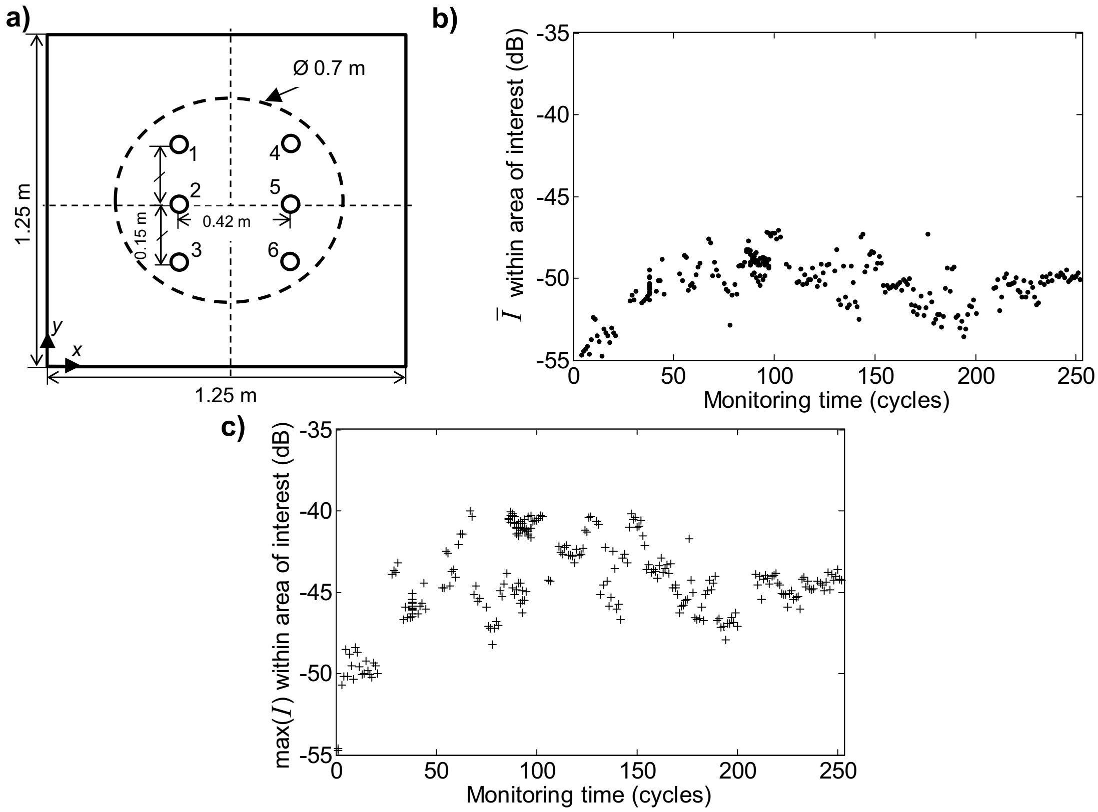

Figure 6.14: (a) The plate with the sensor array and dashed region for which statistics of pixel intensities I were computed, (b) the mean values $\bar{I}$, and (c) the maximum values of I computed for images generated using data collected at 25°C plotted as a function of monitoring time.

6.3.3 Variability analysis

An investigation was used to quantitatively study the variability affecting the SHM data from different sensor pairs. For these purposes, signal-to-random-variability ratios (SRVR) were computed as defined in Section 5.2.3 using the raw current signals and relevant optimal baselines. The percent change in SRVR relative to the initial values are plotted as a function of monitoring time in Figure 6.15(a); a subset of the results which were computed using the test data obtained at 25°C are shown and the percent change in values are plotted in order to highlight key characteristics and facilitate comparisons of trends for pairs for which values are different respectively. The plot shows that the SRVR indicator generally declines. The Hilbert envelope based amplitudes of the breakthrough and the wavepacket at the S0 arrival were also tracked. Figure 6.15(b)-(c) shows the tracked amplitudes of the breakthrough signal and those of the wavepacket at the S0 arrival relative to the initial values as a function of monitoring time. The results indicate that the breakthrough amplitudes exhibit large changes while the amplitudes of the S0 arrival remain predominantly stable. These findings confirm that the SRVR declines are due to increased variability in the portions of signals preceding the arrival of the fastest guided wave mode rather than changes in S0 arrival amplitudes. The changes must be due to electromagnetic influences. As any signal in the region before the fastest guided wave arrival does not contribute to delay-and-sum imaging produced with pitch catch data by definition, the variability in this portion of the data does not affect imaging results.

An analysis was used to study the variability which affects the amplitudes of the images at the points near the plate edges. For these purposes, signal-to-coherent-variability ratios (SCVR) were computed in the vicinity of the arrival of the S0 reflection from the edge involving the minimum propagation distance for each sensor pair (as in Section 5.2.3 again.) The percent change in the SCVR indicator relative to initial values are plotted as a function of monitoring time in Figure 6.15(d). The results show that there are declines in the SCVR indicator as is expected based on the finding that the pixel intensities increase at points near the plate edges in the images of Figure 6.13. Both SCVR and SRVR indicators show similar declines with increasing numbers of thermal cycles. These findings suggest that the variations which contribute to increases in the amplitudes of the pixel intensities near points at the edges in the imaging results of Section 6.3.2 may be reflective of effects that underlie SRVR variations as well.

The key finding of this section is that the SHM system exhibits stable monitoring capabilities compared to what is achieved using bonded PZTs. Research is necessary to determine what causes increases in the amplitudes of variability in portions of signals at which no mechanical waves are expected; these changes may prevent reliable defect detection near EMATs used in pulse/echo mode in particular. The pre-first S0 arrival changes indicate that EMI likely affected the performance of the SHM system. It is believed that these influences introduce the variations observed in values of SCVR at the near edge which contribute to the increased amplitudes of variability at points near the edges of the plate in the images of Figure 6.13. Thus, it is suggested that studies investigate aspects of the bespoke instrumentation which can be improved including the design of the multiplexer, the wiring and shielding of transducers, as well as the preampilifer in order to eliminate sources of variability and enhance the capabilities of this relatively stable SHM system.

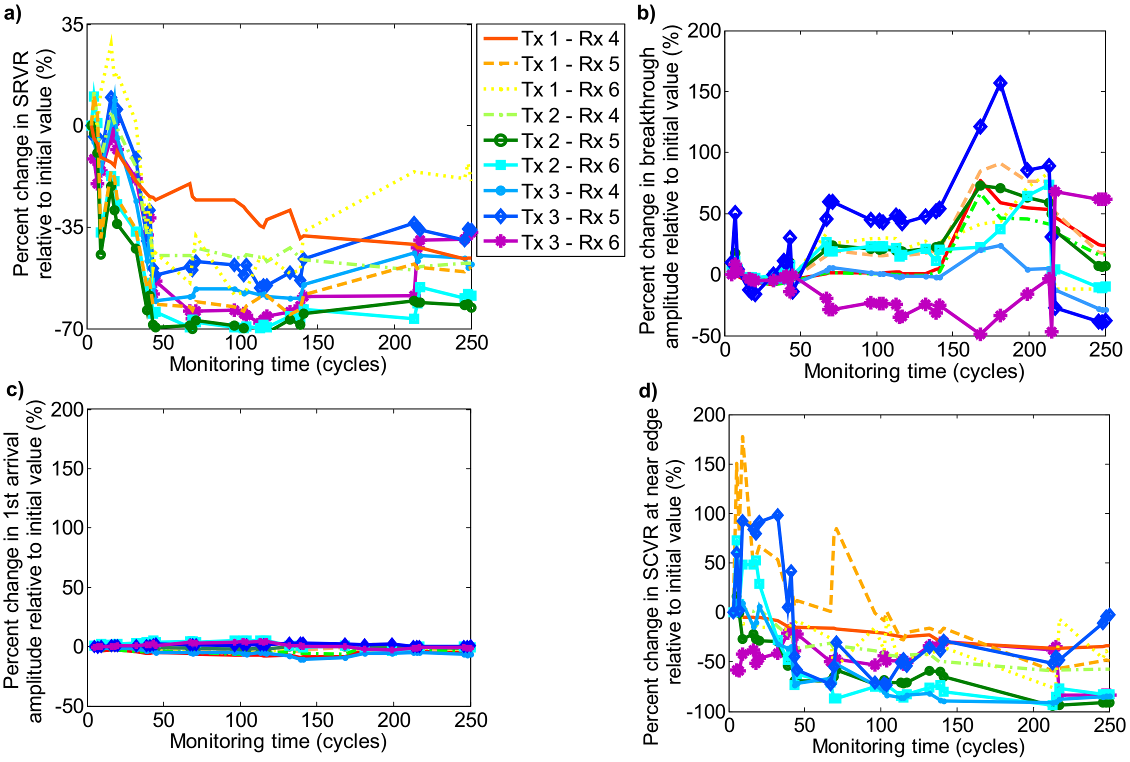

Figure 6.15: Percent change in (a) the SRVR indicator, the amplitudes of (b) the breakthrough signal and (c) the wavepacket at the first S0 arrival, and (c) the SCVR indicator in the vicinity of the S0 reflection from the edge that involves minimum propagation distance; all results are relative to initial values and are plotted as a function of monitoring time. Legend in (a) applies to all plots.

6.4 Summary

This chapter described an SHM system which uses EMATs operated at low voltages and cross-correlation approaches to obtain pitch catch signals. Data was collected using an array of the prototype EMATs on a 2 mm thick steel plate, and post-processed using subtraction based methods in order to assess the monitoring capabilities of the SHM system. The results from monitoring the plate while it was exposed to >250 thermal cycles over 150 days indicate that 50% of the sensor pairs consisting of EMATs achieve better performance than is realized with nearly 75% of the PZTs bonded using the most stable adhesive. Imaging results confirm that most increases in amplitudes of variability in the data are spatially concentrated near the edges of the plate. The exact source of this variability has not been established though it is evident that it is not a SNR nor coherent noise issue such as those that were found to affect the performance of bonded PZTs. The results do indicate that the SHM system enables reliable detection of reflection changes having amplitudes on the order of -40 dB over a central area of the plate in the long term. These demonstrations suggest the SHM system can allow reliable detection of small defects of the targeted sizes (signifying ~1.5% reflection change) in structures containing sparse features. The findings indicate reasons to develop the transducers and instrumentation in order to better shield them against EMI, and that it would be worthwhile studying the monitoring capabilities of systems with more sensitive sensors that are designed to achieve higher S0 mode selectivity.

Chapter 7

Conclusions

7.1 Thesis review

This thesis studied the long term capabilities of guided wave SHM systems designed to detect small damage in plate-like structures. The monitoring techniques that were investigated are based on the use of guided ultrasonic waves which can propagate long distances and have energy distributed through the thicknesses of plate-like structures. These characteristics of guided waves imply that measurements of their propagation enable sensitivity to small defects such as holes with few low power sensors at remote locations, a capability that other SHM techniques cannot achieve. As there are various practical ways of generating guided waves as well as sensing and processing signals of their propagation in order to detect damage, this research focused on researching the reliability of guided wave based SHM.

The theoretical characteristics of the guided plate waves as well as techniques that enable detection of small defects are subjects which were reviewed in order to develop a guided wave SHM system for long term stability evaluations. The literature review indicated that it is easier to achieve coverage of larger areas of structures with fewer sensors if monitoring relatively non-dispersive and omnidirectional wavefronts of a preferentially excited guided wave mode. It is feasible to generate omnidirectional waves of either fundamental Lamb mode. There is less directivity in the scattering patterns that result from the interaction of non-dispersive waves of the S0 mode with structural features and small holes which are among the defects of concern in this thesis. In addition to this advantage, the S0 mode exhibits less sensitivity to thermal variations than the A0 mode. These characteristics imply monitoring S0 waves would more likely enable detection of small hole type defects at unknown locations in real structures experiencing environmental variability. The desired goal of detecting damage at arbitrary locations can be facilitated through the use of sparse arrays of sensors operated in pitch catch mode. The data collected at the sensors can be processed using baseline subtraction based methods in order to achieve identification of damage in structures experiencing environmental changes.

The findings from Chapter 2 which are summarized above indicate that monitoring S0 wave propagation with sparse sensor arrays are advantageous to exploit in practice. However, there are concerns about the robustness and reliability of guided wave SHM systems which must be addressed before they are industrially adopted. Therefore, it was decided to implement and study the longer term use of two SHM systems which rely on monitoring omnidirectional wavefronts of the S0 mode using distributed transducers operated in pitch catch mode. Bonded PZT sensors and a conventional approach to data acquisition were used in one SHM system, and another consisted of low voltage EMATs operated according to procedures which enable collection of high SNR signals. In the use of either SHM system, the transducers were used to collect baselines with the structures placed in an environmental chamber. The baselines and the algorithms of Chapter 3 were used to compensate monitored data for thermal effects and compute the baseline subtraction results with which the stability of the SHM systems were assessed.

Prior to testing the SHM system that consisted of bonded PZTs, it was necessary to develop sensors so that they could generate strong waves of the S0 mode compared to the unwanted A0 mode on plates of the thicknesses desired in the applications. Chapter 3 discusses the development of the selective S0 mode transducers as well as encapsulations designed to weatherproof and strain relief the electrical connections to the PZTs. The encapsulated sensors were bonded to a 5 mm thick anodized aluminum plate, and used to the monitor the structure in an outdoor environment over a monitoring period exceeding 9 months as described in Chapter 4. The tests revealed robustness issues that cause weakening of the sensor bonds. The findings provided the motivation for the systematic assessments of the effects that adhesive choice and thermal cycling have on baseline subtraction stability that were undertaken in Chapter 5.

Chapter 6 describes the SHM system consisting of low voltage EMATs which was evaluated primarily because it consists of transducers which do not need to be bonded. A description is provided of the data acquisition procedures and how they are used with low voltage electronics in order to collect guided wave signals of sufficiently high SNR for SHM purposes. The potential of the monitoring system to allow detection of small defects signifying ~1.5% reflection change is analyzed. Finally, the chapter concludes with findings from a study in which a sparse array of EMATs is used to monitor a 2 mm thick steel plate exposed to thermal variations which demonstrate the long term stability of the SHM system.

7.2 Findings

The work presented in this thesis contains results which are useful for developing guided wave SHM systems for monitoring safety critical plate-like structures over longer periods of their service lives. The long term stability of two different transduction mechanisms will be separately discussed. The findings about guided wave SHM systems which use bonded PZT sensors will be summarized before highlighting the key results from the evaluations with the low voltage EMATs.

7.2.1 Bonded piezoelectric sensors

Encapsulated versions of bonded ⌀ 20 mm PZT discs having thicknesses of 0.5 mm and 1 mm were developed in order to strongly excite waves of the S0 mode (relative to the A0 mode) in 2 mm and 5 mm thick aluminum plates respectively. Results confirmed that exciting the PZTs with tonebursts of centre frequencies at which $\lambda_{A0}^{(3D)} \simeq 20$mm enables the best suppression of the unwanted A0 mode. It was found that amplitudes of the S0 wavepackets in pitch catch data collected using the bonded sensors exceed those of the weaker A0 pulses by ≥20 dB. Furthermore, the encapsulations were shown to be effective for strain relieving and waterproofing the electrical connections to the PZTs and they did not change guided wave transduction. In particular, only small amplitude variations and negligible phase change were observed in pitch catch signals when comparing results to those obtained using unencapsulated PZTs. Experiments in which pitch catch signals were monitored with the bonded transducers and processed with the temperature compensation strategies confirmed that the implemented SHM system enables effective suppression of variability associated with 0.5-2°C temperature change as well as reliable detection of a ∅ 5 mm through hole drilled on a 2 mm thick, 1.25 m square aluminum plate.

A sparse array of the encapsulated PZTs was used to monitor a 5 mm thick anodized aluminum plate, and results indicated that the amplitudes of variability in SHM data increase over time. The deterioration in monitoring capabilities was attributed to signal amplitude declines and associated SNR decreases. Impedance readings, ultrasonic c-scans, and inspections of exposed transducer bonds confirmed the development of total and partial disbonds at the sensor electrode-adhesive interface. The results indicated that a special adhesive as well as reliable attachment practices need to be found before the bonded PZT sensors can be used in outdoor evaluations.

Experiments were used to determine the long term stability in defect detection capabilities achievable with four different structural adhesive systems. The results from monitoring thermally cycled plates over extended periods indicated that the use of two component adhesives which had higher glass transition temperatures lead to some improvements in the long term stability of the SHM system. However, increasing variability showed that it was impossible to achieve reliable detection of 1.5% reflection change with the baseline subtraction approach after specimens had been exposed to 250 thermal cycles. A combination of thermal damage and physical ageing effects were thought to affect the results, and FE models of the transducer were used to establish that SHM data could be influenced by changes in the properties of the adhesives used to bond PZTs to plates. The results of the simulations as well as experimental tests on bulk adhesive samples indicated that adhesive modulus changes are a major source of the variability in the SHM data. The tests indicated that changes in v_L on the order of 4% can be encountered after > 170 thermal cycles, and the amount of variability in the bulk properties of adhesives correlated with the losses in SHM performance of PZT sensors bonded using the same epoxies. The FE results also indicate that the quantified changes in bulk properties of the adhesives contribute significant variability to SHM data.

7.2.2 Low voltage EMATs

The feasibility of using previously designed EMATs operated at low voltages in an SHM system was demonstrated in Chapter 6. The excitation of the EMATs with low voltage inputs consisting of encoded tonebursts and post-processing of signals acquired at receiving EMATs with cross-correlation approaches was shown to enable recovery of pitch catch data having sufficiently high SNR for monitoring purposes. An array of the low voltage EMATs was used to monitor a 2 mm thick, 1.25 m square steel plate and demonstrated that detection of 1.5% reflection change can be achieved using the SHM system. Imaging results showed that the system continuously enables reliable detection of 1.5% reflectors anywhere on the plate except at the edges during a period when the plate was exposed to more than 250 thermal cycles. Analysis of the data confirmed that there were increases in the amount of variability within time gates surrounding the group velocity based arrival time of the first S0 edge reflection in waveforms. The source of the variability which affected the SHM data could not be determined. However, similar trends of variability were observed in the portions of signals preceding the first guided wave arrival, which are thought to be due to EMI. Overall, the studies with the prototype SHM system that uses low voltage EMATs confirmed that it exhibits better long term stability compared to the monitoring system which uses bonded PZTs, and indicate it is worthwhile designing shieldings for the transducers and improving the acquisition electronics in order to reduce EMI and improve the signal fidelity.

7.3 Implications for SHM R&D

The findings have implications for research and development into guided wave SHM systems that are to reliably detect small defects or those that grow slowly during the operation of plate-like structures.

A stable adhesive and practices which ensure enhanced robustness of bonds must be found in order for it to be reliable to use strategies based on subtraction of guided wave signals sensed using bonded PZTs to monitor structures over their operational lives. Quantified losses in defect sensitivity levels that were attributable to the weakening of bonds exposed to weather and changes in the properties of the adhesives subject to thermal cycling are expected to be greater with harsher operational exposures (e.g. sensor fatigue and effects at higher altitudes [121, 124].) Research must ensure consistent control of adhesive-dependent properties can be achieved for a range of environmental conditions as a result. The search for a sufficiently stable adhesive may entail significant trial and error and there need to be consideration that variable performance can result with discrepancies between exposures in the lab and those experienced in practice.

The results shown in experiments with EMATs exposed to thermal cycling loads indicates the relative stability of the transduction mechanism and its feasibility to allow detection of defects of targeted sizes at points away from plate edges over long periods. These findings suggest it may be comparatively efficient to pursue research and development into EMATs to expand upon the reliable capabilities demonstrated using the prototype monitoring system. In order to increase the applicability of developed technology for applications in which EMI [18] and mode conversions at features are known to be prevalent [50, 52], the sensitivity of transducers to electromagnetic interference should be limited and the selectivity to the mode being monitored must be enhanced. The specific research tasks viewed as essential to improve the reliability of monitoring systems studied so they become practical for SHM of structures in operating environments are described as suggestions for future work in the next section.

7.4 Suggestions of future work

Future work should be directed toward implementing and testing SHM systems for use in the operational conditions that structures are expected to encounter. In order to enhance the stability of SHM systems that use bonded PZTs, it is necessary to use monitoring trials so that an adhesive is selected which is more stable than those tested in this work. Research should investigate techniques to improve on methods used to bond PZTs. Additionally, an approach can be used to develop damage detection algorithms which incorporate compensation for the effects that ageing of adhesives have on SHM data collected with bonded PZTs; it is suggested to use modeling to determine the effects on transduction (as done in Chapter 5) in order to design intelligent processing methods. The findings of the thesis indicate that the SHM system which uses EMATs is relatively stable and suggest that it would be preferable to develop the use of this transduction mechanism in order to make it more viable for industrial usage. Thus, most of the rest of this section discusses suggestions to develop the SHM system which uses low voltage EMATs.

The major concern with the use of EMATs is their sensitivity to EMI which needs to be shielded against in order to eliminate sources of variability which affect SHM data. It would be worthwhile studying the performance benefits which can be realized by designing appropriate shieldings for the transducers such as those made of mu-metal (whose high magnetic permeability can be exploited to redirect magnetic fields away from the coils of receiving EMATs.) It is also suggested that studies be used to determine how the designs of the acquisition instrumentation can be improved in order to ensure more consistency in measurements. Tests can be used to assess whether it would be worthwhile using twisted pair wiring in the prototype multiplexer or researching strategies to reduce chattering in the reed relays. Other modifications to the acquisition hardware can be used to enhance the capability to accurately resolve small changes in pitch catch data obtained using the data acquisition procedures. In particular, a device can be used which has a larger memory capacity than the Handyscope (HS3, Tie Pie Engineering Ltd., NL) in order to use longer sequences and realize benefits such as the ability to recover smaller amplitude signals of higher fidelity (and eliminate the need to use time averaging in saving received signals of sufficiently high SNR.) The preamplifier could also be redesigned to have an input impedance that more closely matches that of the EMAT coil so that the sensitivity of the sensors can be improved.

There are other issues which would need to be researched in order to make SHM systems based on the use of EMATs more practical than the prototype system that was evaluated. Firstly, EMATs similar to those tested can be readily deployed on steel structures in the oil and gas industry though novel attachment strategies must be researched to develop sensors that are to be used for monitoring aluminum structures (such as those commonly found in the aerospace industry.) The transducers and acquisition electronics must also be adequately miniaturized in order for them to be useable in industrial applications. Finally, the EMATs which were tested in this work were not designed to generate the S0 mode as selectively as the bonded PZT sensors. As studies have confirmed that monitoring capabilities are enhanced by increasing the transducer selectivity to the mode being monitored, it is important to determine the performance that can be achieved with the use of EMATs optimized to achieve higher S0 mode selectivity. Recent research indicates that the use of numerical optimization procedures may be particularly beneficial for realizing transducer designs in an efficient manner [98].

There are other challenges which need to be addressed in making SHM systems for industrial use irrespective of the particular transduction mechanism which is developed. A major issue is that it would be impractical to disassemble and place many of the structures in the aerospace and shipping industries in environmental chambers. Therefore, it is necessary to develop the capability to collect sufficient baseline signals with deployed SHM systems in practical contexts. It may be possible to increase the efficiency of algorithms such as those conceptualized in [68] in order to autonomously collect baselines. However, it may be necessary to develop new strategies so that baselines can be obtained more rapidly than currently possible or in order for monitoring evaluations to be performed using methods which do not require baselines (as are being developed in a project involving collaboration between BP and the NDE Group at Imperial College London.) Also, guided wave SHM has been shown to enable detection of holes and notches at locations far from where structural features are located. However, most industrial applications require capabilities to detect gradual damage which often occur at the interfaces between bolted or bonded parts of structures. It is encouraging that research has demonstrated that baseline subtraction based methods enable detection of a notch at a rivet hole. It would be worthwhile investigating the potential of extending capabilities to detect changes such as crack growth and nonuniform material degradation at features which significantly affect most safety critical structures. Demonstrations of progress on the issues that have been described can make guided wave SHM technologies more viable for use in practice.

Appendix A

Material properties

A.1 FE modeling

Table A.1: Mechanical properties of non-piezoelectric materials from [142]; *Young's modulus of a material is real valued if loss factors is indicated as N/A.

Material	Young's modulus magnitude* (GPa)	Density (kg m^{-3})	Poisson's ratio	Loss factor
aluminum	73	2780	0.333	N/A
epoxy	2.8	1200	0.345	0.3
HDPE	1	950	0.42	N/A

Table A.2: Properties of the PZT from [152].

Property (Units)	Value
Density (kg m^{-3})	7700
c_{11}^E (10^{10} N m^{-2})	14.7
c_{33}^E	11.3
c_{12}^E	10.5
c_{13}^E	9.37
c_{44}^E	2.3
c_{66}^E	2.12
e_{11} (C m^{-2})	-3.09
e_{33}	16
e_{15}	11.64
ϵ_{11}^S (10^{-9} C V^{-1} m^{-1})	9.99
ϵ_{33}^S	8.10

A.2 SPECTRUM simulations

Table A.3: Material properties from [39, 152].

Material	Density (kg m^{-3})	v_L (m s^{-1})
water	1000	1483
aluminum	2700	6320
epoxy	1200	1915
PZT	7700	4510

Appendix B

First radial resonance frequency of bonded PZT discs

A bonded ∅ 20 mm , 1 mm thick PZT disc was initially considered as the sensor to use for aluminum plates of varying thicknesses. In the case of the 2 mm thick plates, however, the FE studies of Section 3.3.2 indicated that it would be difficult to achieve off resonance transduction of selective S0 waves with this PZT. It was thought appropriate to exploit changing the disc thickness th_{PZT} and the expected effects [91] on the PZT stiffness so that the resonance may be shifted away from the frequency at which selective excitation of S0 (relative to A0) occurs (i.e. f_{null}^{A0} =100 kHz as described in Section 3.3.2.) The model of Figure 3.2 was used with ∅ 20 mm PZTs of various th_{PZT} bonded on 2 mm thick plates being excited by 1 V in order to simulate motions of discs. The magnitudes of the velocity responses obtained from motions monitored at the edge node on the PZT surface are plotted in Figure B.1(a). The resonance frequencies f_r were extracted from the plots at the points where the peak in each curve occurs and are shown in Figure B.1(b). These results show the inverse relationship between f_r and th_{PZT} for a bonded PZT of fixed diameter [91]. The 0.5 mm thick disc has f_r =145 kHz, which is far from 100 kHz. Thus this PZT was chosen for use on 2 mm thick aluminum plates in Section 3.3.2.

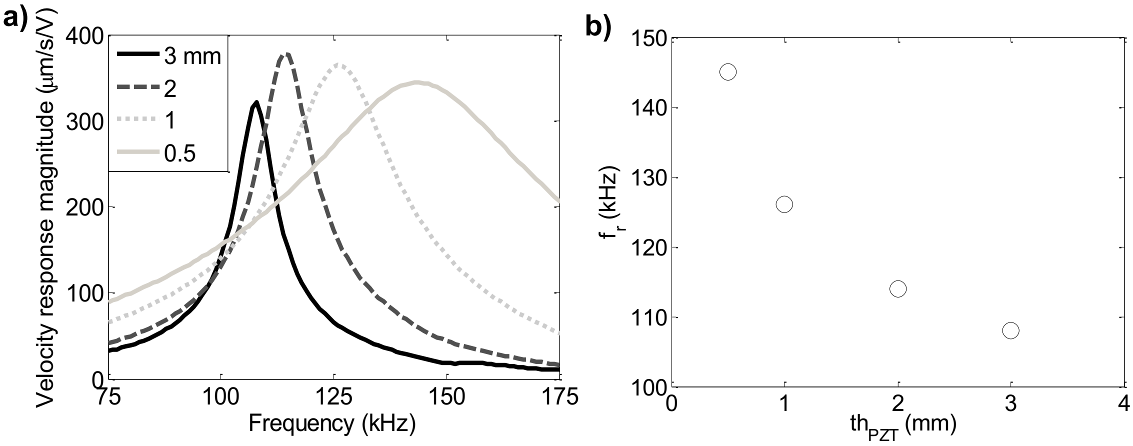

Figure B.1: (a) The magnitudes of the in-plane velocity responses of ∅ 20 mm PZT discs of thicknesses th_{PZT} bonded on 2 mm thick aluminum plates which were obtained from the simulated motions of the node on the circumference of the PZTs with 1 V excitation of them and (b) the extracted resonance frequencies f_r as a function of th_{PZT}.

Appendix C

Correcting data for signal changes in the pulse at the S0 arrival

A signal $W(t)$ containing a Tukey window with a flat section as long as the temporal length of the 8 cycled, 170 kHz input toneburst and 1 cycle long tapers was centered at the Hilbert envelope detected arrival time of the first S0 pulse in each monitored guided wave signal of Chapter 4. $W(t)$ and each of $c(t)$ and $OB(t)$ were multiplied in order to isolate the S0 wavepackets of interest. The spectrum of the gated S0 wavepacket in each optimal baseline was divided by the spectrum of the gated S0 wavepacket in each current signal, and multiplied by the FFT of the current signal prior to computing the corrected time trace by application of an IFFT, i.e.

$$c_{TFcorrected}(t) = \mathcal{F}^{-1}\left(\frac{\mathcal{F}(W(t)OB(t))}{\mathcal{F}(w(t)c(t))}\mathcal{F}(c(t))\right). \tag{C.1}$$

This procedure enabled correction of wave shape changes with low leakage of power at frequencies outside the input bandwidth [104]. Residuals were computed with the corrected current signals in a similar manner as for the original current signals, and images were generated using the ellipse algorithm described in Section 3.4.2. The mean $\bar{I}_{TFcorrected}$ of pixel intensities in the area bounded by the sensors was computed and tracked values of it are plotted (gray points) as a function of monitoring time in Figure C.1. This plot also superimposes the results (black points) that were obtained as described in Section 4.3.3. The correction of data results in nearly 6 dB reduction in the amplitudes of the residuals toward the end of the monitoring period.

Comparing the linear fits to the original, $\hat{I}$, and corrected, $\hat{I}_{TFcorrected}$, mean pixel intensity values suggests that detection sensitivity may improve more generally by 3 dB however; e.g. compare the offsets (43 vs 46 dB) in the fit equations of Figure C.1.

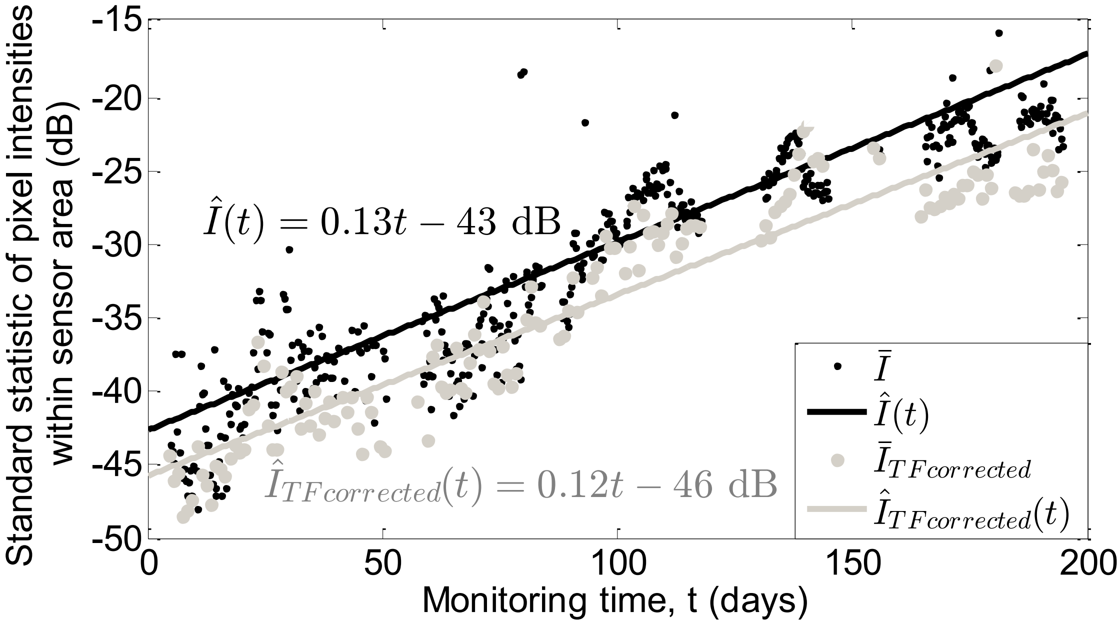

Figure C.1: The mean values $\bar{I}$ of I within the area surrounded by sensors and the corresponding values $\bar{I}_{TFcorrected}$ in gray from images generated using the residuals computed with the data corrected using Equation C.1. Lines are the linear fits applied to the mean values with each data.

Appendix D

Sensitivity of pitch catch data to the properties of the bond between PZTs and a plate

Section 5.3.2 described how simulations with an axisymmetric model of a transducer that is shown in Figure 3.2 were used to study how SHM data could be influenced by changes in the properties of the bond between transmitting PZTs and plates. In order to consider the additional changes that variations in the properties of the bond line of receiving PZTs can produce in pitch catch signals, FE analysis was undertaken using the plane strain models shown in Figure D.1. In particular, Figure D.1(a) shows the model of a transmitting PZT bonded to a plate and the point at which strains were monitored. Figure D.1(a) shows a model of a pair of bonded sensors, and the nodes on the receiving PZT at which voltages were monitored. Square CPE4R elements were used to mesh the plate and epoxy parts while square CPE4E elements were used to mesh PZTs. All parts were assigned the material properties that were used in the models of Chapter 3 and Chapter 5. This section describes the outputs obtained using simulations with each model, and discusses the assessments that were used to determine the amplitudes of variability that changes in the properties of the bond line at a receiving PZT contribute to pitch catch data.

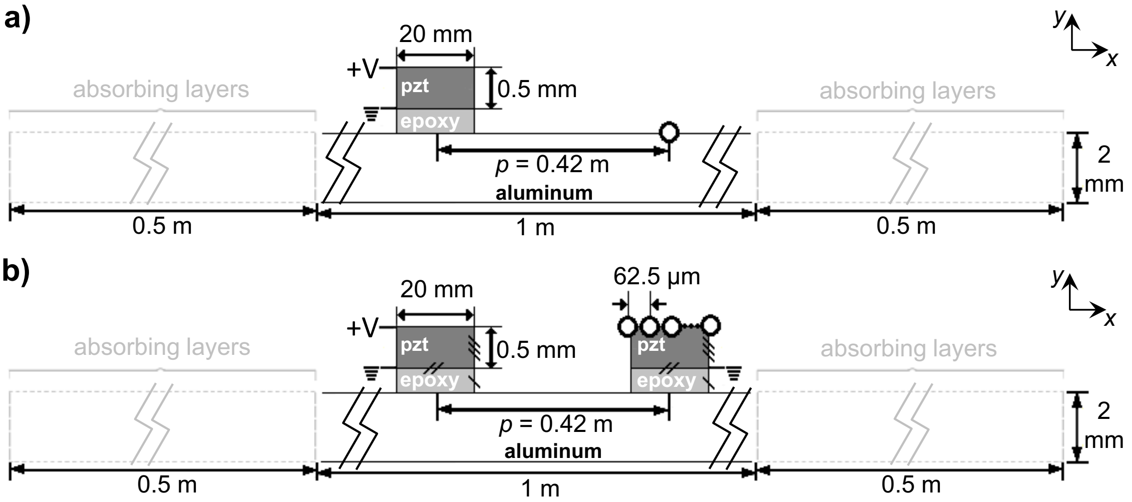

Figure D.1: (a) Plane strain model of a 0.5 mm thick, 20 mm wide transmitting PZT and 250 μm bonding layer on a 2 mm thick aluminum plate and (b) the model with a receiving PZT of the same dimensions included at the distance that matches the sensor pitch used in tests of Chapter 5. Monitoring points are indicated using hollow circles. All other designations signify the same parameters as do corresponding ones in Figure 3.2.

The outputs which were obtained from the FE models correspond to strain signals at the monitoring point in Figure D.1(a) and the potential difference resulting across the electrodes of the receiving PZT in Figure D.1(b). The procedures described in Section 5.3.1 were used to excite the transmitting PZT in both models. The same procedures and outputs from simulations involving the model in Figure D.1(a) were also used to calculate the desired strain signal $\varepsilon(t)$, an example of which is plotted in Figure D.2(a). In order to obtain the desired voltage signal at the receiving PZT in the model of Figure D.1(b), the voltage responses at each of the nodes on the surface of the receiving PZT are monitored. An inverse Fourier transform is applied to the monitored outputs. The resulting signals are summed in order to compute the received signal. The result corresponds to the waveform that is normalized by the maximum of the Hilbert envelope based amplitude and plotted in Figure D.2(b). The methods reviewed in this paragraph were adopted in order to calculate signals with simulations of each model in which the properties of epoxy are systematically perturbed as described in Section 5.3.1-Section 5.3.2.

The signals calculated from outputs of these simulations were subtracted from the relevant baseline signal obtained from simulations with each model having nominal properties. Figure D.3(a) plots the dB values of beam spread corrected results obtained from the simple baseline subtraction of the signals from simulations with the model involving the trasmitting PZT only. Figure D.3(b) contains the results from the simulations with the model in which the receiving PZT is included as well. Note that the amplitudes of variability associated with the 0.25°C temperature change is similar in both sets of results, and agrees with what is obtained in Chapter 5. On the other hand, the maximum amplitude of the results obtained with input changes to the dynamic moduli of the epoxy in the model of Figure D.1(b) consistently exceeds the maximum amplitudes in the results obtained from simulating the effects that epoxy moduli changes have on the strain signals by ~6 dB. This finding is expected according to transmit-receive reciprocity.

Residuals were also calculated by subtracting the signals simulated with each run of the perturbed models and optimally stretched versions of the baselines. The dB values of beam spread corrected residuals are shown in Figure D.4, and illustrate results obtained using post-processing of the outputs from the simulations with the codes which were used to process SHM data collected with the sensors. The maximum amplitudes of residuals calculated using voltage signals estimated using the simulations with the model of Figure D.1(b) exceed the maximum amplitudes of residuals obtained using subtraction of the strain signals by ~4 dB for each level of epoxy moduli variation.

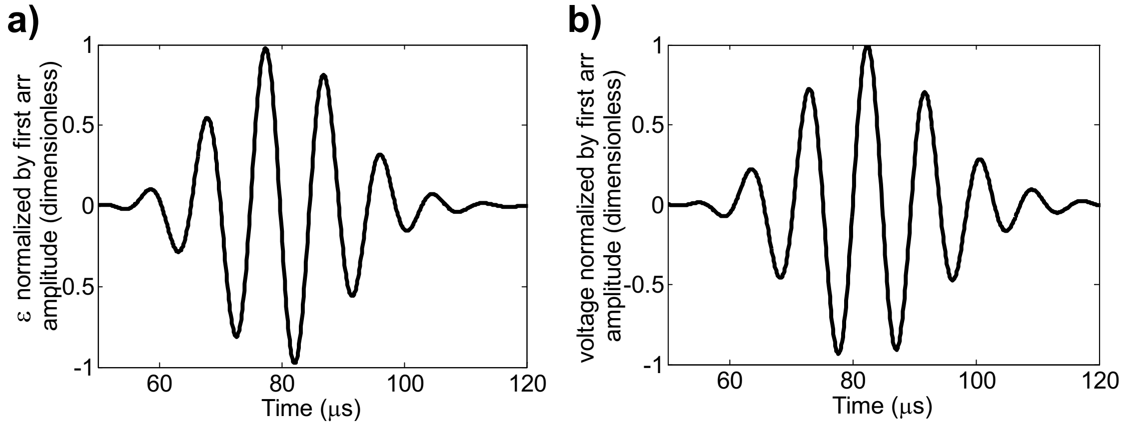

Figure D.2: (a) Strain signal $\varepsilon(t)$ of the S0 arrival at p =0.42 m which was estimated using outputs from simulations with the model of Figure D.1(a) and (b) the wavepacket at the S0 arrival in the received signal computed using monitored voltage responses from simulations with the model of Figure D.1(b); results are normalized to have unity amplitude.

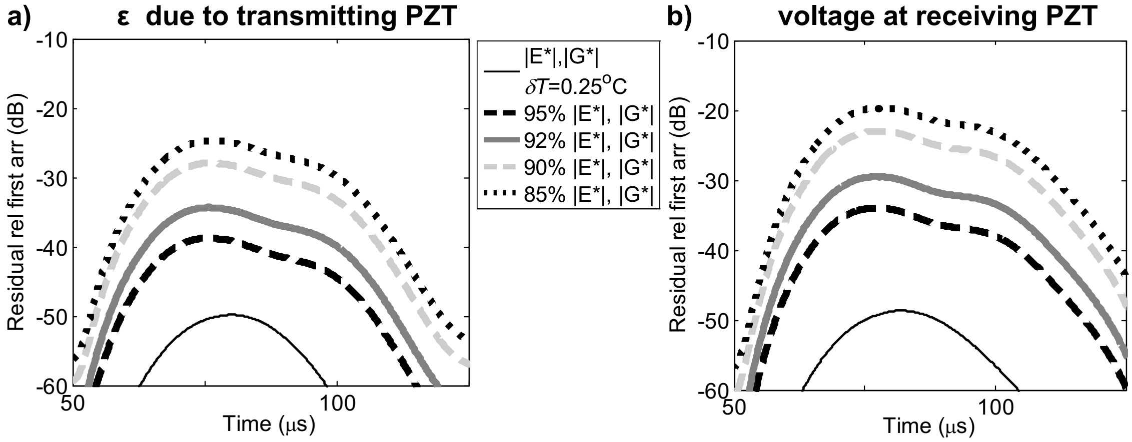

Figure D.3: (a) Results of subtracting the baseline signal computed using simulated outputs from the model of Figure D.1(b) and signals at δT =0.25°C and the signals calculated using outputs with indicated changes input to the epoxy moduli around the S0 arrival, (b) corresponding results computed using outputs from the model of Figure D.1(b).

The results confirm that changes in the properties of the bond line of a receiving PZT that is used to obtain pitch catch signals contribute variability of amplitudes ~4-6 dB greater than those in the strain field at the same distance due to the changes in the bond between the transmitting PZT and the plate.

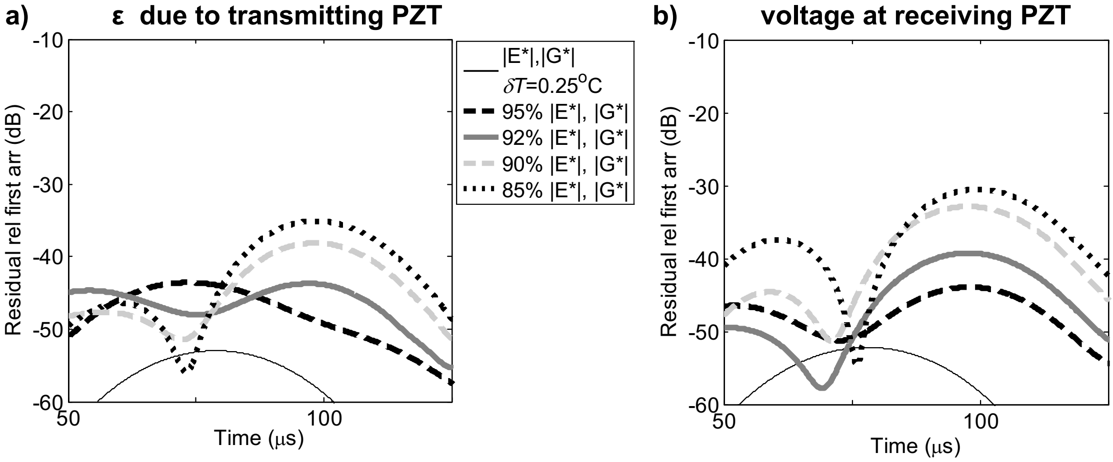

Figure D.4: The residuals computed by subtracting the same signals used in Figure D.2 from optimally stretched versions of baseline signals with simulated outputs from the model of (a) Figure D.1(a) and (b) Figure D.1(b).

References

[1] US DOD. *MIL-STD-1530C(USAF)*, 2005.

[2] W. Staszewski, C. Boller, and G. R. Tomlinson. *Health Monitoring of Aerospace Structures: Smart Sensor Technologies and Signal Processing.* Wiley, Chichester, 2004.

[3] LexTech Inc. *DTD Handbook, Handbook for Damage Tolerant Design*, 2010.

[4] C. Boller and M. Buderath. Fatigue in aerostructures - where structural health monitoring can contribute to a complex subject. *Phil. Trans. R. Soc. A*, 365(1851):561–587, 2007.

[5] H. Kapoor, C. Braun, and C. Boller. Modelling and optimisation of maintenance intervals to realize structural health monitoring applications on aircraft. In F. Casciati and M. Giordano, editors, *Proceedings of the Fifth European Workshop on Structural Health Monitoring 2010*, pages 55–62, Lancaster, PA, 2010. DEStech Publications, Inc.

[6] E. A. Lindgren, J. S. Knopp, J. C. Aldrin, G. J. Steffes, and C. F. Buynak. Aging aircraft nde: capabilities, challenges, and opportunities. In D. Thompson and D. E. Chimenti, editors, *Review of Progress in Quantitative Nondestructive Evaluation*, volume 26A, pages 1731–1738, Melville, NY, 2007. AIP.

[7] K. Ono. Structural integrity evaluation using acoustic emission. *Journal of Acoustic Emission*, 25:1–20, 2007.

[8] GDV. *Container Handbook (CHB).* GDV e.V., Berlin, 2013.

[9] S. L. Caldwall and T. M. Persons. Container security technologies. Technical Report GAO-10-887, US GAO, Washington D.C., 2010.

[10] H. Sohn, C. R. Farrar, F. M. Hemez, D. D. Shunk, D. W. Stinemates, B. R. Nadler, and J. J. Czarnecki. A review of structural health monitoring literature: 1996-2001. Technical Report LA-13976-MS, Los Alamos National Laboratory, Los Alamos, NM, 2004.

[11] A. Deraemaeker, E. Reynders, G. De Roeck, and J. Kullaa. Vibration-based structural health monitoring using output-only measurements under changing environment. *Mechanical Systems and Signal Processing*, 22(1):34–56, 2008.

[12] W. Fan and P. Qiao. Vibration-based damage identification methods: a review and comparative study. *Structural Health Monitoring*, 10(1):83–111, 2011.

[13] K. F. Voss and K. H. Wanser. Fiber sensors for monitoring structural strain and cracks. In A. McDonach, P. T. Gardiner, R. S. McEwen, and B. Culshaw, editors, *Second European Conference on Smart Structures and Materials*, volume 2361, pages 144–147. International Society for Optics and Photonics, 1994.

[14] S. Yashiro, T. Okabe, and N. Takeda. Damage identification in a holed cfrp laminate using a chirped fiber bragg grating sensor. *Compos. Sci. Technol.*, 67(2):286–295, 2007.

[15] A. Raghavan and C.E.S. Cesnik. Review of guided-wave structural health monitoring. *The Shock and Vibration Digest*, 39(2):91–114, 2007.

[16] M. R. Gorman and S. M. Ziola. Plate waves produced by transverse matrix cracking. *Ultrasonics*, 29(3):245–251, 1991.

[17] A. V. Bakulin, S. N. Isaev, and A. P. Tishkin. Acoustic-emission location of corrosion centers. *NDT & E Int.*, 27(4):217, 1994.

[18] R. K. Miller and P. McIntire. *Nondestructive Testing Handbook. Vol. 5: Acoustic Emission Testing.* American Society for Nondestructive Testing, Columbus, OH, 2nd edition, 1987.

[19] R. P. Dalton, P. Cawley, and M. J. Lowe. Propagation of acoustic emission signals in metallic fuselage structure. *IEE Proceedings Science, Measurement & Technology*, 148(4):169–177, 2001.

[20] M. R. Gorman. Some connections between ae testing of large structures and small samples. *Nondestructive Testing and Evaluation*, 14(1-2):89–104, 1998.

[21] O. Diligent, T. Grahn, A. Bostrom, P. Cawley, and M. J. S. Lowe. The low-frequency reflection and scattering of the s0 lamb mode from a circular through-thickness hole in a plate: Finite element, analytical and experimental studies. *J. Acoust. Soc. Am*, 112(6):2589–2601, 2002.

[22] P. Fromme and M. B. Sayir. Measurement of the scattering of a lamb wave by a through hole in a plate. *J. Acoust. Soc. Am*, 111(3):1165–1170, 2002.

[23] O. Diligent and M. J. S. Lowe. Reflection of the s0 lamb mode from a flat bottom circular hole. *J. Acoust. Soc. Am*, 118(5):2869–2879, 2005.

[24] F. B. Cegla, A. Rohde, and M. Veidt. Analytical prediction and experimental measurement for mode conversion and scattering of plate waves at non-symmetric circular blind holes in isotropic plates. *Wave Motion*, 45(3):162–177, 2008.

[25] M. J. S. Lowe, P. Cawley, J. Y. Kao, and O. Diligent. The low frequency reflection characteristics of the fundamental antisymmetric lamb wave a0 from a rectangular notch in a plate. *J. Acoust. Soc. Am*, 112(6):2612–2622, 2002.

[26] M. J. S. Lowe and O. Diligent. Low-frequency reflection characteristics of the s0 lamb wave from a rectangular notch in a plate. *J. Acoust. Soc. Am*, 111(1):64–74, 2002.

[27] D. N. Alleyne and P. Cawley. The interaction of lamb waves with defects. *IEEE Trans. Ultrason. Ferroelectr. Freq. Control*, 39(3):381–397, 1992.

[28] Y. Lu, L. Ye, Z. Su, and C. Yang. Quantitative assessment of through-thickness crack size based on lamb wave scattering in aluminium plates. *NDT & E Int.*, 41(1):59–68, 2008.

[29] E. Kostson and P. Fromme. Defect detection in multi-layered structures using guided ultrasonic waves. In D. Thompson and D. E. Chimenti, editors, *Review of Progress in Quantitative Nondestructive Evaluation*, volume 28A, pages 209–216, Melville, NY, 2009. AIP.

[30] P. Fromme. Influence of guided ultrasonic wave scattering directionality on the detection sensitivity for shm of fatigue cracks. In T. Kundu, editor, *Proceedings of the SPIE (Health Monitoring of Structural and Biological Systems)*, volume 7650, pages 76501M–76501M. SPIE, 2010.

[31] P. Cawley. Practical guided wave inspection and applications to structural health monitoring. In M. Veidt, F. Albermani, B. Daniel, J. Griffiths, D. Hargreaves, McArea R., P. Meehan, and A. Tan, editors, *Fifth Australasian Congress on Applied Mechanics (ACAM 2007)*, pages 12–21, Brisbane, 2007. Engineers Australia.

[32] P. Wilcox, B. Pavlakovic, M. Evans, K. Vine, P. Cawley, M. Lowe, and D. N. Alleyne. Long range inspection of rail using guided waves. In D. Thompson and D. E. Chimenti, editors, *Review of Progress in Quantitative Nondestructive Evaluation*, volume 22B, pages 236–243, Melville, NY, 2003. AIP.

[33] D. N. Alleyne and P. Cawley. Optimization of lamb wave inspection techniques. *NDT & E Int.*, 25(1):11–22, 1992.

[34] P. Fromme. Monitoring of plate structures using guided ultrasonic waves. In D. Thompson and D. E. Chimenti, editors, *Review of Progress in Quantitative Nondestructive Evaluation*, volume 27B, pages 78–85, Melville, NY, 2008. AIP.

[35] A.J Croxford, P.D Wilcox, B.W Drinkwater, and G Konstantinidis. Strategies for guided-wave structural health monitoring. *Proc. R. Soc. A*, 463(2087):2961–2981, 2007.

[36] T. Clarke, P. Cawley, P. D. Wilcox, and A. J. Croxford. Evaluation of the damage detection capability of a sparse-array guided-wave shm system applied to a complex structure under varying thermal conditions. *IEEE Trans. Ultrason. Ferroelectr. Freq. Control*, 56(12):2666–2678, 2009.

[37] K. F. Graff. *Wave Motion in Elastic Solids.* Dover Publications, Inc., Mineola, NY, 1991.

[38] J. L. Rose. *Ultrasonic Waves in Solid Media.* Cambridge University Press, Cambridge, 1999.

[39] B. N. Pavlakovic, M.J.S. Lowe, D. N. Alleyne, and P. Cawley. Disperse: A general purpose program for creating dispersion curves. In D. Thompson and D. E. Chimenti, editors, *Review of Progress in Quantitative Nondestructive Evaluation*, volume 16A, pages 185–192, New York, 1997. Plenum Press.

[40] P. D. Wilcox, M. J. S. Lowe, and P. Cawley. The excitation and detection of lamb waves with planar coil electromagnetic acoustic transducers. *IEEE Trans. Ultrason. Ferroelectr. Freq. Control*, 52(12):2370–2383, 2005.

[41] T. Clarke. *Guided wave health monitoring of complex structures*. PhD thesis, Imperial College London, 2009.

[42] H. M. Seung, H. W. Kim, and Y. Y. Kim. Development of an omni-directional shear-horizontal wave magnetostrictive patch transducer for plates. *Ultrasonics*, 53(7):1304–1308, 2013.

[43] P. Belanger. *Feasibility of thickness mapping using ultrasonic guided waves*. PhD thesis, Imperial College London, 2010.

[44] J. E. Michaels, S. J. Lee, J. S. Hall, and T. E. Michaels. Multi-mode and multi-frequency guided wave imaging via chirp excitations. In T. Kundu, editor, *Proceedings of the SPIE (Health Monitoring of Structural and Biological Systems)*, volume 7984, pages 79840I–1–79840I–10. SPIE, 2011.

[45] A. Croxford, P. Wilcox, and B. Drinkwater. Quantification of shm sensor array performance. In D. Thompson and D. E. Chimenti, editors, *Review of Progress in Quantitative Nondestructive Evaluation*, volume 28A, pages 942–949, Melville, NY, 2009. AIP.

[46] P. Fromme. Directionality of the scattering of the a0 lamb wave mode at cracks. In D. Thompson and D. E. Chimenti, editors, *Review of Progress in Quantitative Nondestructive Evaluation*, volume 1211, pages 129–136, Melville, NY, 2010. AIP.

[47] J. S. Hall, P. Fromme, and J. E. Michaels. Ultrasonic guided wave imaging for damage characterization. In *2011 Aircraft Airworthiness and Sustainment Conference*, San Diego, CA, 2011.

[48] P. Fromme. Noncontact measurement of guided ultrasonic wave scattering for fatigue crack characterization. In J. P. Lynch, C-B. Yun, and K. W. Wang, editors, *Proceedings of the SPIE (Sensors and Smart Structures Technologies for Civil, Mechanical, and Aerospace Systems 2013)*, volume 8692, pages 86921N–86921N–8. SPIE, 2013.

[49] Y. Lu, L. Ye, Z. Su, and N. Huang. Quantitative evaluation of crack orientation in aluminium plates based on lamb waves. *Smart Mater. Struct.*, 16(5):1907, 2007.

[50] S. Santhanam and R. Demirli. Reflection of lamb waves obliquely incident on the free edge of a plate. *Ultrasonics*, 53(1):271–282, 2013.

[51] M. J. S. Lowe and O. Diligent. Reflection of the fundamental lamb modes from the ends of plates. In D. Thompson and D. E. Chimenti, editors, *Review of Progress in Quantitative Nondestructive Evaluation*, volume 20A, pages 89–96, Melville, NY, 2001. AIP.

[52] P. D. Wilcox, A. Velichko, B. W. Drinkwater, A. J. Croxford, and M. D. Todd. Scattering of plane guided waves obliquely incident on a straight feature with uniform cross-section. *J. Acoust. Soc. Am*, 128(5):2715–2725, 2010.

[53] L. Taupin, A. Lhmery, V. Baronian, and A-S. Bonnet-BenDhia. Scattering of obliquely incident guided waves by a stiffener bonded to a plate. In *Journal of Physics: Conference Series*, volume 353, page 012011. IOP Publishing.

[54] H. Sohn. Effects of environmental and operational variability on structural health monitoring. *Proc. R. Soc. A.*, 365(1851):539–560, 2007.

[55] S. J. Lee, N. Gandhi, J. E. Michaels, and T. E. Michaels. Comparison of the effects of applied loads and temperature variations on guided wave propagation. In D. Thompson and D. E. Chimenti, editors, *Review of Progress in Quantitative Nondestructive Evaluation*, volume 30A, pages 175–182, Melville, NY, 2011. AIP.

[56] J. C. Dodson and D. J. Inman. Thermal sensitivity of lamb waves for structural health monitoring applications. *Ultrasonics*, 53(3):677–685, 2013.

[57] F. Chen and P. D. Wilcox. The effect of load on guided wave propagation. *Ultrasonics*, 47(1-4):111–122, 2007.

[58] M. Vospernig, R. Heuer, and M. Reiterer. Demonstration of guided wave sensor signals effected by cyclic loads and breathing fatigue cracks. In Christian Boller, editor, *Proceedings of the Sixth European Workshop on Structural Health Monitoring*, Berlin, 2012. DGZfP e.V.

[59] N. Gandhi, J. E. Michaels, and S. J. Lee. Acoustoelastic lamb wave propagation in biaxially stressed plates. *J. Acoust. Soc. Am*, 132(3):1284–1293, 2012.

[60] P. Cawley, M. J. S. Lowe, and P. D. Wilcox. An emat array for the rapid inspection of large structures using guided waves. *Journal of Nondestructive Testing*, 9(2):1–8, 2004.

[61] J. E. Michaels. Detection, localization and characterization of damage in plates with an in situ array of spatially distributed ultrasonic sensors. *Smart Mater. Struct.*, 17(3):035035, 2008.

[62] P. Fromme and C. Rouge. Directivity of guided ultrasonic wave scattering at notches and cracks. In *Journal of Physics: Conference Series*, volume 269, page 012018. IOP Publishing, 2011.

[63] T. Cicero. *Signal processing for guided wave structural health monitoring.* PhD thesis, Imperial College London, 2009.

[64] T. Carandente. *Interaction between the fundamental torsional guided wave mode and complex defects in pipes.* PhD thesis, Imperial College London, 2012.

[65] W. Zhu, J. L. Rose, J. N. Barshinger, and V. S. Agarwala. Ultrasonic guided wave ndt for hidden corrosion detection. *Journal of Research in Nondestructive Evaluation*, 10(4):205–225, 1998.

[66] E. J. Cross, G. Manson, K. Worden, and S. G. Pierce. Features for damage detection with insensitivity to environmental and operational variations. *Proc. R. Soc. A*, 468(2148):4098–4122, 2012.

[67] H. Kwun, G. M. Light, S. Kim, R. H. Peterson, and R. L. Spinks. Permanently installable, active guided-wave sensor for structural health monitoring. In D. Balageas, editor, *Proceedings of the First European Workshop on Structural Health Monitoring*, pages 390–397, Lancaster, PA, 2002. DEStech Publications, Inc.

[68] O. Putkis and A. J. Croxford. Continuous baseline growth and monitoring for guided wave shm. *Smart Mater. Struct.*, 22(5):055029, 2013.

[69] P. Fromme, P. D. Wilcox, M. J. S. Lowe, and P. Cawley. On the development and testing of a guided ultrasonic wave array for structural integrity monitoring. *IEEE Trans. Ultrason. Ferroelectr. Freq. Control*, 53(4):777–785, 2006.

[70] P. Fromme and M. B. Sayir. Detection of cracks at rivet holes using guided waves. *Ultrasonics*, 40(1):199–203, 2002.

[71] Z. Xiaoliang, H. Gao, G. Zhang, B. Ayhan, F. Yan, C. Kwan, and J. L. Rose. Active health monitoring of an aircraft wing with embedded piezoelectric sensor/actuator network: I. defect detection, localization and growth monitoring. *Smart Mater. Struct.*, 16(4):1208–1217, 2007.

[72] J. E. Michaels. Effectiveness of in situ damage localization methods using sparse ultrasonic arrays. In T. Kundu, editor, *Proceedings of the SPIE (Health Monitoring of Structural and Biological Systems)*, volume 6935, pages 35–46. SPIE, 2008.

[73] E. B. Flynn, M. D. Todd, P. D. Wilcox, B. W. Drinkwater, and A. J. Croxford. Maximum-likelihood estimation of damage location in guided-wave structural health monitoring. *Proc. R. Soc. A.*, 467(2133):2575–2596, 2011.

[74] J. S. Hall and J. E. Michaels. Minimum variance ultrasonic imaging applied to an in situ sparse guided wave array. *IEEE Trans. Ultrason. Ferroelectr. Freq. Control*, 57(10):2311–2323, 2010.

[75] C. M. Yeum, H. Sohn, J. B. Ihn, and H. J. Lim. Instantaneous delamination detection in a composite plate using a dual piezoelectric transducer network. *Compos. Struct.*, 94(12):3490–3499, 2012.

[76] S. R. Anton, D. J. Inman, and G. Park. Reference-free damage detection using instantaneous baseline measurements. *AIAA Journal*, 47:1952, 2009.

[77] S. S. Kessler, S. M. Spearing, and M. J. Atalla. In-situ damage detection of composites structures using lamb wave methods. In D. Balageas, editor, *Proceedings of the First European Workshop on Structural Health Monitoring*, pages 374–381, Lancaster, PA, 2002. DEStech Publications, Inc.

[78] A. Bagheri, K. Li, and P. Rizzo. Reference-free damage detection by means of wavelet transform and empirical mode decomposition applied to lamb waves. *J. Intel. Mat. Syst. Str.*, 2012.

[79] H. Sohn, D. Dutta, and Y-K. An. Temperature independent damage detection in plates using redundant signal measurements. *J. Nondestruct. Eval.*, 30(2):106–116, 2011.

[80] S. J. Lee, N. Gandhi, J. S. Hall, J. E. Michaels, B. Xu, T. E. Michaels, and M. Ruzzene. Baseline-free guided wave imaging via adaptive source removal. *Structural Health Monitoring*, 11(4):472–481, 2012.

[81] G. Konstantinidis, P. D. Wilcox, and B. W. Drinkwater. An investigation into the temperature stability of a guided wave structural health monitoring system using permanently attached sensors. *IEEE Sensors Journal*, 7(5):905–912, 2007.

[82] G. Manson, S. G. Pierce, and K. Worden. On the long-term stability of normal condition for damage detection in a composite panel. *Key Eng. Mat.*, 204-205:359–370, 2001.

[83] X. Chen, J. E. Michaels, S. J. Lee, and T. E. Michaels. Load-differential imaging for detection and localization of fatigue cracks using lamb waves. *NDT & E Int.*, 51(0):142–149, 2012.

[84] T. Clarke, F. Simonetti, and P. Cawley. Guided wave health monitoring of complex structures by sparse array systems: Influence of temperature changes on performance. *J. Sound Vib.*, 329(12):2306–2322, 2010.

[85] A. J. Croxford, J. Moll, P. D. Wilcox, and J. E. Michaels. Efficient temperature compensation strategies for guided wave structural health monitoring. *Ultrasonics*, 50(4-5):517–528, 2010.

[86] J. Moll and C. P. Fritzen. Guided waves for autonomous online identification of structural defects under ambient temperature variations. *J. Sound Vib.*, 331(20):4587–4597, 2012.

[87] A. J. Croxford, P. D. Wilcox, G. Konstantinidis, and B. W. Drinkwater. Strategies for overcoming the effect of temperature on guided wave structural health monitoring. In T. Kundu, editor, *Proceedings of the SPIE (Health Monitoring of Structural and Biological Systems)*, volume 6532, pages 11–19. SPIE, 2007.

[88] J. B. Harley and J. M. F. Moura. Scale transform signal processing for optimal ultrasonic temperature compensation. *IEEE Trans. Ultrason. Ferroelectr. Freq. Control*, 59(10):2226–2236, 2012.

[89] F. Shi, J. E. Michaels, and S. J. Lee. In situ estimation of applied biaxial loads with lamb waves. *J. Acoust. Soc. Am*, 133:677, 2013.

[90] G. Konstantinidis, B. W. Drinkwater, and P. D. Wilcox. The temperature stability of guided wave structural health monitoring systems. *Smart Mater. Struct.*, 15(4):967, 2006.

[91] V. Giurgiutiu. *Structural health monitoring: with piezoelectric wafer active sensors.* Elsevier Academic Press, Amsterdam, 2008.

[92] K. J. Schubert and A. S. Herrmann. On attenuation and measurement of lamb waves in viscoelastic composites. *Compos. Struct.*, 94(1):177–185, 2011.

[93] G. D. Connolly, J. Li, and S. I. Rokhlin. Fatigue crack monitoring in engine-grade titanium alloy by dynamic subtraction of surface acoustic wavemodulation. *NDT & E Int.*, 55(0):47–56, 2013.

[94] S. G. Taylor, G. Park, K. M. Farinholt, and M. D. Todd. Diagnostics for piezoelectric transducers under cyclic loads deployed for structural health monitoring applications. *Smart Mater. Struct.*, 22(2):025024, 2013.

[95] R. Kazys, L. Mazeika, R. Barauskas, R. Raisutis, V. Cicenas, and A. Demcenko. 3d analysis of interaction of lamb waves with defects in loaded steel plates. *Ultrasonics*, 44, Supplement(22):e1127–e1130, 2006.

[96] T. Clarke, F. Simonetti, S. Rokhlin, and P. Cawley. Development of a low-frequency high purity a0 mode transducer for shm applications. *IEEE Trans. Ultrason. Ferroelectr. Freq. Control*, 56(7):1457 –1468, 2009.

[97] D. N. Alleyne and P. Cawley. The excitation of lamb waves in pipes using dry-coupled piezoelectric transducers. *J. Nondestruct. Eval.*, 15(1):11–20, 1996.

[98] M. Seher, P. Huthwaite, M. J. S. Lowe, P. Nagy, and P. Cawley. Numerical design optimization of an emat for a0 lamb wave generation in steel plates. In D. Thompson and D. E. Chimenti, editors, *Review of Progress in Quantitative Nondestructive Evaluation*, volume 33, Melville, NY, 2014. AIP. Forthcoming.

[99] MKCNDT. Mssr-2020d brochure, 2010. Available online at http://www.mkckorea.com/export/swri/MsSR-2020.htm.

[100] G. Instanes, M. Toppe, S. Kristiansen, and P. Nagy. The use of non-intrusive ultrasonic intelligent sensors for corrosion and erosion monitoring. In *SPE International Conference on Oilfield Corrosion*. Society of Petroleum Engineers, 2010.

[101] G. M. Light, H. Kwun, S. Kim, and R. L. Spinks. Magnetostrictive sensor for active health monitoring in structures. In T. Kundu, editor, *Proceedings of the SPIE (Smart Nondestructive Evaluation for Health Monitoring of Structural and Biological Systems)*, volume 4702, pages 282–288. SPIE, 2002.

[102] A. Raghavan and C.E.S. Cesnik. Finite-dimensional piezoelectric transducer modeling for guided wave based structural health monitoring. *Smart Mater. Struct.*, 14(6):1448–1461, 2005.

[103] M. Drozdz, L. Moreau, M. Castaings, M. J. S. Lowe, and P. Cawley. Efficient numerical modelling of absorbing regions for boundaries of guided waves problems. In D. Thompson and D. E. Chimenti, editors, *Review of Progress in Quantitative Nondestructive Evaluation*, volume 25B, pages 126–133, Melville, NY, 2006. AIP.

[104] J. S. Bendat and A. G. Piersol. *Random Data: Analysis and Measurement Procedures*. John Wiley and Sons, Inc., New York, 3 edition, 2000.

[105] R. Blevins. *Formulas for Natural Frequency and Mode Shape*. Krieger Publishing, Malabar, FL, 2001.

[106] Polytec GMBH, Waldbronn, Germany. *Three-Dimensional Laser Vibrometer - Preliminary User Manual*, 2001.

[107] J. E. Michaels, A. J. Croxford, and P. D. Wilcox. Imaging algorithms for locating damage via in situ ultrasonic sensors. In *IEEE Sensors Applications Symposium 2008*, pages 63–67, 2008.

[108] Y. Lu and J. E. Michaels. A methodology for structural health monitoring with diffuse ultrasonic waves in the presence of temperature variations. *Ultrasonics*, 43(9):717–731, 2005.

[109] T. Clarke and P. Cawley. Enhancing the defect localization capability of a guided wave shm system applied to a complex structure. *Structural Health Monitoring*, 10(3):247–259, 2011.

[110] C. H. Wang, J. T. Rose, and F-K. Chang. A synthetic time-reversal imaging method for structural health monitoring. *Smart Mater. Struct.*, 13(2):415, 2004.

[111] J. L. Blackshire and A. T. Cooney. Characterization of bonded piezoelectric sensor performance and durability in simulated aircraft environments. In D. Thompson and D. E. Chimenti, editors, *Review of Progress in Quantitative Nondestructive Evaluation*, volume 25B, pages 1694–1701, Melville, NY, 2006. AIP.

[112] C. A. Paget, K. Levin, and C. Delebarre. Behavior of an embedded piezoceramic transducer for lamb wave generation in mechanical loading. In N. M. Wereley, editor, *Proceedings of the SPIE (Smart Structures and Materials 2000: Smart Structures and Integrated Systems)*, volume 3985, pages 510–520. SPIE, 2000.

[113] A. Raghavan and C. E. S. Cesnik. Effects of elevated temperature on guided-wave structural health monitoring. *J. Intel. Mat. Syst. Str.*, 19(12):1383–1398, 2008.

[114] J. T. Chambers, B. L. Wardle, and S. Kessler. Durability assessment of lamb wave-based structural health monitoring nodes. In *Proceedings of the 47th AIAA/ASME/ASCE/AHS/ASC Structures, Structural Dynamics and Materials Conference*, volume 11, pages 7920–7931, 2006.

[115] K. R. Mulligan, N. Quaegebeur, P. Masson, and S. Ltourneau. Correction of data gathered by degraded transducers for damage prognosis in composite structures. In *Annual Conference of the Prognostics and Health Management Society 2012*, volume 3, page 9, 2012.

[116] L. Yinghui and J. E. Michaels. Feature extraction and sensor fusion for ultrasonic structural health monitoring under changing environmental conditions. *IEEE Sensors Journal*, 9(11):1462–1471, 2009.

[117] M. Cinquin, M. Castaings, B. Hosten, P. Brassier, and P. Prs. Monitoring of the moisture content in carbon-epoxy plates using lamb waves. *NDT & E Int.*, 38(1):37–44, 2005.

[118] R. S. Martin, J. E. Michaels, and T. E. Michaels. Ultrasonic characterization of thermal gradients in a homogeneous plate. In D. Thompson and D. E. Chimenti, editors, *Review of Progress in Quantitative Nondestructive Evaluation*, volume 27B, pages 1199–1206. AIP, 2008.

[119] A. J. Kinloch. *Durability of Structural Adhesives.* Applied Science, London, 1983.

[120] K. Vine, P. Cawley, and A. J. Kinloch. Comparison of normal and oblique incidence ultrasonic measurements for the detection of environmental degradation of adhesive joints. *NDT & E Int.*, 35(4):241–253, 2002.

[121] R. D. Adams. *Adhesive bonding: Science, technology and applications.* CRC Press, Woodhead Publishing, Cambridge, 2005.

[122] Henkel Loctite. Loctite ®E-05CL ™ Hysol ®Epoxy Adhesive-Henkel. Available online at http://www.henkelna.com/product-search-1554.htm?nodeid=8797911449601.

[123] J. M. Allin. *Disbond detection in adhesive joints using low frequency ultrasound*. PhD thesis, Imperial College London, 2002.

[124] S. I. Rokhlin, B. Xie, and A. Baltazar. Quantitative ultrasonic characterization of environmental degradation of adhesive bonds. *J. Adhes. Sci. Technol.*, 18(3):327–359, 2004.

[125] M. J. S. Lowe. Matrix techniques for modeling ultrasonic waves in multilayered media. *IEEE Trans. Ultrason. Ferroelectr. Freq. Control*, 42(4):525–542, 2002.

[126] T. P. Pialucha. *The reflection coefficient from interface layers in NDT of adhesive joints*. PhD thesis, Imperial College London, 1992.

[127] V. K. Khanna. Adhesion delamination phenomena at the surfaces and interfaces in microelectronics and mems structures and packaged devices. *J. Phys. D. Appl. Phys.*, 44(3):034004, 2011.

[128] F. Sarvar, D. A. Hutt, and D. C. Whalley. Application of adhesives in mems and moems assembly: a review. In *Proceedings of the 2nd International IEEE Conference on Polymers and Adhesives in Microelectronics and Photonics, 2002*, pages 22–28, 2002.

[129] C. Bockenheimer, D. Fata, and W. Possart. New aspects of aging in epoxy networks. i. thermal aging. *J. Appl. Polym. Sci.*, 91(1):361–368, 2004.

[130] 3M. 3M Scotch-Weld Epoxy Adhesive DP105 Clear, 1.7 oz-Shop 3M. Available online at www.shop3m.com/62328714357.html.

[131] Hunstman. Araldite®2000 plus. Available online at http://www.huntsman.com/advanced_materials/a/Home/Adhesives/Araldite_R2000PLUS.

[132] X. Buch and M. E. R. Shanahan. Thermal and thermo-oxidative ageing of an epoxy adhesive. *Polym. Degrad. Stabil.*, 68(3):403–411, 2000.

[133] J. Park and J. Osenbach. Processability and reliability of epoxy adhesive used in microelectronic devices linked to effects of degree of cure and damp heat aging. *Microelectron. Reliab.*, 46(24):503–511, 2006.

[134] M. Frigione, M. Lettieri, and A. Mecchi. Environmental effects on epoxy adhesives employed for restoration of historical buildings. *Journal of Materials in Civil Engineering*, 18(5):715–722, 2006.

[135] R. Jourdain and S. Wilson. Thermally induced stresses in an adhesively bonded multilayer structure with 30-micron thick film piezoelectric ceramic and metal components. In W. Menz, S. Dimov, and B. Fillon, editors, *4M 2006 - Second International Conference on Multi-Material Micro Manufacture*, pages 259–262, Oxford, 2006. Elsevier.

[136] E. Kong. *Physical aging in epoxy matrices and composites*, volume 80 of *Advances in Polymer Science*, pages 125–171. Springer Berlin, Heidelberg, 1986.

[137] T. D. Chang and J. O. Brittain. Studies of epoxy resin systems: Part c: Effect of sub-tg aging on the physical properties of a fully cured epoxy resin. *Polym. Eng. Sci.*, 22(18):1221–1227, 1982.

[138] V. V. Belloncle and M. Rousseau. Ultrasonic measurements of pretreated aluminium joints durability during hot cycles. *Res. Nondestruct. Eval.*, 20(3):131–144, 2009.

[139] G. M. Odegard and A. Bandyopadhyay. Physical aging of epoxy polymers and their composites. *J. Polym. Sci. Pol. Phys.*, 49(24):1695–1716, 2011.

[140] C. V. Cagle. *Handbook of adhesive bonding.* McGraw-Hill, New York, 1973.

[141] C. Boller. Monitoring the integrity of aircraft structures - current procedures and smart sensing options. In P. D. Mangalgiri, A. R. Upadhya, and A. Selvarajan, editors, *Proceedings of International Conference on Smart Materials, Structures and Systems*, pages 31–42, New Delhi, 1999. Allied Publishers Ltd.

[142] G. W. C. Kaye and T. H. Laby. *Tables of Physical and Chemical Constants.* Longman Group Limited, Essex, 16 edition, 1995.

[143] P. M. Sutton. The variation of the elastic constants of crystalline aluminum with temperature between 63°k and 773°k. *Phys. Rev.*, 91(4):816–821, 1953.

[144] A. Lindrose. Ultrasonic wave and moduli changes in a curing epoxy resin. *Exp. Mech.*, 18(6):227–232, 1978.

[145] P. Wilcox, M. Lowe, and P. Cawley. Omnidirectional guided wave inspection of large metallic plate structures using an emat array. *IEEE Trans. Ultrason. Ferroelectr. Freq. Control*, 52(4):653–665, 2005.

[146] R. Ribichini, F. Cegla, PB Nagy, and P. Cawley. Experimental and numerical evaluation of electromagnetic acoustic transducer performance on steel materials. *NDT & E Int.*, 45(1):32–38, 2012.

[147] R. B. Thompson. A model for the electromagnetic generation and detection of rayleigh and lamb waves. *IEEE Trans. Sonics Ultrason.*, 20(4):340–346, 1973.

[148] P. Jeong, R. B. Thompson, and Y. H. Kim. Performance evaluation of the golay code pulse compression technique. *Res. Nondestruct. Eval.*, 8(3):125–147, 1996.

[149] S. Foster. Impulse response measurement using golay codes. In *ICASSP '86 Proceedings IEEE International Conference on Acoustics, Speech, and Signal Processing*, volume 11, pages 929–932. IEEE, 1986.

[150] A. P. Y. Phang, R. E. Challis, V. G. Ivchenko, and A. N. Kalashnikov. A field programmable gate array-based ultrasonic spectrometer. *Meas. Sci. Technol.*, 19(4):045802, 2008.

[151] S. Z. Budisin. New complementary pairs of sequences. *Electronics Letters*, 26(13):881–883, 1990.

[152] Ferroperm. Ferroperm - high quality piezoelectric ceramics for the electronics industry. Available online at `http://www.ferroperm-piezo.com/`.